IMT School for Advanced Studies, Lucca
Lucca, Italy

Phase Field methods for Fracture Mechanics in coupled problems

PhD Program in Systems Science

Curriculum in Computer Science and Systems Engineering

XXXV Cycle

By

Ángel de Jesús Valverde González

2023

The dissertation of Ángel de Jesús Valverde González is approved.

PhD Program Coordinator: Prof. Alberto Bemporad, IMT School for Advanced Studies Lucca

Advisor: Prof. Marco Paggi, IMT School for Advanced Studies Lucca

Co-Advisor: Prof. Jose Antonio Reinoso Cuevas, Universidad de Sevilla

The dissertation of Ángel de Jesús Valverde González has been reviewed by:

Prof. Fadi Aldakheel, Leibniz Universität Hannover

Prof. Emanuela Bosco, Eindhoven University of Technology

Prof. Javier Segurado, Universidad Politécnica de Madrid

IMT School for Advanced Studies Lucca
2023

Dedicado a la memoria de D. Miguel Ángel Valverde Vera y D.ª Antonia Margarita Guardia.

Contents

xi

List of Figures

xv

List of Tables

Acknowledgements

First of all, I would like to express my heartfelt gratitude to my advisors, Prof. José Antonio Reinoso Cuevas and Prof. Marco Paggi for their mentorship and guidance during my doctoral period. Their invaluable support not only enabled me to embark on this remarkable research endeavor but also paved the way for my future academic pursuits. Beyond their research supervision, I am deeply grateful for their personal support during hard times.

Most of the present Thesis is based on the articles listed in the Publications Section. Chapter 5 is based on a paper in preparation.

Chapter 2 is based on the article co-authored with Prof. Emilio Martínez-Pañeda, Dr. Adrià Quintanas-Corominas, Prof. José Reinoso and Prof. Marco Paggi. I would like to express my gratitude to Prof. Emilio Martínez-Pañeda for generously providing the essential materials along with their guidance that ultimately enabled the successful publication of this work. My special gratitude also goes to Dr. Adriá Quintanas-Corominas for always being available and a supportive colleague.

I want to dedicate a paragraph to my IMT Lucca friends who became my family during these last four years. First of all, a profound thank you goes to my dearest collaborators, Pavan and Maria Rosaria, who have proven to be more than just colleagues, supporting me in the difficult times. Outside of my line of work, my heartfelt gratitude to my dear friends Kristina, Stefano, Adam, Willemijn, Surya, Sean, Na, Mengjia, Ajinkya, Nicole, Chiara, Francesca R., Francesca S., Francesca M., Erica, Michal Lynn, Emanuele and Linda for providing personal support, while at the same time, organizing the best plans inside and outside the campus. Without all the students I met in IMT Lucca, doing the Ph.D. would have been much more complicated and tedious task.

Aprovecho este momento para cambiar al español, mi lengua materna, para dedicar unas palabras a mis amigos e investigadores españoles del IMT Lucca y de la Universidad de Sevilla. Empiezo expresando mi más profundo agradecimiento a mis queridos Juanfran y Alberto, con quienes espero que la vida nos brinde aún más momentos llenos de chistes, discusiones y aventuras compartidas. También le quiero dedicar unas palabras a Pablo y Víctor, quienes se destacan como los mejores cocineros y organizadores de fiestas en todo el campus del IMT. No puedo olvidarme de las nuevas generaciones: a Antonio y a Irene os deseo mucho ánimo en vuestro camino hacia el doctorado. En cuanto a Sevilla, aunque mi tiempo ha sido más irregular, quiero agradecer los buenos ratos y quedadas que hemos compartido tanto en la facultad como fuera de ella a mis compañeros de departamento y de sala: Ana, Alejandro, Juan Antonio, Sara, María, Juanjo, Teresa, Lorenzo, María Luisa, Eva, Pablo, Serafín y Carlos, así como a los profesores Israel García, Vladislav Mantic y Alejandro Estefani. Todos vosotros os merecéis todo lo bueno que os depare la vida de investigador, tanto profesional como personal. Gracias por ser parte de mi experiencia en el IMT Lucca y en la Universidad de Sevilla

Un agradecimiento especial va dirigido a los amigos que la vida me ha brindado, quienes han estado siempre apoyándome, incluso a pesar de la distancia. Muchísimas gracias a TODOS: Rafa, Charlie, Pablo, Alfonso, Encarni, Alberto, Miguel, Antonio, Javi, Adra, Marian, Ángel, Violeta, Ángela, Stefan, Cristina, Jesús, Inma, Gabri, Fran, Raúl, Álvaro, Carolina, Silvia, Marta, Juan, Sergio, Carlos, Stephanie, Robert... Entre ustedes se encuentran mis amigos de conciertos, con los que simplemente deseo que siempre haya uno más al que asistir; amigos con los que asistir religiosamente cada jueves al trivial en ese santuario que se ha convertido el Arcade para nosotros; amigos de escapadas a donde sea, ya sea de turismo

local, a descubrir un restaurante nuevo o a la playa; en general, amigos para compartir ese conjunto de vivencias que es la vida. Gracias a todos por ser parte de ella.

Quiero también dedicar unas palabras a unas personas muy especiales que llevan ya un tiempo conmigo. Aunque los vea poco, a diario se han dedicado desde siempre a dar los consejos más acertados, a brindar el mejor apoyo mediante sus bromas y en general, a hacer el día más llevadero. Muchas gracias a Sergio, Nil, Dodani, Dani, Andrey, Mauricio, Antonio, Revu, Juan, David, José Pedro y Felipe. Por último, quiero dedicar estas palabras a mis amigos Rocío, Dani y a la banda de rock Lèpoka por brindarme un inolvidable concierto en Madrid, que me permitió desconectar en un momento critico en el que la presión de finalizar este manuscrito pesaba duramente sobre mis hombros.

Finalmente, dejo este párrafo final para dedicar unas palabras a las personas más importantes de mi vida: mi familia. Quiero dar las gracias a mi madre María Dolores, a mi hermano Rubén y su pareja Andrea, a mi tío Francis y a mi primo Alejandro por su cariño, paciencia, apoyo y amor durante todos estos años y los que quedan por vivir. Mención especial para alguien que ha aparecido hace poco en mi vida y que ya ha hecho mucho, mi pareja Elvira, a la cual agradezco que siempre me esté animando a dar lo mejor de mí. Para acabar, quiero concluir acordándome de los que nos han dejado durante estos cuatro años pero que siempre han estado ahí, ya sea por las enseñanzas y el cariño que me dieron: mi padre Miguel Ángel y mi abuela Margarita. Descansad en paz, vuestro hijo y nieto no os olvida.

Publications

1. M.R. Marulli, A. Valverde-González, A. Quintanas-Corominas, M. Paggi, J. Reinoso, "A combined phase-field and cohesive zone model approach for crack propagation in layered structures made of nonlinear rubber-like materials", Computer Methods in Applied Mechanics and Engineering, ISSN 0045-7825, vol. 395, pp. 115007, May 2022.

2. A. Valverde-González, E. Martínez-Pañeda, A. Quintanas-Corominas, J. Reinoso, M. Paggi, "Computational modelling of hydrogen assisted fracture in polycrystalline materials", International Journal of Hydrogen Energy, ISSN 0360-3199, vol. 47(75), pp. 32235-32251, Sep. 2022.

3. A. Valverde-González, J. Reinoso, N. K. Jha, J. Merodio, M. Paggi, "A phase field approach to fracture for hyperelastic and visco-hyperelastic materials applied to pre-stressed cylindrical structures", Mechanics of Advanced Materials and Structures, ISSN 1537-6494, Oct. 2022.

4. A. Valverde-González, J. Reinoso, B. Dortdivanlioglu, M. Paggi, "Locking treatment of penalty-based gradient-enhanced damage formulation for failure of compressible and nearly incompressible hyperelastic materials", Computational Mechanics, ISSN 0178-7675, vol. 72(4), pp. 635-662, Oct. 2023.

Abstract

Nowadays, cutting-edge industry processes cannot thrive without the integration of multidisciplinary perspectives in all its associated processes. Even the field of Mechanics is not exempt from such approaches, since most recent studies now incorporate considerations spanning multiple size scales (multiscale) and encompassing various branches such as Chemistry, Biology, Electricity, and Magnetism, among others (multi-physics).

This is what constitutes the very essence of a coupled problem in Mechanics. The principal objective of this thesis is to specifically explore their impact on structural integrity and reliability in the field of Fracture Mechanics. Consequently, it is necessary to establish a robust mathematical framework to assess the mechanical behavior and failure strength, considering the intricate influence of the multi-scale and multiphysics fields associated with each problem. To accomplish this mission, we have primarily utilized the phase-field approach for fracture, alongside the continuum damage mechanics technique.

Our efforts have been devoted to shed light on representative coupled problems in Fracture Mechanics. To exemplify the breadth of this field, our research comprises a diverse spectrum of topics. First, the research deals on the problem of hydrogen embrittlement in polycrystalline materials. Moreover, the residual stress influence on the integrity of soft cylindrical tubes has been investigated. Furthermore, a computational framework for incompressible materials has been proposed. The final topic concerns the application of this last formulation in the simulation of swelling of thermoresponsive hydrogels.

Resumen

Hoy en día, los procesos industriales más innovadores no pueden prosperar sin la consideración de un punto de vista multidisciplinar aplicado a todos sus procesos. Incluso el campo de la Mecánica no se encuentra exento de ello, ya que los estudios más recientes en esta rama incorporan evaluaciones a múltiples escalas de tamaño (ejemplos multi-escala) y engloban diversas ramas como la Química, la Biología, la Electricidad y el Magnetismo, entre otras (multi-física).

Esto es lo que constituye la esencia misma de un problema acoplado en la Mecánica. El objetivo principal que persigue esta tesis es explorar específicamente su impacto en la integridad estructural en el campo de la Mecánica de la Fractura. En consecuencia, es necesario establecer un marco matemático sólido para evaluar el comportamiento mecánico y la resistencia a la falla, considerando la influencia de los campos multi-escala y multi-física asociados. Para ello, hemos utilizado principalmente el método *phase-field* enfocado a fractura, junto con la técnica de *continuum damage mechanics*.

Esta tesis se ha dedicado a analizar diversos problemas acoplados representativos con un enfoque en la Mecánica de la Fractura. Para ejemplificar la amplitud de este tema, esta investigación abarca un espectro diverso de temas. En primer lugar, se trata el problema de la fragilización por hidrógeno en materiales policristalinos. A continuación, se ha investigado la influencia que tienen las tensiones residuales en la integridad de tubos cilíndricos blandos. Además, se ha propuesto un marco computacional para estudiar materiales incompresibles. En el último capítulo se aplicará esta última formulación en la simulación de hinchazón en hidrogeles termosensibles.

Chapter 1

Introduction

1.1 A brief introduction to coupled problems in Computational Mechanics

Material is the definition given to what possesses a form, a body, a volume and occupies a position in the space. The area of engineering dedicated to characterize them and study possible manners of innovation is called Materials Engineering. Considering that the formation of such substance is owed to an assembly of particles called molecules, there exists a multitude of criteria for categorizing them from different points of view, being one of them based on scales: either through microscopic or macroscopic approaches. The choice between one or another scope depends on the specific engineering application's interests and requirements. The former is studied by means of magnifying instruments such a microscope, is efficient on the microscale level and is performed specially to explore a variety of physical phenomena reaching the atomic level. Such perspective leans more towards the domain of Materials Science.

Therefore, to enhance the engineering perspective, we can consider a macroscopic system in which the very large number of molecules is replaced as a continuous medium characterized by certain field quantities which are associated with the internal structure, giving birth to the disci-

pline of Continuum Mechanics. This approach is employed to shed light on various physical phenomena successfully without detailed information on the complexity of the microstructure. The predictions that Continuum Mechanics provides for engineering systems are effective for the design and the estimation of the service life for a wide range of materials and structures. Nonetheless, it is crucial not to disregard the fact that the macroscopic mechanical behavior depends on the microstructure, i.e., the physics and chemistry that they are built-on. In fact, materials are not isolated systems that do not interact with their environment, because that will be denying the existence of their microstructure. As a consequence of this, nowadays, in numerical analysis, mathematical models and computational techniques employing Continuum Mechanics are being exploited for solving coupled problems of multidisciplinary character in science and engineering, combining both approaches in terms of scale.

In order to express what are the ranges of such problems in a numerical context, the words from profs. Zienkiewicz and Chan in [1] can be recalled, stating the following: "Coupled problems are those applicable to multiple domains and dependent variables which usually (but not always) describe different physical phenomena". Coupled problems can be categorized following different criteria: whether their various domains do completely, partially or not overlap at all, meaning that the coupling happens via the partial differential equations used to describe the different phenomena or by the interactions of the boundary conditions imposed. Another standard to consider in their classification concerns if all the involved phenomena are from identical or different physics. Even they can be distinguished between for transient or steady-state solution in the event that the coupling happens only in time-dependent forms or once the steady state conditions are reached.

At this stage, it is instructive to include some typical examples of coupled problems for illustrative purposes. First of all, for different physics, we consider the classical thermo-mechanical coupling approach; under the influence of temperature, thermal strains and stresses are introduced into the mechanical model, subsequently changing the material response

of the material. This can be observed for example, in plasticity, where the thermal field affects the plastic flow of the material, due to the dependence of the plastic entropy in this parameter, according to Simo and Miehe [2]. On the other hand, following Li et al. [3], plastic deformation by slip generates heat, so the points of the materials might act as a heat source that should be considered for the thermal problem. Applications within this context concern industrial processes such as the forming and machining of steels and other alloys considering their microstructure. Additional examples where the thermal field affects the mechanical response can be observed in the behavior and integrity of polymers such as short fiber polymer composites [4, 5], elastomers [6] and hydrogels [7, 8], to cite a few of them.

Concerning chemo-mechanical approaches, it is worth mentioning corrosion phenomena, for instance, due to its practical impact. Referring to one of the most common yet difficult to reproduce, multiple failure mechanisms of several metals and alloys are associated with the exposition to corrosive environments. Accordingly, the surrounding atmosphere causes an electrochemical reaction with the material, leading to the creation of small pits within the metal that affects the structural integrity of the material, as it compromises its ductility and toughness and induces tensile stresses that lead to crack propagation. Examples of chemo-mechanical approaches involving corrosion are pitting [9, 10], stress-corrosion cracking [11, 12] and hydrogen embrittlement [13, 14]. Alternatively, chemo-mechanical approaches can involve another different physics such as electrical fields, for example Lithium batteries modelling [15, 16], or biological magnitudes, such as the bio-chemo-mechanical analysis of animal cells [17]. In addition to this, we can have coupled problems involving two different Mechanics fields modelled by different techniques: a solid illustration of that can be located in the modelling of the mechanics of arteries, as the growth and remodeling in the context of the arterial wall tissue can cause the apparition of radial residual stresses that can have fatal consequences in the form of aneurysms [18, 19, 20].

As mentioned above, coupled problems also exist through the inter-

action of two or more phases by means of an interface. That includes, for example, fluid-structure dynamic approaches, which have been vastly covered in the literature in the form of deformations and stresses [21, 22, 23] or changes of geometry [24] induced by pressure or friction fluid forces, to cite a few. Therefore, it could be envisaged that the term of "coupled problems" encompasses a wide range of different topics, where all the external or internal multiphysics affecting the material lead to changes in its structure that are inherent to their microscopic nature and that are reflected by the Continuum Mechanics theory in order to provide the problem with an engineering viewpoint. One vital property that is affected by these real life problems with a multidisciplinary vision is the structural integrity of the material itself, leading us to the next Section of this Chapter.

1.2 Fracture Mechanics in coupled problems

We have introduced thermal, electrical, chemical and biological concepts, among others, while speaking about coupled problems in the previous Section. For the sake of vividly illustrating the immensity and the complexity of the issue, on Fig. 1, we can graphically envisage the wide spectrum of possibilities to address (some of them have not been covered yet) in coupled problems for Computational Mechanics, benefited with the increase of multidisciplinary studies in both academic and industrial environments.

Common to each one of these problems, from a theoretical viewpoint reflected in Fig. 1, is the inherent existence of partial differential equations (PDEs) for their modelling. Such equations play a pivotal role in the modern scientific understanding of their behavior. Through the combination of this mathematical framework with the employment of a numerical method such as the Boundary Element Method (BEM) or fast Fourier transforms (FFT), among others, we can numerically solve the PDEs to delve deeper into the intricate events of these phenomena while gaining insight into their performance.
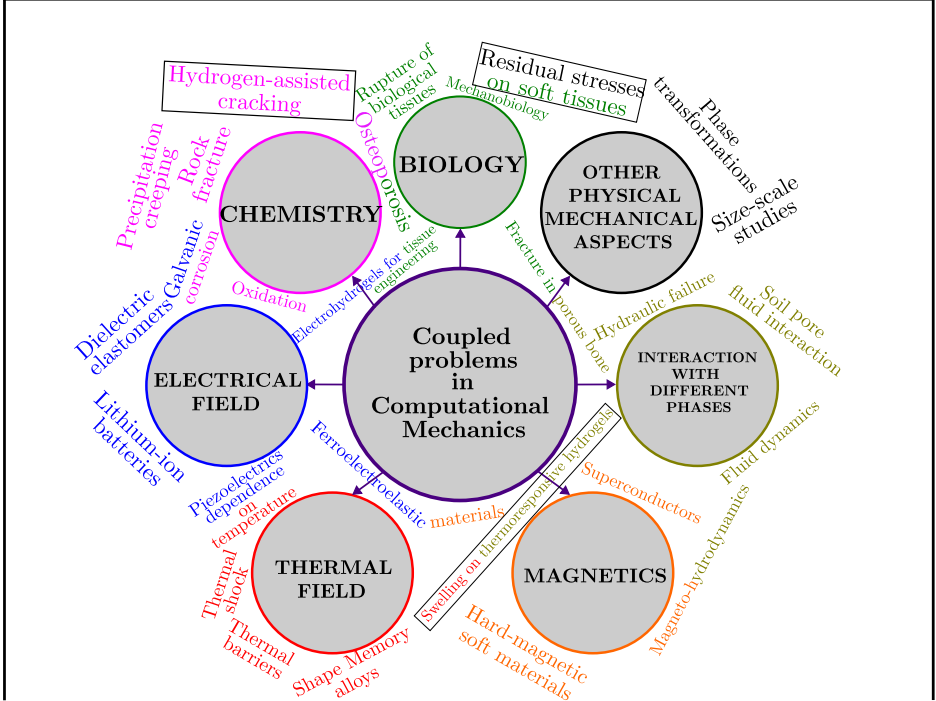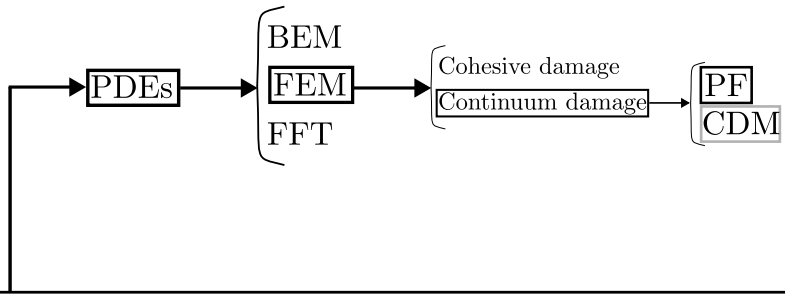
Figure 1: Graphical diagram trying to capture the spectrum of possibilities for fracture and damage modelling in Computational Mechanics for coupled problems, encompassing the disciplines of physics, chemistry, biology, fluid dynamics, magneticism and thermal and electrical energy, among others. Arising from the diagram, an outline is plotted unveiling the possible numerical techniques to carry out such analysis. **The covered topics and techniques inside this thesis are depicted within the frames on this picture.**

Throughout the content of this thesis, it is employed the numerical technique of the Finite Element Method (FEM) to solve the PDEs referred to some of the coupled problems exhibited in Fig. 1, with a prevailing focus in the field of Continuum Mechanics, specifically in the branch of Fracture Mechanics. This is the field of Mechanics concerned with the degree of safety of a structure against a crack, which represents a discontinuity present on the material, serving as the point where brittle fracture nucleates. It can vary from an extremely small size to much larger weld or fatigue cracks. Another matter of interest for the discipline of Fracture Mechanics are the conditions necessary for crack initiation, propagation and arrest. Their comprehension is facilitated through the assessment of the stress level, which measures the intensity of tensile stresses, necessary for the fracture of the material. From such study, we can obtain main fracture properties of the material such as the toughness, which is the ability to carry loads or deform plastically in the presence of a notch, a crucial feature in the design of materials.

The origin of the engineering field of Fracture Mechanics can be traced back to the pioneering works made by Griffith [25], who seminally investigated the phenomenon of brittle fracture on glasses. Over a hundred years after the publication of this theory, its relevance is still intact, as it provides an essential tool on industry to shed light on the analysis of flaws of manufactured pieces to discover which are safe and which are liable to propagate and subsequently, collapse. On the research level, the field of Fracture Mechanics has grown at an accelerated rate caused by the advent of techniques of damage and fracture modelling in Mechanics, and proof of that is the overwhelming number of predictive approaches and formulations derived from this theory that have been applied to countless problems, including coupled problems.

1.2.1 Numerical methods stemmed from Fracture Mechanics: synthesis of the current state of the art

Within failure analysis of cracking events, several methods have been proposed from Fracture Mechanics to model crack propagation in solids

employing the FEM. Following the outline plotted in Fig. 1, depending on how cracks are modelled, it can be distinguished two main categories of methods proposed within the related literature: discrete (cohesive damage) and diffuse (continuum damage) methods. The first category of techniques consist of methods which model the crack as a sharp discontinuity that divides the solid into two crack surfaces and consider that fracture propagation happens via separation of both surfaces. This kind of methods encompasses techniques such as the weakest-link methods [26, 27], path-independent J-integral formulations [28, 29, 30], dislocation-based models [31, 32], and, specially, cohesive zone methods [33, 34, 35, 36], that have been extensively applied in the literature for fracture for coupled problems. Nevertheless, discrete methods display limitations when dealing with complex conditions of fracture: first of all, they require the mesh generated for FEM analysis to conform with the crack geometry (unlike other techniques such as the BEM), which is a difficult task considering that crack propagation may happen in arbitrary directions. In addition to this, several complex conditions of practical applications may arise during this process, such as mixed mode, interacting cracks, branching, among others, which require special yet computationally costly modifications to perform in the model [37].

On the other category of techniques, we have smeared damage approaches that, contrary to the discrete methods, do not pretend to capture pre-defined cracks, but to incorporate internal damage parameters to characterize the stiffness degradation of materials. Within this approach, fracture is conceived as the result of damage accumulation due to the development of microcracks. As a consequence of this, dependence on the mesh size and alignment sensitivity may happen once failure is being approached. This may lead to a softening in the strain that can be fixed by introducing an internal length scale on the system [38, 39]. Applied to coupled problems, techniques from this branch can be classified into Continuum Damage approaches (CDM) [40, 41], peridynamical approaches [42, 43, 44] and phase field (PF) methods. Following the outline given in Fig. 1, as PF techniques have proven to be one of the most suitable tools to model fracture in coupled problems, we have dedicated

most of the work of this thesis to study them and subsequently, extend the range of application of this technique in several multiphysics problems. On a smaller scale, some explorations have been performed with the CDM method within this thesis, being them developed in Chapter 4 of the current manuscript.

1.2.2 The Phase Field approach for fracture

Basic definitions

The PF method is based on Griffith's idea of competition between the elastic strain energy density Ψ and fracture energy $\mathcal{G}_C$. According to Griffith's theory for brittle fracture [25], during crack propagation, fracture energy increases because of the onset of crack surfaces, causing the elastic energy within the solid to reduce. Therefore, this theoretical framework establishes that a crack will propagate when this elastic energy is reduced more or equally than the increase of the crack surface energy. This parameter is referred to as $\mathcal{G}$, being $\mathcal{G}_C$ the critical value that leads to crack propagation, also called fracture toughness, which is a property of the material independent from the geometry. In terms of equations, this competition can be expressed in the form of the global potential of the problem Π:

$$\Pi(\varepsilon) = \underbrace{\int_{\Omega/\Gamma} \Psi \, dV + \int_{\Gamma} \mathcal{G}_C \, dA}_{\Pi_{\text{int}}} - \Pi_{\text{ext}} \tag{1.1}$$

being ε the symmetric strain tensor; Ω, the solid domain; and Γ, a discrete internal discontinuity within the body. The contribution to the internal functional rendering of the energy dissipation due to fracture events is recalled through the PF approach of fracture postulated by [45]. In order to start with its approximation for fracture, consider Fig. 2, in a one-dimensional setting the topology of a sharp and a diffusive crack topology.

For the sharp crack (Fig. 2(a)), such behavior can be described by the auxiliar field variable $\mathfrak{d}(x) \in [0, 1]$ with
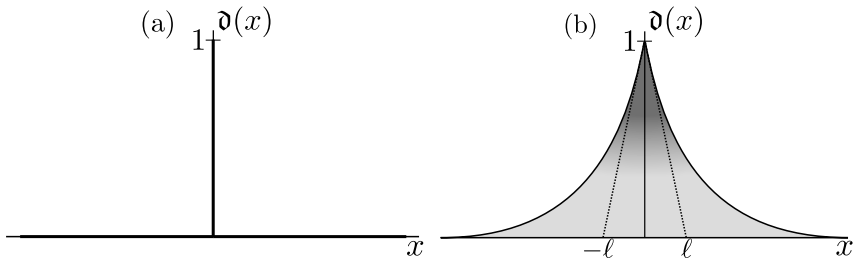
Figure 2: Sharp (a) and diffusive (b) crack morphologies.

$$\mathfrak{d}(x) = \begin{cases} 1 & \text{if } x = 0 \\ 0 & \text{elsewhere} \end{cases} \tag{1.2}$$

which is referred to as the crack PF parameter, with $\mathfrak{d} = 0$ and $\mathfrak{d} = 1$ denoting the pristine and broken states of the solid, respectively. The smooth PF, in Fig. 2(b), representing a diffusive crack pathology can be represented by the following function:

$$\mathfrak{d}(x) = e^{\frac{|-x|}{\ell}} \tag{1.3}$$

where the length scale parameter ℓ is what determines the width of the smearing function and at the limit of $\ell \to 0$ approximates the discrete crack topology.

The variational approach from Francfort and Marigo [45] substitutes the idea of the sharp crack with a gradient region ranging from intact to damaged material. Thus finding a global minimizer in the potential of the problem, which following Griffith's theory, the PF method relies on the aforementioned competition postulated in Eq. (1.1). By regularizing the crack functional in the solid, for the term of the surface energy, we can perform:

$$\int_\Gamma \mathcal{G}_C \, \mathrm{d}A \approx \int_\Omega \mathcal{G}_C \gamma_l(\mathfrak{d}, \nabla \mathfrak{d}) \, \mathrm{d}V \tag{1.4}$$

Here, $\gamma_l(\mathfrak{d}, \nabla \mathfrak{d})$ is the crack surface density function, which has the following expression, according to a Poisson-type equation:

$$\int_\Omega \gamma_l(\eth, \nabla\eth) \, \mathrm{d}V = \int_\Omega \frac{1}{c_w} \left[\frac{1}{\ell} w(\eth) + \ell|\nabla\eth|^2\right] \mathrm{d}V \qquad (1.5)$$

where $w(\eth)$ is called the geometric crack function, and can be written as:

$$w(\eth) = \upsilon\eth + (1 - \upsilon)\eth^2 \qquad (1.6)$$

where υ is a coefficient. $w(\eth)$ determines the crack distribution according to the PF parameter; and c_w is the scaling parameter and is computed as:

$$c_w = 4 \int_0^1 w^{-1/2}(\hat\eth) \, \mathrm{d}\hat\eth \qquad (1.7)$$

Recalling the previous derivations, the crack can be regularised by this transition region, and therefore, the potential strain energy function expressed in Eq. (1.1) can be rewritten as:

$$\Pi(\varepsilon, \eth) = \int_\Omega g(\eth)\Psi(\varepsilon) \, \mathrm{d}V + \int_\Omega \mathcal{G}_C\gamma_l(\eth, \nabla\eth) \, \mathrm{d}V - \Pi_{\text{ext}} \qquad (1.8)$$

where $g(\eth)$ is the degradation function and its role is to reduce the elastic strength of the material upon crack propagation.

As it is observed, there are several parameters that differ in the state of art for the variational PF formulation. They can be split in the criterion used to track the damaged material stiffness, in the conditions used to enforce crack irreversibility and in the modelling of the sharp crack. For all the works carried out within this thesis, in general (with some modifications, as we will see in the forthcoming Chapters), the so called AT-2 approach proposed by Bourdin et al. [46] is employed. This theoretical framework postulate that the degradation function will have a quadratic dependence on $\eth$ that reads

$$g(\eth) = (1 - \eth)^2 + \mathcal{K} \qquad (1.9)$$

where $\mathcal{K}$ is a small parameter used to avoid ill-conditioning in the stiffness matrix upon broken stage. In addition to this, this variational formulation proposes the following value for γ_l

$$\int_\Omega \gamma_l(\mathfrak{d}, \nabla\mathfrak{d}) \; \mathrm{d}V = \int_\Omega \frac{1}{2\ell}\mathfrak{d}^2 + \frac{\ell}{2}|\nabla\mathfrak{d}|^2 \; \mathrm{d}V \qquad (1.10)$$

meaning that the AT-2 approach considers $c_0 = 2$ and $w(\mathfrak{d}) = \mathfrak{d}^2$ (obtained by considering $\xi = 0$). As stated by Bourdin et al. [46] and Miehe et al. [47], by developing Eq. (1.8) and considering the Gauss divergence theorem, the local governing functions of the problem can be obtained. As can be observed in Eqs. (1.11)-(1.12), they are two partial differential equations: one for the stress equilibrium criterion, accounting for the damage in the stiffness; and the energy dissipation equation, using to compute the crack evolution:

$$\boldsymbol{\nabla} \cdot \left\{ [(1-\mathfrak{d})^2 + \mathcal{K}]\boldsymbol{\sigma}_0 \right\} = \mathbf{0} \quad \text{in } \Omega \qquad (1.11)$$

$$\mathcal{G}_C \left(\frac{1}{\ell}\mathfrak{d} - \ell\nabla^2\mathfrak{d} \right) - 2(1-\mathfrak{d})\Psi = 0 \quad \text{in } \Omega \qquad (1.12)$$

where $\boldsymbol{\sigma}_0$ is the intact stress tensor. One of the most appealing aspects of the PF formulation is its simplicity to model fracture, as it only requires two Euler-type PDEs to model brittle fracture, serving as compelling evidence for its exploitation to model a wide variety of different problems concerning failure in Computational Mechanics.

Phase field studies: extensions, current boundaries and applications for coupled problems

Upon the publication of the seminal variational framework by Francfort and Marigo [45], important efforts have been dedicated towards this technique to improve algorithm robustness [47, 48, 49], to implement new methods for discretization [50, 51] and to propose new aspects for implementation [46, 52, 53]. From these devoted efforts and the various approximations, its original approach residing in Griffith's thermodynamics framework has been extended for ductile fracture [54, 55, 56], dynamic fracture [57, 58], cohesive fracture [59], composite delamination [60, 61, 62], among others.

In the light of all the previous advantages presented for PF modelling and the extensions observed to model all kinds of failure within the solid,

the expansion of its applicability to model fracture in coupled problems is hardly unexpected. Such exploitation is due to, i) for multi-physics problems involving electrical, thermal or chemical fields it normally only requires to add the Euler-type PDE modelling its behavior, thus only adding computational cost to the problem and ii) its straightforward implementation to model problems involving different size-scales (meso-scale problems, on the level of grain modelling), complex geometries (that may lead to arbitrary cracking, such as corrosion pits) and, even, with different phases. These two benefits have significantly eased the implementation of the PF technique for the various multiphysics topics that have been tackled within this thesis, which are the ones framed in the graphic represented in Fig. 1.

With these advantages at hand, an introduction is provided in this Section for the many fields where this approach for fracture has been exploited: concerning the classical thermo-mechanical approach, we have the pioneering works from Miehe et al., where is presented a generalized approach for thermo-elastic [63] and thermo-plastic [64] solids concerning the crack driving force from the energetic definition coupled with the heat conduction and convection with the crack surfaces. More applied frameworks concerning problems of this field can be found for example in the works for anisotropic fracture of rock salt performed by Na and Sun [65], in the simulation of chemo-thermo-mechanical fracture in cement-based materials carried out by Nguyen et al. [66] and for thermo-dynamic fracture implemented by Svolos et al. [67]. Recently, the approach has been extended from solid formulation to solid shells in the works performed by Kumar et al. to analyze thin-walled structures [68] and functionally graded materials [69].

Moving on to diffusion-related problems, the literature of PF problems proposed in this literature is also relevant. Starting with fluid-structure methods, we have the works of Miehe et al. on hydraulic fracture of porous media [70, 71]. Similar to this is the problem for hydrogels, which will be covered in detail in this thesis. They are elastomeric materials able to absorb an enormous quantity of water without altering its polymeric network, forming a swollen aggregate with the fluid

molecules called hydrogel. The modelling of its failure mechanisms employing the PF technique has been briefly studied [72, 73, 74].

Another important diffusion-related problem is hydrogen embrittlement, a specific kind of corrosion involving the entrance of hydrogen within the lattice of the solid, leading to a subsequent weaking of the metallic bonds that causes a drop in the ductility and toughness of the material. With all the sights pointing towards a hydrogen economy, it is not surprising to see that the fracture induced by this phenomenon has been properly covered within the literature in the form of macroscopic approaches [75, 76, 77, 78]. However, as hydrogen embrittlement is a problem for a microscopic viewpoint due to the size of the atom of hydrogen, it is necessary an approach for fracture combining both macroscopic and microscopic viewpoints to analyze its induced failure and that is one of the topics will be digging within this thesis.

The thoughts that may come from this Section is that the PF method is a robust and solid method to model all kinds of problems on the level of Finite Element (FE) implementations. However, the main problem that all continuum damage models held, PF approaches among them, is that all the damage-associated variables are simply accumulated on the Gauss integration points, different from the explicit representation of fracture that one might get from discrete approaches such as the Cohesive Zone Model. As a consequence of this, they are conceived to be less accurate than discrete Fracture Mechanics methods to model failure of pre-existent cracks.

However, one should not forget that fracture onset and subsequent propagation in a material is strongly influenced by the presence of inhomogeneities, such as grain boundaries, voids, inclusions, crack tortuosity... meaning that the toughness of the material can be increased or reduced by these different phenomenon, thus meaning that the simplest failure on the material level is not that elementary. Correspondigly, this is where the PF approach for fracture comes handy, as it has proven its utility in its robust performance to model fracture in different heterogeneous media [79, 80, 81, 82]. The modelling of heterogeneous materials constitutes another motivation on why the PF technique is a fitting choice

when dealing with coupled problems in fracture and why we have decided to dedicate a thesis on its application to multiple multi-physics applications.

1.3 Objectives

With the advent of new interdisciplinary research in the industrial field, when designing a structure for commercial sectors such as the hydraulic or ship-building industries, among others, the study dedicated to the degree of safety cannot just be limited to the Mechanics field.

In light of this, the objective of this methodology relies on the design and testing of several materials taking into account the exposition to several multi-physics fields encompassing thermal, chemical and biological concepts, among others. Within this context, the PF method, a well-established technique for modeling fracture in the discipline of Continuum Mechanics, has been successfully exploited to monitor the crack initiation and propagation in materials under different operational and environmental conditions. This method has proven its applicability in various coupled problems. Following this input, the primary goals of the present thesis have been:

- The implementation and development of several innovative PF formulations for modelling failure in coupled problems. This has been performed by exploring complex multidisciplinary problems by incorporating the PDE that regulates their multiphysics behavior into the PF variational formulation.

- Special focus is devoted to the insertion of the PF on coupled problems that have little connection between each one, as a manner to quantify its potential. The rationale behind this decision stems from the author's recognition that the existing knowledge on this subject remains somewhat shallow, given the immensity of the field (and even after the completion of this thesis, the surface of the problem will have been merely scratched). Thus, the goal is to push the

boundaries of the PF method in modeling different yet challenging multiphysics issues, i.e., the ones framed in Fig. 1.

- The long-term objective of this research is to shed light into the understanding of the tackled coupled problems. As the presented topic is covered, by delving deeper into the peculiarities of the physical and chemical constitutions inherent to these phenomena will unveil additional insights for further research. Such plausible extensions will be displayed in the Section for Future developments tackled in Chapter 6.

The specific objectives of this thesis encompass relevant challenges for the following scenarios:

- The modelling of hydrogen embrittlement phenomena considering the polycrystalline microstructure of metals following a micro-embedded into macro-scale FE approach. Previous studies have not accounted for the interactions between the grain boundaries and the hydrogen in terms of structural integrity, which lead to a competition between transgranular and intergranular fracture that is thoroughly covered.

- Aiming to introduce PF theory into large strains formulation, the simulation of pre-stressed cylindrical structures subject to axial pulling loads is accomplished. The presence of such residual stresses is owed to the manufacture and growth of such tubes and, among other fields of investigation, they play an important role in arterial failure, as they can trigger the formation and rupture of aneurysms. Such events can give rise to life-threatening situations, serving as compelling evidence for the utmost relevance and importance of this study.

- This thesis seeks to include damage modeling within another non-local diffuse fracture framework. In the light of this idea, employing the CDM approach, damage on hyperelastic materials vulnerable to locking pathologies is addressed in this thesis by introducing

an innovative element technology that incorporates mixed interpolation within the FEM.

- Finally, the culmination of this thesis involves the integration of the theory for large strains with the mixed element technology in order to model thermoresponsive hydrogels. These materials, to circumvent the locking pathologies inherent in single-field formulations, need extra degrees of freedom (DOFs) along with special interpolation to alleviate such inconveniences. This thesis is aimed to solve them by leveraging the aforementioned element technology, with the ultimate goal of extending its application to address fracture within these materials.

Each one of these challenges for coupled problems are outlined in Section 1.4.

1.4 Covered approaches

1.4.1 Hydrogen embrittlement

Hydrogen is at the core of the most promising solutions to the global energy crisis. Hydrogen isotopes fuel the nuclear fusion reaction, the most efficient potentially useable energy process. Moreover, hydrogen is widely seen as the energy carrier of the future and the most versatile means of energy storage. It can be produced via electrolysis from renewable sources, such as wind or solar power, and stored to be employed as a fuel or as a raw material in the chemical industry. Hampering these opportunities, hydrogen is known for causing catastrophic failures in metallic structures. Through a phenomenon often termed hydrogen embrittlement, metals exposed to hydrogen containing environments experience a significant reduction in ductility, fracture toughness and fatigue resistance [83, 84, 85]. In the presence of hydrogen, otherwise ductile metals generally fail in a brittle manner, with cracking often nucleating and propagating along grain boundaries [86, 27]. This ductile-to-brittle shift of metallic alloys in hydrogeneous environments is arguably one of

Figure 3: On the left, Cheesegrater Building, second tallest building in London, UK. Source [89].

the biggest threats to the deployment of a hydrogen energy infrastructure, making it to the headlines of severe important journals around the world. For example, in 2015, concerns were raised when the Cheesegrater bulding (Fig. 3), the second tallest building in London, lost three bolts due to fracture in less than three months [87]. Further studies revealed that these failures were due to hydrogen embrittlement and while there were no apparent satefy issues, dozens of long bolts of the structure were replaced after these series of incidents. A similar situation happened in the San Francisco-Oakland Bay Bridge in 2008 (Fig. 4) [88], where a number of rods installed earlier that year failed prematurely due to the combination of hydrogen-induced fracture, while simultaneously being immersed in water.

In order to analyze these phenomena, in Chapter 2 a combined PF and cohesive zone formulation for hydrogen embrittlement that resolves

Figure 4: San Francisco–Oakland Bay Bridge in California, USA. Source [90].

the polycrystalline microstructure of metals is presented. Unlike previous studies, the current deformation-diffusion-fracture modelling framework accounts for hydrogen-microstructure interactions and explicitly captures the interplay between bulk (transgranular) fracture and intergranular fracture, with the latter being facilitated by hydrogen through mechanisms such as grain boundary decohesion. We demonstrate the potential of the theoretical and computational formulation presented by simulating inter- and trans-granular cracking in relevant case studies. Firstly, verification calculations are conducted in order to analyze how the framework predicts the expected qualitative trends. Secondly, the model is used to simulate recent experiments on pure Ni and a Ni-Cu superalloy that have attracted particular interest. We show that the model is able to provide a good quantitative agreement with testing data and yields a mechanistic rationale for the experimental observations. On Fig. 5, a graphic sketch of the problem presented in Chapter 2 for hydrogen embrittlement and subsequent induced fracture of polycrystalline materials is depicted.
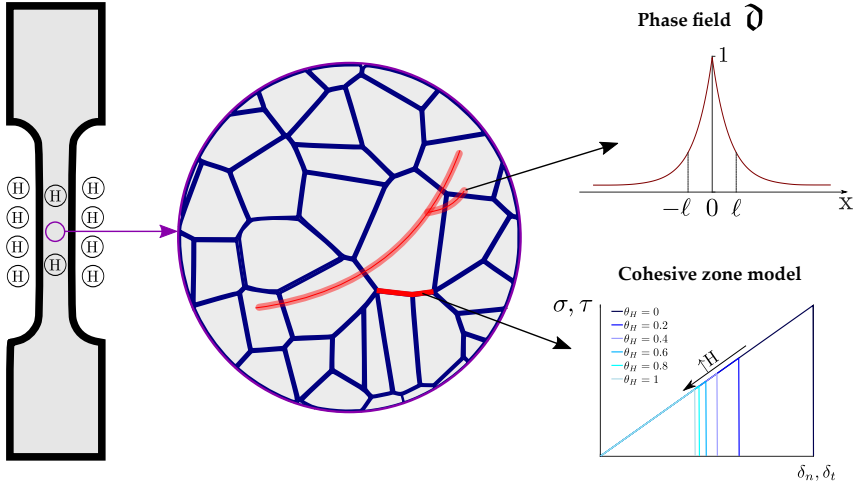
Figure 5: Sketch summarising the modelling framework: the polycrystalline microstructure of metals exposed to hydrogen is explicitly simulated, with the PF method being employed to describe the growth of ductile transgranular cracks while hydrogen-assisted grain boundary decohesion is captured by means of a cohesive zone model. Some of the key variables of the model, that is covered in Chapter 3, are shown; namely, the PF order parameter $\mathfrak{d}$, the PF length scale ℓ (governing the size of the interface region), the hydrogen coverage θ_H, and the cohesive tractions (σ, τ) and separations (δ_n, δ_t).

1.4.2 Residual stresses on cylindrical visco-hyperelastic soft tissues

Cylindrical structures (tube mechanics) are elements of considerable interest in applications concerning rubber-like materials and soft tissues and can be categorized as either thin or thick-walled structures. Complying with this structural feature, the existence of residual stresses within the body does affect its mechanical behavior. Residual stresses are associated with different processes used to manufacture materials [91] as well as with living tissues growth [92], among other areas. Specifically, within the biomechanics field, residual stresses can be revealed by cutting (closed and unloaded) axial segments of arteries since they deform

when they are slit [93]. It is well known that residual stresses play an important role in the biological process of homeostasis, which is the state of steady internal, physical and chemical conditions maintained during optimal functioning by living systems [94]. A matter of upmost important to the scientific community (with a clear benefit for the society) is the role that residual stresses, and other factors, play in the understanding of arterial failure. From the mechanical standpoint, arterial failure is affected by bulging- and bending-related instabilities of inflated and extended tubes. These aspects have been lately investigated within the context of aneurysms formation and rupture caused by high blood pressure and weakening of the artery wall [95, 96, 97]. Critical clinical applications of such study are vital, for instance, to people who suffer the Marfan syndrome, which is an inherited connective tissue disorder affecting the heart tissues and can lead to aortic aneurysms, heart valve diseases and, in the worst cases, to life-threatening aortic dissections (see Fig. 6). Contrary to the metals modelled in Chapter 2 under small strains theory, such tubes require to be modelled as visco-hyperelastic materials with the more complex large strain theory, adding the visco-elastic contribution from the microscopical description of the chains movement, being this microscopic-based approach embedded into the current continuous framework of finite viscoelasticity coupled with the incorporation of residual stresses.

Encompassing this investigation, in Chapter 3, the mechanical modeling of nonlinear visco-hyperelastic residually stressed materials obtained from an invariant-based constitutive energy framework is coupled with the PF approach to fracture. The main target regards the extension of the PF method to simulate pre-stressed cylindrical structures subjected to monotonic axial pulling load upon failure. This formulation is incorporated into a numerical procedure using the Finite Element Method (FEM), in particular, it is implemented in the commercial FE package ABAQUS as a user subroutine UMAT. Results suggest the dependence of the mechanical behavior and the crack pattern of these structures on not only viscous parameters like the relaxation time and the displacement rate, but also on the strength of the residual stress field, which in turn
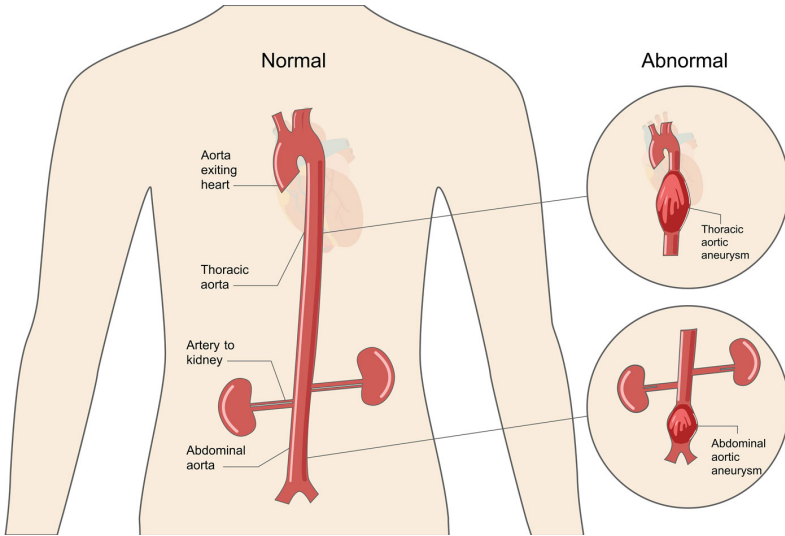
Figure 6: Representation of an aortic aneurysm and an aortic dissection, conditions to whom people suffering from Marfan syndrome are most vulnerable to. Residual stresses in arteries constitute an important risk factor to this pathologies. Source [98].

depends on geometrical characteristics of the cylindrical structure such as the radius or the length. A range of solutions related to crack propagation is shown for different cylindrical structures, from azimuthal crack propagation to axial one. The proposed framework aims to provide an extended application for the already-defined visco-hyperelastic formulation by the inclusion of residual stresses.

1.4.3 Volumetric and shear locking of hyperelastic materials

We have devoted the vast majority of this thesis on exhibiting the potential that PF displays on modelling coupled problems. In line with it, another diffuse failure approach called gradient-enhanced Continuum Damage (CDM) has emerged as a robust formulation that ensures the well-posedness of equations, avoiding strong mesh sensitivity and thus

leading to vanishing localized failure regions by the employment of internal length scales accompanying an Euler-Lagrange equation [99, 100]. These kinds of contributions have been discussed in detail; see [101, 102, 103]. In particular, gradient-enhanced CDM has been successfully exploited for a countless variety of both geometrically linear [104, 105, 106] and nonlinear models [107, 108, 109, 110, 111], including the extension to gradient-enhanced damage plasticity [112, 113, 114, 115].

This similar approach to PF presents several yet-to-fully-tackle damage applications. In Chapter 4, and on parallel to what has been presented for soft tissues in Chapter 3, we will cover damage on deformable nearly incompressible and compressible hyperelastic materials prone to volumetric and shear locking, respectively.

On volumetric locking, being amply reported in the related literature, numerical modelling of nearly incompressible hyperelastic materials using displacement-based (single field) FE schemes suffer from the well-known volumetric locking, which overestimates the stiffness of materials when the Poisson ratio is high ($\nu \sim 0.5$) [116]. In engineering practice, the problem can be solved by the use of meshless techniques [117, 118, 119, 120], smothered FE approaches (sFEM) [121, 122, 123], discontinuous Galerkin methods [124, 125, 126, 127] or by lower integration algorithms of the divergence terms, among other alternatives. In particular, a mixed three-field displacement-pressure-Jacobian mixed FE formulation which uses a lower-order approximation for the Lagrange multipliers associated with the volumetric pressure [128, 129, 130, 131, 132, 133] has been employed, being named `Q1P0` or Simo-Taylor-Pister elements. In Chapter 4, we have aimed for the development of a `Q1Q1P0` formulation with the combination of such elements with the gradient-enhanced CDM technique with the target of modelling damage in nearly incompressible hyperelastic materials avoiding volumetric locking issues.

Importantly, shear locking can also alter the compliance of the specimen with bending effects in large deformation analysis [134]. In order to overcome this shear locking pathology, several techniques have been proposed in the last decades: use of higher order FE formulations [135, 136, 137], isogeometric analysis [138, 139, 140, 141], reduced integra-

tion [142, 143] and the application of mixed methods and formulations, such as the approach for incompatible modes [144] or the enhanced assumed strain technique [145, 146, 147], among others. In Chapter 4, we also aim at developing a full integration formulation combining the EAS method considering 24 incompatible deformation modes, `Q1E24`, with a gradient-enhanced CDM approach to analyze damage in samples under bending loads which are prone to display shear locking phenomena, i.e., `Q1Q1E24`.

In summary, in Chapter 4, we will present the consistent formulation and the assessment of the corresponding performance of (i) a mixed displacement-enhanced assumed strain (EAS) `Q1Q1E24` employing a total Lagrangian formulation, and (ii) a three-field mixed displacement-pressure-Jacobian `Q1Q1P0` formulation. The novel `Q1Q1E24` and `Q1Q1P0` formulations are consistently derived and numerically implemented, providing a satisfactory agreement with respect to `ABAQUS` built-in elements handling the treatment of shear and volumetric locking, respectively, in conjunction to the modelling damage phenomena via the use of a penalty-based gradient-enhanced formulation. This performance is examined via several numerical applications. Furthermore, the final example justifies the need for a formulation combining both mixed FE approaches to simulate problems encompassing both locking issues (shear and volumetric locking), which can be performed using a combination of the `Q1Q1E24` and `Q1Q1P0` herein proposed.

1.4.4 Thermoresponsive hydrogels

Elastomeric materials which can absorb large quantities of water without disrupting their polymeric network form a swollen aggregate called hydrogel. Their applications concern a wide range of different fields, such as smart valves [148, 149, 150], sensors [151, 152, 153, 154], tissue engineering [155, 156, 157, 158] and drug delivery systems [159, 160, 161, 162, 163]. The reason behind this displayed versatility is related to their ability to withstand large deformations combined to the dependence of their mechanical response on environmental changes in chem-

ical fields and pH [164, 165], electric fields [166, 167], light [168, 169], humidity [170, 171] and temperature [172, 173, 174], among others. Focusing on the latter property, there exists a subclass of hydrogels called thermoresponsive hydrogels, which, when saturated in an aqueous solution, exhibit swelling to a large extent when being heated above or cooled down a critical temperature T_c. The former ones exhibit an upper critical swelling temperature (UCST) point, belonging to this behavior natural hydrogels such as like agarose, agar, collagen and gelatin [175, 176, 177]. On the other side, hydrogels exhibiting a lower critical swelling temperature (LCST) swells by a factor of ten times when they are cooled below the typical temperature, being framed within this pattern considerably employed hydrogels like poly(N-isopropylacrylamide) (PNIPAM) [178, 179, 180, 181] and polyethylene glicol (PEG) [182, 183, 184], among others. The behavior of both thermoresponsive hydrogels is represented graphically in Fig. 7 and on the course of our experiments to characterize them, we have managed to capture this in the lab with agarose experiments plotted in Fig. 8, where it is observed that in the interval of 40ºC to 45.6ºC, the critical temperature is hit for this UCST hydrogel. The proposed framework will be dedicated specially to the analysis of thermoresponsive gels.

On Chapter 5 of the current thesis, a stable thermo-chemo-mechanical user-element subroutine (UEL) dedicated to study the complex material behavior of thermoresponsive hydrogels along several examples of transient diffusion-driven swelling deformations is presented, encompassing the large strain theory developed in Chapter 3 with the idea of a mixed formulation based in the content of Chapter 4. For this purpose, the research focuses on the development of a new FE formulation that approximates the displacement via quadratic shape functions and both the chemical potential and the temperature by linear functions, all along with a mixed variational approach, this new element presented is denoted as Q2Q1Q1. Throughout the content that encompasses this Chapter, the proposed formulation will be validated by its capture of the LCST and UCST behavior that the thermoresponsive hydrogels display and subsequently, it will be used from a quantitative standpoint to address
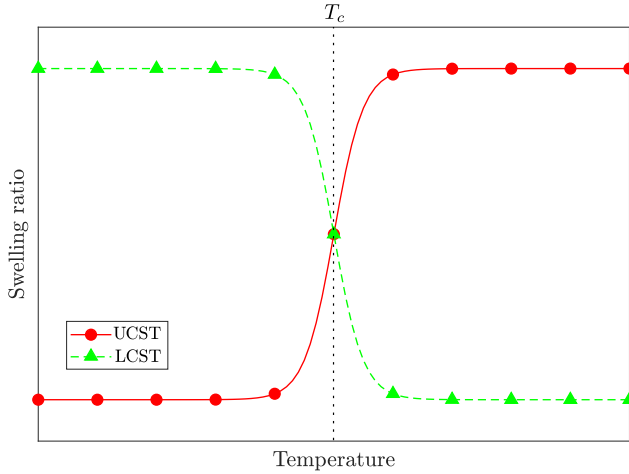
Figure 7: Symbolic graphic representation on the evolution against temperature for UCST and LCST hydrogels.

its robustness and accuracy in capturing experimental tests with different boundary conditions. Together with this new formulation and complying with the outline of this thesis, we will be presenting the preliminary results that come from coupling this new formulation with the PF method for fracture.

The extension that this Chapter aims to represent within the Computational Mechanics field is to be first inf-sup stable formulation for modelling on thermoresponsive hydrogels. In multi-field schemes, instabilities often occur in the assumed strain and stress fields. When dealing with incompressible materials, single-field formulations exhibit what is called volumetric locking, which is the over-stiffening of the elements of the material when the Poisson ratio ν is close to 0.5. In order to remove this pathology, mixed formulations concerning the pressure as a Lagrange multiplier are introduced. Nevertheless, these systems are prone to suffer spatial instabilities, as they do not fulfill the inf-sup condition, also called Ladyzhenskaya–Babuška–Brezzi (LBB) condition [185, 186], that is the sufficient condition that partial differential equation sys-
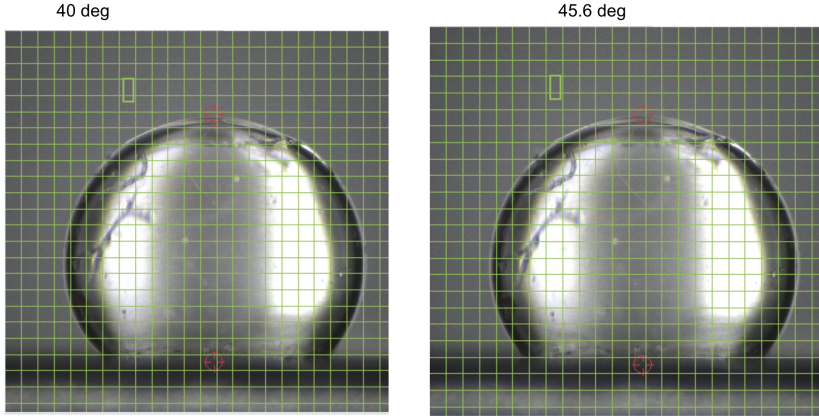
Figure 8: Dependence on temperature for UCST hydrogel *agarose*. It is observed that between the interval of 40ºC and 45.6ºC where the swelling ratio is increased. Obtained from the collaboration with prof. Dortdivanlioglu from the Soft Mechanics group in The University of Texas at Austin.

tems have to attain for a saddle point problem to have an unique solution to the problem. What happens with mixed formulations like linear displacement-pressure elements is that, as they do not attain this condition, they tend to suffer spurious oscillations in the result. Therefore, the Q2Q1Q1 element aims to encompass an inf-sup stable element, while, at the same time, to prove its accuracy with the physics by resolving and capturing some representative experimental problems for thermoresponsive hydrogels. Such framework aims to be extended in the immediate future to model fracture for these kind of gels, as there is no LBB-stable user-element subroutine available in the literature that encompasses the PF technique to model failure for UCST and LCST hydrogels.

1.5 Outline of the thesis

The content within this thesis is sorted according to the complexity of the constitutive theory, arranged in ascending order. Chapter 2 delves into the development of the hydrogen embrittlement phenomenon in poly-

crystalline materials comprising small strains theory with PF and CZM methods. In Chapter 3, for a large displacement theory, the PF fracture modelling of pre-stressed cylindrical soft tissues is introduced. Chapter 4 presents the combination of the mixed element formulation with the nonlocal diffuse damage framework of CDM. Consequently, Chapter 5 progresses through the framework for thermoresponsive hydrogels modelling built-on the integration of the mixed element technology with the large strain theory. Lastly, Chapter 6 delves into the conclusions and future developments for each one of the presented approaches, in both English and Spanish languages.

Chapter 2

Hydrogen-induced fracture in polycrystalline materials

Chapter 2 is based on our own publication [187].

The first coupled problem to address within this thesis is the Hydrogen Embrittlement (HE) issue, which has been known to be a cause of fracture in metals since the 19th-Century [188]. This phenomenon consists of a dangerous and unpredictable degradation of ductility and strength caused by the presence of gaseous Hydrogen (H) in the local environment [189]. It threatens the progress made on metallurgical optimization, being this a negative effect on several industrial sectors, such as the aerospace, transport, marine, and energy ones [190, 191, 192]. The structural integrity of the employed materials for these areas is a highly relevant multiphysics problem because of their interaction with corrosive environments. As of today, the micro-mechanism governing HE is yet to be fully understood. Proof of that is the absence of a database on the mechanical response of steels affected by HE [193]. Hence, there is a strong need to understand, quantify, and model how hydrogen affects the mechanical performance of metals, inducing fracture, and reduces its durability.

A vast literature has been devoted to shed light into the physical mechanisms behind HE [194, 32, 195, 192, 196, 197], and to develop

mechanistic predictive models that can prevent failures and map safe regimes of operation [198, 199, 200, 201, 78]. The vast majority of the computational models developed for predicting hydrogen assisted cracking fall into two categories: (i) discrete methods, such as cohesive zone models [13, 202, 203, 204], and (ii) diffuse approaches, such as phase field or other non-local damage models [75, 205, 206, 76, 207, 77]. Cohesive zone models and other discrete methodologies are suitable to describe the nucleation and propagation of sharp cracks through a predefined path. Phase field fracture methods have additional modelling capabilities and can also deliver predictions when the crack trajectory is unknown, when failure is triggered by defects of arbitrary shape, and when the fracture process is complex (e.g., involving the interaction between multiple defects). Both classes of models can be readily coupled with the hydrogen transport equation and have been successful in qualitatively capturing the main experimental trends, such as the sensitivity to loading rate, hydrogen concentration, and material strength. However, these modelling studies treat materials as isotropic continuum solids, without resolving the underlying microstructure. Microstructurally-sensitive works have been recently carried out [208, 14, 209, 210, 211, 212, 213], but these are limited to capture the interplay between diffusion and deformation, and do not explicitly simulate fracture. The micromechanical fracture of polycrystalline materials in hydrogen-containing environments has been simulated in the works of Rimoli and Ortiz [214], Benedetti *et al.* [215], and De Francisco *et al.* [216]. In these works, a cohesive zone formulation was used to predict the failure of grain boundaries, neglecting transgranular cracks.

On the mark of this thesis, we present a new microstructurally-sensitive computational framework employing the small deformation theory for predicting hydrogen assisted fractures. For the first time, the model combines a phase field description of bulk fracture with a cohesive zone model for intergranular cracking. This enables capturing both ductile transgranular fracture and brittle intergranular fracture, and the transition from one to the other. The mechanical and hydrogen transport

problems are strongly coupled, with the hydrostastic stress driving hydrogen transport and the hydrogen content reducing the grain boundary strength. The fracture of polycrystalline solids is simulated, with the bulk deformation response being characterised by von Mises plasticity theory. All this theoretical information is provided in Section 2.1 and Section 2.2 gives insight on the numerical tools used for the implementation of the model. Numerical experiments are conducted to gain insight into the mechanisms of hydrogen-assisted grain boundary decohesion. To validate the proposed formulation, we present some verification examples in the form of 10-grain and 50-grain single edge notched tension specimens in Section 2.3.1. Main focus is on Ni and Ni superalloys, where hydrogen assisted failures are known to be governed by grain boundary decohesion [86, 217]. Among other case studies, the model is used to provide a mechanistic rationale to two recent sets of experiments on Monel K-500 [218] (Section 2.3.2) and pure Ni [86] (Section 2.3.3) that have attracted particular interest in the hydrogen embrittlement community.

Nomenclature

Ω	Body domain
$\mathbb{R}^n$	Collection of ordered lists of n real numbers
$\partial\Omega$	Boundary of the solid
$\mathbf{n}$	Normal outward vector
Γ_ℓ	Discrete internal discontinuity
Γ_i	Pre-existing interfaces
$\mathbf{x}$	Position vector
$\mathbf{u}$	Displacement field vector
$\partial\Omega_u$	Boundary region with a Dirichlet condition of prescribed displacements
$\partial\Omega_t$	Boundary region with a Neumann condition of prescribed tractions
$\mathbf{t}$	Traction vector
$\boldsymbol{\varepsilon}$	Small deformation tensor
∇	Gradient operator
$\mathfrak{d}$	Phase-field parameter
ℓ	Length scale parameter
$\partial\Omega_q$	Boundary region with a Neumann condition of prescribed hydrogen flux
$\mathbf{J}$	Hydrogen flux
$\partial\Omega_C$	Boundary region with a Dirichlet condition of prescribed hydrogen concentration
C	Hydrogen concentration
γ_C	Interfacial fracture energy
$\mathcal{G}_C$	Bulk material toughness
Ψ	Strain energy density

Nomenclature

Π_{int}	Internal potential energy
$\Pi^{(b)}$	Bulk potential energy
$\Pi^{(i)}$	Interface potential energy
D	Diffusion coefficient
$\mathrm{d}V$	Differential of volume
$\mathrm{d}A$	Differential of area
$\nabla \cdot [\bullet]$	Divergence operator
q	Concentration of flux exiting the body
μ	Chemical potential
μ^0	Chemical potential in the standard case
R	Ideal gas constant
T	Temperature
θ_L	Occupancy of lattice sites
$\bar{V}_H$	Partial molar volume of hydrogen in solid solution
σ_H	Hydrostatic stress
N	Number of lattice sites
Ψ^e	Strain energy density term associated with the elastic part
Ψ^p	Strain energy density term associated with the elastic part
λ	First Lamé constant
G	Second Lamé constant (shear modulus)
$\mathrm{tr}(\bullet)$	Trace operator
$\boldsymbol{\sigma}$	Cauchy stress tensor
$\boldsymbol{\varepsilon}^e$	Elastic term of the small deformation tensor
$\boldsymbol{\varepsilon}^p$	Plastic term of the small deformation tensor
σ_f	Current yield stress
σ_y	Initial yield stress
$\varepsilon^{\mathrm{eq}}$	Accumulated equivalent plastic strain
E	Young's modulus
n	Strain hardening exponent
W_C	Work required to create two new surfaces
$g(\mathfrak{d})$	Degradation function
γ_l	Crack energy density functional
$\mathcal{K}$	Residual stiffness parameter
$\partial_{[\bullet]}$	Partial derivative operator
Ψ^e_+	Elastic part of the strain energy density associated with tensile states
Ψ^e_-	Elastic part of the strain energy density associated with compressive states
K	Bulk modulus
$\mathcal{H}$	History field variable
$\boldsymbol{\sigma}_0$	Undamaged Cauchy stress tensor
t_n	Normal cohesive traction
t_{nc}	Critical normal cohesive traction
t_t	Tangential cohesive traction
t_{tc}	Critical tangential cohesive traction
δ_{nc}	Critical normal cohesive separation
δ_{tc}	Critical tangential cohesive separation
γ_{IC}	Mode-I interfacial fracture energy
γ_{IIC}	Mode-II interfacial fracture energy
θ_H	Hydrogen coverage

Nomenclature

$\gamma_{C,0}$	Critical interfacial energy in absence of hydrogen
χ	Hydrogen damage coefficient
Δg_b^0	Gibbs free energy
$\mathbf{N}$	Shape functions
m	Number of nodes
$\mathbf{d}$	Nodal displacements
$\hat{\mathfrak{d}}$	Nodal phase field parameter
$\hat{\mathbf{C}}$	Nodal hydrogen concentration
$\mathbf{B_d}$	Standard strain matrix
$\mathbf{B}$	Compatibility matrix
$\mathbf{R^d}$	Residual of the displacement field $\mathbf{u}$
$\mathbf{R}^{\hat{\mathfrak{d}}}$	Residual of the phase-field parameter $\mathfrak{d}$
$\mathbf{K^{dd}}$	Displacement-displacement Jacobian term for global N-R scheme
$\mathbb{C}$	Local Jacobi tangent
$\mathbf{K}^{\hat{\mathfrak{d}}\hat{\mathfrak{d}}}$	PF-PF Jacobian term for global N-R scheme
$\mathbf{R}^{\hat{C}}$	Residual of the hydrogen concentration C
$\mathbf{K}^{\hat{C}\hat{C}}$	Hydrogen concentration-hydrogen concentration Jacobian term for global N-R scheme
$\mathbf{M}^{\hat{C}\hat{C}}$	Hydrogen concentration capacity matrix
ν	Poisson's ratio
u_y	Vertical displacement
C_{env}	Environmental hydrogen concentration
a_t	Transition flaw size
K_{Ic}	Critical stress intensity factor
u_x	Horizontal displacement

2.1 Theoretical formulation

Complying with the infinitesimal deformation setting, the point of departure of the current modeling framework concerns the consideration of an arbitrary body $\Omega \in \mathbb{R}^{n_{dim}}$ with a delimiting external surface $\partial\Omega \in \mathbb{R}^{n_{dim}-1}$ with outward normal $\mathbf{n}$. It is also assumed the existence of a discrete internal discontinuity Γ_l due to the potential development of fracture events and pre-existing interfaces arranged in the set Γ_i. This body is surrounded by a hydrogen-rich atmosphere that provokes the diffusion of hydrogen concentration throughout the body. As detailed in the forthcoming subsections, this leads to a three-field boundary value problem, where the displacement field, the fracture status, and the hydrogen concentration are the primary unknowns.

Recalling basic aspects on the theoretical formulation, the position
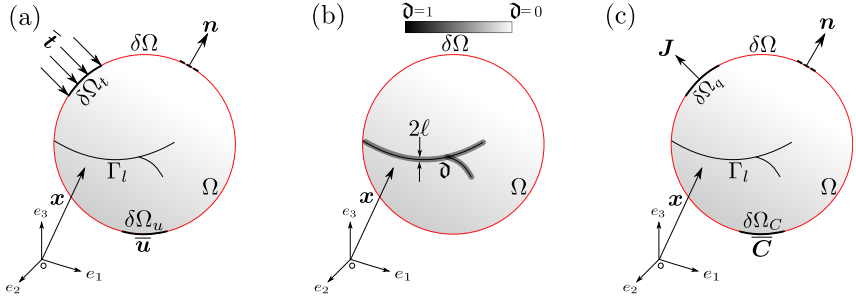
Figure 9: Schematic representation of the three-field boundary value problem: (a) displacement, (b) phase-field fracture, and (c) hydrogen diffusion.

of an arbitrary point in the bulk is noted by the vector $\mathbf{x}$ in the global Cartesian setting (Fig. 9(a)). The delimiting surface of the body is decomposed into: the region $\partial\Omega_u$, where the displacement $\mathbf{u}$ is prescribed by Dirichlet-type boundary conditions (BCs) and $\partial\Omega_t$, where the traction $\mathbf{t}$ is prescribed via Neumann-type conditions, such that $\partial\Omega = \partial\Omega_u \cup \partial\Omega_t$ and $\partial\Omega_u \cap \partial\Omega_t = \emptyset$. The deformation process is characterized by the small deformation tensor $\varepsilon(\mathbf{x})$, which is defined as the symmetric part of the displacement gradient: $\varepsilon(\mathbf{x}) := \nabla_{\mathbf{x}}^{\mathrm{sym}}\mathbf{u}(\mathbf{x})$.

Concerning the cracking phenomena, the so-called phase-field fracture approach is herewith exploited, which resembles a non-local damage model. This approach triggers the occurrence of fracture using the consideration of a scalar-valued variable $\mathfrak{d}$. This methodology allows the regularization of sharp cracks within a diffusive region characterized by the length ℓ (Fig. 9(b)), following the diffusive crack morphology stated in Fig. 1(b).

Regarding the hydrogen concentration diffusion problem, the surface of the body is divided into two parts: the region $\partial\Omega_q$, where the hydrogen flux $\mathbf{J}$ is prescribed featuring a Neumann-type boundary condition, and the region $\partial\Omega_C$ where the hydrogen concentration C is prescribed. (Fig. 9(c)).

In addition to bulk fracture, our microstructurally-sensitive formulation employs a cohesive zone model to describe the failure of grain

boundaries. As shown in Fig. 5, we explicitly model the polycrystalline microstructure of metals and predict intergranular and transgranular cracking events. The phase field fracture method is used to describe transgranular cracks, which are associated with a ductile fracture process, while a cohesive zone model is employed to predict the decohesion of grain boundaries. Since the latter correspond to a brittle failure and are triggered by the presence of hydrogen, the interfacial fracture energy γ_C is defined as a function of the hydrogen concentration C. Conversely, the bulk material toughness $\mathcal{G}_C$ is considered to be a hydrogen-insensitive constant that characterises the resistance of the material to undergo microvoid cracking. Accordingly, for a solid with strain energy density $\Psi(\varepsilon, \mathfrak{d})$, the internal functional of the mechanical system comprises the bulk ($\Pi_{int}^{(b)}$) and interfacial ($\Pi_{int}^{(i)}$) contributions, reading

$$\Pi_{int}(\mathbf{u}, \mathfrak{d}, C) = \underbrace{\int_{\Omega/\Gamma_l} \Psi(\varepsilon, \mathfrak{d}) \mathrm{dV} + \int_{\Gamma_l} \mathcal{G}_C \mathrm{d}\Gamma_l}_{\Pi_{int}^{(b)}} + \underbrace{\int_{\Gamma_i} \gamma_C(C) \mathrm{d}\Gamma_i}_{\Pi_{int}^{(i)}} \quad (2.1)$$

2.1.1 Material formulation: chemo-elastoplasticity

The deformation and diffusion problems are intrinsically coupled as hydrogen transport within the crystal lattice is driven by gradients of concentration and hydrostatic stress. We focus our attention on the transport of diffusible hydrogen and consider the influence of traps in the cracking process by using the Langmuir-Mclean isotherm to estimate the hydrogen coverage at grain boundaries. The role of microstructural traps upon slowing down diffusion can also be taken into account through an appropriate choice of the (apparent) diffusion coefficient D. Mass conservation requirements relate the rate of change of the hydrogen concentration C to the hydrogen flux through the external surface,

$$\int_{\Omega} \frac{\mathrm{d}C}{\mathrm{d}t} \mathrm{d}V + \int_{\partial\Omega} \mathbf{J} \cdot \mathbf{n} \, \mathrm{d}A = 0 \quad (2.2)$$

The strong form of the balance equation can be readily obtained by

making use of the divergence theorem and noting that the expression must hold for any arbitrary volume,

$$\frac{\mathrm{d}C}{\mathrm{d}t} + \nabla \cdot \mathbf{J} = 0 \tag{2.3}$$

For an arbitrary, suitably continuous, scalar field, δC, the variational statement (Eq. (2.3)) reads,

$$\int_\Omega \delta C \left(\frac{\mathrm{d}C}{\mathrm{d}t} + \nabla \cdot \mathbf{J} \right) \mathrm{d}V = 0 \tag{2.4}$$

Rearranging, and making use of the divergence theorem, the weak form renders,

$$\int_\Omega \left[\delta C \left(\frac{\mathrm{d}C}{\mathrm{d}t} \right) - \mathbf{J} \cdot \nabla \delta C \right] \mathrm{d}V + \int_{\partial\Omega_q} \delta C q \, \mathrm{d}A = 0 \tag{2.5}$$

where $q = \mathbf{J} \cdot \mathbf{n}$ is the concentration flux exiting the body across $\partial\Omega_q$. The diffusion is driven by the gradient of the chemical potential $\nabla\mu$, with the chemical potential of hydrogen in lattice sites being given by,

$$\mu = \mu^0 + RT \ln \frac{\theta_L}{1 - \theta_L} - \bar{V}_H \sigma_H \tag{2.6}$$

Here, θ_L is the occupancy of lattice sites, which is related to the concentration and number of sites as $\theta_L = C/N$. Also, μ^0 denotes the chemical potential in the standard case, and σ_H is the hydrostatic stress. The last term of Eq. (2.6) corresponds to the so-called stress-dependent part of the chemical potential μ_σ, with $\bar{V}_H$ being the partial molar volume of hydrogen in solid solution. The mass flux follows a linear Onsager relationship with μ_σ, which is often derived from Eq. (2.6) by adopting the assumptions of low occupancy ($\theta_L \ll 1$) and constant interstitial sites concentration ($\nabla N = 0$) (see, e.g., [219, 220]), such that

$$\mathbf{J} = -\frac{DC}{RT} \nabla\mu = -D\nabla C + \frac{D}{RT} C \bar{V}_H \nabla \sigma_H \tag{2.7}$$

where T is the absolute temperature and R is the ideal gas constant. Accordingly, the hydrogen transport equation becomes

$$\int_\Omega \left[\delta C \left(\frac{1}{D} \frac{dC}{dt} \right) + \nabla \delta C \nabla C - \nabla \delta C \left(\frac{\bar{V}_H C}{RT} \nabla \sigma_H \right) \right] \mathrm{d}V = -\frac{1}{D} \int_{\partial\Omega_q} \delta C q \, \mathrm{d}A$$

(2.8)

As evident from Eqs. (2.6)-(2.8), the presence of hydrostatic stresses (or volumetric strains) brings a reduction in chemical potential and an increase in hydrogen solubility. Thus, an appropriate description of the stress state in the solid is needed to quantitatively estimate the hydrogen distribution. Here, we choose to describe the deformation of the solid using conventional von Mises plasticity. Accordingly, the total strain energy density of the solid is given by the sum of the elastic and plastic parts,

$$\Psi = \Psi^e \left(\varepsilon^e \right) + \Psi^p \left(\varepsilon^p \right) = \frac{1}{2} \lambda \left[\mathrm{tr} \left(\varepsilon^e \right) \right]^2 + G \, \mathrm{tr} \left[\left(\varepsilon^e \right)^2 \right] + \int_0^t \left(\boldsymbol{\sigma} : \dot{\varepsilon}^p \right) \mathrm{d}t$$

(2.9)

where λ is the first Lamé parameter and G is the shear modulus. Also, the Cauchy stress tensor is given by $\boldsymbol{\sigma}$, and ε^e and ε^p respectively denote the elastic and plastic strain tensors. Isotropic power law hardening behaviour is assumed by adopting the following hardening law:

$$\sigma_f = \sigma_y \left(1 + \frac{E \varepsilon^{\mathrm{eq}}}{\sigma_y} \right)^{(1/n)}$$

(2.10)

where σ_f and σ_y are the current and initial yield stresses, E is Young's modulus, $\varepsilon^{\mathrm{eq}}$ is the accumulated equivalent plastic strain and n is the strain hardening exponent. One should note that, for simplicity, we have chosen to neglect the role of plastic strain gradients; however, large plastic strain gradients arise in the vicinity of cracks and other stress concentrators and lead to large crack tip tensile stresses and hydrogen concentrations [221, 222]. The extension of the present framework to account for the role of plastic strain gradients and geometrically necessary dislocations (GNDs) will be addressed in future work.

2.1.2 A phase field description of transgranular fractures

The phase field fracture method is used to regularise the internal discontinuity Γ_ℓ, representing the nucleation and growth of transgranular (ductile) cracks. An auxiliary phase field variable $\mathfrak{d}(\mathbf{x})$ is used to describe the evolution of the solid-crack interface, taking the value of $\mathfrak{d} = 0$ for the pristine state and of $\mathfrak{d} = 1$ for the fully damaged state. The evolution of the phase field equation is dictated by the energy balance associated with the thermodynamics of fracture, as first presented by Griffith [25] and later extended to elastic-plastic solids by Orowan [223]. Thus, under prescribed displacements, the variation of the total energy Π due to an incremental increase of the crack area dA is given by, in the form of variational [45], Eq. (1.1); where we have two terms: the first one is related to the stored strain energy density, while the second part denotes the material toughness $\mathcal{G}_C = dW_C/dA$, which can be as low as some tens of J/m² for brittle solids or as high as thousands of kJ/m² for ductile metals where plastic dissipation enhances fracture resistance, being W_C the work required to create two new surfaces.

The energy balance is now global and fracture phenomena can be predicted by minimizing the total energy Π. However, minimization of Eq. (1.1) is hindered by the unknown nature of the discontinuous crack surface Γ. The phase field regularization can then be exploited to smear this sharp interface into a diffuse region, whose thickness is governed by a phase field length scale ℓ. Accordingly, the energy balance can be approximated as [46] states, mentioned in Eq. (1.8). We choose to adopt the standard or `AT2` phase field formulation, and accordingly make the following constitutive choices,

$$g(\mathfrak{d}) = (1 - \mathfrak{d})^2 + \mathcal{K}, \tag{2.11}$$

$$\gamma_l(\mathfrak{d}, \nabla\mathfrak{d}, \ell) = \frac{1}{2\ell}\mathfrak{d}^2 + \frac{\ell}{2}|\nabla\mathfrak{d}|^2, \tag{2.12}$$

where $\mathcal{K}$ is a small numerical parameter to retain residual stiffness when $\mathfrak{d} = 1$, so as to avoid an ill-conditioned system of equations. Noting that $\boldsymbol{\sigma} = \partial_\varepsilon\psi$, the strong form of the coupled deformation-fracture problem can be readily obtained by inserting Eqs. (2.11)-(2.12) into Eq. (1.8),

taking the variation with respect to **u** and $\mathfrak{d}$, and applying Gauss theorem. However, such a formulation would predict cracking also under compressive stress states. Hence, we adopt the so-called volumetric-deviatoric split [52] to decompose the elastic strain energy density into a tensile part,

$$\Psi_+^e(\varepsilon^e) = \frac{K}{2}\langle \text{tr}[\varepsilon^e]\rangle_+^2 + G[(\varepsilon^e)' : (\varepsilon^e)'] \qquad (2.13)$$

and a compressive part,

$$\Psi_-^e(\varepsilon^e) = \frac{K}{2}\langle \text{tr}[\varepsilon^e]\rangle_-^2 \qquad (2.14)$$

Here, K is the bulk modulus, $\text{tr}[\bullet]$ is the trace operator, $\langle \bullet \rangle = (\bullet \pm | \bullet |)/2$ and $(\varepsilon^e)' = \varepsilon^e - \text{tr}[\varepsilon^e]\mathbf{I}/3$. Furthermore, a history field $\mathcal{H}$ is defined to enforce damage irreversibility. Among the various choices available (see, e.g., [224, 55]), we choose to assume that fracture is driven by the energy stored in the system, in consistency with the energy balance above [225]; accordingly: $\mathcal{H} = \max_{t\in[0,\tau]} \psi_+^e(\varepsilon^e, t)$. The local governing equations then read,

$$\nabla \cdot \left\{ [(1-\mathfrak{d})^2 + \mathcal{K}]\boldsymbol{\sigma}_0 \right\} = \mathbf{0} \quad \text{in } \Omega \qquad (2.15)$$

$$\mathcal{G}_C\left(\frac{1}{\ell}\mathfrak{d} - \ell\nabla^2\mathfrak{d}\right) - 2(1-\mathfrak{d})\mathcal{H} = 0 \quad \text{in } \Omega \qquad (2.16)$$

where $\boldsymbol{\sigma}_0$ is the undamaged Cauchy stress tensor. As can be inferred by inspecting Eq. (2.15)-(2.16), a so-called hybrid approach is used, where the strain energy split is considered only in the phase field evolution equation [54].

2.1.3 Hydrogen-sensitive interface formulation for grain boundaries

In this modelling framework, the polycrystalline nature of the material is resolved and the decohesion of grain boundaries is explicitly captured by means of a cohesive zone model. Specifically, a traction-separation law is adopted that assumes a tension cut-off relation [79]. This interface

formulation assumes a linear and reversible (elastic) evolution until the critical traction is reached. The damage criterion relates the normal t_n and tangential t_t tractions with their critical counterparts as follows,

$$\left(\frac{t_n}{t_{nc}}\right)^2 + \left(\frac{t_t}{t_{tc}}\right)^2 = 1 \tag{2.17}$$

Accordingly, a critical normal δ_{nc} and shear δ_{tc} separations can be defined, which leads to the following definitions of fracture energy for Mode I and Mode II fractures

$$\gamma_{IC} = \frac{1}{2} t_{nc} \delta_{nc}, \quad \gamma_{IIC} = \frac{1}{2} t_{tc} \delta_{tc} \tag{2.18}$$

As sketched in Fig. 5, the role of hydrogen in weakening the grain boundaries is accounted for by degrading the interface fracture energy. Thus, the focus here is on materials that exhibit hydrogen assisted intergranular fracture, such a Ni and Ni alloys [86]. Atomistic calculations have shown a linear relationship between the surface (or fracture) energy and the hydrogen coverage (see, e.g., [226, 227]). Accordingly, and following Martínez-Pañeda *et al.* [75], we define the following relationship between the fracture energy and the hydrogen coverage θ_H,

$$\gamma_C(\theta_H) = \gamma_{C,0}(1 - \chi \theta_H) \tag{2.19}$$

where $\gamma_{C,0}$ is the fracture energy in the absence of hydrogen and χ is the so-called hydrogen damage coefficient. The same expression is employed for γ_{IC} and γ_{IIC}. Finally, the hydrogen coverage is estimated from the hydrogen concentration by means of the Langmuir-McLean isotherm:

$$\theta_H = \frac{C}{C + \exp\left(\frac{-\Delta g_b^0}{RT}\right)} \tag{2.20}$$

where Δg_b^0 is the Gibbs free energy difference between the interface and the surrounding material, also referred to as the segregation energy. Unless indicated otherwise, a value of $\Delta g_b^0 = 30\text{kJ/mol}$ is here employed, based on the spectrum of experimental data available for the trapping energy at grain boundaries [13, 75].

2.1.4 Finite Element implementation

The Finite Element Method (FEM) is employed to solve the coupled deformation-PF-transport problem. If Voigt notation is employed, the nodal values of the displacements, phase-field parameter, and hydrogen concentration are interpolated as follows

$$\mathbf{u} = \sum_{i=1}^{m} \mathbf{N}(\boldsymbol{\xi}) \cdot \mathbf{d}, \quad \mathfrak{d} = \sum_{i=1}^{m} \mathbf{N}(\boldsymbol{\xi}) \cdot \hat{\mathfrak{d}}, \quad C = \sum_{i=1}^{m} \mathbf{N}(\boldsymbol{\xi}) \cdot \hat{\mathbf{C}} \qquad (2.21)$$

where m stands for the number of nodes and $\mathbf{N}$ are the interpolation matrices, which are diagonal matrices with nodal shape functions N_i as components.

The corresponding gradient quantities may be discretized as

$$\boldsymbol{\epsilon} = \sum_{i=1}^{m} \mathbf{B}_u(\boldsymbol{\xi}) \cdot \mathbf{d}, \quad \nabla\mathfrak{d} = \sum_{i=1}^{m} \mathbf{B}(\boldsymbol{\xi}) \cdot \hat{\mathfrak{d}}, \quad \nabla C = \sum_{i=1}^{m} \mathbf{B}(\boldsymbol{\xi}) \cdot \hat{\mathbf{C}} \qquad (2.22)$$

where $\mathbf{B}$ are the vectors with the spatial derivatives of the shape functions, and $\mathbf{B}_u$ is the standard strain matrix.

Employing this technique, Eq. (2.15), i.e., the displacement equilibrium condition is rewritten as a residual concerning the displacement field $\mathbf{R^d}$.

$$\mathbf{R^d}(\mathbf{d}, \Delta\mathbf{d}, \hat{\mathfrak{d}}, \Delta\hat{\mathfrak{d}}, \hat{C}, \Delta\hat{C}) = \int_{\Omega} [(1-\mathfrak{d})^2 + \mathcal{K}]\mathbf{B}_u^{\mathrm{T}} \cdot \boldsymbol{\sigma_0} \, \mathrm{d}V \qquad (2.23)$$

Similarly, the force residual with respect to the phase-field fracture $\mathbf{R}^{\hat{\mathfrak{d}}}$ is obtained by modifying Eq. (2.16).

$$\mathbf{R}^{\hat{\mathfrak{d}}}(\mathbf{d}, \Delta\mathbf{d}, \hat{\mathfrak{d}}, \Delta\hat{\mathfrak{d}}, \hat{C}, \Delta\hat{C}) = \int_{\Omega} \left[-2(1-\mathfrak{d})\mathbf{N}^{\mathrm{T}}\mathcal{H} + \mathcal{G}_C\left(\frac{1}{\ell}\mathbf{N}^{\mathrm{T}}\mathfrak{d} + \ell\mathbf{B}^{\mathrm{T}}\cdot\nabla\mathfrak{d}\right) \right] \mathrm{d}V \qquad (2.24)$$

Components of the corresponding stiffness matrices are obtained by differentiating the residuals with respect to the incremental nodal variables.

$$\mathbf{K^{dd}} = \int_{\Omega} [(1 - \mathfrak{d})^2 + \mathcal{K}] \mathbf{B}_u^{\mathrm{T}} \cdot \mathbb{C} \cdot \mathbf{B}_u \ \mathrm{d}V \qquad (2.25)$$

$$\mathbf{K}^{\hat{\mathfrak{d}}\hat{\mathfrak{d}}} = \int_{\Omega} \left[\left(2\mathcal{H} + \frac{\mathcal{G}_C}{\ell} \right) \mathbf{N}^{\mathrm{T}} \cdot \mathbf{N} + \mathcal{G}_C \ell \mathbf{B}^{\mathrm{T}} \cdot \mathbf{B} \right] \mathrm{d}V \qquad (2.26)$$

where $\mathbb{C}$ denotes the local Jacobian tangent. The residual concerning the Hydrogen concentration $\mathbf{R}^{\hat{C}}$ is obtained by discretizing Eq. (2.8).

$$\mathbf{R}^{\hat{C}} = \int_{\Omega} \left[\mathbf{N}^{\mathrm{T}} \left(\frac{1}{D} \frac{dC}{dt} \right) + \mathbf{B}^{\mathrm{T}} \cdot \nabla C - \mathbf{B}^{\mathrm{T}} \left(\frac{\bar{V}_H C}{RT} \nabla \sigma_H \right) \right] \mathrm{d}V \qquad (2.27)$$

in which the stiffness matrix is herein denoted as

$$\mathbf{K}^{\hat{C}\hat{C}} = \int_{\Omega} \left(\mathbf{B}^{\mathrm{T}} \cdot \mathbf{B} - \frac{\bar{V}_H}{RT} \nabla \sigma_H \mathbf{B}^{\mathrm{T}} \cdot \mathbf{N} \right) \mathrm{d}V \qquad (2.28)$$

This matrix is affected by the gradient of the hydrostatic stress, $\nabla \sigma_H$, which is computed at the integration points from the nodal displacements, extrapolated to the nodes by the employment of the shape functions, and consequently, multiplied by $\mathbf{B}$. 8-node quadrilateral finite elements with C_0 continuity are employed in this framework for the bulk.

On the other hand, the concentration capacity matrix $\mathbf{M}_{ij}$ may be identified as

$$\mathbf{M}^{\hat{C}\hat{C}} = \int_{\Omega} \frac{1}{D} \mathbf{N}^{\mathrm{T}} \cdot \mathbf{N} \mathrm{d}\Omega \qquad (2.29)$$

Consequently, the global equation for hydrogen renders as

$$\mathbf{K}^{\hat{C}\hat{C}} \hat{\mathbf{C}} + \mathbf{M}^{\hat{C}\hat{C}} \dot{\hat{\mathbf{C}}} = \mathbf{0} \qquad (2.30)$$

Lastly, after these discretizations of the three field equations, the following linear finite element system is herein proposed to be solved

$$\begin{bmatrix} \mathbf{K^{dd}} & 0 & 0 \\ 0 & \mathbf{K}^{\hat{\mathfrak{d}}\hat{\mathfrak{d}}} & 0 \\ 0 & 0 & \mathbf{K}^{\hat{C}\hat{C}} \end{bmatrix} \begin{bmatrix} \mathbf{d} \\ \hat{\mathfrak{d}} \\ \hat{\mathbf{C}} \end{bmatrix} + \begin{bmatrix} 0 & 0 & 0 \\ 0 & 0 & 0 \\ 0 & 0 & \mathbf{M}^{\hat{C}\hat{C}} \end{bmatrix} \begin{bmatrix} \dot{\mathbf{d}} \\ \dot{\hat{\mathfrak{d}}} \\ \dot{\hat{\mathbf{C}}} \end{bmatrix} = \begin{bmatrix} \mathbf{R^d} \\ \mathbf{R}^{\hat{\mathfrak{d}}} \\ \mathbf{R}^{\hat{C}} \end{bmatrix} \qquad (2.31)$$

A time parametrization and an incremental-iterative scheme are employed in conjunction with the Newton-Raphson method to solve this coupled problem, along with the staggered solution scheme proposed by [53].

2.2 Numerical tools for the FEM implementation

The theoretical model presented in Section 2.1 is numerically implemented in the commercial finite element package `ABAQUS/Standard` *via* a user element (`UEL`) subroutine. In addition, the `Abaqus2Matlab` software [228] is used to generate the input files and the `MATLAB` supplementary codes given in Ref. [80] are used to generate the microstructure. Fig. 10 provides a flowchart of the steps followed in the definition and analysis of the microstructure sensitive boundary value problems investigated. Specifically, the microstructure is generated by using a Voronoi-based tessellation algorithm, programmed in `MATLAB` [80], and this step is followed by the introduction of the resulting microstructure into the `ABAQUS` input file using a `Python` script. The coupled deformation-diffusion-fracture system is solved in a staggered fashion, with every sub-problem being solved by means of a backward Euler solution scheme. Typical calculation times are of a few hours.

2.3 Representative results

This Section comprises the outline of the presentation of representative results. The main objective of the proposed computational analysis is reproducing the transition between ductile and brittle fracture in polycrystalline materials associated with the effect of the presence of hydrogen-rich environmental conditions. Due to the inherent microscopic nature of this phenomenon, current FE computations rely on a microscopic description using Voronoi tessellations.

First, in Section 2.3.1, a benchmark example is analysed, whereby
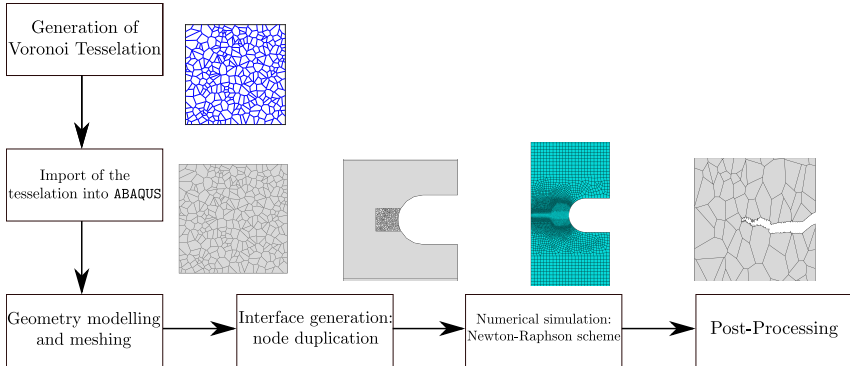
Figure 10: Flowchart that summarises the methodology adopted in the numerical deformation-diffusion-fracture analysis of polycrystalline solids exposed to hydrogen.

cracking is predicted in a single edged notched tension specimen containing 10 and 50 grains, respectively, and exposed to various hydrogen-containing environments. Second, we simulate recent slow strain rate tests (SSRTs) on different Monel K-500 lots in Section 2.3.2, so as to assess the ability of the model in providing a quantitative agreement with experiments and shedding light into the suitability of SSRTs to measure hydrogen susceptibility. Finally, in Section 2.3.3, the model is used to simulate, for the first time, the seminal experiments by Harris *et al.* [86] on pure Ni under cryogenic and ambient temperature conditions.

2.3.1 Benchmark: fracture of a multi-grained SENT plate

With the aim of assessing the capabilities of the proposed framework, a parametric study regarding hydrogen concentration in the environment has been conducted in a single edge notched tension (SENT) plate with dimensions 0.5×0.5 mm (Fig. 11) that is specialized with Voronoi tessellations for 10 and 50 grains. These verification examples aim to show the competition between transgranular (ductile fracture) and intergranular (brittle fracture) failure patterns in the presence of hydrogen-rich environments and the dependence of such fracture patterns on the given
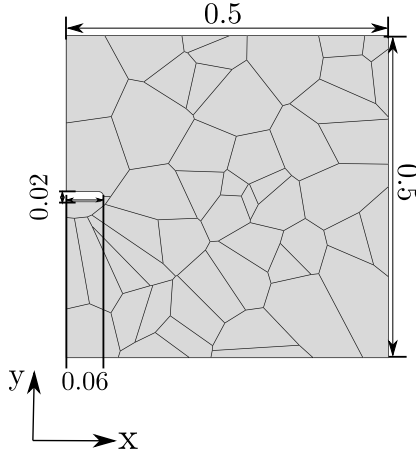
Figure 11: Geometry for the 50-grained SENT place with dimensions in mm.

hydrogen concentration.

The load is applied by prescribing the vertical displacement at the upper edge, at a rate of $\dot{u}_y = 10^{-10}$ mm/s, while the vertical displacement is constrained at the bottom edge. To prevent rigid body motion, the horizontal displacement is constrained at the bottom-right corner. The sample is exposed to hydrogen on its left side, where the notch is located. No pre-charging time in considered, with both hydrogen and mechanical charging starting simultaneously. The magnitude of the environmental hydrogen concentration C_{env} is varied between 0 and 0.9 ppm wt with the aim of capturing a reduced critical load with increasing hydrogen content, and a transition from ductile (bulk) fracture to intergranular cracking. The material properties assumed for the bulk and the interface are given in Table 1.

10-grain models

For these first series of tests, 10 subdomains (grains) are considered within the probe. 37,186 quadratic quadrilateral elements are employed for the FE mesh.

Table 1: Material properties of the bulk and the interface adopted in the SENT benchmark case study.

Bulk properties						
E (GPa)	ν	ℓ (mm)	$\mathcal{G}_C$ (kJ/m^2)	D (mm^2/s)	σ_y (MPa)	n
185	0.3	0.025	0.05	1.3×10^{-8}	794.3	0.064
Interface properties						
k_n, k_t (MPa/mm)		$t_{nc,0}, t_{tc,0}$ (MPa)		$\gamma_{IC,0}, \gamma_{IIC,0}$ (kJ/m^2)		χ
2×10^8		2.25×10^3		1.27×10^{-2}		0.86

The isocontour for the phase-field variable $\mathfrak{d}$ during crack nucleation and propagation is depicted in Figs. 12(a)-12(f) for $C = 0$ wppm, where transgranular fracture events are identified. Analyzing these graphs, it can be observed how the transgranular crack path evolves from the notch, where a stress concentration is initially set, to the closest grain front where the largest differences in stress states between adjacent grains occur, see Figs. 12(a)-12(d). Subsequently, in Figs. 12(e)-12(f), the crack propagates following the interface path of the grains: we believe that such behavior is due to a stress mismatch that takes place between adjacent grains due to differences between the stiffness of the bulk and that of the interface.

The case for $C = 0.25$ wppm is showed in Figs. 13(a)-13(f). This application is characterized by the prediction of intergranular fracture processes, where the crack evolution is represented. The crack nucleation is predicted to occur in the junction close to the initial notch, see Fig. 13(a). This location is estimated due to both hydrogen concentration and cohesive traction being considerably high in this region. Upon further loading, Figs. 13(b)-13(f), the crack evolves following the grain boundaries until the fracture of the sample. This failure pattern is reproduced for all the cases with H-charged ($C > 0$ wppm). Moreover, compared to the previous application ($C = 0$ wppm), it is possible to identify a completely different failure mechanism. This phenomenon can be envisaged by plotting the isocontour for the equivalent plastic strain in the final

(a) $u = 3.08 \times 10^{-4}$ mm   **(b)** $u = 4.88 \times 10^{-4}$ mm   **(c)** $u = 6.80 \times 10^{-4}$ mm

(d) $u = 7.17 \times 10^{-4}$ mm (1)   **(e)** $u = 7.17 \times 10^{-4}$ mm (2)   **(f)** $u = 7.17 \times 10^{-4}$ mm (3)
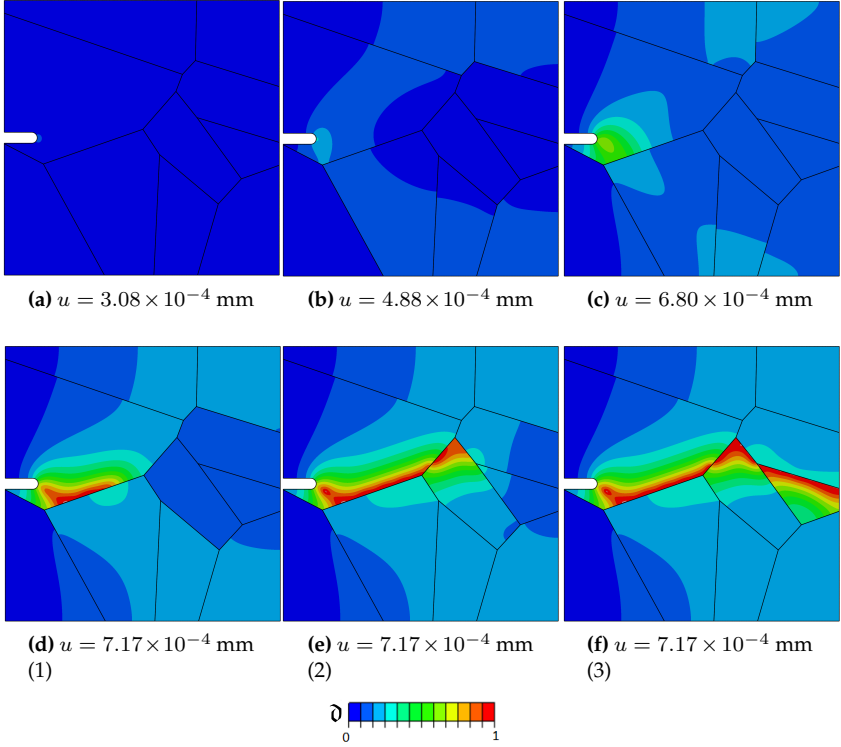
Figure 12: Crack evolution resulting in transgranular fracture for the 10-grain benchmark sample with $C = 0$ wppm sorted by displacement. Plotted is the phase-field parameter.

step in Figs. 14(a)-14(b), where transgranular fracture is remarked by the appearance of plasticity ($\varepsilon_{eq} > 0$), whereas for intergranular failure this value remains as zero, characteristic of brittleness. Particularly, the reason the crack mechanism switches from transgranular to intergranular is attributed to the effect of the undermining in the mechanical performance of grain boundaries that hydrogen causes following the interface law described in Section 2.1.3.

In order to quantify how HE affects the mechanical performance of the samples, the reaction force-displacement curves are plotted for the

46

(a) $u = 3.35 \times 10^{-4}$ mm (1)

(b) $u = 3.35 \times 10^{-4}$ mm (2)

(c) $u = 3.35 \times 10^{-4}$ mm (3)

(d) $u = 3.35 \times 10^{-4}$ mm (4)

(e) $u = 3.35 \times 10^{-4}$ mm (5)

(f) $u = 3.35 \times 10^{-4}$ mm (6)
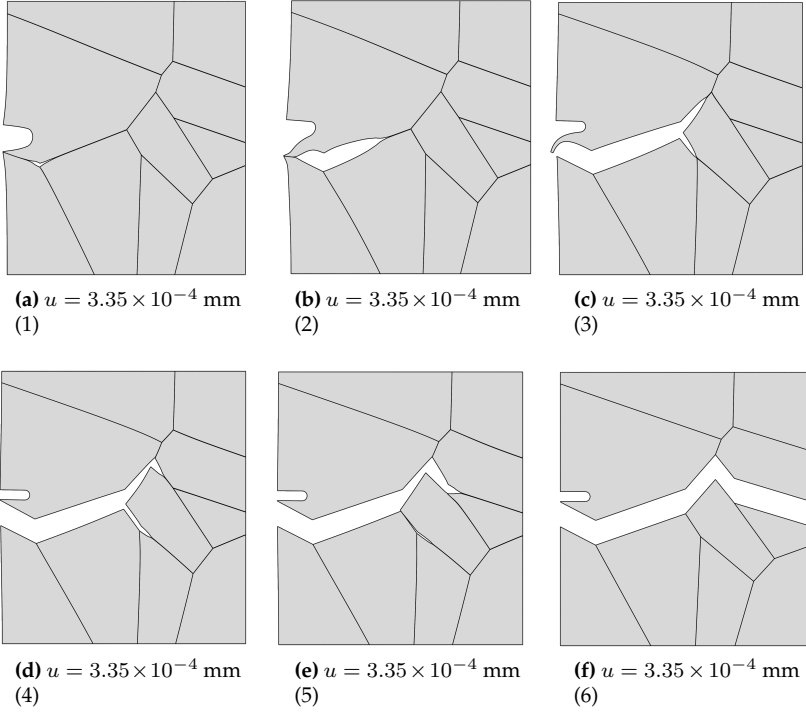
Figure 13: Crack evolution resulting in intergranular fracture for the 10-grain benchmark sample with $C = 0.25$ wppm sorted by displacement.

conducted tests in Fig. 15. Envisaging the degradation of the ductility and strength of these samples, one can extract that this follows the behavior law for critical interfacial energy stated in Eq. (2.19). Similarly to this, the increasing introduction of hydrogen in the atmosphere is associated with a saturated state for high values of C.

50-grain models

Crack nucleation and growth in a SENT plate with a microstructure of 50 grains is investigated. Within this domain, 48,554 quadratic quadrilateral elements are used for the parametric study.

The results obtained for the case of $C_{\text{env}} = 0$ ppm wt are shown in
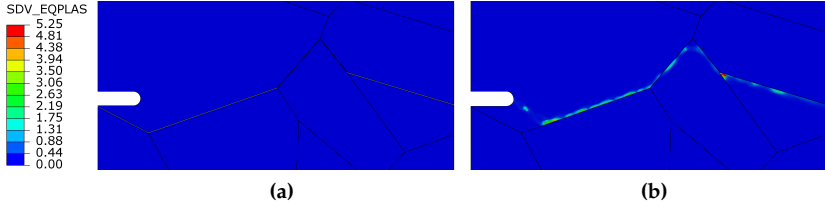
Figure 14: Isocontours depicting the equivalent plastic strain at the end of the analysis for the patterns with a) brittle and b) ductile fracture for the 10-grains benchmark examples.

Figs. (16(a)-16(f)), in terms of the phase field contours. In the absence of hydrogen, the crack nucleates inside of the grain, in the vicinity of the notch tip, and propagates in a transgranular manner, analog to the 10-grain case previously presented.

Contrarily, as with the 10-grained case, when the sample is exposed to hydrogen, cracking initiates along the grain boundaries and propagates in an intergranular manner. This is shown in Fig. 17, where the deformation and separation of the grains is shown as a function of the applied displacement for the case of $C_{\mathrm{env}} = 0.25$ ppm wt. The crack nucleates close to the notch, where both hydrogen content and tensile stresses are large (see Fig. 17(a)). As the remote load increases, the crack spreads to neighboring grain boundaries (Figs. 17(b)-17(e)) and eventually leads to the complete failure of the specimen (Fig. 17(f)).

Finally, the resulting force versus displacement curves are shown in Fig. 18. The result shows that the model not only captures the shift in cracking patterns but can also predict the progressive degradation of fracture properties with increasing hydrogen content. Furthermore, the results also showcase the robustness of the numerical model, as the entire fracture process can be captured, until the complete rupture and loss of load carrying capacity.
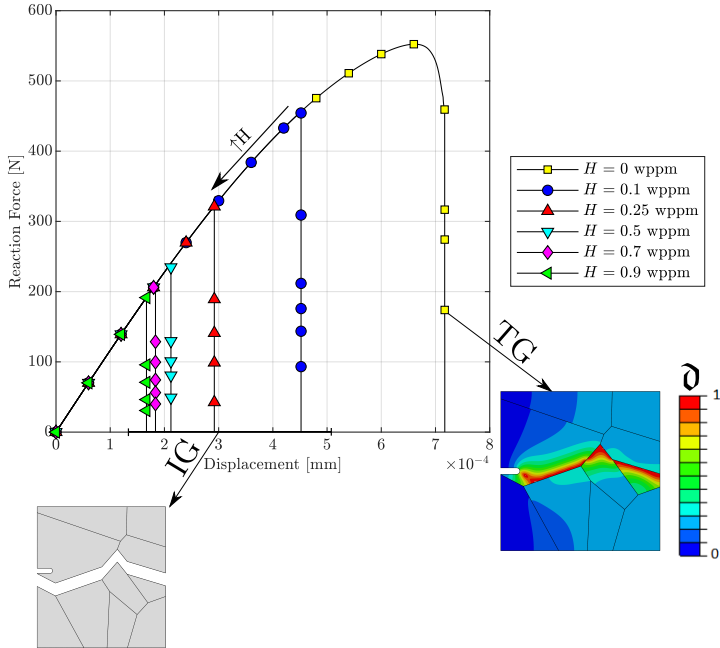
Figure 15: Predicted force versus displacement curves for the 10-grain SENT benchmark. The results are presented as a function of the environmental hydrogen concentration C_{env}, and images are embedded to showcase the different intergranular (IG) and transgranular (TG) cracking patterns observed.

2.3.2 Virtual slow strain rate testing on Monel K-500 samples

Recent slow strain rate tests (SSRTs) on a Ni–Cu superalloy (Monel K-500) have revealed significant intergranular cracking depths, much larger than those expected from diffusion calculations for relevant exposure times [218]. Hence, these experiments suggest that crack initiation is likely to take place much before final failure, allowing for the hydrogen-containing solution to reach significant depths by following the crack. Early sub-critical crack growth would imply the need for a fracture anal-

(a) $u = 5.96 \times 10^{-4}$ mm   **(b)** $u = 6.68 \times 10^{-4}$ mm   **(c)** $u = 6.97 \times 10^{-4}$ mm (1)

(d) $u = 6.97 \times 10^{-4}$ mm (2)   **(e)** $u = 6.97 \times 10^{-4}$ mm (3)   **(f)** $u = 6.97 \times 10^{-4}$ mm (4)
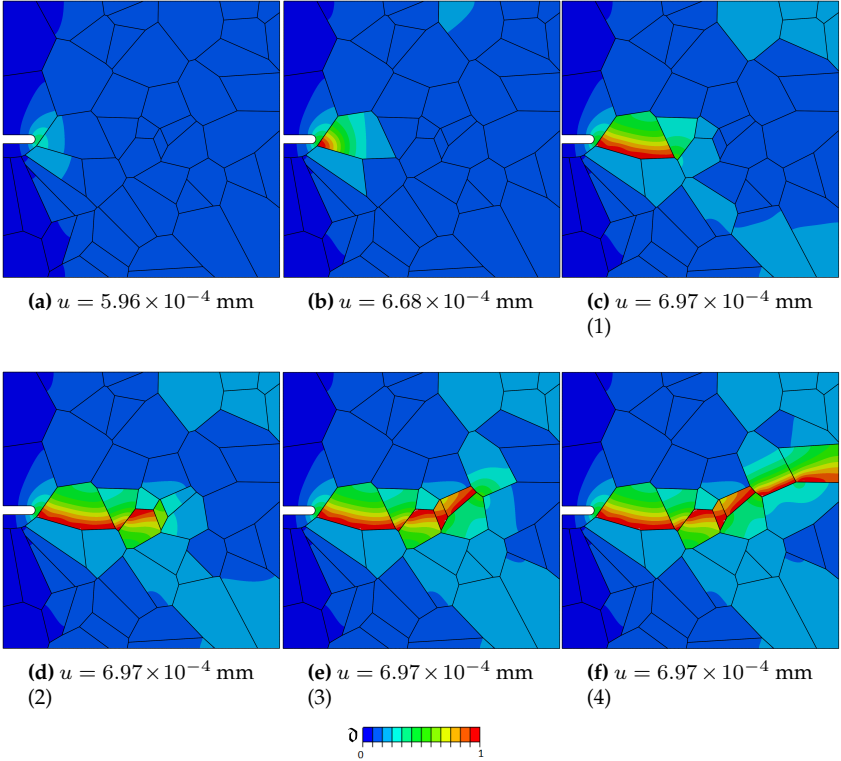
Figure 16: Crack evolution resulting in transgranular fracture for the 50-grain benchmark sample with $C = 0$ wppm sorted by displacement. Plotted is the phase-field parameter.

ysis, compromising the suitability of the SSRT experiment and its metrics (e.g., time to failure) in assessing hydrogen embrittlement susceptibility. The micromechanical formulation presented can be used to gain complementary insight into these paradigmatic experiments and the early cracking hypothesis. Mimicking the testing conditions, notched cylindrical specimens with the dimensions shown in Fig. 19(a) are considered in our simulations. The samples are subjected to uniaxial loading and thus one can take advantage of axially symmetric conditions. Accord-

(a) $u = 2.75 \times 10^{-4}$ mm   **(b)** $u = 2.75 \times 10^{-4}$ mm   **(c)** $u = 2.75 \times 10^{-4}$ mm

(d) $u = 2.75 \times 10^{-4}$ mm   **(e)** $u = 2.75 \times 10^{-4}$ mm   **(f)** $u = 2.75 \times 10^{-4}$ mm
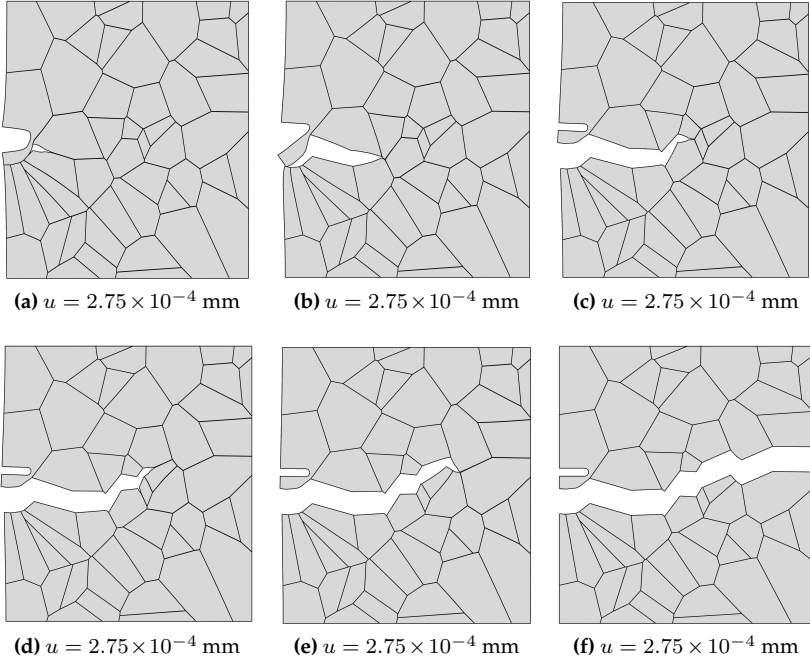
Figure 17: Crack evolution resulting in intergranular fracture for the 50-grain benchmark sample with $C = 0.25$ wppm sorted by displacement.

ingly, the sample is discretised using axisymmetrical finite elements; a total of 64,835 quadratic elements are employed. A microscopic region is introduced near the notch, see Fig. 19(b). This region spans a width of 0.5 mm and includes 280 grains, while the remaining part of the solid is modelled as an isotropic continuum without interfaces. In this way, the model can capture the two cracking modes observed in the experiments; in the absence of hydrogen, cracking occurred at the centre of the sample due to plastic instabilities, while in the presence of hydrogen, cracking took place near the notch tip and was of intergranular nature [218].

As in the experiments, the remote vertical displacement is applied at the top edge with a rate of $\dot{u}_y = 1 \times 10^{-6}$ mm/s. On the other hand, both vertical and horizontal displacements are constrained at the bot-
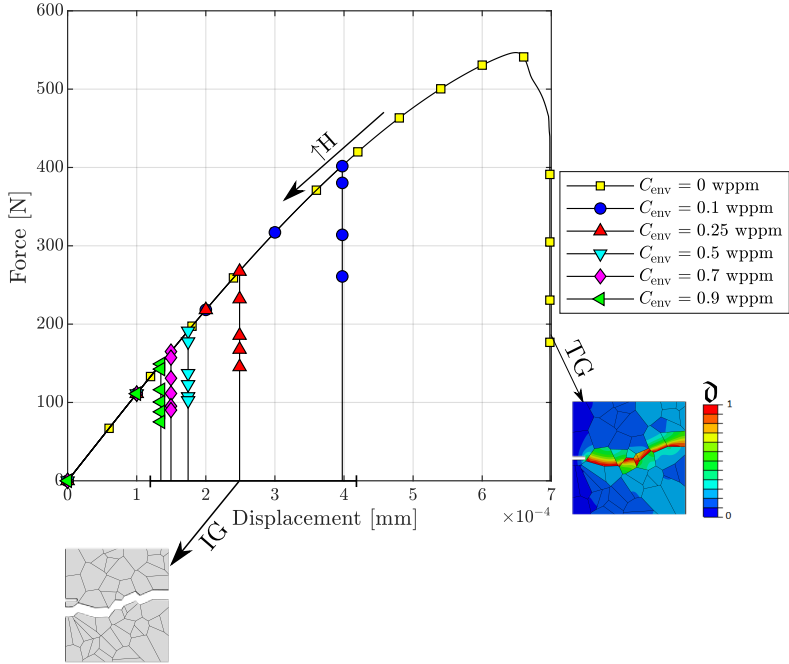
Figure 18: Predicted force versus displacement curves for the 50-grain SENT benchmark. The results are presented as a function of the environmental hydrogen concentration C_{env}, and images are embedded to showcase the different intergranular (IG) and transgranular (TG) cracking patterns observed.

tom edge. Also mimicking the experimental campaign, four Monel K-500 material heats were considered (Allvac, NRL LS, TR2 and NRL HS), with their macroscopic properties being given in Table 2. The reader is referred to Ref. [218] for a comprehensive description on the different ageing and heat treatments employed for each lot. The phase field length scale is assumed to be equal to $\ell = 0.025$ mm and the material diffusivity equals $D = 1.3 \times 10^{-8}$ mm/s [218]. The remaining fracture properties for the bulk and interface are calibrated as follows. First, $\mathcal{G}_C$ is chosen so as to reproduce the experimental force versus time response in air. Then,

52
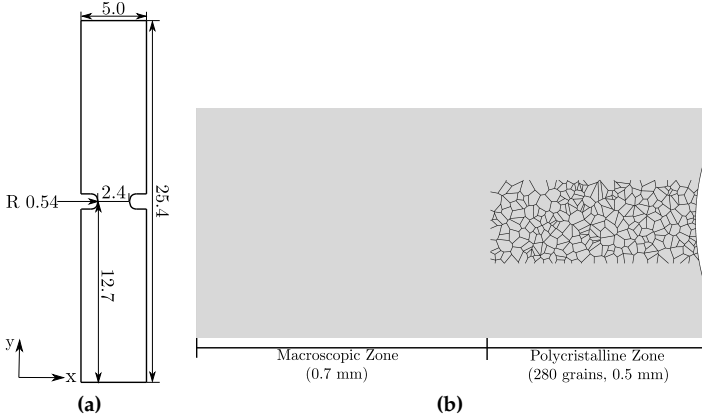
Figure 19: Virtual SSRT experiments on Monel K-500: (a) geometry of the specimens, with dimensions in mm, and (b) augmented view of the region ahead of the notch, showcasing the division between macroscopic and microscopic regions.

Table 2: Material properties for the different heats of Monel K-500 considered.

Heat	E (GPa)	ν	σ_y (MPa)	n
Allvac	180	0.3	794.3	0.058
NRL LS	198	0.3	715.7	0.054
TR2	202	0.3	795	0.055
NRL HS	191	0.3	910.1	0.050

the cohesive interface parameters and the hydrogen damage coefficient χ are calibrated with the experiments conducted at the most aggressive conditions (applied potential of $E_A = -1.1$ V$_{SCE}$), and subsequently used to evaluate their predictive capabilities in other scenarios (different E_A values).

Each Monel K-500 heat was tested in four different environments: in air (i.e., in the absence of a hydrogen-containing solution) and while being exposed to solutions with the applied potentials $E_A = -0.85$ V$_{SCE}$, $E_A = -0.95$ V$_{SCE}$, and $E_A = -1.1$ V$_{SCE}$. The diffusible hydrogen con-

Table 3: Diffusible C (wppm) for each Monel K-500 heat for each applied potential E_A.

Heat	$E_A = -0.85 \text{ V}_{\text{SCE}}$	$E_A = -0.95 \text{ V}_{\text{SCE}}$	$E_A = -1.1 \text{ V}_{\text{SCE}}$
Allvac	1.9	4.1	7.5
NRL LS	1.3	4.7	18.3
TR2	3.7	18.6	26.2
NRL HS	4.7	11.9	23.4

centration associated with each charging condition was experimentally measured and used as input in the model - a prescribed C_{env} magnitude at the surface. The values measured are given in Table 3 (in ppm wt).

Current simulations are performed as follows:

- First, uncharged Hydrogen specimens are conducted in order to calibrate the value of the critical energy release rate $\mathcal{G}_C$ for the bulk.

- Subsequently, the Hydrogen-assisted cracking phenomenon is studied in these structures incorporating the cohesive traction-separation law (TSL). The predicted interface properties are obtained utilizing an adjustment procedure with respect to the experimental data by directly correlating with the load-time curves and failure mechanisms.

Simulations are first conducted in the absence of hydrogen. As shown in Fig. 20, damage initiates at the centre of the sample for sufficiently large loads, in agreement with experimental observations. The material toughness $\mathcal{G}_C$ for each Monel K-500 lot is chosen so as to quantitatively reproduce the macroscopic force versus time curve, with the fitted values being 18.5, 18.1, 15.4 and 16.9 kJ/m^2 for, respectively, Allvac, NRL LS, TR2, and NRL HS. The force versus time curves obtained for each material lot are shown in Fig. 21. A good agreement is attained with experimental observations, with only small differences being observed in the early stages due to the additional compliance brought in by the machine displacement (an extensometer was not used [218]).
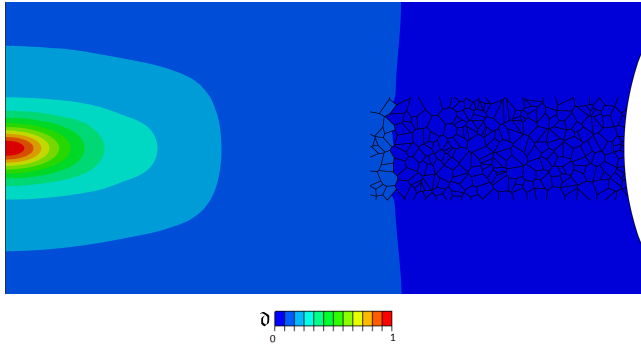
Figure 20: Virtual SSRT experiments on Monel K-500: phase field fracture contour at the time of crack initiation. In the absence of hydrogen, cracking takes place at the centre of the sample, in agreement with experimental observations.

The samples with a higher degree of hydrogen uptake (those charged at $E_A = -1.1$ V_{SCE}) exhibit an intergranular fracture pattern, as shown in Fig. 22. A crack nucleates in a grain boundary adjacent to the notch tip and subsequently propagates along neighboring grain boundaries. The force versus time curves obtained for the four material lots under an applied potential of $E_A = -1.1$ V_{SCE} are shown in Fig. 23. In all cases the failure is intergranular, starting at the notch tip and triggering a significant drop in the load carrying capacity before any noticeable increase in the phase field variable is observed. Thus, the calibrated model is also able to capture the ductile-to-brittle transition observed in this case study.

Interestingly, the cracking event appears to occur rather suddenly, with the intergranular crack propagating into regions with low hydrogen content. This would suggest that the crack resulting from the decohesion of the grain boundaries exposed to a high hydrogen content would be sufficiently large to propagate in an unstable fashion through grain boundaries that have only been negligibly weakened by hydrogen. If that were to be the case, then these numerical results would suggest that SSRT is not compromised by early cracking and thus remains a valid test
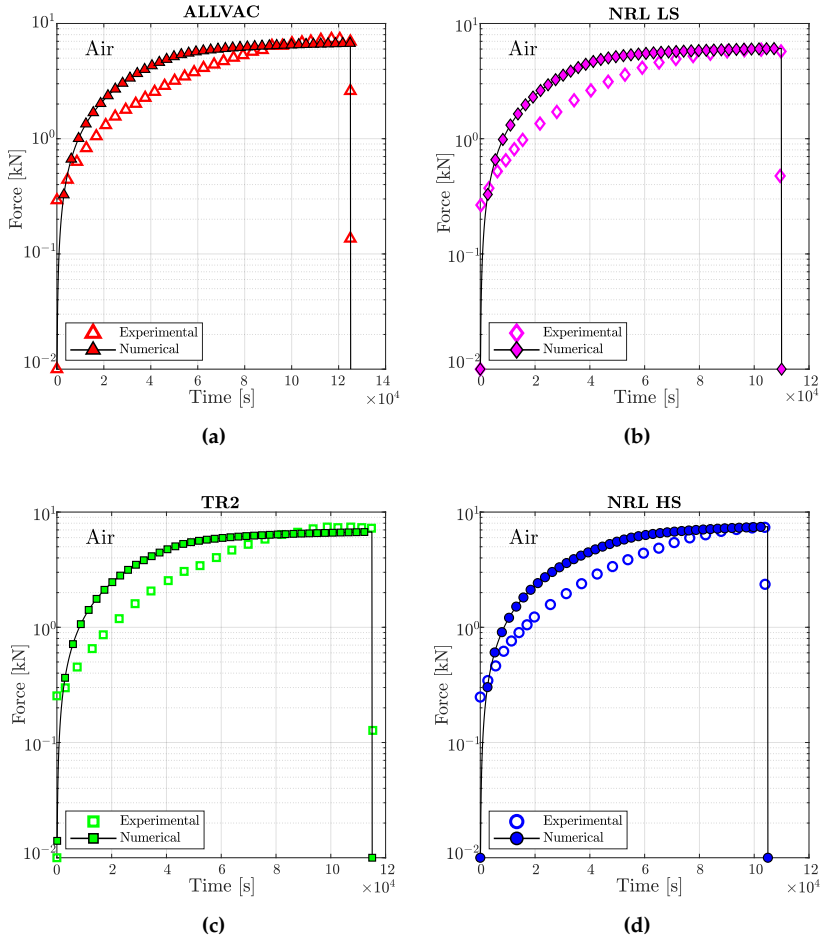
Figure 21: Virtual SSRT experiments on Monel K-500: numerical and experimental force versus time curves obtained in the absence of hydrogen for each material lot; namely, (a) Allvac, (b) NRL LS, (c) TR2 and (d) NRL HS.

for measuring hydrogen embrittlement susceptibility. Additional, albeit limited, insight can be gained by a simple estimate of the transition flaw size $a_t = K_{Ic}^2/(\pi\sigma_Y^2)$. For Monel K-500 exposed to a relatively uniform
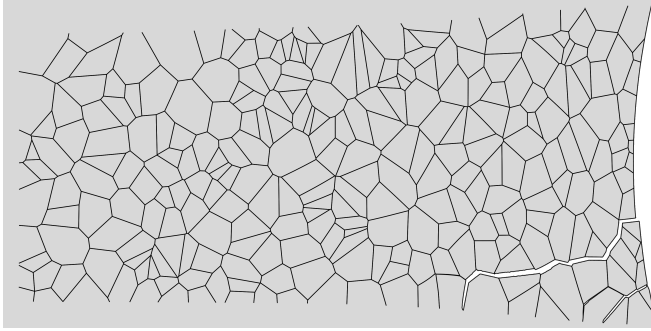
Figure 22: Virtual SSRT experiments on Monel K-500: representative result of intergranular cracking for a sample exposed to an applied potential of $E_A = -1.1$ V$_{\text{SCE}}$. A crack nucleates at a grain boundary adjacent to the notch tip and then propagates in-between grains towards the centre of the sample.

hydrogen distribution resulting from an applied potential of $E_A = -1.1$ V$_{\text{SCE}}$, the transition flaw size would be on the order of 0.04 mm (see Table 2 and the K_{TH} measurements of Ref. [32]). However, this quantity can increase to up to 4 mm in the absence of hydrogen. Thus, the magnitude of a_t relevant to this scenario (a non-uniform distribution of hydrogen) falls between those two limiting cases, and could therefore be higher or lower than the crack extensions predicted (0.1-0.5 mm). Another source of uncertainty is the specific traction-separation law adopted, as assuming the existence of a damage dissipation region could add an additional source of fracture resistance.

The interface parameters that provide a quantitative agreement with experiments are given in Table 4. The damage coefficient χ was estimated based on previous (microstructurally-insensitive) phase field simulations [218]. The values of χ used are higher than those estimated using atomistic calculations for most common types of Ni grain boundaries [227]. However, the choices of χ values are notably sensitive to the magnitude of the grain boundary binding energy considered in Eq. (2.20), and the estimation of this magnitude carries a degree of uncertainty [229].
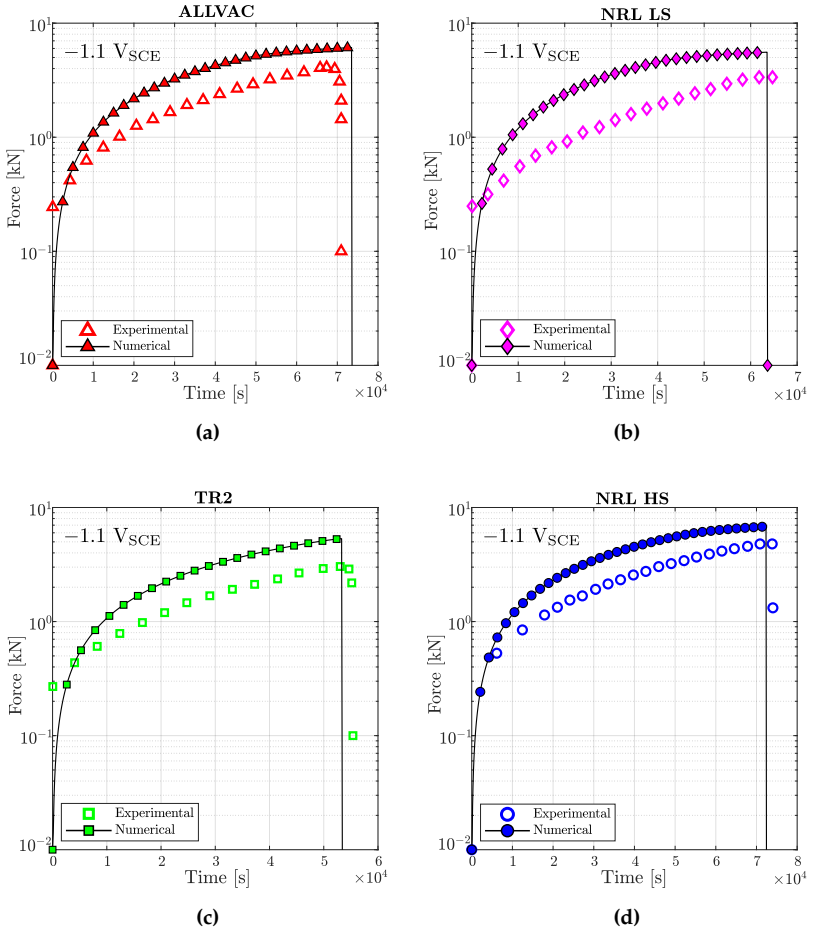
Figure 23: Virtual SSRT experiments on Monel K-500: numerical and experimental force versus time curves obtained under an applied potential of $E_A = -1.1$ V_{SCE} for each material lot; namely, (a) Allvac, (b) NRL LS, (c) TR2 and (d) NRL HS.

The calibrated model is used to reproduce the entire experimental campaign, conducting virtual experiments on the four material lots over the four environments considered. We summarise the outcome of the

Table 4: Interface material parameters, as estimated by quantitatively reproducing the experiments conducted at an applied potential of $E_A = -1.1$ V_{SCE}.

	Allvac	NRL LS	TR2	NRL HS
k_n, k_t (10^8 MPa/mm)	2.00	2.00	2.00	2.00
$t_{nc,0}, t_{tc,0}$ (10^4 MPa)	2.07	2.78	2.23	2.13
$\gamma_{IC,0}, \gamma_{IIC,0}$ (kJ/m^2)	1.07	1.92	1.24	1.12
χ	0.85	0.82	0.86	0.79

Table 5: Virtual SSRT experiments on Monel K-500: predicted fracture mechanism (IG = intergranular, TG = transgranular) for each combination of material heat and environment. Green check marks and red crosses are used to respectively denote when predicted mode of cracking agrees or disagrees with the experimental observation.

E_A (V_{SCE})	Allvac	NRL LS	TR2	NRL HS
0 (Air)	TG ✓	TG ✓	TG ✓	TG ✓
0.85	TG ✓	TG ✗	TG ✓	-
0.95	TG ✓	IG ✓	IG ✓	TG ✓
1.1	IG ✓	IG ✓	IG ✓	IG ✓

simulations in Table 5, indicating the failure model predicted (brittle intergranular/IG or ductile transgranular/TG). Green check marks are used to denote when the predicted mode of cracking agrees with the experimental observation, with red crosses denoting otherwise. As observed, the model is capable of predicting the occurrence of hydrogen-assisted brittle failures in all but one case - the experiment on the NRL LS heat at $E_A = -0.85$ V_{SCE}. As discussed in Ref. [218], this is a rare case as SEM images of the fracture region reveal intergranular features but the time to failure happens to be larger than that measured in the absence of hydrogen. It is thus concluded that the micromechanical model presented is capable of predicting hydrogen embrittlement upon appropriate calibration.

2.3.3 Failure of pure Ni samples at ambient and cryogenic temperatures

Finally, we employ the micromechanical cohesive zone - phase field formulation developed to shed light on the interplay between diffusion, deformation, temperature, and embrittlement on pure Ni. Harris *et al.* [86] investigated the contribution of mobile hydrogen-deformation interactions to hydrogen-induced intergranular cracking in polycrystalline Ni by testing hydrogen charged samples at both ambient (298 K) and cryogenic (77 K) temperatures. Their uniaxial mechanical tests showed that embrittlement (hydrogen-assisted intergranular cracking) occurred even at cryogenic temperatures, where dislocation-hydrogen interactions are precluded. This suggests that hydrogen-assisted decohesion of grain boundaries is a first-order mechanism in hydrogen embrittlement. It was also found that intergranular microcrack evolution was enhanced at room temperature, relative to 77 K, but a mechanistic interpretation of this finding was deemed complicated due to the multiple factors at play. Here, we examine the ability of our micromechanical model to quantitatively reproduce the seminal experiments by Harris *et al.* [86] and use the numerical insight provided to gain further understanding on the role of temperature in enhancing embrittlement. The material properties adopted correspond to those reported by Harris *et al.* [86], which are listed in Table 6 as a function of the temperature and the environment. Two environmental conditions are considered: (i) samples tested in air, without any hydrogen pre-charging, and (ii) samples exposed to a hydrogen content of 4000 appm (79.5 wppm). In the latter, gaseous hydrogen charging is used and the hydrogen is distributed uniformly within the samples. Mimicking the experimental conditions, the uniaxial load is prescribed by applying a remote vertical displacement with a rate of $\dot{u}_y = 0.0078$ mm/s, while the bottom edge is completely constrained ($u_x = u_y = 0$).

The samples are cylindrical bars with the dimensions given in Fig. 24(a). As in the previous case study, we take advantage of axial symmetry and model half of the 2D section using axisymmetric elements. A to-

Table 6: Material properties reported for polycrystalline Ni samples at the two temperatures (77 and 298 K) and environments (79.5 wppm H and air) considered.

Temperature	77 K		RT	
	no H	**H**	**no H**	**H**
E (GPa)	227	227	202	202
ν	0.3	0.3	0.3	0.3
σ_y (MPa)	222	233	182	192
n	0.159	0.159	0.140	0.140
D (mm^2/s)	10^{-15}	10^{-15}	10^{-9}	10^{-9}

Table 7: Calibrated traction-separation law parameters to describe the decohesion of pure Ni grain boundaries.

$\mathbf{k_n, k_t}$ **(MPa/mm)**	$\mathbf{t_{nc,0}, t_{tc,0}}$ **(MPa)**	$\boldsymbol{\gamma_{IC,0}, \gamma_{IIC,0}}$ **(MPa $\times$ mm)**
2×10^8	7.83×10^4	0.88

tal of approximately 80,000 quadratic axisymmetric elements are used to discretise the model. As shown in Fig. 24(b), we introduce a microstructural domain of 200 grains in the central region of the sample. The phase field length scale is taken to be equal to $\ell = 0.025$ mm, and the toughness $\mathcal{G}_C$ is calibrated to reproduce the experiments in the absence of hydrogen, rendering values of 4 kJ/m^2 (77 K) and 2.5 kJ/m^2 (RT). The interfacial cohesive properties are adjusted to reproduce the experiments at 77 K and then used to see if the results at room temperature can be predicted. The specific values used are given in Table 7 and, following the approach of Ref. [78], a phenomenological degradation law is adopted, such that

$$\gamma_c(\theta_H) = \gamma_{C,0}\Big(17.52 \exp(-2.75\theta_H)\Big) \tag{2.32}$$

with the Gibbs free energy being equal to 17 kJ/mol [230].

As shown in Figs. 24(c)-24(d) and Fig. 25, the model is able to reproduce experimental measurements beyond the regimes of calibration, both qualitatively and quantitatively. Consider first the cracking patterns shown in Fig. 24. In the absence of hydrogen (Fig. 24(c), failure takes
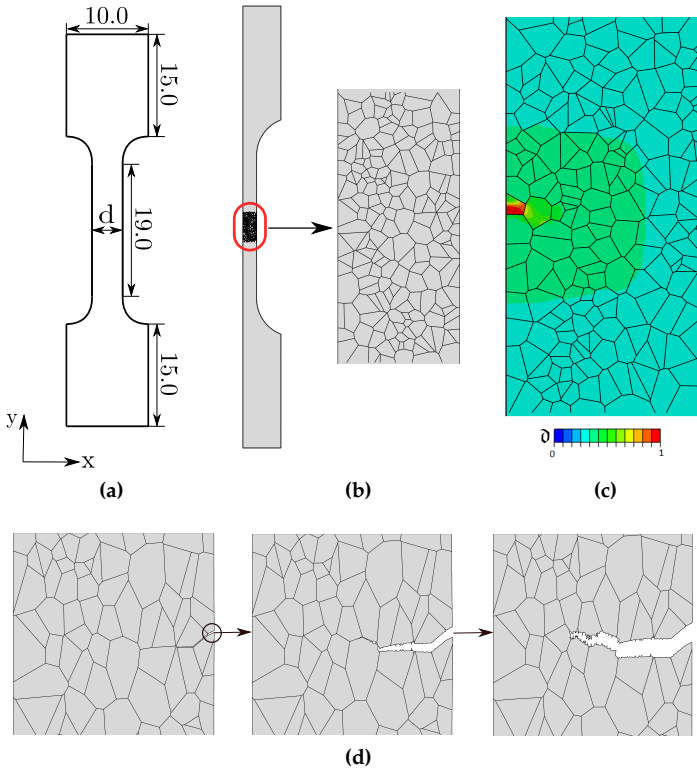
Figure 24: Role of temperature on the failure of polycrystalline Ni samples: (a) geometry with dimensions in mm, where d = 4 mm for 77 K and d = 3.6 mm for RT specimens [86], (b) augmented view of the microstructure region, with 200 grains, (c) ductile (transgranular) damage, as predicted by the phase field, and (d) intergranular crack nucleation and growth, as assisted by hydrogen. Representative results shown from calculations at ambient temperature.

place due to the onset of ductile (transgranular) damage in the centre of the sample, as predicted by the phase field order parameter. However, when the sample is exposed to hydrogen, then cracking takes place in an intergranular fashion, as a result of the failure of the cohesive zone interfaces. The location of the grain boundary decohesion event that nu-
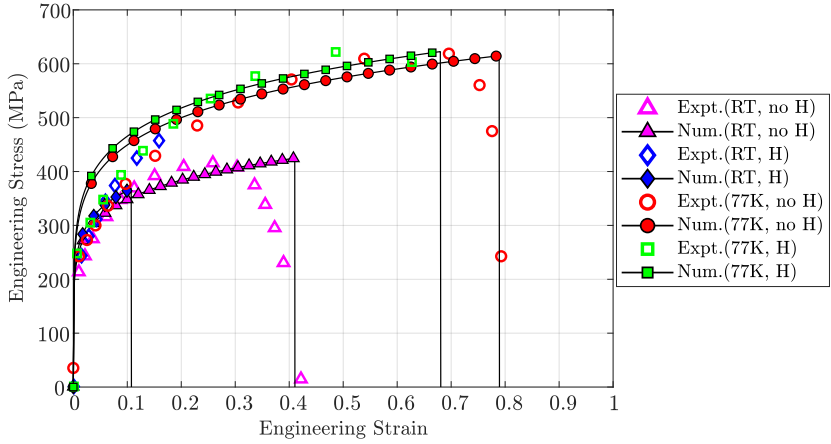
Figure 25: Role of temperature on the failure of polycrystalline Ni samples: engineering stress-strain curves for both H-charged and non-charged samples pulled to failure at 77K and at ambient temperature (298 K).

cleates the brittle crack is random. For the microstructure and conditions of Fig. 24(d), it occurs close to the edge of the sample, with the crack growing then both towards the outer surface and towards the centre of the sample. This change from ductile transgranular damage to brittle intergranular cracking due to hydrogen is observed at both 77 and 298 K, as in the experiments.

The quantitative results obtained for the four scenarios are shown in Fig. 25, in terms of the predicted and measured engineering stress-strain curves. A very good agreement with the experiments is observed. Interestingly, the good agreement observed for the case of the hydrogen-charged sample suggests that the higher degree of embrittlement observed at room temperature can be rationalised by the additional accumulation of hydrogen at grain boundaries due to diffusion, without the need for additional contributions from mechanisms such as those associated with hydrogen-deformation interactions.

Chapter 3

Fracture in pre-stressed cylindrical bio-inspired elastomer-like materials

Chapter 3 is based on our own publication [231].

In order to analyze, mitigate and potentially prevent failure of pre-stressed cylindrical structures, the development of a rigorous and sophisticated theoretical analysis, within the more complex large deformation theory, is required. This is usually complemented with the advent of reliable numerical techniques to obtain a general modelling framework that allows qualitatively and quantitatively different aspects such as the non-linear behavior of (visco-hyperelastic) materials to be considered [232]. This constitutive material model is often related to its microstructure including a network of highly flexible and mobile chains which are three dimensional cross linked. Particularly, in polymers, the movement of the chains is associated with viscous effects occurring in the rubber-like material, see [233] and references therein. Moreover, as reported in [234], in materials prone to experience viscous effects, the principal failure mechanism of a considerable number of elastomers is strongly affected by the inelastic term and the rate of deformation. Accordingly, several rheological models have been developed to describe the viscoelastic constitutive

law for elastomers which can be split into linear [235, 236, 237, 238, 239] and non-linear viscoelasticity [240, 241, 242].

Within failure analysis of cracking events, fracture in elastomer-like materials is often related to either nucleation of cavities (cavitation) [243] or crack propagation. The latter is the focus of this work and a macrome-chanics approach is pursued. In the literature, several methods have been proposed to model fracture for visco-hyperelastic materials [244]. These methods include fracture mechanics-based methodologies [245, 246], path-independent J-integral formulations [247, 248, 249], cohesive methods [250, 251] and peridynamical approaches [252, 253], among others. Recently, the phase field approach to fracture has emerged as a new modelling technique to simulate rate-dependent fracture evolution. Concerning the application to different kinds of materials, in addition to brittle fracture [47, 254, 255, 256], it is known that the phase field technique has been extended to ductile fracture [224, 257, 55, 258, 259, 260, 261], anisotropic fracture [262, 263, 80, 264, 265, 266], dynamic fracture [267, 268, 49], and failure of heterogeneous media [79, 269, 60, 270, 271, 272]. Therefore, it is not unexpected to see its implementation to simulate fracture phenomena in visco-elastic materials [273, 274, 275, 276, 277], along with another nonlocal damage techniques like the element failure method [278, 279]. Arterial tissues are encompassed in the field of visco-hyperelastic materials, and its fracture modelling by the phase field technique has been already proposed in absence of residual stresses [280].

We aim, by employing the current visco-hyperelastic theory, to formulate a phase field model able to capture fracture events in hyperelastic and visco-elastic solids, a topic broadly covered as has been aforementioned. Once this framework is implemented, the salient novelty of the present research is the subsequent incorporation of residual stresses in order to model fracture for pre-stressed cylindrical structures based in arteries, being this combined modelling the main aim of the paper. For that last purpose, we use a constitutive law for residually stressed hyperelastic materials given in terms of invariants, see [281, 282, 283, 284, 285, 20].

In order to tackle the targets of this work, the phase field approach for visco-elastic fracture proposed by [275] is combined with the rheological approach given in [233]. Accordingly, a new model is generated enabling the investigation of fracture phenomena for elastomers with viscous response. Furthermore, the model is extended to simulate pre-stressed cylindrical structures based in arteries using the constitutive framework proposed in [281]. The viscoelastic effect and the residual stresses are defined separately and are added subsequently to give the total energy driving force of the system complying with thermodynamic restrictions and establishing the corresponding modular format of the theoretical framework.

Chapter 3 is structured as follows. The formulation, which consists in the hyperelastic viscoelastic material law at hand, is developed in Section 3.1. The phase-field governing functional along with its computational implementation in an `UMAT` subroutine is presented in Section 3.2. A benchmark example is carried out in Section 3.3.1 to verify the hyper-visco elastic formulation. Cylindrical structures are simulated in Section 3.3.2 where a deep parametric study is carried out for viscosity-dependent parameters such as relaxation time and displacement rate and for different residual stress fields. Since many vanguard technologies are employing multi-layered structures with different mechanical and fracture properties [286, 287], in Section 3.3.3, the analysis of a two-layer hollow thick-walled cylinder is executed to address the dependence of shear modulus mismatch between the layers, as well as fracture energy mismatch, and the presence of pre-stresses on the mechanical performance of this structural element.

Nomenclature

Ω_0	Body domain in the initial configuration
$\mathbb{R}^n$	Collection of ordered lists of n real numbers
$\mathbf{X}$	Arbitrary spatial point on the initial configuration
Γ_ℓ	Discrete internal discontinuity
t	Current time
Ω	Body domain in the current configuration
$\mathbf{x}$	Arbitrary spatial point on the current configuration
$\partial\Omega_0$	Boundary of the solid in the reference configuration
$\mathbf{N}$	Initial normal outward vector

Nomenclature

$\partial\Omega_{0,u}$	Boundary region with a Dirichlet condition of prescribed displacements in Ω_0
$\mathbf{u}$	Displacement field
$\partial\Omega_{0,t}$	Boundary region with a Neumann condition of prescribed tractions in Ω_0
$\mathbf{T}$	First Piola-Kirchhoff traction vector
$\boldsymbol{\varphi}$	Nonlinear deformation map
$\mathbf{F}$	Deformation gradient
$\nabla_{\mathbf{X}}$	Gradient operator in the reference configuration
$\nabla_{\mathbf{x}}$	Gradient operator in the current configuration
$\mathbf{1}$	Second order identity tensor
$\mathbf{H}$	Material displacement gradient tensor
J	Jacobian, determinant of $\mathbf{F}$
det	Determinant
$\mathbf{C}$	Right Cauchy-Green tensor
$\mathbf{b}$	Left Cauchy-Green tensor
$\mathbf{t}$	Cauchy traction vector
$\mathbf{n}$	Current normal outward vector
$\boldsymbol{\sigma}$	Cauchy's stress tensor
$\mathbf{P}$	First Piola-Kirchhoff stress tensor
$\mathrm{d}A$	Differential of nominal area
$\mathrm{d}a$	Different of engineering area
$\mathbf{S}$	Second Piola-Kirchhoff stress tensor
Π	Total potential energy
Ψ	Strain energy density
$\mathcal{G}$	Energy release rate
$\mathcal{G}_C$	Material toughness
Π^{ext}	External potential energy
$\mathfrak{d}$	Phase-field parameter
ℓ	Length scale parameter
γ_l	Crack surface density function
w	Geometric crack function
c_w	Phase-field scaling parameter
$g(\mathfrak{d})$	Degradation function
Ψ^{hyp}	Strain energy density term dedicated to the constitutive hyperelastic branch
$\Psi^{\mathrm{visco},\alpha}$	Strain energy density term dedicated to every viscous branch
n	Number of viscous terms considered
α	Viscous branch
Ψ^{res}	Strain energy density term dedicated to the residual stresses
$\mathbf{A}$	Tensor that considers the microscopical stretches in the reference configuration
$\boldsymbol{\lambda}$	Chain stretch vector
$\boldsymbol{\sigma_0}$	Residual stress field
Ψ^{vol}	Volumetric contribution for the strain energy density term
Ψ^{iso}	Isochoric contribution for the strain energy density term
G	Shear modulus
κ	Bulk modulus
$\bar{I}_n$	Deviatoric n-th invariant
I_n	N-th invariant
$\mathrm{tr}(\bullet)$	Trace operator
p	Probability function associated to the state of the polymeric chains

Nomenclature

$\mathcal{L}_{\mathbf{x}}$	Stretch space in the current configuration
$\mathcal{L}_{\mathbf{X}}$	Stretch space in the reference configuration
$\bar{\mathbf{P}}$	Microdeformation map tensor
$\bar{\mathbf{P}}_{\mathbf{X}}$	Pre-microdeformation map tensor
$\bar{\mathbf{F}}$	Isochoric part of the deformation gradient
τ^{α}	Relaxation time for the viscous branch α
$\mathbb{P}$	Fourth-order projector operator
$\nabla \cdot [\bullet]$	Divergence operator
f	Weight of the invariants for the residual stresses
Π_{Ω}	Term of the energy functional associated with the energy stored in the solid
Π_{Γ_ℓ}	Term of the energy functional associated with the energy necessary to create a crack
$\mathcal{H}$	History variable parameter
t_f	Final time of test
Ψ_+	Term of the strain energy density associated with tensile states
Ψ_-	Term of the strain energy density associated with compressive states
$\mathcal{H}^+$	History variable parameter associated to tensile states
$\mathcal{K}$	Residual stiffness
$\mathbf{E}$	Green-Lagrange strain tensor
χ	Pseudo-viscous resistance
φ_*	Push-forward operator
ρ	Mass density
c_p	Heat capacity
$\mathbf{q}$	Heat flux
k	Heat conductivity
T	Temperature
r_T	Spatial heat source
Δt	Time increment
$\mathbf{a}$	Tensor that considers the microscopical stretches in the current configuration
δ_{ij}	Kronecker's delta
$\mathbb{C}_{ijkl}$	Material tangent
$\mathbb{C}_{ijkl}^{\mathrm{mat}}$	Contribution of the visco-hyperelastic law to the material tangent
$\mathbb{C}_{ijkl}^{\mathrm{res}}$	Contribution of the residual stresses to the material tangent
a	Crack length
v	Displacement rate
R, Θ, Z	Cylindric coordinates
σ_{0RR}	Radial residual stress
σ_{0RZ}	Shear radial-axial residual stress
$\sigma_{0\Theta\Theta}$	Azimuthal residual stress
σ_{0ZZ}	Axial residual stress
$\sigma_{0\Theta Z}$	Shear azimuthal-axial residual stress
$\sigma_{0R\Theta}$	Shear radial-azimuthal residual stress
A	Inner radius of the cylindrical structure
B	Outer radius of the cylindrical structure
α_c	R-dependent dimensionless residual stress intensity parameter
α_d	Z-dependent dimensionless residual stress intensity parameter
L	Length of the cylinder
H	Thickness of the cylinder
ν	Poisson's ratio

3.1 Governing equations and constitutive formulation

This section outlines the fundamental concepts and definitions for hyperelastic and visco-hyperelastic solids within the scope of the phase field approach to fracture.

3.1.1 Basic definitions

Complying with standard nonlinear Continuum Mechanics, the reference configuration of an arbitrary body is denoted by $\Omega_0 \subset \mathbb{R}^n$, being the arbitrary material points in the reference placement denoted by the vector $\mathbf{X}$ and it possesses an internal discontinuity Γ_ℓ. Throughout the deformation process this reference configuration is mapped at an arbitrary elapsed time t, with $\mathcal{T} = [0, t]$ onto the corresponding current configuration $\Omega \subset \mathbb{R}^n$ whose position vectors are identified by the vector $\mathbf{x}(\mathbf{X}, t)$. This transformation is exhibited in Fig. 26. With a reference normal outward, $\mathbf{N}$, the delimiting surface $\partial \Omega_0$ of the body is decomposed into: the region $\partial \Omega_{0,u}$, where the displacement $\mathbf{u}$ is prescribed by Dirichlet-type boundary conditions (BCs) and $\partial \Omega_{0,t}$, where the nominal tractions $\mathbf{T}$ is prescribed via Neumann-type conditions.

The transformation of the differential line elements throughout the deformation process is characterized by the deformation gradient $\mathbf{F}$ whose definition renders

$$\mathbf{F} := \nabla_{\mathbf{X}} \varphi(\mathbf{X}, t) = \mathbf{1} + \mathbf{H}(\mathbf{X}, t) \tag{3.1}$$

being $\mathbf{1}$ the second order identity tensor and $\mathbf{H}(\mathbf{X}, t)$, the material displacement gradient tensor. The Jacobian, i.e. the ratio of the deformed to the undeformed volume, being the determinant of $\mathbf{F}$ fulfills the condition of $J = \det[\mathbf{F}] > 0$. In order to track the motion of the body from the material to the spatial configuration at time t, the displacement vector is defined as:

$$\mathbf{u}(\mathbf{X}, t) := \mathbf{x}(\mathbf{X}, t) - \mathbf{X} \tag{3.2}$$
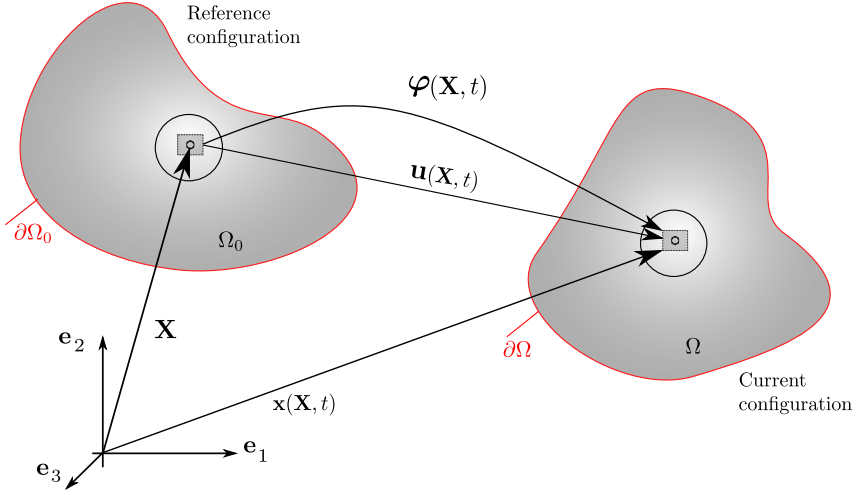
Figure 26: Deformation process from the reference configuration to the current one.

Accordingly, the right and left Cauchy-Green tensors are obtained as, respectively:

$$\mathbf{C} := \mathbf{F}^{\mathrm{T}} \cdot \mathbf{F}; \quad \mathbf{b} := \mathbf{F} \cdot \mathbf{F}^{\mathrm{T}} \tag{3.3}$$

The delimiting surface of the body is decomposed into two regions: one where the displacements $\mathbf{u}$ are prescribed through Dirichlet-type boundary conditions (BCs), $\partial\Omega_{0,u}$ and one where the tractions $\mathbf{T}$ are prescribed via a Neumann-type BC, $\partial\Omega_{0,t}$, such that $\partial\Omega = \partial\Omega_{0,u} \cup \partial\Omega_{0,t}$ and $\partial\Omega_{0,u} \cap \partial\Omega_{0,t} = \emptyset$. For the Neumann condition, we can establish a linear dependency between the nominal traction vector $\mathbf{T}$ and the reference normal outward $\mathbf{N}$ through the following theorem:

$$\mathbf{T} = \mathbf{P} \cdot \mathbf{N} \tag{3.4}$$

where $\mathbf{P}$ is the first Piola-Kirchhoff stress tensor. Equivalently, the Cauchy stress tensor $\boldsymbol{\sigma}$ can be defined via this theorem by performing a push-forward operation to refer to the current configuration Ω:
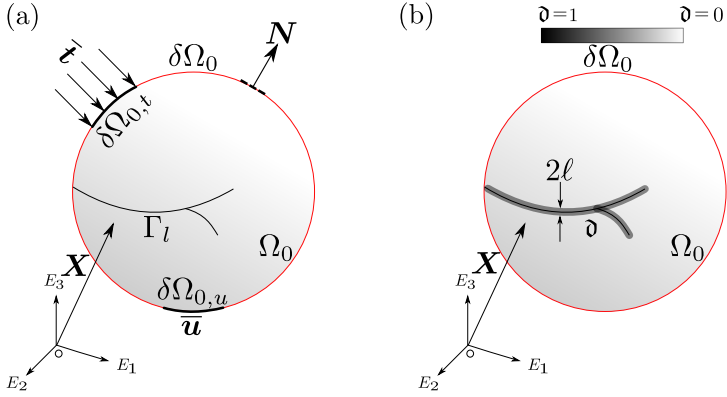
Figure 27: Schematic representation of the two-field large deformation boundary value problem concerning residual stresses: (a) displacement field and (b) phase field parameter for fracture.

$$\mathbf{t} = \boldsymbol{\sigma} \cdot \mathbf{n} \quad \text{with} \quad \boldsymbol{\sigma} = J^{-1}\mathbf{P} \cdot \mathbf{F^T} \tag{3.5}$$

The relation between Eqs. (3.4) and (3.5) is obtained by considering $\mathbf{T}\mathrm{d}A = \mathbf{t}\mathrm{d}a$. In order to compute a symmetric Langragian tensor, the second Piola-Kirchoff stress tensor $\mathbf{S}$ serves for this duty in the reference configuration and it reads as

$$\mathbf{S} = \mathbf{F^{-1}} \cdot \mathbf{P} = J\,\mathbf{F^{-1}} \cdot \boldsymbol{\sigma} \cdot \mathbf{F^{-T}} \tag{3.6}$$

Crack events in the proposed modelling framework are accounted for the consideration of the phase field approach [46]. The crack-phase field variable is described via the material variable $\mathfrak{d}(\mathbf{X}, t)$:

$$\mathfrak{d}(\mathbf{X}, t) : \Omega_0 \times \mathcal{T} \rightarrow [0, 1] \tag{3.7}$$

where the state $\mathfrak{d}(\mathbf{X}, t) = 0$ identifies an intact stiffness at the material point level, whereas $\mathfrak{d}(\mathbf{X}, t) = 1$ denotes a fully deteriorated stiffness, all of them referred to the reference configuration. The large deformation problem is represented in Fig. 27 comprising the two fields to be solved: the displacement field $\mathbf{u}$ and the phase field parameter $\mathfrak{d}$.

71
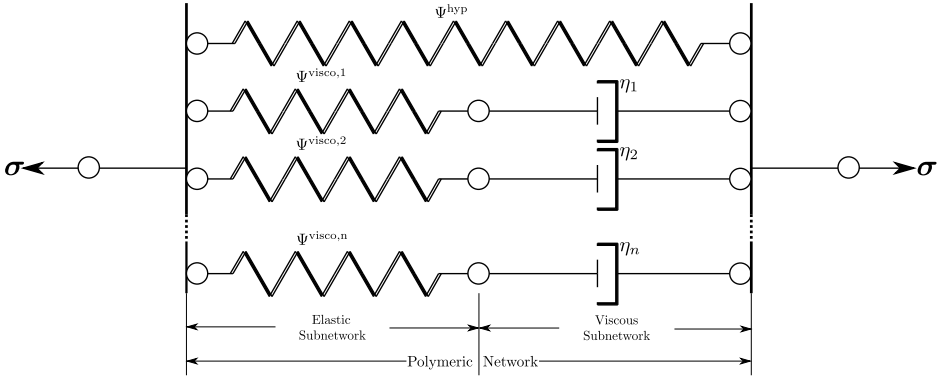
Figure 28: Maxwellian rheological model of the response of the material consisting of the elastic branches, representing the strongly cross-linked network, and the viscous branches, representing the highly mobile with entanglements subnetwork.

3.1.2 Constitutive formulation

With regard to the constitutive formulation, this subsection presents the particular visco-hyperlasticity model adopted from [233]. This formulation relies on the consideration of its microstructure (highly mobile and flexible macro-molecules). The resulting constitutive equations of rubber viscoelasticity are obtained under the assumption of the polymer microstructure behaving like several idealized polymer networks. This mechanical response is characterized by macromolecules which are strongly cross-linked in a network, where there is a sub-network with highly mobile and temporary entanglement mechanisms. The cross-linking is related to the elastic response, whereas the subnetwork is responsible for the viscous behaviour. The macroscopic representation of the system is seen in Fig. 28. Following this definition, the macroscopic finite rubber response can be defined based on a volumetric-isochoric decomposition, where the latter part itself is decomposed into an elastic and a viscous term, respectively.

Concerning the incorporation of residual stresses, a nonlinear constitutive law that depends on a number of invariants is considered recall-

ing the original framework developed in [288, 281]. This formulation presents the following advantages: (i) it can be implemented into standard FE codes in a straightforward manner, (ii) it can be combined with different kinds of mechanical problems, and (iii) it precludes the use of the multiplicative descomposition as is proposed in [289]. With these arguments, the Helmholtz free energy function $\Psi(\mathbf{C}, \mathbf{A}, \boldsymbol{\sigma_0})$ is postulated as follows:

$$\Psi(\mathbf{C}, \mathbf{A}, \boldsymbol{\sigma_0}) = \Psi^{\text{hyp}}(\mathbf{C}) + \sum_{\alpha=1}^{n} \Psi^{\text{visco},\alpha}(\mathbf{C}, \mathbf{A}) + \Psi^{\text{res}}(\mathbf{C}, \boldsymbol{\sigma_0}) \qquad (3.8)$$

where we have the expression for the free energy divided in three terms associated to the main features of the model: (i) Ψ^{hyp}, related to the hyperelastic constitutive part; (ii) $\Psi^{\text{visco},\alpha}$, dedicated to every α viscous branch; and (iii) Ψ^{res}, referred to the residual stresses present in the model. n makes reference to the number of viscous terms considered in the rheological model; $\mathbf{A}$, to the tensor that considers the stretches $\boldsymbol{\lambda}$ from the microscopical system of polymer chains; and $\boldsymbol{\sigma_0}$, to the residual stress field in the reference configuration.

First, focusing on the hyperelastic term, Ψ^{hyp}, this also can be split into the corresponding volumetric (Ψ^{vol}) and isochoric (Ψ^{iso}) contributions:

$$\Psi^{\text{hyp}}(\mathbf{C}) = \Psi^{\text{iso}} + \Psi^{\text{vol}} \qquad (3.9)$$

which can be specialized to a standard neo-Hookean model:

$$\Psi^{\text{iso}} = \frac{G}{2}(\bar{I}_1 - 3), \quad \Psi^{\text{vol}} = \frac{\kappa}{2}(J - 1)^2 \qquad (3.10)$$

where G and κ denote the shear and the volumetric constant, respectively; and $\bar{I}_1$ is the first invariant of the deviatoric left Cauchy-Green tensor which has the value of $\bar{I}_1 = J^{-2/3}I_1 = J^{-2/3}\text{tr}[\mathbf{C}]$.

The second Piola-Kirchhoff stress for the hyperelastic term $\mathbf{S}^{\text{hyp}}$ is evaluated as:

$$\mathbf{S}^{\text{hyp}} := 2\frac{\partial \Psi^{\text{hyp}}}{\partial \mathbf{C}} = 2J^{-2/3}G\left(\mathbf{1} - \frac{I_1 \mathbf{C}^{-1}}{3}\right) \qquad (3.11)$$

73

For the second term in Eq. (3.8), the viscous part of the model, Ψ^{visco}, and the corresponding second Piola-Kirchhoff viscous overstress, $\mathbf{S}^{\text{visco}}$, is particularized without any loss of generality to the model proposed by Linder and co-authors [233]. In this work, it is observed how the visco-elastic contribution is constructed from the microscopical description of the polymer chains movement, being this microscopic-based approach embedded into the current continuous framework of finite rubber vis-coelasticity. The temporary state of such system of polymer chains is measured by a probability function $p(\boldsymbol{\lambda}, t)$ obtained from the diffusion process. This magnitude is dependent from the stretch state of the chain $\boldsymbol{\lambda}$. By representing this probability function in a tensorial form, we can associate a stretch space $\mathcal{L}_{\mathbf{x}}$ connected locally to a material point with position $\mathbf{x}$ in the current configuration $\Omega \subset \mathbb{R}^n$ and map his evolution from the initial stretch space $\mathcal{L}_{\mathbf{X}}$, linked to a material point with position $\mathbf{X}$ in the reference configuration $\Omega_0 \subset \mathbb{R}^n$, by means of the microdeformation map $\bar{\mathbf{P}}$. More particular details are omitted here for the sake of brevity and the reader is referred to [233]. Recalling this constitutive model, via the definition of a so-called microdeformation map $\bar{\mathbf{P}}$, it is possible to account for the micromechanics of the system by defining:

$$\bar{\mathbf{P}} = \bar{\mathbf{F}}\bar{\mathbf{P}}_{\mathbf{X}} \tag{3.12}$$

where $\bar{\mathbf{P}}_{\mathbf{X}}$ stands for the pre-deformation map tensor, and $\bar{\mathbf{F}}$ is the iso-choric part of the deformation gradient at the macroscopic level.

After some operations, one reaches the definition of the tensor $\mathbf{A}$

$$\mathbf{A} = \bar{\mathbf{P}}_{\mathbf{X}}\bar{\mathbf{P}}_{\mathbf{X}}^{\mathsf{T}}. \tag{3.13}$$

Note that the tensor $\mathbf{A}$ provides the information concerning the mi-crodeformation of the visco-elastic subnetwork in the initial configura-tion and it depends on macroscopic variables. Accordingly, the time evo-lution equation of this tensor reads

$$\dot{\mathbf{A}} = \frac{1}{\tau^{\alpha}}(\bar{\mathbf{C}}^{-1} - \mathbf{A}) \tag{3.14}$$

where $\bar{\mathbf{C}}^{-1}$ is the inverse of the isochoric part of the right Cauchy-Green

tensor, and τ^α, the relaxation time associated to the viscous mechanism α.

After the previous definitions, the viscous counterpart of the free energy density is obtained for every α polymer chain network

$$\Psi^{\text{visco},\alpha}(\mathbf{C},\mathbf{A}) = \frac{1}{2}G^{\text{visco},\alpha}[(\mathbf{A}^{(\alpha)} : \bar{\mathbf{C}}) - \ln(\det\mathbf{A}^{(\alpha)})] \tag{3.15}$$

being $G^{\text{visco},\alpha}$ the shear modulus for each mechanism.

After some algebraic manipulations, the resulting closed form expression for the viscous part of the hyperelastic energy allows the computation of the second Piola-Kirchhoff viscous overstress tensor $\mathbf{S}^{(\text{visco},\alpha)}$ for each α mechanism, which reads

$$\mathbf{S}^{(\text{visco},\alpha)} = J^{-2/3}\mathbb{P} : \left(G^{\text{visco},\alpha}\mathbf{A}^{(\alpha)}\right) \tag{3.16}$$

where $\mathbb{P}$ is the fourth-order projector operator

$$\mathbb{P} : (\bullet) = \bullet - \frac{1}{3}[(\bullet) : \mathbf{C}]\mathbf{C}^{-1}. \tag{3.17}$$

Regarding the last term, associated with residual stresses, Ψ^{res}, in Eq. (3.8), a few assumptions are made about the particular form of the stress field $\boldsymbol{\sigma_0}$ that is defined in the reference configuration. Following [281], this stress field is assumed to be symmetric, and fulfilling the conditions:

$$\nabla_{\mathbf{X}} \cdot \boldsymbol{\sigma_0} = \mathbf{0} \text{ in } \Omega_0, \tag{3.18}$$

$$\boldsymbol{\sigma_0} \cdot \mathbf{N} = \mathbf{0} \text{ on } \partial\Omega_{0,t} \tag{3.19}$$

Exploiting the previous assumptions, the particular form of $\Psi^{\text{res}}(\mathbf{C},\boldsymbol{\sigma_0})$ is given by

$$\Psi^{\text{res}}(\mathbf{C},\boldsymbol{\sigma_0}) = \frac{f}{2}(I_5 - \text{tr}\boldsymbol{\sigma_0}) + \frac{1-f}{4}(I_6 - \text{tr}\boldsymbol{\sigma_0}) \tag{3.20}$$

where $I_5 = \text{tr}(\boldsymbol{\sigma_0}\mathbf{C})$ and $I_6 = \text{tr}(\boldsymbol{\sigma_0}\mathbf{C}^2)$ are the invariants associated with the residual stress field and f is a parameter that accounts for the

weight of these invariants in the equation. As this is a nonlinear problem, the residual stresses are necessarily nonuniform and geometrically dependent, and the elastic response of the system will be in-homogeneous [282].

For the subsequent numerical implementation, the contribution of the residual stresses to the Second Piola-Kirchhoff stress is computed as:

$$\mathbf{S}^{\text{res}} = 2\frac{\partial \Psi^{\text{res}}}{\partial \mathbf{C}} = 2J^{-1/3}\left(\frac{f\boldsymbol{\sigma_0}}{2} - \frac{fI_5\mathbf{C}^{-1}}{6}\right) + (1-f)J^{-2/3}\left(\frac{1}{4}\frac{\partial I_6}{\partial \mathbf{C}} - \frac{I_6\mathbf{C}^{-1}}{6}\right).$$
(3.21)

where we have needed the forthcoming expressions to account for the derivative $\frac{\partial \Psi^{\text{res}}}{\partial \mathbf{C}}$

$$\frac{\partial I_5}{\partial \mathbf{C}} = \boldsymbol{\sigma_0}, \quad \frac{\partial I_6}{\partial \mathbf{C}} = \boldsymbol{\sigma_0}\mathbf{C} + \mathbf{C}\boldsymbol{\sigma_0}$$
(3.22)

Considering Eqs. (3.11), (3.16) and (3.21), one reaches the complete form of total second Piola-Kirchhoff stresses herein proposed:

$$\mathbf{S} = \mathbf{S}^{\text{hyp}} + \sum_{\alpha=1}^{n} \mathbf{S}^{\text{visco},\alpha} + \mathbf{S}^{\text{res}}.$$
(3.23)

3.2 Phase-field: governing functional and implementation details

3.2.1 Governing functional

The governing functional of the phase field approach to fracture (governing crack nucleation, propagation and branching) is recalled by the definition of the corresponding energy functional [47, 57]. In line with the ideas of [45], we define the energy functional $\Pi(\mathbf{u}, \Gamma_\ell)$ of the system in the reference configuration as:

$$\Pi(\mathbf{u}, \Gamma_\ell) = \Pi_\Omega(\mathbf{u}, \Gamma_\ell) + \Pi_{\Gamma_\ell}(\Gamma_\ell) = \int_{\Omega_0} \Psi(\mathbf{C}, \mathbf{A}, \boldsymbol{\sigma_0}, \mathfrak{d})\mathrm{d}V + \int_{\Omega_0} \mathcal{G}_C\gamma_l(\mathfrak{d}, \nabla_{\mathbf{X}}\mathfrak{d})\mathrm{d}V$$
(3.24)

where $\Psi(\mathbf{C}, \mathbf{A}, \boldsymbol{\sigma_0}, \mathfrak{d})$ refers to the expression defined in Eq. (3.8), $\mathcal{G}_C$ stands for the fracture energy (independent of viscoelastic parameters);

and γ_l is the crack energy density functional. There are two different terms in Eq. (3.24), being $\Pi_\Omega(\mathbf{u}, \Gamma_\ell)$ the one that represents the energy stored in the solid and $\Pi_{\Gamma_\ell}(\Gamma_\ell)$, the energy necessary to create the crack according to Griffith theory.

Without loss of generality, the driving force for damage evolution is assumed to be driven by the free energy function stated above, $\Psi(\mathbf{C}, \mathbf{A}, \boldsymbol{\sigma_0}, \mathfrak{d})$. Therefore, upon the occurrence of cracking events, we postulate a degradation function $g(\mathfrak{d})$ affecting to $\Psi(\mathbf{C}, \mathbf{A}, \boldsymbol{\sigma_0})$: $\Psi(\mathbf{C}, \mathbf{A}, \boldsymbol{\sigma_0}, \mathfrak{d}) = g(\mathfrak{d})\Psi(\mathbf{C}, \mathbf{A}, \boldsymbol{\sigma_0})$.

Moreover, in order to prevent self-healing at the material point level, the engineering formulation proposed by Miehe and co-authors [47] is used. This formulation assumes a time-dependent t history variable parameter $\mathcal{H}$:

$$\mathcal{H} = \max_{t\in[0,t_f]}\Psi(\mathbf{C}, \mathbf{A}, \boldsymbol{\sigma_0}, t). \tag{3.25}$$

The so-called crack density functional defined above, $\gamma_l(\mathfrak{d}, \nabla_\mathbf{X}\mathfrak{d})$, depends upon the length-scale parameter ℓ and the continuous scalar-valued phase field variable $\mathfrak{d}$. As we adopt the AT-2 approach [46], we adopt the value for the crack density functional stated in Eq. (1.10), the degradation function stated in (1.9) and the values for the parameters $w(\mathfrak{d}) = \mathfrak{d}^2$ and $c_w = \frac{1}{2}$.

It is important to remark the necessity to propose a formulation where crack growth only accounts while in a tension state. Therefore, to distinguish these states, we will consider the approach proposed by Borden and co-authors [55]. In here, there is a decomposition of the elastic strain energy density Ψ to distinguish between tensile Ψ^+ and compressive states Ψ^-. With these ingredients at hand, Eq. (3.24) is reformulated as:

$$\begin{aligned} \Pi(\mathbf{u}, \mathfrak{d}) &= \int_{\Omega_0} [g(\mathfrak{d})\Psi^+(\mathbf{C}, \mathbf{A}, \boldsymbol{\sigma_0}, J) + \Psi^-(J)]\mathrm{d}V \\ &+ \int_{\Omega_0} \left[\frac{\mathcal{G}_C}{2\ell}\mathfrak{d}^2 + \mathcal{G}_C\ell|\nabla_\mathbf{X}\mathfrak{d}|^2\right]\mathrm{d}V. \end{aligned} \tag{3.26}$$

In order to define the tensile and compressive states for the strain energy density, we employ the isochoric-volumetric decomposition of

Amor and co-authors [52]:

$$\Psi^+(\mathbf{C}, \mathbf{A}, \boldsymbol{\sigma_0}, J) = \begin{cases} \Psi^{\text{hyp}}(\mathbf{C}) + \sum_{\alpha=1}^{n} \Psi^{\text{visco},\alpha}(\mathbf{C}, \mathbf{A}) + \Psi^{\text{res}}(\mathbf{C}, \boldsymbol{\sigma_0}) & \text{if } J \geq 1 \\ \Psi^{\text{iso}}(\mathbf{C}) + \sum_{\alpha=1}^{n} \Psi^{\text{visco},\alpha}(\mathbf{C}, \mathbf{A}) + \Psi^{\text{res}}(\mathbf{C}, \boldsymbol{\sigma_0}) & \text{if } J < 1 \end{cases}$$

(3.27)

$$\Psi^-(J) = \begin{cases} 0 & \text{if } J \geq 1 \\ \Psi^{\text{vol}}(J) & \text{if } J < 1 \end{cases}$$

(3.28)

where the expressions for the isochoric Ψ^{iso} and the volumetric Ψ^{vol} can be found in Eq. (3.10).

Therefore, as the degradation function only multiplies the positive cases Ψ^+, the history field variable is defined upon them $\mathcal{H}^+$.

$$\mathcal{H}^+ = \max_{t\in[0,t_f]} \Psi^+(\mathbf{C}, \mathbf{A}, \boldsymbol{\sigma_0}, t).$$

(3.29)

The solution of Eq. (3.26) can be obtained by solving it as a minimization problem.

$$\boxed{\begin{array}{l} \text{Determine} \quad (\mathbf{u}, \mathfrak{d}) \quad \text{from} \\ (\mathbf{u}^*, \mathfrak{d}^*) = \arg \min_{\mathcal{S}} \Pi(\mathbf{u}, \mathfrak{d}), \end{array}}$$

(3.30)

with $\mathcal{S} = \{\dot{\mathfrak{d}} \geq 0 \text{ for all } \mathbf{X} \in \Omega_0\}$.

Following a standard Galerkin procedure, the weak form of the coupled displacement $\mathbf{u}$ and fracture problem $\mathfrak{d}$ in Eq. (3.26) can be obtained as:

$$\delta\Pi(\mathbf{u}, \delta\mathbf{u}, \mathfrak{d}, \delta\mathfrak{d}) = \underbrace{\int_{\Omega_0} \mathbf{S} : \delta\mathbf{E} \, \mathrm{d}V}_{\delta\Pi_{\text{int}}^{\mathbf{u}}} -$$

$$\underbrace{\int_{\Omega_0} [g'(\mathfrak{d})(\delta\mathfrak{d})\Psi^+] \mathrm{d}V + \int_{\Omega_0} \mathcal{G}_C\ell \left[\frac{\mathfrak{d}}{\ell^2}\delta\mathfrak{d} + \nabla_{\mathbf{X}}\mathfrak{d} \cdot \nabla_{\mathbf{X}}(\delta\mathfrak{d})\right] \mathrm{d}V}_{\delta\Pi_{\text{int}}^{\mathfrak{d}}}.$$

(3.31)

where $\mathbf{E}$ refers to the Green-Lagrange strain tensor, which reads as $\mathbf{E} = \frac{1}{2}(\mathbf{C} - \mathbf{1})$. Upon the exploitation of the product rule and the Gauss' divergence theory on Eq. (3.31), the phase field evolution equation is obtained as

$$-2(1 - \eth) \underbrace{\Psi^+(\mathbf{C}, \mathbf{A}, \boldsymbol{\sigma_0})}_{\mathcal{H}^+} + \mathcal{G}_C \left(\frac{1}{\ell} - \ell \nabla_{\mathbf{X}}^2 \eth \right) = 0. \qquad (3.32)$$

Despite the robustness of the proposed formulation, convergence issues may arise due to local instabilities. Therefore, according to [275], a pseudo-viscous resistance against phase field evolution χ is added as a positive viscous damping term. This is a parameter is employed in order to increase the numerical stability and to account for the results of quasi-brittle fracture, which are obtained for $\chi = 0$. By increasing χ, the fracture gets delayed compared to brittle fracture. However, χ should be kept as a very small number, since large values of this parameter leads to numerical instabilities in achieving equilibrum solutions. The term is added to Eq. (3.32) and it yields

$$-2(1 - \eth) \underbrace{\Psi^+(\mathbf{C}, \boldsymbol{\sigma_0})}_{\mathcal{H}^+} + \mathcal{G}_C \left(\frac{1}{\ell} - \ell \nabla_{\mathbf{X}}^2 \eth \right) + \chi \dot{\eth} = 0. \qquad (3.33)$$

3.2.2 Implementation details

This section briefly describes the numerical implementation of the current phase field model for hyperelastic (rate independent) and visco-hyperelastic (rate dependent) media including residual stresses.

General remarks

The numerical implementation of the current model complies with the use of a thermo-mechanically coupled FE formulation. This scheme has been already exploited by different authors, see Ostwald and co-authors [290] for its application to nonlocal regularized damage models and Navidtehrani

and co-authors [291, 292] for phase field methods. In particular, we exploit a modified version of the numerical approach developed in [291] in the software `ABAQUS` using a user material subroutine `UMAT` in conjunction to the functionality `HETVAL`, that provides an internal heat generation in heat transfer analysis at the integration point level [1]. The principal reason motivating this option for the current numerical framework is twofold: (i) from the user's perspective, it is not required to implement a user-defined element via the subroutine `UEL` of `ABAQUS` for the phase field governing functional and, (ii) the use of the initial state dependent variable routine `SDVINI` for the incorporation of residual stresses can be employed without any restriction.

According to Navidtehrani and coauthors [291, 292], the resulting coupled thermo-mechanical problem is solved using a staggered iterative solution for the obtention of the solution of the displacement and the phase field variables. Note that staggered iterative solution procedures generally require the use of sufficiently small load increments in order to ensure that the solution does not deviate from the equilibrium one [47]. Concerning the FE mesh characteristics, the present formulation are integrated into first-order hexahedral (quadrangular in 2D) hybrid elements with full integration.

Regarding the mechanical sub-problem, the mechanical user-defined material model using the `UMAT` capability requires the computation of the Cauchy stress tensor (`STRESS` in `ABAQUS`), the mechanical tangent (`DDSDDE` in `ABAQUS`), and the state dependent variables vector `STATEV`. In line with the derivation presented in Section 3.1.2, the material formulation is formulated in terms of the right Cauchy-Green deformation tensor $\mathbf{C}$ and the second Piola-Kirchhoff stress tensor $\mathbf{S}$. The Cauchy stress tensor $\boldsymbol{\sigma}$ can be obtained from a weighted push-forward of $\mathbf{S}$ such that $\boldsymbol{\sigma} = J^{-1}\varphi_*[\mathbf{S}]$, see Eq. (3.36) for the corresponding definition. The mechanical tangent can be accordingly derived as is presented in Section 3.1.2. Finally, a set of state dependent variables is also defined encompassing: (i) the current value of the free-energy function, (ii) the maxi-

---

[1]This is required since previous versions of `ABAQUS` 2019 do not compute properly the volumetric heat generation.

mum value of the driving force $\mathcal{H}$ throughout the loading process, (iii) the fracture toughness, and (iv) the length scale parameter.

With respect to the thermal problem, we start the derivation from the local spatial form of the heat equation. Assuming an homogeneous and temperature independent mass density ρ, a homogenous and temperature independent heat capacity c_p, and thermal isotropy recalling the Duhamel's law of heat conduction that yields to Fourier's law, $\mathbf{q} = -k\nabla_{\mathbf{x}}T$ (where $\mathbf{q}$ is the heat flux, thermal conductivity k and $\nabla_{\mathbf{x}}T$ is the gradient of the temperature T), the heat equation can be expressed as:

$$\rho c_p \frac{\partial T}{\partial t} - k\nabla_{\mathbf{x}} \cdot [\nabla_{\mathbf{x}}T] = r_T, \tag{3.34}$$

where r_T is the spatial heat source.

The governing equation, Eq.(3.33) for the phase field resembles the form of the heat equation given in Eq. (3.34) after rearranging some of the terms. The main difference between both expressions lies in the computation of the gradient of phase field variable that should be mapped onto the current configuration. For this purpose we recall standard push-forward operations, where the gradient of the phase field in analogy with the temperature:

$$\nabla_{\mathbf{x}}\eth = \mathbf{F}^{-\mathrm{T}}\nabla_{\mathbf{X}}\eth \tag{3.35}$$

Moreover, in line with Hortig [293], a unit mass density can be defined yielding to the identification of the variable χ with the heat capacity c_p, whereas the heat generation should be also activated and setting as material property the thermal conductivity k equal to 1.

Derivation of the numerical implementation of the constitutive model

To fully implement the `UMAT` subroutine, the stress field and the Jacobian matrix are required to be computed for the current system of coordinates. For that reason, there is a need to perform a push-forward operation for these magnitudes to obtain the Cauchy stress and the spatial constitutive tensor. It is important to highlight that all the calculations are made

for the reference configuration and then, we push-forward the required variables at the end to adjust to the requirements of the UMAT subroutine.

Starting with the terms for the stresses, these are known to be easily computed by doing the following product to the different terms for the second Piola-Kirchhoff stress in Eq. (3.23)

$$\boldsymbol{\sigma} = J^{-1}\mathbf{F} \cdot \mathbf{S} \cdot \mathbf{F}^{\mathrm{T}}. \tag{3.36}$$

This operation is straightforward for the terms related to the hyperelastic (Eq. (3.11)) and the prestresses (Eq. (3.21)). However, it is important to highlight some remarks about the evolution in time of the viscous stresses (Eq. (3.16)), regarding the time dependence of the tensor $\mathbf{A}$, which needs to be properly addressed. This magnitude is updated for every iteration in the staggered scheme following the expression:

$$\mathbf{A}_{n+1}^{(\alpha)} = \mathbf{A}_n^{(\alpha)} + \Delta t \dot{\mathbf{A}}_{n+1}^{(\alpha)} \tag{3.37}$$

which can be developed by considering the expression for $\dot{\mathbf{A}}^{(\alpha)}$ in Eq. (3.14) as

$$\mathbf{A}_{n+1}^{(\alpha)} = \left(\frac{1}{1 + \Delta t/\tau^{(\alpha)}}\right)\left[\mathbf{A}_n^{(\alpha)} + \frac{\Delta t}{\tau^{(\alpha)}}(\bar{\mathbf{C}}_{n+1}^{-1})\right]. \tag{3.38}$$

where Δt is the time increment. Subsequently after this, we decide to perform the push-forward operation in the tensor $\mathbf{A}^{(\alpha)}$ like: $\mathbf{a}_{n+1}^{(\alpha)} = \mathbf{F}_{n+1}\mathbf{A}_{n+1}^{(\alpha)}\mathbf{F}_{n+1}^{\mathrm{T}}$. The reason on why performing this action here rather than when computing $\mathbf{S}_{n+1}^{(\mathrm{visco},\alpha)}$ relies on a considerable improvement in the convergence rate. Therefore, after doing some algebra, the expression for the Cauchy viscous overstress in the UMAT is found

$$\boldsymbol{\sigma}_{n+1}^{(\mathrm{visco},\alpha)} = J^{-5/3}\left(\frac{G^{\mathrm{visco},\alpha}}{1 + \Delta t/\tau^{(\alpha)}}\right)\left[\mathbf{a}_{n+1}^{(\alpha)} - \frac{1}{3}\mathrm{tr}(\mathbf{a}_{n+1}^{(\alpha)})\mathbf{1}\right]. \tag{3.39}$$

Next, in order to compute the material Jacobian in the current configuration, it is considered two separate terms: at first, one for the material (hyper-viscoelastic law), which has the formula of

$$\mathbb{C}^{\text{mat}}_{ijkl} = \frac{1}{2}J^{-1}\left(F_{lm}\frac{\partial(J\sigma_{ij})}{\partial F_{km}} + F_{km}\frac{\partial(J\sigma_{ij})}{\partial F_{lm}}\right) \tag{3.40}$$

where

$$\frac{\partial(J\sigma_{ij})}{\partial F_{km}} = GJ^{-2/3}\left(\delta_{ik}F_{jm} + \delta_{jk}F_{im} - \frac{2}{3}\delta_{ij}F_{km} - \frac{2}{3}b_{ij}F_{mk}^{-1} + \frac{2}{9}(\text{tr }\mathbf{b})\delta_{ij}F_{mk}^{-1}\right)$$
$$+ \kappa\delta_{ij}F_{mk}^{-1} + \sum_{\alpha}\left\{J^{-2/3}\left(\frac{G^{\text{visco},\alpha}}{1 + \Delta t/\tau^{(\alpha)}}\right)\left[-\frac{2}{3}F_{mk}^{-1}(\mathbf{F}_{n+1}\mathbf{A}_n^{(\alpha)}\mathbf{F}_{n+1}^{\text{T}})_{ij}\right.\right.$$
$$+ \frac{2}{9}F_{mk}^{-1}\text{tr}(\mathbf{F}_{n+1}\mathbf{A}_n^{(\alpha)}\mathbf{F}_{n+1}^{\text{T}})\delta_{ij} + \delta_{ik}(\mathbf{A}_n^{(\alpha)}\mathbf{F}_{n+1}^{\text{T}})_{mj} + (\mathbf{F}_{n+1}\mathbf{A}_n^{(\alpha)})_{im}\delta_{jk}$$
$$\left.\left. - \frac{1}{3}(\mathbf{A}_n^{(\alpha)}\mathbf{F}_{n+1}^{\text{T}})_{mk}\delta_{ij} - \frac{1}{3}(\mathbf{F}_{n+1}\mathbf{A}_n^{(\alpha)})_{km}\delta_{ij}\right]\right\}. \tag{3.41}$$

On the other hand, the other Jacobian term accounts for the residual stresses contribution. Its stiffness matrix can be computed as

$$\mathbb{C}^{\text{res}}_{ijkl} = \mathbb{C}^{\text{c,res}}_{ijkl} + \frac{1}{2}(\delta_{ik}\sigma_{lj}^{\text{res}} + \delta_{il}\sigma_{kj}^{\text{res}} + \delta_{jl}\sigma_{ik}^{\text{res}} + \delta_{jk}\sigma_{il}^{\text{res}}), \tag{3.42}$$

$$\mathbb{C}^{\text{c,res}}_{ijkl} = \frac{4}{J}F_{i\alpha}F_{j\beta}F_{k\gamma}F_{l\delta}\frac{\partial^2\Psi^{\text{res}}}{\partial\mathbf{C}^2}\bigg|_{\alpha\beta\gamma\delta}. \tag{3.43}$$

For the second derivative, the following terms are needed

$$\frac{\partial\mathbf{C}^{-1}}{\partial\mathbf{C}}\bigg|_{ijkl} = \frac{1}{2}(C_{ik}^{-1}C_{lj}^{-1} + C_{il}^{-1}C_{kj}^{-1}), \tag{3.44}$$

$$\frac{\partial^2 I_6}{\partial\mathbf{C}^2}\bigg|_{ijkl} = \frac{1}{2}(\delta_{ik}\sigma_{0lj} + \delta_{il}\sigma_{0kj} + \delta_{jl}\sigma_{0ik} + \delta_{jk}\sigma_{0il}). \tag{3.45}$$

By employing them, one reaches

Table 8: Mechanical properties of the double-notched plane strain specimen.

Property (Unit)	G (MPa)	κ (MPa)	G^{visco} (MPa)	$\mathcal{G}_{\mathrm{C}}$ (N/mm)	ℓ (mm)	f	χ
Value	0.41	3.96	0.36	20.0	2.0	0.5	10^{-16}

$$
\frac{\partial^2 \Psi^{\mathrm{res}}}{\partial \mathbf{C}^2}\bigg|_{\alpha\beta\gamma\delta} = J^{-1/3}\left[-\frac{f}{6}(\boldsymbol{\sigma_0}\otimes\mathbf{C}^{-1}+\mathbf{C}^{-1}\otimes\boldsymbol{\sigma_0})+\frac{fI_5}{18}\mathbf{C}^{-1}\otimes\mathbf{C}^{-1}-\frac{fI_5}{6}\frac{\partial\mathbf{C}^{-1}}{\partial\mathbf{C}}\right]
$$
$$
+(1-f)J^{-2/3}\left[\frac{I_6}{9}\mathbf{C}^{-1}\otimes\mathbf{C}^{-1}-\frac{1}{6}\left(\mathbf{C}^{-1}\otimes\frac{\partial I_6}{\partial\mathbf{C}}+\frac{\partial I_6}{\partial\mathbf{C}}\otimes\mathbf{C}^{-1}\right)-I_6\frac{\partial\mathbf{C}^{-1}}{\partial\mathbf{C}}+\frac{1}{4}\frac{\partial^2 I_6}{\partial\mathbf{C}^2}\right].
$$

$$(3.46)$$

Finally, both terms of Eqs. (3.40) and (3.42) are added to form the material Jacobian

$$
\mathbb{C}_{ijkl} = \mathbb{C}_{ijkl}^{\mathrm{mat}} + \mathbb{C}_{ijkl}^{\mathrm{res}}. \tag{3.47}
$$

3.3 Representative applications

3.3.1 Verification example

In order to verify the present hyperelastic and visco-hyperelastic formulation, a benchmark application is first considered. For this purpose, a two-dimensional plane strain example of a double-notched specimen conducted by Hocine and co-authors [248] is taken as reference solution in conjunction with the corresponding correlation with experimental data. The geometric description is displayed in Fig. 29(a), whereas the material properties are listed in Table 8.

In line with previous phase field models [294, 295], the current formulation is first validated under rate-independent fracture evolution conditions. Fig. 29(b) shows the different load-displacement evolution curves
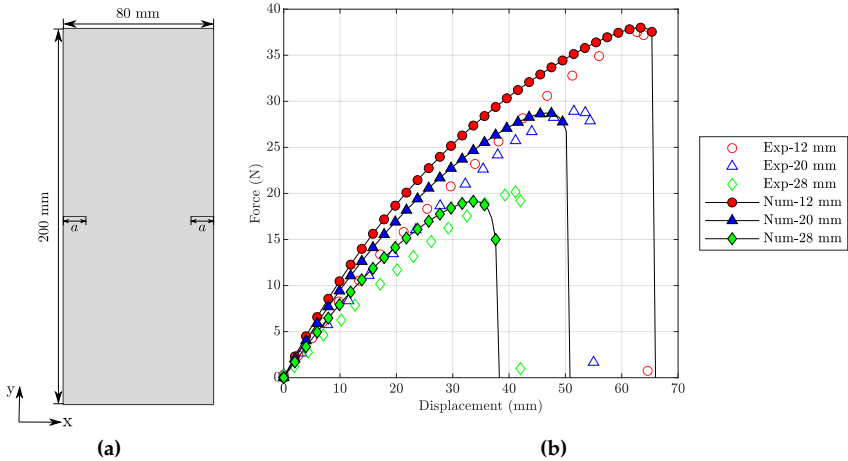
Figure 29: (a) Geometry setup of the double-notched specimen conducted by [248] with (b) the corresponding load-displacement curves (numerical, Num, and experimental, Exp) for verification, precluding viscous effects.

for different sizes of the initial notches, exhibiting a very satisfactory correlation with respect to the available experimental tests for $a = [12, 20, 28]$ mm.

This application is further analyzed in order to elucidate the rate-dependent response, analyzing the effect of a series of relaxation times $\tau = [0.05, 0.1]$ s and velocities v $= [125, 250, 500, 1000]$ mm/s for a length of the prescribed notch $a = 20$ mm considering only one viscous sub-domain. The corresponding force-displacement evolution curves are depicted in Figs. 30(a)-30(b). Analyzing this graph it is possible to observe that the maximum force increases and the peak displacement decreases as the loading rate augments (both reported in Table 9).

Examining the mechanical response with respect to the relaxation time, the behaviour of a specimen at a constant loading rate v $= 500$ mm/s is compared in Fig. 31 for relaxation times $\tau = [0.01, 0.05, 0.1, 0.5]$ s. This graph evidences that smaller values of the relaxation times leads to higher values for the maximum displacement and smaller lower forces (see Table 10 for the values of these magnitudes). This response shows
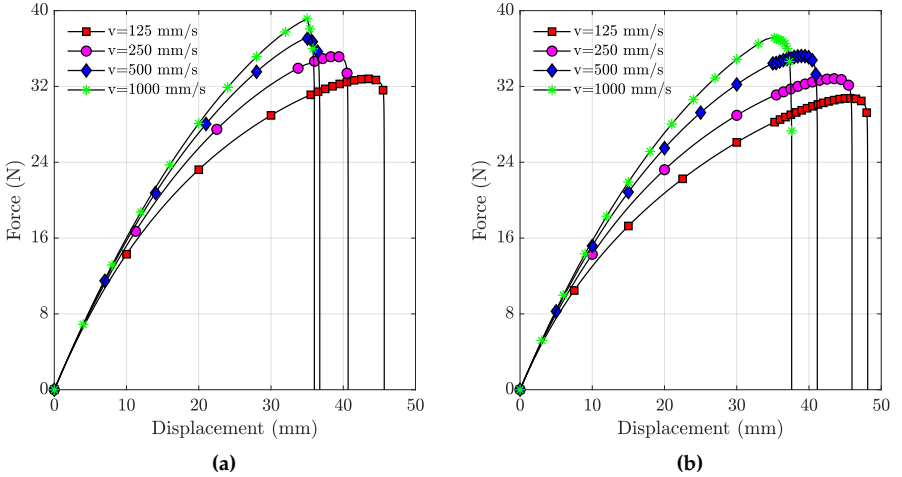
Figure 30: Load-displacement curves for tests with (a) $\tau = 0.1$ s and (b) $\tau = 0.05$ s and different displacement rates on the double-notched specimens.

a very good qualitative correlation with the findings reported in [275]. The phase field evolution for one representative case is plotted in Fig. 32, where, as it is expected, the initiation and evolution of the crack complies with Mode I fracture.

A further verification of this case is reported in Appendix A right after Section 3.4, where this parametric study is repeated for a square single-notched plate and the outlined results display a similar behavior to the ones aforementioned in this Section.

3.3.2 Cylindrical structures

The main objective of this section concerns the simulation of pre-stressed cylindrical structures using the current modelling framework. For this purpose, a parametric analysis for hollow cylinders is conducted. Particularly, this is performed by modifying the viscous and residual intensity parameters in order to assess their influence on the mechanical perfor-

86

Table 9: Comparison of the maximum force and displacement for different test rates on the double-notched specimen.

Displacement rate (mm/s)	1000	500	250	125
Relax time (s)	0.05 \ 0.1	0.05 \ 0.1	0.05 \ 0.1	0.05 \ 0.1
Maximum Force (N)	18.60 \ 19.57	17.60 \ 18.52	16.41 \ 17.58	15.38 \ 16.40
Maximum Displacement (mm)	37.60 \ 36.00	41.15 \ 36.75	45.95 \ 40.68	48.12 \ 45.68
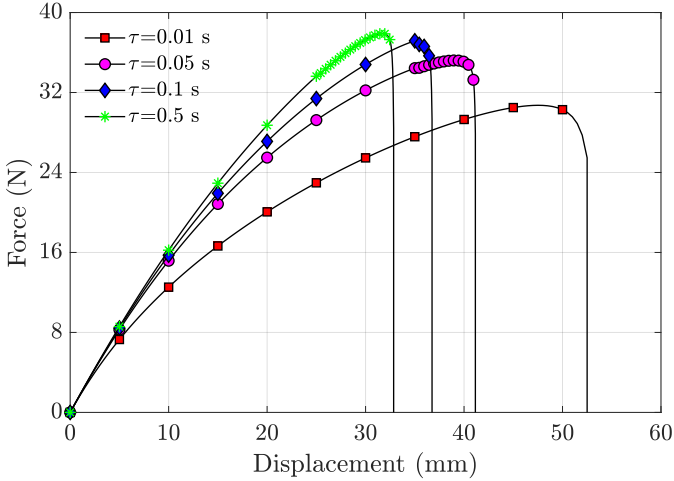
Figure 31: Load-displacement curves for tests with $v = 500$ mm/s and different relaxation times on the double-notched plane strain specimens.

mance of the structure.

The general features of the tests are presented up next, which are used for the simulation of two baseline configurations: (i) intact hollow cylindrical structures and (ii) samples with a initial notch at the centre of the major axis; it is worth mentioning that this initial notch is inserted via setting a prescribed boundary condition on the phase field value $\mathfrak{d} = 0.5$.

Table 10: Comparison of the maximum force and displacement for different relaxation times of the double-notched specimen.

Displacement rate (mm/s)	500	500	500	500
Relax time(s)	0.01	0.05	0.1	0.5
Maximum Force (N)	18.95	18.58	17.60	15.36
Maximum Displacement (mm)	52.50	41.15	36.75	32.85

1) $u = 39.20$ mm   2) $u = 41.15$ mm
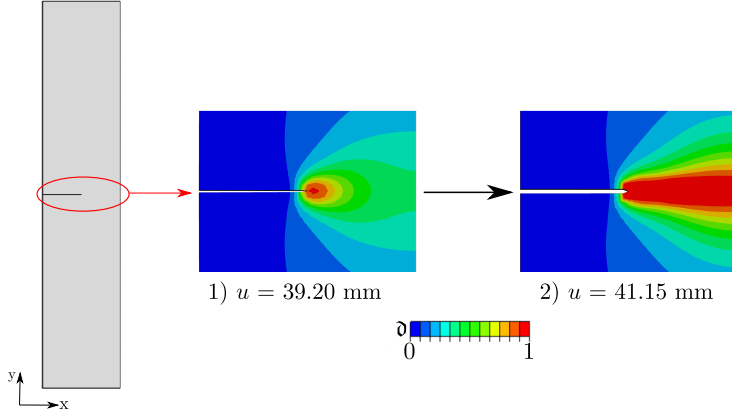
Figure 32: Zoom in the notched area during: Mode I (1) crack initiation and (2) propagation for the case with parameters v $=$ 500mm/s and $\tau = 0.1$ s. Plotted is the phase field parameter isocontour with the legend case, where blue and red denote intact and broken states, respectively.

Test characteristics

This section describes the specimen geometry and the particular form of the residual stress field henceforth considered. In conjunction with the constitutive models for the bulk described above, we adopt the following form for the residual stress field, adapted from [285, 296]:

$$\sigma_{0RR} = \alpha_c(R - A)(R - B) \tag{3.48}$$

$$\sigma_{0RZ} = \frac{\alpha_d}{R}[(R - A)(R - B)(4Z^3 - 6Z^2L + 2ZL^2)] \tag{3.49}$$

Table 11: Mechanical properties of the cylindrical structures.

Property (Unit)	G (MPa)	κ (MPa)	G^{visco} (MPa)	$\mathcal{G}_\text{C}$ (N/mm)	ℓ (mm)	f	χ
Value	25.00	616.67	21.74	3.0	2.0	0	10^{-10}

$$\sigma_{0\Theta\Theta} = \alpha_c[3R^2 - 2(A+B)R + AB] + \alpha_d[(R-A)(R-B)(12Z^2 - 12ZL + 2L^2)] \tag{3.50}$$

$$\sigma_{0ZZ} = -\frac{\alpha_d}{R}[(2R - A - B)(Z(L-Z))^2] \tag{3.51}$$

$$\sigma_{0\Theta Z} = \sigma_{0R\Theta} = 0 \tag{3.52}$$

where A and B are the inner and outer radius, respectively, of the cylindrical structure; α_c and α_d are coefficients which follow the formula $\alpha_c = G\bar{\alpha}_c/2BH$ and $\alpha_d = G\bar{\alpha}_d/2L^4$; and H and L are the thickness and length of the cylinder.

The strength of the residual stress field is controlled by the dimensionless parameters $\bar{\alpha}_c$ and $\bar{\alpha}_d$ which account for the dependence of the system on the R and Z coordinates of the cylindrical system. It follows that by setting $\bar{\alpha}_d = 0$, the pre-stress field only relies on R. Further research on how to obtain a qualitative behavior of the residual stress field for their different components can be found in [296].

Without any loss of generality, we prescribe the following dimensions for the cylinder: length L = 150 mm, diameter D = 5 mm and thickness T = 0.5 mm. Several simulations for the parametric tests are conducted by changing the displacement rate, relaxation time and the residual stresses field on cylinders with or without a phase field initial condition on the center for $\mathfrak{d} = 0.5$.

The mechanical properties for the current applications are listed in Table 11. Note that a nearly incompressible neo-Hookean material (ν=0.49) is set. Concerning the spatial discretization of the system, we employ 23,250 8-node hexahedral elements with one viscous subdomain in the bulk material description.

In line with [281], present computations consist of two steps: (i) the first step is defined for the application of the residual stresses field presented in Eqs. (3.48)-(3.52), without prescribing any additional action,

and (*ii*) the second step comprises the application of a pulling action along the longitudinal axis of the cylinder till the complete failure of the structure. Every numerical experiment requires one or two hours of computational run in the aforementioned station until its completion.

The BCs configuration for the geometry is like it follows: for the first step, the cylinder is restricted completely in the azimuthal direction in both topmost and bottommost surfaces along the major axis in order to let the radial coordinate free for the application of the residual stresses. For the final step, the bottommost surface is fixed whereas the topmost surface is pulled in the Z direction until the failure of the cylindrical specimen.

Pristine cylinders

Dependence on visco-elastic parameters   The first series of parametric tests concerns the analysis of rate-dependent effects on crack propagation, in line with Section 3.3.1. Without the application of residual stress, the effect of different relaxation times $\tau = [0.05, 0.1, 0.2, 0.5]$ s and displacement rates $v = [10, 25, 500, 100]$ mm/s on the mechanical response of the current hollow cylinders are examined.

Results for the reaction force-imposed displacement evolution curves of the probes for different relaxation times and imposed velocities are obtained. Fig. 33(a) shows these curves for the different relaxation times setting $v = 25$ mm/s, whereas Fig. 33(b) depicts the results for $\tau = 0.1$ s and various displacement rates. Analyzing these plots, it can be seen that the dependence of the results on these viscoelastic parameters is in line with the verification results reported in Section 3.3.1, i.e. for higher relaxation time or test velocity the estimated peak force increases but ultimate displacement decreases. This trend is identified for all the cases under consideration as it is reported in Tables 12 and 13.

A representative phase field isocontour at the end of the computation is shown in Fig. 34 displaying that the crack initiates from the center of the probe and propagates axially provoking the failure of the specimen.

Dependence on residual stress parameters   Continuing with the numerical tests for pre-stressed pristine cylinders, the next two series of
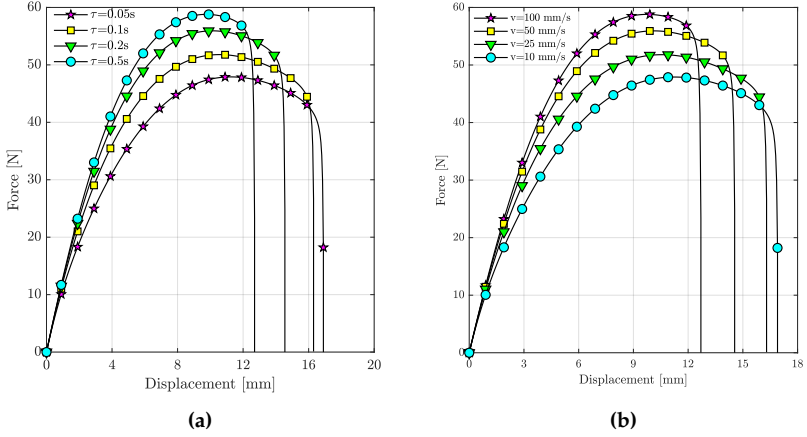
Figure 33: Load-displacement curves for cases with different (a) relaxation times and (b) displacement velocities for the non pre-stressed cylinders.

Table 12: Comparison of the maximum force and displacement for the tests with different relaxation times and v = 25 mm/s for the non pre-stressed cylinders.

Relax time (s)	0.05	0.1	0.2	0.5
Maximum Force (N)	48.60	51.79	55.93	59.16
Maximum Displacement (mm)	16.90	16.30	14.55	12.25

parametric computations are dedicated to the examination of the dependence of the results on both residual stress intensity factors $\bar{\alpha}_c$ and $\bar{\alpha}_d$. The effect of both parameters are analyzed separately in order to assess the damage that they cause to the cylindrical structures.

First, results for cases with plane residual stresses are considered ($\bar{\alpha}_c > 0$ and $\bar{\alpha}_d = 0$) with a prescribed velocity equal to v = 25 mm/s and a relaxation time of $\tau = 0.1$ s. Current predictions qualitatively coincide with that reported in [281] for the same residual stress field, whose von Mises stress isocontour at the step of the application of the residual stress is shown in Fig. 35. The reaction-force displacement curves for plane

Table 13: Comparison of the maximum force and displacement for the tests with different displacement rates and $\tau = 0.1$ s for the non pre-stressed cylinders.

Displacement rate (mm/s)	100	50	25	10
Maximum Force (N)	58.80	55.93	51.79	47.91
Maximum Displacement (mm)	12.70	14.55	16.30	16.90
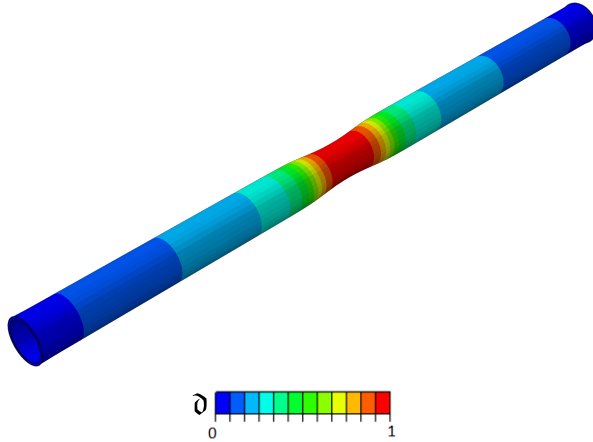
Figure 34: Phase field isocontour at the moment of failure for the non pre-stressed hollow cylinder.

residual stress cases are depicted in Fig. 36. This graph reveals that both ultimate force and ultimate displacement decrease for greater values of the coefficient $\bar{\alpha}_c$. This can be concluded as expected since the inclusion of residual stresses is associated with a decrease in both strength and stiffness properties, which leads to premature failure.

For the sake of quantifying the curves, in Table 14, it is plotted both peak load and displacement for the overall experiment. It is worth highlighting that applications with higher residual stresses associated with $\bar{\alpha}_c > 3.5$ have been carried out but they are not considered since an abrupt change in the pattern of failure occurs, provoking in the model a severe radial strain.
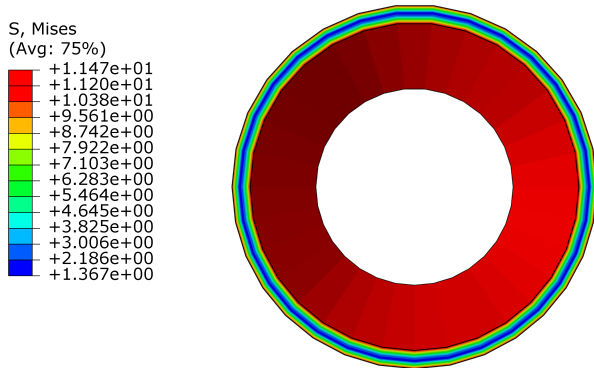
Figure 35: Von Mises stresses distribution for a residual stress with $\bar{\alpha}_c = 1$.

Subsequently, specimens with both R- and Z-dependent residual stresses ($\bar{\alpha}_c = 0$ and $\bar{\alpha}_d > 0$) are taken into consideration in this last series of tests. Under these circumstances, a typical von Mises stresses isocontour is shown in Fig. 37 exhibiting an increase in the value of this magnitude (von Mises stress) while approaching the center of the major axis of the cylinder. This is in accordance with the patterns displayed in [296].

In line with the previous analysis for plane residual stresses, current load-displacement curves plotted in Fig. 38 show an overall similar trend, with some nuances: the higher the value of $\bar{\alpha}_d$ is set, the lower the values of the maximum force and maximum displacement are obtained, being considerably increased this difference for $\bar{\alpha}_d > 50$, when the peak values collapse due to this effect (see Table 15 for exact results). In addition to this, it can be identified that the nucleation zone for failure is more concentrated towards the centre of the major axis for higher values of $\bar{\alpha}_d$, see Fig. 39.

Cylinders with a initial flaw prescribing the phase field values at the center of the geometry

This section is focused on analyzing cases with a prescribed initial defect at the center of the cylinder. This is incorporated into the simulation by setting an initial value of the phase field variable at this location of
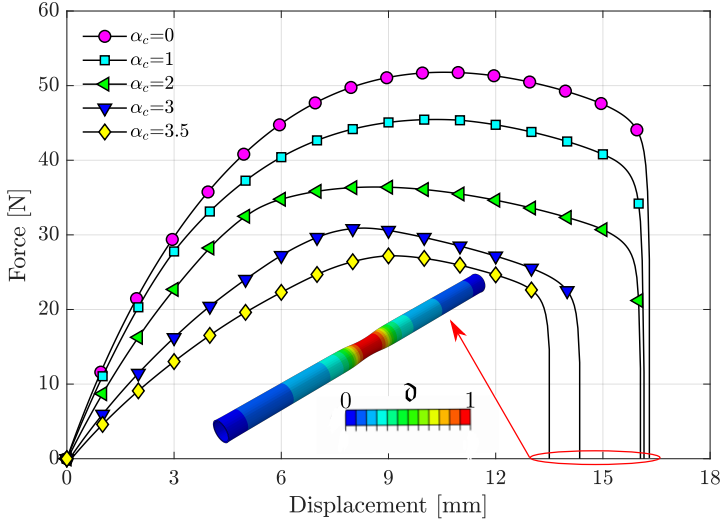
Figure 36: Load-displacement curves for cylinders with different residual stress intensity parameter $\bar{\alpha}_c$, along with the phase field isocontour in the final step.

Table 14: Comparison of the maximum force and ultimate displacement for the tests with different $\bar{\alpha}_c$.

$\bar{\alpha}_\mathbf{c}$	0	1	2	3	3.5
Maximum Force (N)	51.79	45.47	36.41	30.91	27.19
Maximum Displacement (mm)	16.30	16.15	16.05	14.35	13.50

$\mathfrak{d} = 0.5$. Current simulations are carried out with a displacement rate of $v = 25$ mm/s and a relaxation time $\tau = 0.1$ s for a cylinder with the material parameters given in Table 11.

The corresponding reaction-force displacement curves for these cases are shown in Fig. 40. These results display that while the peak force is reduced slightly with the application of the phase field initial condition, the main difference between scenarios with and without prescribed initial defect concerns the premature failure of the structure, which is
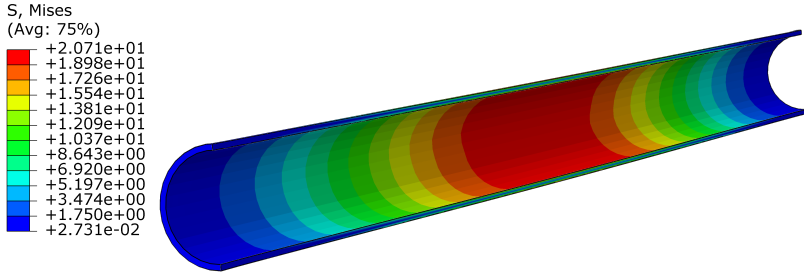
Figure 37: Von Mises stresses distribution associated with a residual stress field in which $\bar{\alpha}_{\mathrm{d}} = 500$.
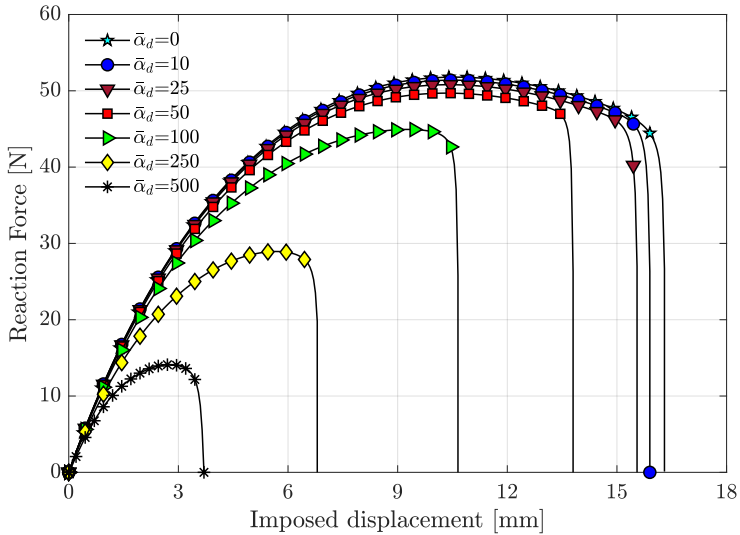
Figure 38: Load-displacement curves for cylinders with different residual stress intensity parameters $\bar{\alpha}_d$.

predicted to occur when the initial flaw is considered, see Table 16.

Figs. 41(a) and 41(b) depict the initial state of the phase field variable and its propagation, respectively, in a representative case for a hollow cylinder with an initial flaw.

Table 15: Comparison of the maximum force and ultimate displacement for the tests with different $\bar{\alpha}_d$.

$\bar{\alpha}_\mathbf{d}$	0	10	25	50	100	250	500
Maximum Force (N)	51.79	51.39	50.79	49.70	44.93	28.94	14.12
Maximum Displacement (mm)	16.30	15.90	15.55	13.80	10.65	6.80	3.70

(a) $\bar{\alpha}_d = 0$

(b) $\bar{\alpha}_d = 50$

(c) $\bar{\alpha}_d = 250$
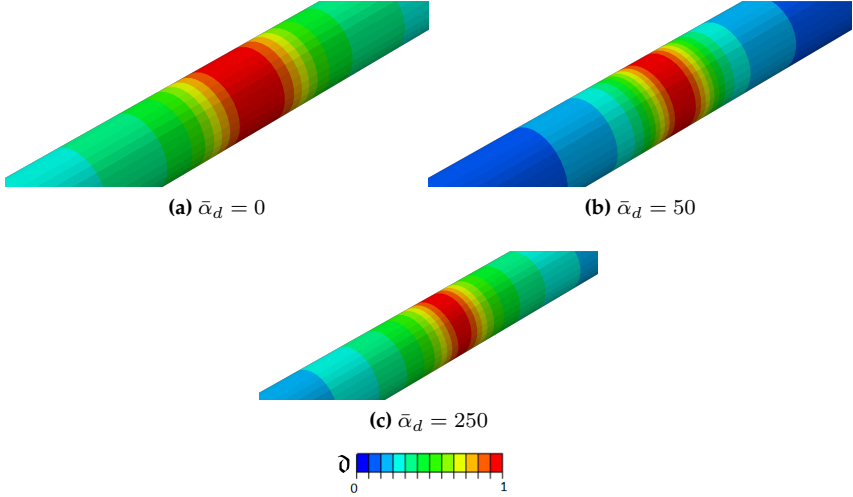
Figure 39: Phase field isocontour at the moment of failure for the residually stressed hollow cylinder with different values of $\bar{\alpha}_d$.

3.3.3 Two-layered cylinders

Test characteristics

The simulation capabilities of the proposed model are further examined by considering multilayered cylindrical structures. The two-layered cylinder systems are particularized as follows: (i) a prescribed flaw over the thickness with a radius of 0.1 mm is defined at the center of the outer layer, and (ii) a residual stress field with $\bar{\alpha}_c = 0.5$ and $\bar{\alpha}_d = 40$ is set at the inner layer of the system, see the details displayed in Figs. 42(a)-42(b). The goal is to show that the methodology at hand can be used
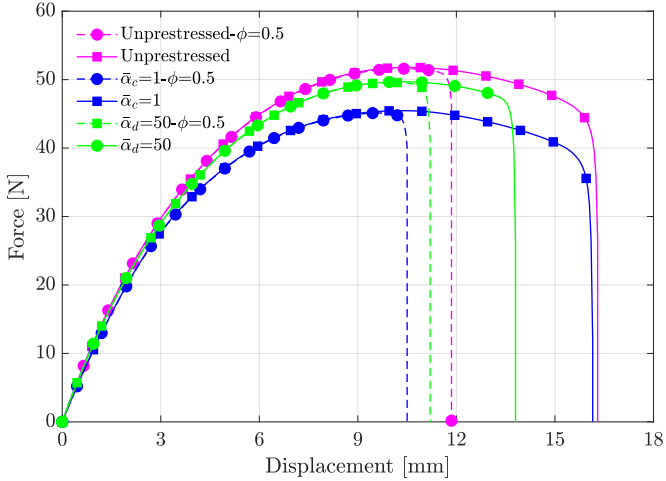
Figure 40: Load-displacement curves comparing the tests on cylinders with no residual stress, with $\bar{\alpha}_c = 1$ and $\bar{\alpha}_d = 40$ and additional cases with $\mathfrak{d} = 0.5$ as it is indicated in the labels of the curves.

Table 16: Comparison of the maximum force and ultimate displacement obtained in the tests with and without flaw for both pre-stressed and non pre-stressed cylinders.

Residual stresses	No		$\bar{\alpha}_c = 1$		$\bar{\alpha}_d = 50$	
$\mathfrak{d}$ BC	$\mathfrak{d} = 0.5$	$\mathfrak{d} = 0$	$\mathfrak{d} = 0.5$	$\mathfrak{d} = 0$	$\mathfrak{d} = 0.5$	$\mathfrak{d} = 0$
Maximum Force (N)	51.59	51.79	45.14	45.46	49.58	49.70
Maximum displacement (mm)	11.85	16.30	10.50	16.15	11.20	13.80

to handle these structures. A residual stress field is established in the inner layer of the cylinder, which triggers a residual stress field in the outer layer, as, in general, displacements and radial components of traction have to be continuous through the interface. Numerically, some iterations might be needed to establish the initial equilibrium of the residually-stressed tube.

For the particularization of the system, a nearly incompressible neo-Hookean material is employed ($\nu = 0.49$) using a finite element mesh of
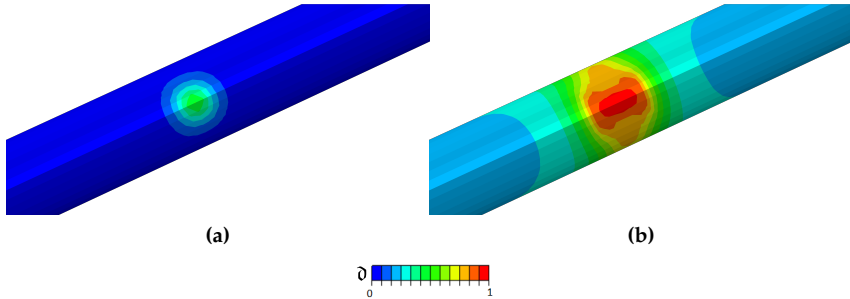
Figure 41: Axial propagation of the phase field parameter for the cylinders with the BC of $\mathfrak{d} = 0.5$: (a) first step and (b) last load step (axial propagation).

Table 17: Mechanical properties of the inner cylindrical layer.

Property (Unit)	G (MPa)	κ (MPa)	G^{visco} (MPa)	$\mathcal{G}_C$ (N/mm)	ℓ (mm)	f	χ
Value	10	500	12	0.1	1.2	0	10^{-10}

50,024 8-node hexahedral elements. Each test requires a run time in the aforementioned station between 1-2 hours for its the completion.

The test conditions are as follows: a displacement rate of $v = 25\,\text{mm/s}$ and a relaxation time $\tau = 0.1$ s for only one viscous subdomain are employed. The BCs do coincide with those presented in Section 3.3.2, with the exception that now in the step for the application of the residual stresses, only the inner bottommost and topmost surfaces are restricted in the azimuthal direction.

A parametric study is conducted to analyze the influence of the mismatch in several mechanical parameters on the behaviour of the sample, in particular, on the crack initiation region and on the mechanical performance of the sample. Special attention is paid to the effect of: (i) different shear modulus ratios and (ii) different critical fracture energy ratios.

For the current parametric analysis, the inner region is kept unchanged in terms of some mechanical properties with respect to previous analyses, and those values are listed in Table 17. The only parameter that
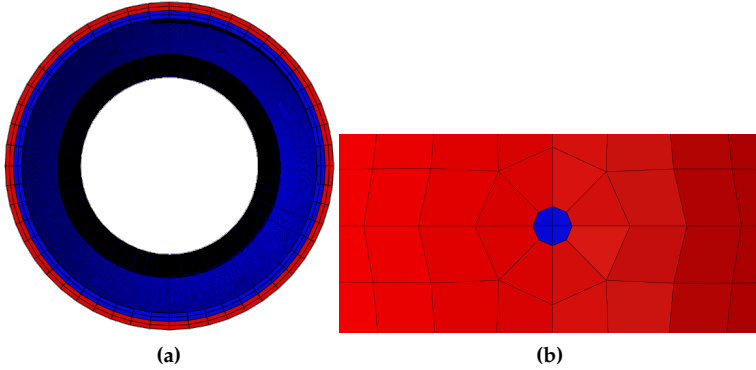
Figure 42: (a) Isommetric and (b) zoomed-in-the-notch view of the cylindrical structure with two layers, distinguishing the layer by the color.

takes different values (compared to the previous cases) is the residual stress field since it is considered simultaneously that $\bar{\alpha}_c = 0.5$-$\bar{\alpha}_d = 40$ [296]. Hoop ($\sigma_{\theta\theta0}$) and radial (σ_{RR0}) stresses are represented across the thickness of the cylinder at Z = L/4 in Fig. 43. Results for both stresses in the inner layer of the cylinder $\left(\frac{R-A}{T} \leq 0.5\right)$ replicate qualitatively those obtained in Figure 10 of [281], and shows that the procedure captures the initial stress field. In the outer layer, it is observed the presence of residual stresses. To compliment this result, the von Mises stresses in the inner and outer layer are displayed in Figs. 44(a)-44(b), where the difference in the magnitude of the stress field for both layers is pinpointed in the legend box of both isocontours.

Shear modulus influence

First, it is analyzed the role of the shear modulus ratio between both layers G_1/G_2, where the index 1 refers to the outer layer and the index 2 refers to the inner layer. The particular cases that are henceforth detailed concern the ratios: $G_1/G_2 = [0.2, 0.5, 1, 2, 5]$. Note that as the bulk modulus κ depends on G and a fixed ratio of $G^{visco}/G = 1.2$ is considered, these parameters are also affected by the mismatch between G_1 and G_2.

Load-displacement curves for cases without residual stresses are de-
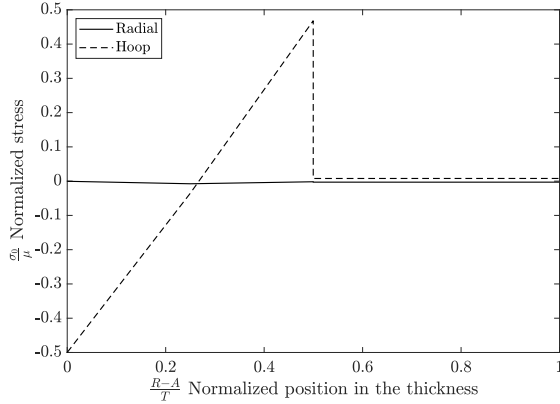
Figure 43: Values of hoop and radial residual stresses along the thickness of the cylinder structure for a path located at Z = L/4.

(a)   **(b)**
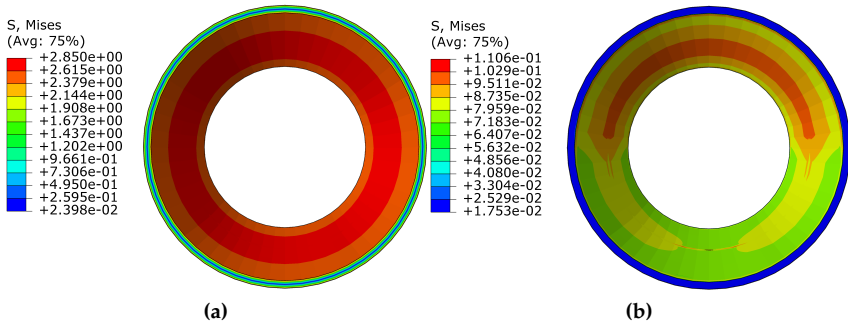
Figure 44: Von Mises stress isocontourn for (a) the inner and (b) the outer layer, respectively, for a pre-stressed bi-layered cylindrical structure.

picted in Fig. 45. The failure displacement is increased for decreasing values of the ratio G_1/G_2 and, as it is expected, results feature a compliant response since the greater the ratio G_1/G_2 is, the greater is the mismatch between other corresponding mechanical properties ratios between the two layers. Failure reaction and imposed displacements are reported in Table 18 for several cases. From a qualitative point of view,
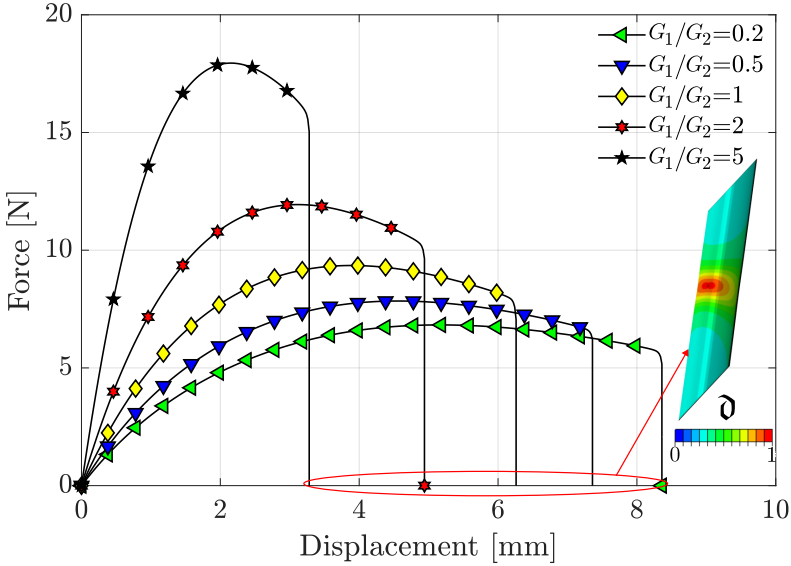
Figure 45: Reaction force-imposed displacement curves for the parametric study changing the shear modulus ratio without residual stress.

the phase field isocontour at the final step is plotted, which displays a damage initiation region concentrated around the initial flaw for both outer and inner layers.

The residual stress field at the inner layer notably affects the response of the system. Force-displacement evolution curves are shown in Fig. 46, which exhibit the same behaviour as the non pre-stressed cases. Nevertheless, the effect of the residual stress can be appreciated in the specific failure magnitudes detailed in Table 19, where the values for both peak force and displacement are subtly smaller than the bi-layered cylinders without residual stress (see Table 18).

The effect of the shear modulus ratio on the pre-stressed cylinder is shown in Figs. 47(a)-47(e). From these graphs, it can be observed that the crack is captured to be initiated at the center, where the notch is located. Note also that the peak residual von Mises stress is at the center in the inner layer, see Fig. 44(a). Analyzing all the cases, one envisages that the

Table 18: Comparison of the maximum force and displacement for non pre-stressed two-layered cylinders with different G_1/G_2 ratios.

G_1/G_2	0.2	0.5	1	2	5
Maximum Force (N)	6.83	7.84	9.35	11.94	17.95
Maximum Displacement (mm)	8.36	7.36	6.26	4.94	3.28
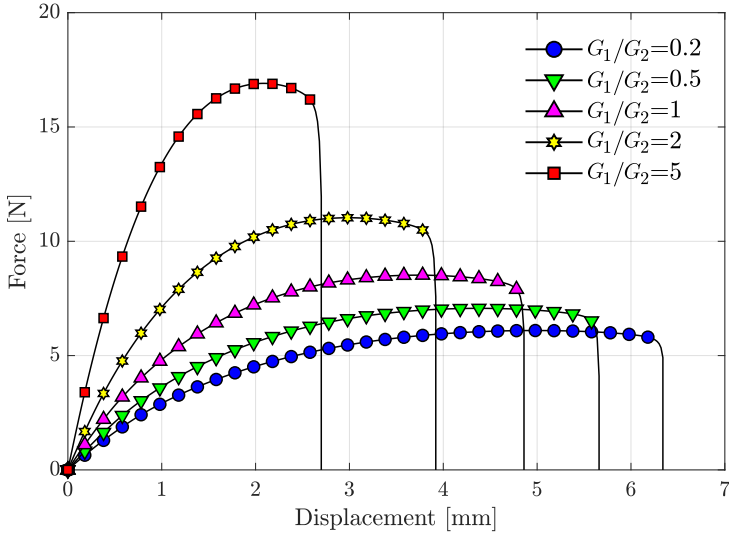
Figure 46: Reaction force-imposed displacement curves for the parametric study changing the shear modulus ratio with residual stress parameters $\bar{\alpha}_c = 0.5$-$\bar{\alpha}_d = 40$.

Table 19: Comparison of the maximum force and ultimate displacement for residually stressed ($\bar{\alpha}_c = 0.5 - \bar{\alpha}_d = 40$) two-layered cylinders with different G_1/G_2 ratios.

G_1/G_2	0.2	0.5	1	2	5
Maximum Force (N)	6.10	7.07	8.52	11.03	16.91
Maximum Displacement (mm)	6.34	5.66	4.86	3.92	2.70
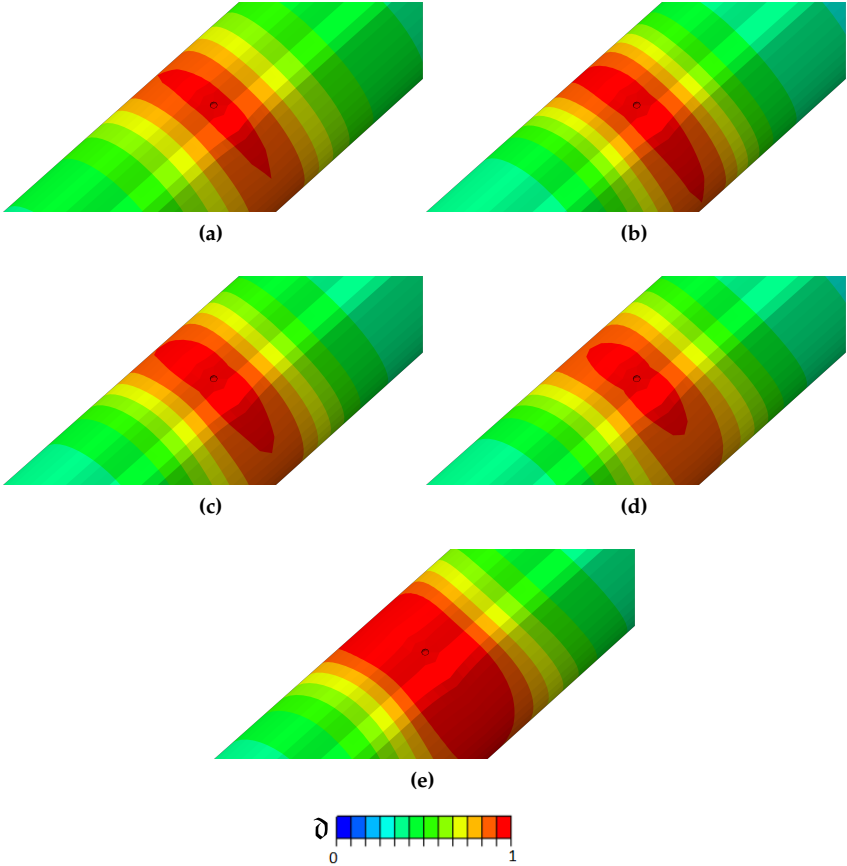
Figure 47: Crack pattern for the different critical Shear Modulus ratios with residual stress parameters $\bar{\alpha}_c = 0.5\text{-}\bar{\alpha}_d = 40$. Here displayed (a) $G_1/G_2 = 0.2$, (b) $G_1/G_2 = 0.5$, (c) $G_1/G_2 = 1$, (d) $G_1/G_2 = 2$ and (e) $G_1/G_2 = 5$.

G ratio influences the crack initiation and propagation mode, displaying a dominant azimuthal pattern for $G_1/G_2 < 1$ (Figs. 47(a)-47(b)) which is switched to a Mixed-Mode propagating crack with both axial and circumferential modes for greater values of G_1/G_2 (Figs. 47(d)-47(e)).
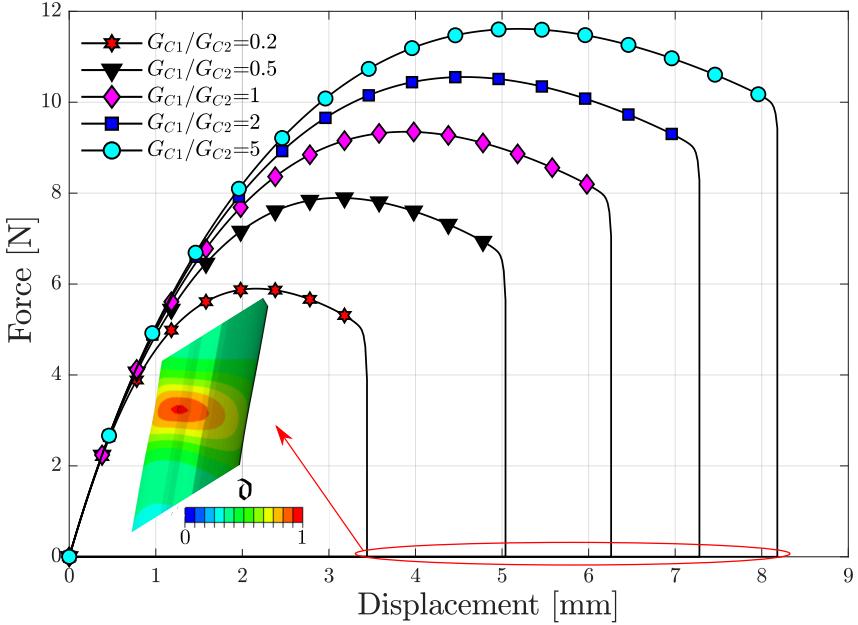
Figure 48: Reaction force-imposed displacement curves for the parametric study changing the critical energy release rate ratio without residual stress.

Critical energy release rate influence

Considering now the role of $\mathcal{G}_C$, a mismatch of this parameter between both layers is studied, in particular, it is considered $\mathcal{G}_{C,1}/\mathcal{G}_{C,2} = [0.2, 0.5, 1, 2, 5]$. In the load-displacement curves depicted in Fig. 48 for cases without residual stresses, it is exhibited an expected behavior: when the $\mathcal{G}_C$ ratio (toughness) is increased the area under the curve grows i.e. the maximum load and displacement augment, being these values quantified in Table 20. Regarding a qualitative standpoint, by taking a look at the crack pattern, it is observed that nucleation is again located at the area (for both inner and outer layers) close to the notch, in agreement with the results for non pre-stressed probes in Fig. 45.

Taking into account residual stresses ($\bar{\alpha}_c = 0.5$ and $\bar{\alpha}_d = 40$), the load-displacement curves are plotted in Fig. 49. These curves follow the

Table 20: Comparison of the maximum force and displacement for the tests with different $\mathcal{G}_C$ ratios in non pre-stressed two-layered cylinders.

$\mathcal{G}_{C,1}/\mathcal{G}_{C,2}$	0.2	0.5	1	2	5
Maximum Force (N)	5.90	7.90	9.35	10.55	11.61
Maximum Displacement (mm)	3.44	5.04	6.26	7.28	8.18
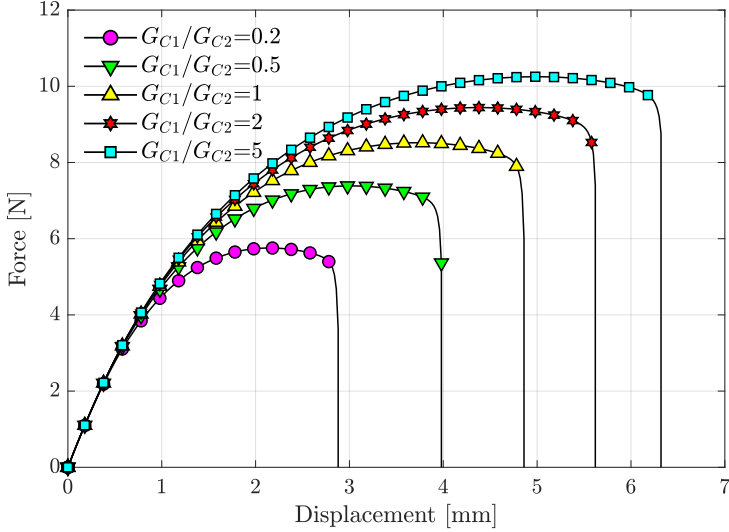
Figure 49: Reaction force-imposed displacement curves for the parametric study changing the critical energy release rate ratio with residual stress parameters $\bar{\alpha}_c = 0.5$-$\bar{\alpha}_d = 40$.

same behavior than the curves of Fig. 48 for non pre-stressed tubes, in the sense that peak force and displacement are directly proportional to the ratio of critical strength (see Table 21).

Nevertheless, the effect of the residual stresses is clearly observed in the crack pattern plotted for each case in Figs. 50(a)-50(e). The crack patterns display a fracture propagating azimuthally from the flawed region, being again consistent with the Von Mises stresses isocontourn displayed in Figs. 44(a)-44(b). The failure mechanism for different $\mathcal{G}_{C,1}/\mathcal{G}_{C,2}$ ratios

Table 21: Comparison of the maximum force and ultimate displacement for residually stressed ($\bar{\alpha}_c = 0.5 - \bar{\alpha}_d = 40$) two-layered cylinders with different $\mathcal{G}_C$ ratios.

$\mathcal{G}_{C1}/\mathcal{G}_{C2}$	0.2	0.5	1	2	5
Maximum Force (N)	5.76	7.39	8.52	9.44	10.25
Maximum Displacement (mm)	2.88	3.98	4.86	5.62	6.32

is observed in the fracture initiation region, which shrinks for increasing values of the critical energy ratio.

3.4 Appendix A: Additional benchmark example

Further verification simulations are carried out on a square single-notched plate, whose dimensions are shown in Fig. 51(a). The discretization of the plate has been performed using 10,000 elements for these series of examples with a common element size of 2.5 mm, see Fig. 51(b). The mechanical properties can be found in Table 22. These computations have been carried out with the exclusive consideration of hyper-viscoelastic effects for verification purposes using a staggered solution scheme. Regarding the boundary conditions of the 2-D model: the bottommost surface is fixed along the Y-direction, with the right corner also being in X-direction; and the topmost surface is submitted to a monotonically increasing vertical displacement.

A parametric study has been done to study the rate-dependency of phase field approach. Therefore, a set of relaxation times $\tau = [0.05, 0.1, 0.2]$ h and displacement rates v $= [5, 10, 20]$ mm/h are applied.

The phase field isocontour evolution at the crack initiation and propagation is shown in Figs. 51(c)-51(d). The crack starts at the notch tip and propagates straight towards the end of the notch. This finding agrees with what is found in similar cases in viscoelastic phase field fracture like [260] and with alternative phase field models without including viscoelastic effects [248, 47].
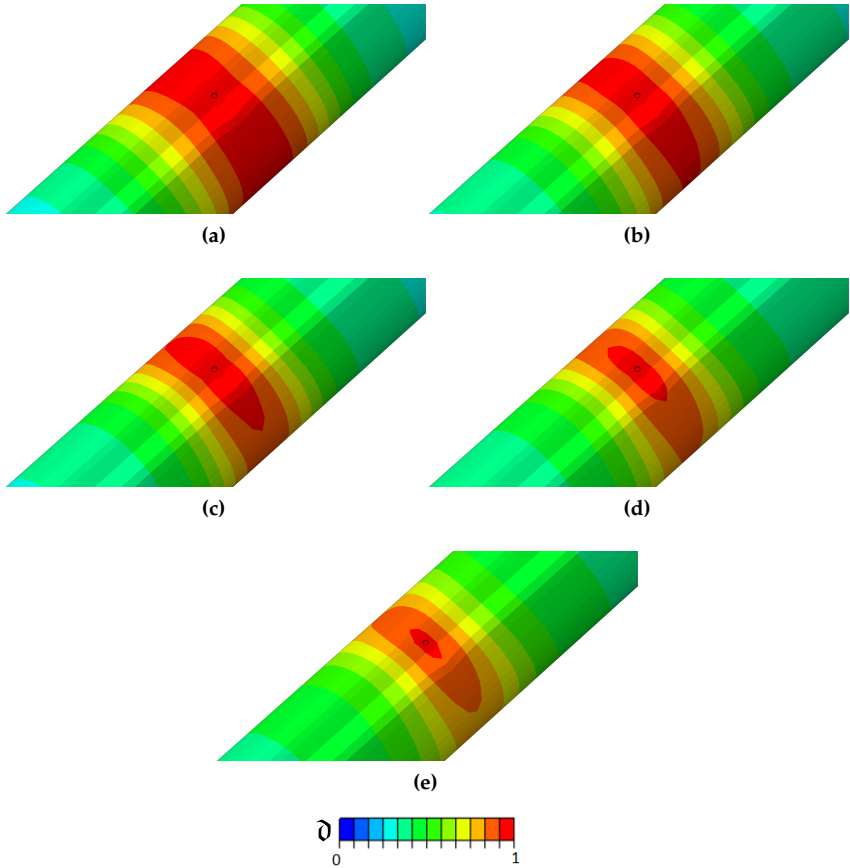
Figure 50: Crack pattern for the different critical energy release rate ratios with residual stress parameters $\bar{\alpha}_c = 0.5$-$\bar{\alpha}_d = 40$. Here displayed (a) $\mathcal{G}_{C1}/\mathcal{G}_{C2} = 0.2$, (b) $\mathcal{G}_{C1}/\mathcal{G}_{C2} = 0.5$, (c) $\mathcal{G}_{C1}/\mathcal{G}_{C2} = 1$, (d) $\mathcal{G}_{C1}/\mathcal{G}_{C2} = 2$ and (e) $\mathcal{G}_{C1}/\mathcal{G}_{C2} = 5$.

The reaction forces comparing the tests at different relaxation times with v = 10 mm/h (Fig. 52) and at different displacement rates with $\tau = 0.1$ h (Fig. 53) show the clear effect of the viscosity on the specimen response. Analyzing these plots, it can be seen that for higher relaxation
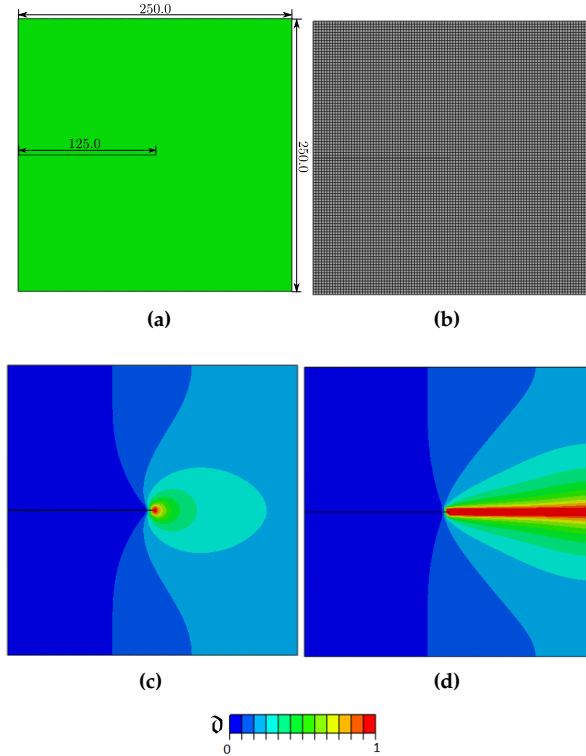
Figure 51: (a) Dimensions in mm, (b) mesh (c) and phase field isocontour for Mode I crack initiation and d) propagation of the single edge notched plate.

time, the peak force increases but the ultimate displacement becomes lower. Related to the velocity, both the final displacement and maximum force increase along with the increasing of the strain rate. The postpeak behavior shown at both of these curves, where the failure of the structure is prolonged, is in good agreement with the experimental results of [274] in a qualitative manner.

Table 22: Mechanical properties of the single edge notched square plate.

Property	Value
G (MPa)	480
κ (MPa)	1440
G^{visco} (MPa)	576
$\mathcal{G}_c$ (MPa $\cdot$ mm)	5
ℓ (mm)	1
f	0.5
χ	10^{-5}
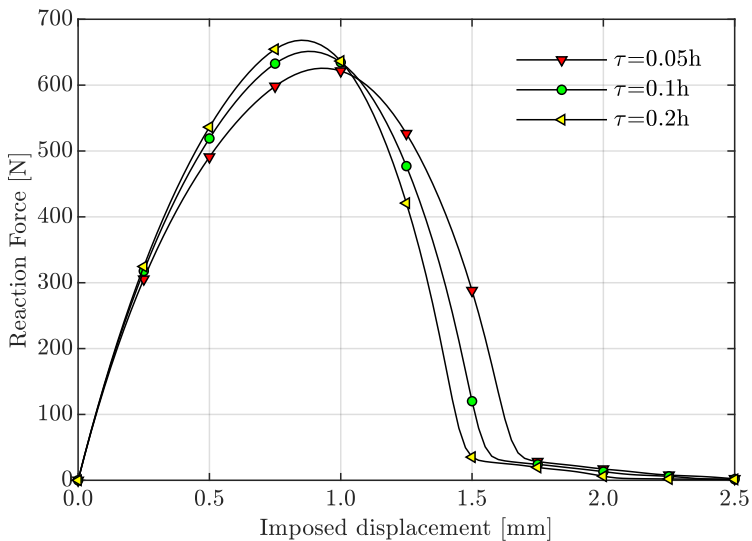
Figure 52: Load-displacement curves for tests of the single-notched square plate with different relaxation times.
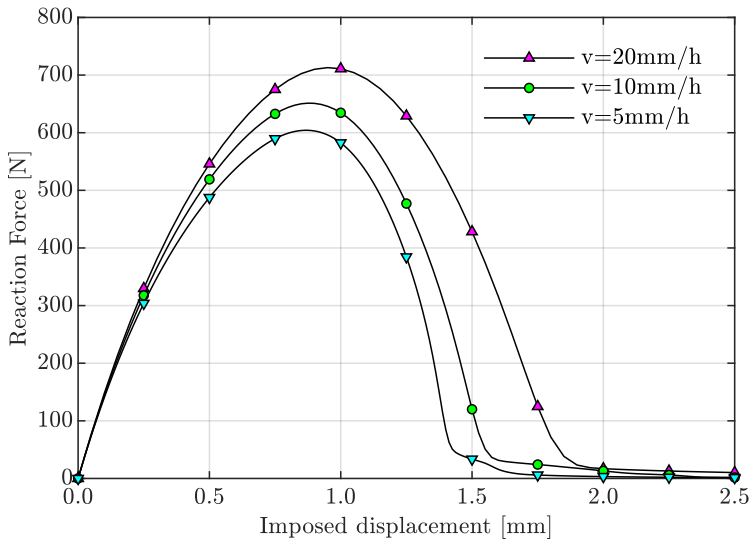
Figure 53: Load-displacement curves for tests of the single-notched square plate with different testing rates.

Chapter 4

Another nonlocal method for failure: gradient-enhanced damage models in compressible and nearly incompressible hyperelastic materials

Chapter 4 is based on our own publication [297].

We have observed in Chapter 3 that soft materials are of major interest for biomechanics applications due to their high deformability and susceptibility to experience damage events under different loading scenarios. In this Chapter, we will present a study concerned with modelling damage evolution processes in these nonlinear materials whose structural responses are prone to locking when low-order kinematic interpolation is employed in the context of nonlinear Finite Element schemes. For this mission, we have employed a similar method for diffuse fracture called gradient-enhanced Continuum Damage (CDM) technique, which,

like the phase-field method, disposes of length scale parameters to regularize the region for failure.

Depending on the Poisson ratio of the structure, a hyperelastic specimen is prone to exhibit volumetric or shear locking. The first pathology is displayed when, for testing a nearly incompressible material ($\nu \sim 0.5$), it is employed a displacement-based (single field) FE scheme, causing the specimen to be stiffer than what actually is. In order to cover this pathology, we have employed the `Q1P0` or Simo-Taylor-Pister elements. This formulation, pioneered by the aforementioned authors [129] and enhanced by Simo and Taylor [298], and Miehe [299], is based on a local multiplicative split of the deformation gradient into deviatoric and volumetric parts, considering both the pressure and the Jacobian, which appear in the volumetric contribution, as primary unknowns, besides the displacement field. A disadvantage of the `Q1P0` formulation is that it might provide unphysical solutions for compressible problems [300]. Being recently applied to model ductile damage [301] and fracture by means of a PF approach [302, 303, 304], we have implemented a `Q1Q1P0` formulation. It should be mentioned that the proposed formulation for `Q1Q1P0` element differs from the one utilized by `ABAQUS` hybrid elements, as the latter only employs a two-field displacement-pressure formulation, being it employed to model CDM by Ostwald et al. [290].

The other pathology, called shear locking, is shown when bending loads are applied to the sample, causing another overstiffening in the mechanical behavior of the material. To overcome this problem, we have adopted the Enhanced Assumed Strain (EAS) technique in the Finite Element formulation. Also named `Q1E[●]`, being ● the number of incompatible modes considered, is a method developed by Simo and Armero [146] for nonlinear continuum elements which, relying on the Hu-Washizu variational principle, enrich the deformation modes stemming from the single field displacement solution by means of several incompatible deformation modes at the element level. This method relies crucially on an additive decomposition of the deformation gradient into a conforming and an enhanced part which accounts for these incompatible modes. The resulting formulation corrects the over-stiffening of the structure by

avoiding the phenomenon of shear locking. This technique has been widely applied to solid shells in order to suppress shear locking associated with bending modes [305, 306, 307, 308, 309, 310]. This technique's major drawback lies in the instability associated with rank deficiency in the stiffness matrix which appears under compressive states [311], which remains an open question in the Computational Mechanics field. EAS has also been applied to non-local damage approaches such as PF frameworks [269, 35, 69] and very recently to CDM with reduced integration schemes [312].

In light of this discussion and after addressing potential locking events in CDM using non-local formulations, we present in this Chapter two non-local gradient-enhanced CDM approaches to solve locking issues. They are tailored within the geometrically nonlinear setting based on the work of Dimitrijević and Hackl [109], but by introducing an internal damage variable based on the model of Liebe et al. [313], in the line of the work by Waffenschmidt et al. [111]. Within the cited approach, the concept of enhancing the energy function via a gradient term of the independent damage variable is combined with a penalty parameter that simulates the equivalence between the local and non-local damage parameter, being this approach in line with the micromorphic gradient-type dissipative framework proposed by Forest [314]. This coupled two-equation (linear momentum and non-local damage balance) framework for large deformations is formulated in a weak form. The hyperelastic constitutive response is affected by the non-local damage scalar, which is approximated via an exponential law that triggers the deterioration of the structure when it overpasses a threshold.

To summarize, two displacement-continuum damage approaches are built over this primary framework to capture damage in hyperelastic materials prone to shear and volumetric locking. For the former application, the EAS technique is included to encompass 24 incompatible deformation modes, implementing a formulation Q1Q1E24 that is suitable to model compressible samples subjected to bending. Then, separately, the mixed three-field Q1Q1P0 approach is formulated to tackle volumetric locking in nearly incompressible samples. The resulting cou-

pled, highly nonlinear system of equations is solved via two Newton-Raphson type solution schemes: one local and one global employing a user-element subroutine `UEL` in the FE commercial software `ABAQUS`. In summary, we are presenting in this Chapter the first full-integration enhanced assumed strain (`Q1Q1E24`) and a novel mixed displacement-pressure-Jacobian (`Q1Q1P0`) schemes for gradient-enhanced CDM modelling and we have tested their performance by comparing them with the already-formulated standard CDM damage approach, i.e., `Q1Q1`.

This Chapter is structured as follows. The basic theory, which includes the constitutive behavior, the non-local gradient-enhanced damage formulation, and the thermodynamical postulates for the standard `Q1Q1` element, is developed in Section 4.1. Section 4.2 displays the variational theorems for this `Q1Q1` formulation and the two proposed ones, i.e., `Q1Q1E24` and `Q1Q1P0`, providing a further insight on the numerical implementation in Section 4.3. To validate and test the potential of the proposed frameworks, a wide variety of numerical examples which consists of compressible and nearly incompressible large deformation problems prone to exhibit volumetric and shear locking have been addressed in Section 4.4.

Nomenclature

$\mathbf{x}$	Arbitrary spatial point on the current configuration
$\boldsymbol{\varphi}$	Nonlinear deformation map
$\mathbf{X}$	Arbitrary spatial point on the initial configuration
t	Current time
Ω_0	Body domain in the initial configuration
$\mathbb{R}^n$	Collection of ordered lists of n real numbers
Ω	Body domain in the current configuration
$\mathbf{F}$	Deformation gradient
$\nabla_{\mathbf{X}}$	Gradient operator in the reference configuration
$\nabla_{\mathbf{x}}$	Gradient operator in the current configuration
$\mathbf{1}$	Second order identity tensor
$\mathbf{H}$	Material displacement gradient tensor
J	Jacobian, determinant of $\mathbf{F}$
det	Determinant
$\mathbf{u}$	Displacement field
$\mathbf{C}$	Right Cauchy-Green tensor
$\mathbf{b}$	Left Cauchy-Green tensor
$\partial\Omega$	Boundary of the solid
$\partial\Omega_u$	Boundary region with a Dirichlet condition of prescribed displacements

Nomenclature

$\partial\Omega_t$	Boundary region with a Neumann condition of prescribed tractions
$\bar{\mathbf{t}}$	Cauchy traction vector
$\mathbf{n}$	Current normal outward vector
$\boldsymbol{\sigma}$	Cauchy's stress tensor
$\mathbf{P}$	First Piola-Kirchhoff stress tensor
$\mathbf{T}$	First Piola-Kirchhoff traction vector
$\mathbf{N}$	Initial normal outward vector
$\mathrm{d}A$	Differential of nominal area
$\mathrm{d}a$	Different of engineering area
$\mathbf{S}$	Second Piola-Kirchhoff stress tensor
Ψ^{loc}	Local free energy function
G	Second Lamé parameter
λ	First Lamé parameter
K	Bulk modulus
I_n	N-th invariant
$\mathbb{C}$	Material description for the Jacobian of the constitutive law
$\mathbb{c}$	Spatial description for the Jacobian of the constitutive law
f_d	Damage function
κ	Local damage variable
κ_d	Local damage threshold
Ψ^{nloc}	Nonlocal free energy function
$\Psi^{\mathrm{nloc}}_{\mathrm{grd}}$	Nonlocal free energy contribution containing the gradient of ϕ
ϕ	Nonlocal damage parameter
$\Psi^{\mathrm{nloc}}_{\mathrm{plty}}$	Nonlocal free energy contribution containing the penalty term
c_d	Damage regularisation parameter
β_d	Correlation parameter between local and nonlocal damage
γ_d	Switch parameter between local and nonlocal gradient-enhanced model
Ψ	Free energy function
$\mathbf{Y}$	Damage-like vector field in the material configuration
Y	Scalar damage-like variable in the material configuration
$\mathbf{y}$	Damage-like vector field in the spatial configuration
y	Scalar damage-like variable in the spatial configuration
$\mathcal{D}_{int}$	Local internal dissipation energy
$\partial_{[\bullet]}$	Partial derivative operator
$\mathcal{D}_{\mathrm{red}}$	Reduced local dissipation energy
g	Thermodynamic force for local damage variable
d	Scalar damage variable
q	Thermodynamic force for scalar damage variable
Φ_d	Damage flag
λ_d	Local damage Lagrange multiplier
η_d	Exponential saturation parameter
Π	Total potential of the system
Π_{int}	Internal potential of the system
Π_{ext}	External potential of the system
$\mathbf{F}^V$	Body force in the initial configuration
$\bar{\mathbf{T}}$	Traction vector in the initial configuration
$\mathfrak{V}^u$	Space of admissible displacement variation

Nomenclature

$\mathfrak{V}^{\phi}$	Space of admissible nonlocal damage variation
$\mathbf{f}^V$	Body force in the current configuration
$\mathbf{E}$	Green-Lagrange strain tensor
$\mathbf{E^u}$	Displacement-derived contribution to Green-Lagrange strain tensor
$\tilde{\mathbf{E}}$	Enhancing counterpart contribution to Green-Lagrange strain tensor
$\mathfrak{V}^{\tilde{E}}$	Space of admissible enhanced strains
$\tilde{p}$	Lagrange multiplier for the pressure variable
$\tilde{J}$	Lagrange multiplier for the Jacobian variable
$[\bullet]_{\text{iso}}$	Isochoric contribution
$[\bullet]_{\text{vol}}$	Volumetric contribution
Δt	Time increment
$[\bullet]_{n+1}$	Current increment
$[\bullet]_n$	Previous increment
$[\bullet]^{\text{und}}$	Intact variables
$\mathbf{r}$	Residual in the local Newton-Raphson scheme
$\mathrm{d}_\gamma \mathbf{r}$	Jacobian of the residual in the local N-R scheme
$\boldsymbol{\xi}$	Parametric space
ξ, η, ζ	Parametric coordinates
$\mathbf{N}$	Shape functions
m	Number of nodes
$\mathbf{d}$	Nodal displacements
$\hat{\phi}$	Nodal nonlocal damage
$\mathbf{J_e}$	Material Jacobian of the isoparametric transformation
$\mathbf{j_e}$	Spatial Jacobian of the isoparametric transformation
$\mathbf{R^d}$	Residual of the displacement field $\mathbf{u}$
$\mathbf{R}^{\hat{\phi}}$	Residual of the nonlocal damage parameter ϕ
$\hat{L}$	Lie's derivative operator
$\mathbf{R^d}$	Residual of the displacement field $\mathbf{u}$
$\mathbf{R}^{\hat{\phi}}$	Residual of the nonlocal damage parameter ϕ
$\mathbf{K^{dd}}$	Displacement-displacement Jacobian term for global N-R scheme
$\mathbf{K^{d\hat{\phi}}}$	Displacement-nonlocal damage Jacobian term for global N-R scheme
$\mathbf{K^{\hat{\phi}d}}$	Nonlocal damage-displacement Jacobian term for global N-R scheme
$\mathbf{K^{\hat{\phi}\hat{\phi}}}$	Nonlocal damage-nonlocal damage Jacobian term for global N-R scheme
$\Delta \mathbf{u}$	Nodal displacement variation
$\Delta \hat{\phi}$	Nodal nonlocal damage variation
$\mathbf{M}$	Matrix operator to interpolate nodal incompatible strains
$\boldsymbol{\varsigma}$	Nodal incompatible strains
$\mathbf{T_0}$	Storage matrix for $\mathbf{J_e}$
$\Delta \boldsymbol{\varsigma}$	Nodal incompatible strains variation
$\mathbf{R}^{\varsigma}$	Residual of the incompatible strains
$\mathbf{K^{d\varsigma}}$	Displacement-incompatible strain Jacobian term for global N-R scheme
$\mathbf{K^{\hat{\phi}\varsigma}}$	Nonlocal damage-incompatible strain Jacobian term for global N-R scheme
$\mathbf{K^{\varsigma d}}$	Incompatible strain-displacement Jacobian term for global N-R scheme
$\mathbf{K^{\varsigma\hat{\phi}}}$	Incompatible strain-nonlocal damage Jacobian term for global N-R scheme
$\mathbf{K^{\varsigma\varsigma}}$	Incompatible strain-incompatible strain Jacobian term for global N-R scheme
$R^{\tilde{p}}$	Residual of the pressure

Nomenclature

$N^{\tilde{p}}$	Shape function for interpolation of the pressure
$R^{\tilde{J}}$	Residual of the dilatation
$N^{\tilde{J}}$	Shape function for interpolation of the dilatation
$\mathbf{K}^{\mathbf{d}\tilde{p}}$	Displacement-pressure Jacobian term for global N-R scheme
$\mathbf{K}^{\tilde{p}\mathbf{d}}$	Pressure-displacement Jacobian term for global N-R scheme
$K^{\tilde{p}\tilde{J}}$	Pressure-dilatation Jacobian term for global N-R scheme
$K^{\tilde{J}\tilde{p}}$	Dilatation-pressure Jacobian term for global N-R scheme
$K^{\tilde{J}\tilde{J}}$	Dilatation-dilatation Jacobian term for global N-R scheme
$\Delta\tilde{p}$	Nodal pressure variation
$\Delta\tilde{J}$	Nodal pressure dilatation
u_z	Vertical displacement

4.1 Theoretical formulation

This section outlines the fundamental concepts and definitions of the current numerical framework addressing the use of gradient-enhanced for a standard CDM scheme, being specialized later for EAS and mixed u-p-J formulations. The proposed numerical methodology is specialized for hyperelastic material models.

4.1.1 Basic definitions and constitutive formulation at local level

In order to avoid repetition, to track the mapping and the deformation of the non-linear problem, we refer the reader to Section 3.1.1 (Eqs. (3.1)-(3.6) and Fig. 26).

We postulate the existence of the local free energy function Ψ^{loc}. Without loss of generality, we consider a nonlinear compressible neo-Hookean constitutive law. This expression is plotted in Eq. (4.1)

$$\Psi^{\mathrm{loc}}(\mathbf{C}) = \frac{G}{2}(I_1 - 3) - G\ln(J) + \frac{\lambda}{2}\ln^2(J) \qquad (4.1)$$

where G and λ are the shear constant and $\lambda = K - \frac{2}{3}G$, respectively, with K as the volumetric constant; and I_1 is the first invariant of the right Cauchy-Green tensor that is defined as $I_1 := \mathrm{tr}[\mathbf{C}]$. The particular form given in Eq. (4.1) also holds for the spatial configuration taking the

left Cauchy-Green strain tensor as the main argument, i.e, $\Psi^{\text{loc}}(\mathbf{b})$ and therefore, $I_1 = \text{tr}[\mathbf{b}]$.

From Eq. (4.1), the second Piola-Kirchhoff tensor $\mathbf{S}$ can be computed as follows

$$\mathbf{S} := 2\frac{\partial \Psi^{\text{loc}}(\mathbf{C})}{\partial \mathbf{C}} = G(1 - \mathbf{C}^{-1}) + \lambda \ln J \mathbf{C}^{-1} \tag{4.2}$$

For the spatial configuration, a push-forward operation is performed to obtain the Cauchy stress tensor $\boldsymbol{\sigma}$

$$\boldsymbol{\sigma} = J^{-1}\mathbf{F} \cdot \mathbf{S} \cdot \mathbf{F}^{\text{T}} = \frac{G}{J}(\mathbf{b} - 1) + \frac{\lambda \ln J}{J}\mathbf{1} \tag{4.3}$$

In order to compute an `ABAQUS UEL` subroutine, the local tangent operators, which are required in order to compute the Jacobians, can be computed directly from the derivation from the material description:

$$\mathbb{C} := 2\frac{\partial \mathbf{S}}{\partial \mathbf{C}} = \lambda \mathbf{C}^{-1} \otimes \mathbf{C}^{-1} + 2(G - \lambda \ln J)\mathbf{I}_C^{\text{sym}} \tag{4.4}$$

where $\mathbf{I}_C^{\text{sym}}$ is a fourth-order tensor that has the following expression: $\mathbf{I}_C^{\text{sym}} := -\partial \mathbf{C}^{-1}/\partial \mathbf{C} = [\mathbf{C}^{-1}\overline{\otimes}\mathbf{C}^{-1} + \mathbf{C}^{-1}\underline{\otimes}\mathbf{C}^{-1}]/2 = [C_{ik}^{-1}C_{jl}^{-1} + C_{il}^{-1}C_{jk}^{-1}]/2$, which employs the non-standard dyadic products. To obtain the spatial counterpart $\mathbb{c}$, we perform the push-forward operation on Eq. (4.4)

$$\mathbb{c} = \frac{\lambda}{J}(\mathbf{1} \otimes \mathbf{1}) + \frac{2}{J}(G - \lambda \ln J)\mathbf{I}^{\text{sym}} \tag{4.5}$$

where $\mathbf{I}^{\text{sym}} = [\mathbf{1}\overline{\otimes}\mathbf{1} + \mathbf{1}\underline{\otimes}\mathbf{1}]/2$ denotes the fourth-order symmetric identity tensor.

Based on Liebe et al. [313], we define a scalar damage function $f_d(\kappa)$, which recalling [111], $f_d(\kappa)$ should be at least twice differentiable, and tracks the material degradation relying on the evolution of a local variable $\kappa \in [0, \infty]$, and whose evolution is ruled by the achievement of a threshold value $\kappa > \kappa_d$ in order to cause a loss in the stiffness of the structure. Therefore, we can state:

$$f_d(\kappa) \; : \; \mathbb{R}^+ \to (0, 1] \mid \left\{ f_d(0) = 1, \lim_{\kappa \to \infty} f_d(\kappa) = 0 \right\} \tag{4.6}$$

These conditions guarantee two clearly differentiated states: $f_d = 1$ identifies an intact stiffness at the spatial point level, whereas $f_d = 0$ denotes a fully deteriorated stiffness state. This belongs to the formulation of the local damage model, whose linking procedure with the non-local damage framework will be envisaged in the subsequent sections.

4.1.2 Gradient-enhanced non-local formulation

In line with the approach proposed by Dimitrijević and Hackl [109], a regularized damage material response is achieved by the definition of a gradient-enhanced non-local function term $\Psi^{\text{nloc}}(\phi, \nabla_{\mathbf{X}}\phi, \kappa)$ in the reference configuration:

$$\Psi^{\text{nloc}}(\phi, \nabla_{\mathbf{X}}\phi, \kappa) = \Psi^{\text{nloc}}_{\text{grd}}(\nabla_{\mathbf{X}}\phi) + \Psi^{\text{nloc}}_{\text{plty}}(\phi, \kappa) \tag{4.7}$$

This non-local contribution can be split into two separate terms: $\Psi^{\text{nloc}}_{\text{grd}}(\nabla_{\mathbf{X}}\phi)$ containing the material gradient of the non-local damage field variable ϕ, which stands for the first term of a Taylor series expansion of ϕ at the material point; and $\Psi^{\text{nloc}}_{\text{plty}}(\phi, \kappa)$ is a penalty term which correlates the local damage variable κ with the non-local damage variable ϕ. The energy terms are specified as follows:

$$\Psi^{\text{nloc}}_{\text{grd}}(\nabla_{\mathbf{X}}\phi) = \frac{c_d}{2}\nabla_{\mathbf{X}}\phi \cdot \nabla_{\mathbf{X}}\phi \tag{4.8}$$

$$\Psi^{\text{nloc}}_{\text{plty}}(\phi, \kappa) = \frac{\beta_d}{2}(\phi - \gamma_d\kappa)^2 \tag{4.9}$$

where c_d consists in a parameter that characterises the non-local character of the formulation; β_d, a penalty parameter that enforces the local damage κ and non-local damage ϕ variables to be equivalent; and γ_d, a switch parameter that is introduced to range between a local and non-local gradient-enhanced model, respectively and the corresponding value is ranged like $\gamma_d \in \{0, 1\}$.

Consequently, the expression for the internal free energy function considering the previous non-local terms is given by

$$\Psi(\mathbf{C}, \phi, \nabla_{\mathbf{X}}\phi, \kappa) = \Psi^{\text{loc}}(\mathbf{C}, \kappa) + \Psi^{\text{nloc}}(\phi, \nabla_{\mathbf{X}}\phi, \kappa)$$
$$= f_d(\kappa)\Psi^{\text{loc}}(\mathbf{C}) + \Psi^{\text{nloc}}_{\text{grd}}(\nabla_{\mathbf{X}}\phi) + \Psi^{\text{nloc}}_{\text{plty}}(\phi, \kappa) \tag{4.10}$$

With these expressions at hand, we define the material expressions for the damage-like vector field $\mathbf{Y}$ and the scalar damage-like variable Y:

$$\mathbf{Y} = \frac{\partial\Psi^{nloc}}{\partial\nabla_{\mathbf{X}}\phi} = c_d\nabla_{\mathbf{X}}\phi \tag{4.11}$$

$$Y = -\frac{\partial\Psi^{nloc}}{\partial\phi} = -\beta_d(\phi - \gamma_d\kappa) \tag{4.12}$$

whose spatial values $\mathbf{y}$ and y are obtained via push-forwarding Eqs. (4.11)-(4.12)

$$\mathbf{y} = c_d J^{-1}\nabla_{\mathbf{x}}\phi \cdot \mathbf{b} \tag{4.13}$$

$$y = -\beta_d(\phi - \gamma_d\kappa)J^{-1} \tag{4.14}$$

4.1.3 Thermodynamic consistency

The thermodynamic consistency of the constitutive framework outlined above is examined through the exploitation of the Clausius-Plank inequality (local internal dissipation ($\mathcal{D}_{int}$) inequality) [109], which under isothermal conditions is given by

$$\mathcal{D}_{int} = [\mathbf{S} - \partial_{\mathbf{C}}\Psi] : \dot{\mathbf{C}} - \partial_{\kappa}\Psi\dot{\kappa} \geq 0 \tag{4.15}$$

Following [111], we focus our attention on the corresponding damage-related terms leading to the definition of a reduced local dissipation $\mathcal{D}_{\text{red}}$:

$$\mathcal{D}_{\text{red}} = g\dot{\kappa} \geq 0 \tag{4.16}$$

where we have introduced the thermodynamic force g as the derivative with respect to the local damage variable κ:

$$g = -\partial_\kappa \Psi \tag{4.17}$$

We now define a thermodynamic force $q \geq 0$, which is conjugated to the classical scalar damage variable d, as follows:

$$q = -\partial_d \Psi = -\partial_\kappa \Psi \partial_d \kappa = g \partial_d \kappa \tag{4.18}$$

Accordingly, the Clausius-Plank inequality holds when the reduced dissipation condition satisfies $\mathcal{D}_{\text{red}} \geq 0$, if $\partial_d \kappa > 0$. In fact, q takes the interpretation of the energy release rate, consisting of the addition of a local and a non-local contribution that reads as

$$q^{\text{loc}} = \Psi^{\text{loc}}; \qquad q^{\text{nloc}} = \beta_d \gamma_d [\phi - \gamma_d \kappa] \partial_d \kappa \tag{4.19}$$

Complying with these equations, we can now define the damage condition:

$$\Phi_d = q - \kappa \leq 0 \tag{4.20}$$

where $\Phi_d < 0$ stands for the purely elastic behavior and $\Phi_d = 0$ notes a damaged state. According to Simo and Hughes [315], an optimization problem regarding a Lagrange multiplier λ_d can be proposed to represent the evolution of the damage variable

$$\dot{\kappa} = \lambda_d \frac{\partial \Phi_d}{\partial q} = \lambda_d \quad \text{for} \quad \kappa|_{t=0} = \kappa_d \tag{4.21}$$

where κ_d concerns the initial damage threshold. This last equation gives rise to the Karush-Kuhn-Tucker (KKT) conditions to model both the initiation and termination of damage.

$$\lambda_d \geq 0; \quad \Phi_d \leq 0; \quad \lambda_d \Phi_d = 0 \tag{4.22}$$

which, can be expressed in a more detailed way as

$$\begin{cases} \Phi_d < 0, & \text{elastic case} \\ \Phi_d = 0 \text{ and } \begin{cases} \lambda_d < 0, & \text{elastic unloading} \\ \lambda_d = 0, & \text{neutral loading} \\ \lambda_d > 0, & \text{damage loading} \end{cases} \end{cases} \tag{4.23}$$

The continuous formulation for damage is completed with the definition of the damage function itself $f_d(\kappa)$, which follows an exponential-type law.

$$f_d(\kappa) = 1 - d = \exp[\eta_d(\kappa_d - \kappa)] \tag{4.24}$$

with $\eta_d > 0$ standing for the exponential saturation parameter. It is worth mentioning that we have introduced a damage threshold parameter κ_d that differs from the proposed approach by Dimitrijević and Hackl [109] and that was introduced in Waffenschmidt et al. [111], in order to avoid over-compensation of the damage curve due to the logarithmic expression in Ψ^{loc} (Eq. (4.1)) that may lead to enhance the stress-strain curve, rather than weakening it.

4.2 Variational formulation

4.2.1 Variational formulation of standard gradient-enhanced damage models: material and spatial formulations

The total potential energy of a system, Π, is obtained from the combination of an internal contribution Π_{int}, which considers the action of internal forces, and an external contribution Π_{ext} due to the addition of volume and surface forces, i.e., $\Pi = \Pi_{\text{int}} - \Pi_{\text{ext}}$.

Restricting the analysis of conservative loading cases, we can express the total potential of the system in the reference position of the arbitrary body under consideration as follows

$$\begin{aligned} \Pi(\mathbf{u}, \phi, \nabla_{\mathbf{X}}\phi, \kappa) = &\int_{\Omega_0} \Psi(\mathbf{C}(\mathbf{u}), \phi, \nabla_{\mathbf{X}}\phi, \kappa) \, d\Omega \\ &- \int_{\Omega_0} \overline{\mathbf{F}}^V \cdot \mathbf{u} \, d\Omega - \int_{\partial\Omega_0} \overline{\mathbf{T}} \cdot \mathbf{u} \, d\partial\Omega \end{aligned} \tag{4.25}$$

Since the problem is governed by the principle of minimum potential energy, the expression for the equation concerning the mechanical problem in the material configuration is obtained as

$$\delta\Pi = \frac{\partial\Pi}{\partial\mathbf{u}}\cdot\delta\mathbf{u} + +\frac{\partial\Pi}{\partial\phi}\delta\phi + \frac{\partial\Pi}{\partial\nabla_{\mathbf{X}}\phi}\cdot\nabla_{\mathbf{X}}\delta\phi - \delta\Pi_{\text{ext}} = 0 \tag{4.26}$$

that, can be particularized for each independent field as:

$$\delta\Pi^u(\mathbf{u},\phi,\nabla_{\mathbf{X}}\phi,\kappa) = \underbrace{\int_{\Omega_0}(\mathbf{S}\cdot\mathbf{F}^{\mathrm{T}}):\nabla_{\mathbf{X}}\delta\mathbf{u}\,\mathrm{d}\Omega}_{\delta\Pi_{\text{int}}^{\mathbf{u}}} - \underbrace{\int_{\Omega_0}\overline{\mathbf{F}}^V\cdot\delta\mathbf{u}\,\mathrm{d}\Omega - \int_{\partial\Omega_0}\overline{\mathbf{T}}\cdot\delta\mathbf{u}\,\mathrm{d}\partial\Omega}_{\delta\Pi_{\text{ext}}^{\mathbf{u}}} = 0$$

$$\tag{4.27}$$

$$\delta\Pi^\phi(\mathbf{u},\phi,\nabla_{\mathbf{X}}\phi,\kappa) = \underbrace{\int_{\Omega_0}\mathbf{Y}\cdot\nabla_{\mathbf{X}}\delta\phi\mathrm{d}\Omega}_{\delta\Pi_{\text{int}}^{\phi}} - \underbrace{\int_{\Omega_0}Y\delta\phi\mathrm{d}\Omega}_{\delta\Pi_{\text{ext}}^{\phi}} = 0 \tag{4.28}$$

Let $\mathfrak{V}^u = \left\{\delta\mathbf{u}\in[H^1(\Omega_0)]:\delta\mathbf{u}=\mathbf{0}\text{ on }\partial\Omega_{0,u}\right\}$ be the space of admissible displacement variations, and $\mathfrak{V}^\phi = \left\{\delta\phi\in[H^1(\Omega_0)]:\nabla_{\mathbf{X}}\delta\phi\cdot\mathbf{N}=0\text{ on }\partial\Omega_0\right\}$, the space of admissible test functions for non-local damage function. Furthermore, in the previous expression, the second Piola-Kirchhoff stress tensor renders $\mathbf{S}:=2f_d(\kappa)\partial_{\mathbf{C}}\Psi^{\text{loc}}$, and $\overline{\mathbf{F}}^V$ and $\overline{\mathbf{T}}$ denote the body force and the traction vectors in the reference volume Ω_0 and surface $\partial\Omega_0$, respectively.

The previous system of equations can be expressed in the spatial configuration by applying a standard push-forward operation:

$$\delta\Pi^u(\mathbf{u},\phi,\nabla_{\mathbf{x}}\phi,\kappa) = \underbrace{\int_{\Omega}\boldsymbol{\sigma}:\nabla_{\mathbf{x}}\delta\mathbf{u}\,\mathrm{d}\Omega}_{\delta\Pi_{\text{int}}^{\mathbf{u}}} - \underbrace{\int_{\Omega}\bar{\mathbf{f}}^V\cdot\delta\mathbf{u}\,\mathrm{d}\Omega - \int_{\partial\Omega}\bar{\mathbf{t}}\cdot\delta\mathbf{u}\,\mathrm{d}\partial\Omega}_{\delta\Pi_{\text{ext}}^{\mathbf{u}}} = 0$$

$$\tag{4.29}$$

$$\delta\Pi^\phi(\mathbf{u},\phi,\nabla_{\mathbf{x}}\phi,\kappa) = \underbrace{\int_{\Omega}\mathbf{y}\cdot\nabla_{\mathbf{x}}\delta\phi\,\mathrm{d}\Omega}_{\delta\Pi_{\text{int}}^{\phi}} - \underbrace{\int_{\Omega}y\delta\phi\,\mathrm{d}\Omega}_{\delta\Pi_{\text{ext}}^{\phi}} = 0 \tag{4.30}$$

expressed in the current volume Ω and surface $\partial\Omega$ and with $\boldsymbol{\sigma}$ identifying the Cauchy stress tensor that is accordingly affected by the degradation function $f_d(\kappa)$.

Upon the use of the product rule and the divergence theory on Eqs. (4.27)-(4.28), the governing equations for the balance of linear momentum (Eqs. (4.31)-(4.32)) and evolution of the non-local damage field ϕ (Eqs. (4.33)-(4.34)) are expressed in the reference configuration Ω_0

$$\nabla_{\mathbf{X}} \cdot (\mathbf{F} \cdot \mathbf{S}) + \overline{\mathbf{F}}^V = \mathbf{0} \qquad \text{in } \Omega_0 \tag{4.31}$$

$$(\mathbf{F} \cdot \mathbf{S}) \cdot \mathbf{N} = \overline{\mathbf{T}} \qquad \text{on } \partial\Omega_0 \tag{4.32}$$

$$\nabla_{\mathbf{X}} \cdot \mathbf{Y} + Y = 0 \qquad \text{in } \Omega_0 \tag{4.33}$$

$$\mathbf{Y} \cdot \mathbf{N} = 0 \qquad \text{on } \partial\Omega_0 \tag{4.34}$$

Replicating the previous procedure for Eqs. (4.29)-(4.30) in the case of the current configuration, the Euler-Lagrange equations in the spatial form are given by

$$\nabla_{\mathbf{x}} \cdot \boldsymbol{\sigma} + \overline{\mathbf{f}}^V = \mathbf{0} \qquad \text{in } \Omega \tag{4.35}$$

$$\boldsymbol{\sigma} \cdot \mathbf{n} = \overline{\mathbf{t}} \qquad \text{on } \partial\Omega \tag{4.36}$$

$$\nabla_{\mathbf{x}} \cdot \mathbf{y} + y = 0 \qquad \text{in } \Omega \tag{4.37}$$

$$\mathbf{y} \cdot \mathbf{n} = 0 \qquad \text{on } \partial\Omega \tag{4.38}$$

being $\mathbf{N}$ and $\mathbf{n}$ both the normal vectors in the material and spatial configuration, respectively.

4.2.2 Variational formulation of gradient-enhanced damage models for enhanced assumed strain formulations

This section tailors the already established standard CDM model by combining it with the EAS method. Regarding this novel application, it is performed to alleviate shear locking pathologies in damage using low-order displacement interpolation in the subsequent finite element discretization scheme.

We focus our development on the additive decomposition of the Green-Lagrange strain tensor into a displacement derived ($\mathbf{E}^u$) and an enhancing counterpart $\tilde{\mathbf{E}}$ as follows [316]: $\mathbf{E} = \mathbf{E}^u + \tilde{\mathbf{E}}$. This differs from the alternative EAS scheme proposed by Simo and Armero [146] that accounts

for the additive decomposition of the deformation gradient $\mathbf{F} = \mathbf{F}^u + \tilde{\mathbf{F}}$. Moreover, note that in the following derivation, the free-energy function is expressed in terms of the Green-Lagrange strain tensor. However, there exists a direct relation concerning the right Cauchy-Green tensor.

The point of departure of the formulation is based on the construction of the multi-field Hu-Washizu functional, where the displacement, the enhancing strain, the stress, and the non-local damage variable are the independent fields. This functional is given by

$$\Pi(\mathbf{S}, \tilde{\mathbf{E}}, \mathbf{u}, \phi, \nabla_{\mathbf{X}}\phi, \kappa) = \int_{\Omega_0} \left[f_d(\kappa)\Psi^{\text{loc}}(\mathbf{E}(\mathbf{u})) + \frac{c_d}{2}\nabla_{\mathbf{X}}\phi \cdot \nabla_{\mathbf{X}}\phi - \frac{\beta_d}{2}[\phi - \gamma_d\kappa]^2 \right] \mathrm{d}\Omega$$
$$- \int_{\Omega_0} \mathbf{S} : \tilde{\mathbf{E}}\,\mathrm{d}\Omega - \Pi_{\text{ext}}(\mathbf{u})$$

(4.39)

where $\Pi_{\text{ext}}(\mathbf{u})$ identifies the external contribution due to the prescribed domain and boundary actions.

Let $\mathfrak{V}^u = \left\{ \delta\mathbf{u} \in [H^1(\Omega_0)] : \delta\mathbf{u} = \mathbf{0} \text{ on } \partial\Omega_{0,u} \right\}$ be the space of admissible displacement variations; $\mathfrak{V}^{\tilde{E}} = [L_2(\Omega_0)]$, the space of the admissible enhancing strain; and $\mathfrak{V}^\phi = \left\{ \delta\phi \in [H^1(\Omega_0)] : \nabla_{\mathbf{X}}\delta\phi \cdot \mathbf{N} = 0 \text{ on } \partial\Omega_0 \right\}$, the space of admissible test functions for non-local damage function. The first variation of the total potential energy with respect to independent fields gives the following general expression:

$$\delta\Pi = \frac{\partial\Pi}{\partial\mathbf{u}} \cdot \delta\mathbf{u} + \frac{\partial\Pi}{\partial\tilde{\mathbf{E}}} : \delta\tilde{\mathbf{E}} + \frac{\partial\Pi}{\partial\mathbf{S}} : \delta\mathbf{S} + \frac{\partial\Pi}{\partial\phi}\delta\phi + \frac{\partial\Pi}{\partial\nabla_{\mathbf{X}}\phi} \cdot \nabla_{\mathbf{X}}\delta\phi - \delta\Pi_{\text{ext}} = 0$$

(4.40)

The previous expression can be particularized as follows from Eq. (4.39):

$$\delta\Pi(\mathbf{S}, \tilde{\mathbf{E}}, \mathbf{u}, \phi, \nabla_{\mathbf{X}}\phi, \kappa) = \int_{\Omega_0} f_d(\kappa)\frac{\partial\Psi^{\text{loc}}(\mathbf{E}(\mathbf{u}))}{\partial\mathbf{E}} : \delta\mathbf{E}^u\,\mathrm{d}\Omega$$
$$+ \int_{\Omega_0} \left(f_d(\kappa)\frac{\partial\Psi^{\text{loc}}(\mathbf{E}(\mathbf{u}))}{\partial\mathbf{E}} - \mathbf{S} \right) : \delta\tilde{\mathbf{E}}\,\mathrm{d}\Omega - \int_{\Omega_0} \delta\mathbf{S} : \tilde{\mathbf{E}}\,\mathrm{d}\Omega$$
$$+ \int_{\Omega_0} c_d\nabla_{\mathbf{X}}\phi \cdot \nabla_{\mathbf{X}}\delta\phi\,\mathrm{d}\Omega - \int_{\Omega_0} \beta_d[\phi - \gamma_d\kappa]\delta\phi\,\mathrm{d}\Omega$$
$$- \delta\Pi_{\text{ext}}(\mathbf{u}) = 0, \quad \forall\delta\mathbf{u}, \forall\delta\tilde{\mathbf{E}}, \forall\delta\mathbf{S}, \forall\delta\phi$$

(4.41)

Exploiting the orthogonality condition between the stress field $\mathbf{S}$ and the enhancing strain field $\tilde{\mathbf{E}}$ [146], the weak form of the coupled IBVP (Initial Boundary Value Problem) can be reduced to three independent fields, namely the displacement, the enhancing strain, and the non-local damage fields.

The weak form given in Eq. (4.41) (recalling $\mathbf{S} := 2f_d(\kappa)\partial_{\mathbf{C}}\Psi^{\text{loc}} = f_d(\kappa)\partial_{\mathbf{E}}\Psi^{\text{loc}}$) is given by

$$\delta\Pi^u = \delta\Pi^u_{\text{int}} - \delta\Pi^u_{\text{ext}} = \int_{\Omega_0} \mathbf{S} : \delta\mathbf{E}^u \, \mathrm{d}\Omega - \delta\Pi_{\text{ext}}(\mathbf{u}) = 0 \qquad (4.42)$$

$$\delta\Pi^{\tilde{E}} = \delta\Pi^{\tilde{E}}_{\text{int}} - \delta\Pi^{\tilde{E}}_{\text{ext}} = -\int_{\Omega_0} \mathbf{S} : \delta\tilde{\mathbf{E}} \, \mathrm{d}\Omega = 0 \qquad (4.43)$$

$$\delta\Pi^{\phi} = \delta\Pi^{\phi}_{\text{int}} - \delta\Pi^{\phi}_{\text{ext}} = \int_{\Omega_0} c_d \nabla_{\mathbf{X}}\phi \cdot \nabla_{\mathbf{X}}\delta\phi \, \mathrm{d}\Omega - \int_{\Omega_0} \beta_d[\phi - \gamma_d\kappa]\delta\phi \, \mathrm{d}\Omega = 0. \qquad (4.44)$$

In Eqs. (4.42)-(4.44), $\delta\Pi^*_{\text{int}}$ and $\delta\Pi^*_{\text{ext}}$ stand for the internal and external contributions of the generic field $(*)$. In what follows, we turn our interest to the internal contribution of each independent field.

4.2.3 Variational formulation of gradient-enhanced damage models for penalty-based mixed formulations for nearly incompressible materials

The second presented methodology concerned in this investigation is the mixed Jacobian-pressure formulation originally proposed by Simo et al. [129]. In line with this work, we first perform a modification in the local strain energy density Ψ^{loc} to a nearly incompressible neo-Hookean approach:

$$\Psi^{\text{loc}}(\bar{\mathbf{b}}) = \underbrace{\frac{G}{2}(\bar{I}_1 - 3)}_{\Psi^{\text{loc}}_{\text{iso}}} + \underbrace{\frac{K}{4}(J^2 - 1 - 2\ln J)}_{\Psi^{\text{loc}}_{\text{vol}}} \qquad (4.45)$$

where $\bar{I}_1$ is the first invariant of the isochoric left Cauchy-Green tensor $\bar{\mathbf{b}}$ and reads as $\bar{I}_1 = J^{-2/3}I_1 = J^{-2/3}\text{tr}[\mathbf{b}]$.

For the current three-field variational problem, we consider three fields as primary unknowns of the system $\{\mathbf{u}, \tilde{p}, \tilde{J}\}$, where:

- $\tilde{p}$ is the Lagrange multiplier that accounts for the pressure response $p = \frac{\partial \Psi_{\text{vol}}^{\text{loc}}}{\partial \tilde{J}}$.

- $\tilde{J}$ is the dilatation, a constraint variable for the Jacobian of the material $J(\mathbf{u})$.

For convenience, we express the total potential of the system in the current configuration:

$$\Pi(\mathbf{u}, \tilde{p}, \tilde{J}, \phi, \nabla_{\mathbf{x}}\phi, \kappa) = \int_{\Omega} \left[f_d(\kappa) \left[\Psi_{\text{iso}}(\overline{\mathbf{b}}(\mathbf{u})) \right] + \Psi_{\text{vol}}(\tilde{J}) + \frac{\tilde{p}}{J} \left[J(\mathbf{u}) - \tilde{J} \right] \right.$$
$$\left. + \frac{c_d}{2J} \nabla_{\mathbf{x}}\phi \cdot \nabla_{\mathbf{x}}\phi \cdot \mathbf{b} - \frac{\beta_d}{2J} [\phi - \gamma_d \kappa]^2 \right] \mathrm{d}\Omega - \Pi_{\text{ext}}$$
$$(4.46)$$

Again we denote: (i) $\mathfrak{V}^u = \left\{ \delta\mathbf{u} \in [H^1(\Omega)] : \delta\mathbf{u} = \mathbf{0} \text{ on } \partial\Omega_{0,u} \right\}$ is the space of admissible displacement variations, (ii) $\delta\tilde{p} \in L^2(\Omega)$ stands for the space of virtual pressure, (iii) $\delta\tilde{J} \in L^2(\Omega)$ regards the space of virtual dilatation and (iv) $\mathfrak{V}^\phi = \left\{ \delta\phi \in [H^1(\Omega)] : \nabla_{\mathbf{x}}\delta\phi \cdot \mathbf{n} = 0 \text{ on } \partial\Omega \right\}$ the space of admissible test functions for non-local damage function.

The first variation of the functional with respect to independent fields renders

$$\delta\Pi = \frac{\partial\Pi}{\partial\mathbf{u}} \cdot \delta\mathbf{u} + \frac{\partial\Pi}{\partial\tilde{J}} \delta\tilde{J} + \frac{\partial\Pi}{\partial\tilde{p}} \delta\tilde{p} + \frac{\partial\Pi}{\partial\phi} \delta\phi + \frac{\partial\Pi}{\partial\nabla_{\mathbf{x}}\phi} \cdot \nabla_{\mathbf{x}}\delta\phi - \delta\Pi_{\text{ext}} = 0 \quad (4.47)$$

The previous expression can be expanded as follows.

$$\delta\Pi(\mathbf{u}, \tilde{p}, \tilde{J}, \phi, \nabla_{\mathbf{x}}\phi, \kappa) = \int_{\Omega} \left[(f_d(\kappa)\boldsymbol{\sigma}_{\text{iso}} + \underbrace{\tilde{p}\mathbf{1}}_{\boldsymbol{\sigma}_{\text{vol}}}) \cdot \nabla_{\mathbf{x}}\delta\mathbf{u} + \frac{(J(\mathbf{u}) - \tilde{J})}{J} \delta\tilde{p} \right] \mathrm{d}\Omega$$
$$+ \int_{\Omega} \left[\frac{\left(\frac{\partial\Psi_{\text{vol}}^{\text{loc}}}{\partial\tilde{J}} - \tilde{p} \right)}{J} \delta\tilde{J} \right] \mathrm{d}\Omega + \int_{\Omega} \frac{c_d}{J} \nabla_{\mathbf{x}}\phi \cdot \mathbf{b} \cdot \nabla_{\mathbf{x}}\delta\phi \, \mathrm{d}\Omega$$
$$- \int_{\Omega} \frac{\beta_d}{J} [\phi - \gamma_d\kappa]\delta\phi \, \mathrm{d}\Omega - \delta\Pi_{\text{ext}} = 0 \quad \forall\delta\mathbf{u}, \forall\delta\tilde{J}, \forall\delta\tilde{p}, \forall\delta\phi$$
$$(4.48)$$

The weak form of the coupled IBVP (Initial Boundary Value Problem) can be reduced to four independent fields, namely the displacement, the pressure, the dilatation and the non-local damage fields. It is given by

$$\delta\Pi^u = \delta\Pi^u_{\text{int}} - \delta\Pi^u_{\text{ext}} = \int_\Omega \left[(f_d(\kappa)\boldsymbol{\sigma}_{\text{iso}} + \tilde{p}\mathbf{1}) \cdot \nabla_{\mathbf{x}}\delta\mathbf{u}\ \mathrm{d}\Omega - \delta\Pi_{\text{ext}}(\mathbf{u}) = 0 \right. \tag{4.49}$$

$$\delta\Pi^{\tilde{p}} = \delta\Pi^{\tilde{p}}_{\text{int}} = \int_\Omega \frac{(J(\mathbf{u}) - \tilde{J})\delta\tilde{p}}{J}\ \mathrm{d}\Omega = 0 \tag{4.50}$$

$$\delta\Pi^{\tilde{J}} = \delta\Pi^{\tilde{J}}_{\text{int}} = \int_\Omega \frac{\left(\frac{\partial\Psi^{\text{loc}}_{\text{vol}}}{\partial\tilde{J}} - \tilde{p}\right)}{J}\delta\tilde{J}\ \mathrm{d}\Omega = 0 \tag{4.51}$$

$$\delta\Pi^\phi = \delta\Pi^\phi_{\text{int}} - \delta\Pi^\phi_{\text{ext}} = \int_\Omega \frac{c_d}{J}\nabla_{\mathbf{x}}\phi \cdot \mathbf{b} \cdot \nabla_{\mathbf{x}}\delta\phi\ \mathrm{d}\Omega - \int_\Omega \frac{\beta_d}{J}[\phi - \gamma_d\kappa]\delta\phi\ \mathrm{d}\Omega = 0. \tag{4.52}$$

with the isochoric contribution of the Cauchy stress $\boldsymbol{\sigma}_{\text{iso}}$ being easily obtained from the derivation of the local strain energy density as

$$\boldsymbol{\sigma}_{\text{iso}} = 2J^{-1}\mathbf{b}\frac{\partial\Psi^{\text{loc}}_{\text{iso}}}{\partial\mathbf{b}} = G\bar{\mathbf{b}} - \frac{\bar{I}_1}{3}\mathbf{1} \tag{4.53}$$

In addition to this, it is worth highlighting the expressions for the Jacobians obtained by the volumetric and isochoric contributions:

$$\mathbb{c}^{\text{vol}} = \tilde{p}(\mathbf{1} \otimes \mathbf{1} - 2\mathbf{I}^{\text{sym}}) \tag{4.54}$$

$$\mathbb{c}^{\text{iso}} = \frac{2}{3J}\left[\bar{I}_1[\mathbf{I}^{\text{sym}} - (\mathbf{1} \otimes \mathbf{1})/3] - \boldsymbol{\sigma}_{\text{iso}} \otimes \mathbf{1} - \mathbf{1} \otimes \boldsymbol{\sigma}_{\text{iso}}\right] \tag{4.55}$$

It is observed how the damage function term f_d only multiplies the isochoric term. Therefore, for the forthcoming expressions in Section 4.3.1, when we refer to damaged stress and stiffness, they refer to the isochoric terms. The volumetric contribution is left unchanged.

4.3 Algorithmic treatment and finite element implementation details

This section outlines the description of the algorithmic description for the general gradient-enhanced damage formulation (Section 4.3.1), and subsequently, in Section 4.3.2, we describe the finite element implementation details describing the resulting operators and the interpolation schemes for each of the formulations given in Sections 4.2.1-4.2.3.

4.3.1 Gradient-enhanced damage framework - algorithmic setting

This section details the algorithmic scheme within the context of an iterative and sequential solution scheme using nonlinear FE. In the sequel, we provide condensed information concerning the material and spatial formulations given in Section 4.2.1 in line with the salient results of Waffenschmidt et al. [111].

Recalling Eq. (4.21), this expression represents a nonlinear differential equation that should be numerically integrated within the time step interval $\Delta t = t_{n+1} - t_n \geq 0$ where t_{n+1} is the current time step and t_n is the previous equilibrium solution of the system relying on a Newton-Rahpson-based solution of the corresponding nonlinear FE formulation. The backward Euler integration scheme of the damage variable κ at the current time step $n + 1$ renders

$$\kappa_{n+1} = \kappa_n + \gamma_{n+1} \quad \text{with } \kappa|_{t_0} = \kappa_d \qquad (4.56)$$

where $\gamma_{n+1} = \Delta t \lambda_{d,n+1}$ is the Lagrange multiplier at time t_{n+1}. Therefore, the incremental Karush–Kuhn–Tucker conditions take the form:

$$\gamma_{n+1} \geq 0; \quad \Phi_{d,n+1} \leq 0; \quad \gamma_{n+1} \Phi_{d,n+1} = 0 \qquad (4.57)$$

The flux and source equations can be updated for a material descrip-

tion:

$$\mathbf{S}_{n+1} = f_d(\kappa_{n+1})\mathbf{S}_{n+1}^{\text{und}} \tag{4.58}$$

$$\mathbf{Y}_{n+1} = c_d \nabla_{\mathbf{X}}\phi_{n+1} \tag{4.59}$$

$$Y_{n+1} = -\beta_d[\phi_{n+1} - \kappa_{n+1}\gamma_d] \tag{4.60}$$

where the superscript $[\bullet]^{\text{und}}$ refers to undamaged variables.

The spatial approach is obtained by just push-forwarding the magnitudes:

$$\boldsymbol{\sigma}_{n+1} = f_d(\kappa_{n+1})\boldsymbol{\sigma}_{n+1}^{\text{und}} \tag{4.61}$$

$$\mathbf{y}_{n+1} = c_d \nabla_{\mathbf{x}}\phi_{n+1}/J_{n+1}\mathbf{b}_{n+1} \tag{4.62}$$

$$y_{n+1} = -\beta_d[\phi_{n+1} - \kappa_{n+1}\gamma_d]/J_{n+1} \tag{4.63}$$

where $\kappa_{n+1} = \kappa_n$ for an elastic incremental step. Complying with Eq. (4.20), for our incremental scheme, the incremental Lagrange multiplier γ_{n+1} is obtained by fulfilling the consistency equation:

$$\Phi_{d,n+1} = q_{n+1} - \kappa_{n+1} = \Psi_{n+1}^{\text{loc}} + \frac{\beta_d\gamma_d}{\eta_d f_d(\kappa_{n+1})}[\phi_{n+1} - \gamma_d\kappa_{n+1}] - \kappa_{n+1} = 0 \tag{4.64}$$

This nonlinear equation is solved by means of a Newton-Raphson (N-R) iterative scheme at the material point level: expanding Eq. (4.64) in a first-order Taylor series at γ_{n+1}^k for a k-th N-R iteration, we obtain

$$\gamma_{n+1}^{k+1} = \gamma_{n+1}^k - [\mathbf{d}_\gamma \mathbf{r}_{n+1}^k]^{-1}\mathbf{r}_{n+1}^k \tag{4.65}$$

where $\mathbf{r}_{n+1}^k = \Phi_{d,n+1}(\kappa_{n+1}^k)$ is the residual in the k-th iteration step and $\mathbf{d}_\gamma \mathbf{r}_{n+1}^k$ is the Jacobian of this residual, which reads

$$\mathbf{d}_\gamma \mathbf{r}_{n+1}^k = \frac{\beta_d\gamma_d}{\eta_d f_d(\kappa_{n+1})}[\eta_d[\phi_{n+1} - \gamma_d\kappa_{n+1}] - \gamma_d] - 1 \tag{4.66}$$

Now that we can calculate γ_{n+1}, the N-R scheme checks if the residual is below a pre-defined tolerance, and accordingly, the internal damage variable (Eq. (4.56)) and the flux and source terms for stresses and

non-local damage magnitudes (Eqs. (4.58)-(4.63)) are updated. We now have all the ingredients for the global algorithm setting that is thoroughly summarised in Algorithm 1. For this, we compute the derivatives for all the source values required to complete the Jacobian formulation. For the sake of brevity, we consider $f_d(\kappa_{n+1}) = f_d$ in this series of equations. Complying with a material configuration approach:

$$2\frac{\partial \mathbf{S}_{n+1}}{\partial \mathbf{C}_{n+1}} = f_d \mathbb{C}_{n+1} + \eta_d f_d \beta_d \mathbf{S}_{n+1} \otimes \mathbf{S}_{n+1} \tag{4.67}$$

$$\frac{\partial \mathbf{S}_{n+1}}{\partial \phi_{n+1}} = 2\frac{\partial Y_{n+1}}{\partial \mathbf{C}_{n+1}} = \beta_d \gamma_d \theta_d \mathbf{S}_{n+1} \tag{4.68}$$

$$\frac{\partial Y_{n+1}}{\partial \phi_{n+1}} = -\left[\beta_d + (\beta_d \gamma_d)^2 (\eta_d f_d)^{-1} \theta_d\right] \tag{4.69}$$

$$\frac{\partial Y_{n+1}}{\partial \nabla_{\mathbf{X}} \phi_{n+1}} = c_d \mathbf{1} \tag{4.70}$$

and applying a push-forward for the spatial approach:

$$2\frac{\partial \boldsymbol{\sigma}_{n+1}}{\partial (\mathbf{F}_{n+1} \mathbf{C}_{n+1} \mathbf{F}_{n+1}^{\mathrm{T}})} = f_d \mathbb{c}_{n+1} + J_{n+1} \eta_d f_d \beta_d \boldsymbol{\sigma}_{n+1} \otimes \boldsymbol{\sigma}_{n+1} \tag{4.71}$$

$$\frac{\partial \boldsymbol{\sigma}_{n+1}}{\partial \phi_{n+1}} = 2\frac{\partial y_{n+1}}{\partial (\mathbf{F}_{n+1} \mathbf{C}_{n+1} \mathbf{F}_{n+1}^{\mathrm{T}})} = \beta_d \gamma_d \theta_d \boldsymbol{\sigma}_{n+1} \tag{4.72}$$

$$\frac{\partial y_{n+1}}{\partial \phi_{n+1}} = -\left[\beta_d + (\beta_d \gamma_d)^2 (\eta_d f_d)^{-1} \theta_d\right]/J_{n+1} \tag{4.73}$$

$$\frac{\partial y_{n+1}}{\partial \nabla_{\mathbf{x}} \phi_{n+1}} = c_d \mathbf{b}_{n+1}/J_{n+1} \tag{4.74}$$

with

$$\theta_d = -1 - \frac{\eta_d f_d}{\beta_d \gamma_d [\gamma_d (1 + \eta_d \kappa_{n+1}) - \eta_d \phi_{n+1}]} \tag{4.75}$$

Algorithm 1 Algorithmic box for the local N-R scheme for gradient-enhanced damage constitutive model. MS = material scheme, SS = spatial scheme.

1: **Input:** $\mathbf{F}_{n+1}$, ϕ_{n+1}, $\nabla_{\mathbf{X}}\phi_{n+1}$ (MS), $\nabla_{\mathbf{x}}\phi_{n+1}$ (SS), κ_n ($\kappa|_{t_0} = \phi|_{t_0} = \kappa_d$)

2: Compute $\Psi^{\mathrm{loc}}_{n+1}$ (Eq. (4.1)), $\mathbf{S}^{\mathrm{und}}_{n+1}$ (MS, Eq. (4.2)), $\boldsymbol{\sigma}^{\mathrm{und}}_{n+1}$ (SS, Eq. (4.3)), $\mathbb{C}^{\mathrm{und}}_{n+1}$ (MS, Eq. (4.4)) and $\mathbb{c}^{\mathrm{und}}_{n+1}$ (SS, Eq. (4.5))

3: Calculate driving force

$$q_{n+1} = \Psi^{\mathrm{loc}}_{n+1} + \frac{\beta_d \gamma_d}{\eta_d f_d(\kappa_n)}[\phi_{n+1} - \gamma_d \kappa_n]; \qquad f_d(\kappa_n) = \exp[\eta_d(\kappa_d - \kappa_n)] \tag{4.76}$$

4: Comprobate damage function:

$$\Phi_{d,n+1} = q_{n+1} - \kappa_n \tag{4.77}$$

Set $\kappa_{n+1} = \kappa_n$. If Eq. (4.77) ≤ 0, go to Step 6. Otherwise, go to Step 5.

5: Compute local N-R to obtain incremental Lagrange multiplier γ_{n+1} iteratively

a: Compute residual $\mathbf{r}^k_{n+1}$

$$\mathbf{r}^k_{n+1} = \Psi^{\mathrm{loc}}_{n+1} + \frac{\beta_d \gamma_d}{\eta_d f_d(\kappa^k_{n+1})}[\phi_{n+1} - \gamma_d \kappa^k_{n+1}] - \kappa^k_{n+1};$$
$$f_d(\kappa^k_{n+1}) = \exp[\eta_d(\kappa_d - \kappa^k_{n+1})] \tag{4.78}$$

b: Comprobate the tolerance: if $|\mathbf{r}^k_{n+1}| < $ TOL, go to Step 6, if not, continue to Step 5c.

c: Calculate Jacobian of residual $\mathrm{d}_\gamma \mathbf{r}^k_{n+1}$ (Eq. (4.66)).

d: Compute the variation for the incremental Lagrange multiplier

$$\Delta\gamma^k_{n+1} = -[\mathrm{d}_\gamma \mathbf{r}^k_{n+1}]^{-1}\mathbf{r}^k_{n+1} \tag{4.79}$$

e: Update internal damage variable

$$\kappa^k_{n+1} = \kappa^k_n + \Delta\gamma^k_{n+1} \tag{4.80}$$

and go back to Step 5a.

6: Compute flux and source equations (Eqs. (4.58)-(4.60) for MS or Eqs. (4.61)-(4.63) for SS).

7: Compute tangent moduli (Eqs. (4.67)-(4.70) for MS or Eqs. (4.71)-(4.74) for SS).

4.3.2 Finite Element formulation and implementation details

This section addresses the FE derivation and the main implementation details of the proposed coupled system of nonlinear equations for each of the variational formulations proposed in Section 4.2.

The baseline kinematic description for the displacement approximation complies with standard first-order 3-D 8-node hexahedral elements. The parametric space is defined as: $\mathcal{A} := \{\boldsymbol{\xi} = (\xi, \eta, \zeta) \in \mathbb{R}^3 \mid -1 \leq \xi, \eta, \zeta \leq +1; i = 1, 2, 3\}$. The related literature has deeply reported the poor performance of this fundamental displacement formulation for bending-dominated applications and nearly incompressible elasticity, motivating the development of several mixed FE formulations.

For the sake of clarity, we specify the main differences between the three approaches herewith proposed:

- A nonlinear CDM approach for the spatial configuration using the formulation of Section 4.2.1.

- A novel nonlinear CDM approach for the material configuration considering the enhanced assumed strain (EAS) technique (Section 4.2.2).

- A novel nonlinear CDM approach for the spatial configuration considering a mixed Finite Element formulation that accounts for the influence of the hydrostatic pressure p and the Jacobian J (Section 4.2.3).

First, we outline the interpolation of the displacements and the non-local damage variable that holds for the standard gradient-enhanced damage model and for the mixed formulations herein proposed. Subsequently, we will detail for the discrete representations encompassing the residuals and the Jacobian matrices given for each one of the three different proposed approaches.

Discretisation scheme for the displacement and the non-local damage variable

Complying with standard isoparametric FEM, the reference and the current geometries can be interpolated using standard trilinear shape functions N^I ($\mathbf{N}(\boldsymbol{\xi})$ in matrix notation) as

$$\mathbf{X} = \sum_{I=1}^{m} N^I(\boldsymbol{\xi})\mathbf{X}_I = \mathbf{N}(\boldsymbol{\xi}) \cdot \hat{\mathbf{X}} \quad \text{and} \quad \mathbf{x} = \sum_{I=1}^{m} N^I(\boldsymbol{\xi})\mathbf{x}_I = \mathbf{N}(\boldsymbol{\xi}) \cdot \hat{\mathbf{x}}, \quad (4.81)$$

where $\mathbf{X}_I$ and $\mathbf{x}_I$ stands the nodal positions in the reference and the current configurations, respectively, and setting $m = 8$ is the number of nodes. These nodal locations can be expressed in the corresponding vectors: $\hat{\mathbf{X}}$ and $\hat{\mathbf{x}}$.

The interpolation of the displacements $\mathbf{u}$ and the non-local damage variable ϕ renders

$$\mathbf{u} \approx \mathbf{N}(\boldsymbol{\xi}) \cdot \mathbf{d}, \quad \phi \approx \mathbf{N}(\boldsymbol{\xi}) \cdot \hat{\phi} \tag{4.82}$$

where $\mathbf{d}$ represents the nodal displacement vector, and $\hat{\phi}$ represents the nodal values of the non-local damage variable; both defined at the element level.

The material and spatial gradients of the shape functions $\mathbf{N}$ can be read as

$$\nabla_{\mathbf{X}}\mathbf{N} = \mathbf{J_e}^{-T} \cdot \nabla_{\boldsymbol{\xi}}\mathbf{N}(\boldsymbol{\xi}), \qquad \nabla_{\mathbf{x}}\mathbf{N} = \mathbf{j_e}^{-T} \cdot \nabla_{\boldsymbol{\xi}}\mathbf{N}(\boldsymbol{\xi}) \tag{4.83}$$

with $\boldsymbol{\xi}$ referring to the parametric coordinate system with coordinates $\boldsymbol{\xi} = \{\xi, \eta, \zeta\}$; and $\mathbf{J_e}$ and $\mathbf{j_e}$ as the material and spatial Jacobians of the isoparametric transformation, which allow the computation of the deformation gradient $\mathbf{F}$ as follows:

$$\mathbf{F} = \mathbf{j_e} \cdot \mathbf{J_e}^{-1} \qquad \text{with } J = \det[\mathbf{F}] = \frac{\det[\mathbf{j_e}]}{\det[\mathbf{J_e}]} \tag{4.84}$$

With the previous definitions at hand, the corresponding material gradient quantities can be discretized as, for a material description,

$$\nabla_{\mathbf{X}}\delta\mathbf{u} \approx \delta\mathbf{d} \otimes \nabla_{\mathbf{X}}\mathbf{N}, \qquad \nabla_{\mathbf{X}}\delta\phi \approx \delta\hat{\phi} \otimes \nabla_{\mathbf{X}}\mathbf{N} \tag{4.85}$$

whereas the spatial gradients render

$$\nabla_{\mathbf{x}} \delta \mathbf{u} \approx \delta \mathbf{d} \otimes \nabla_{\mathbf{x}} \mathbf{N}, \qquad \nabla_{\mathbf{x}} \delta \phi \approx \delta \hat{\boldsymbol{\phi}} \otimes \nabla_{\mathbf{x}} \mathbf{N} \qquad (4.86)$$

FE formulation of the gradient-enhanced damage model for spatial configuration - Q1Q1

The point of departure for the finite element formulation of the displacement-based gradient-enhanced damage model recalls the variational formalism defined in Eqs. (4.29)-(4.30), defining a coupled problem.

The insertion of the interpolation scheme for $\mathbf{u}$ and ϕ leads to a discrete version of the residual forms denoted by $\mathbf{R}^{\mathbf{d}}$ and $\mathbf{R}^{\hat{\phi}}$ that are defined as:

$$\mathbf{R}^{\mathbf{d}}(\mathbf{d}, \delta\mathbf{d}, \hat{\phi}) = \int_{\Omega} \nabla_{\mathbf{x}} \mathbf{N}^{\mathrm{T}} \cdot \boldsymbol{\sigma} \, \mathrm{d}\Omega - \int_{\Omega} \mathbf{N}^{\mathrm{T}} \cdot \mathbf{f}^{v} \, \mathrm{d}\Omega - \int_{\partial\Omega} \mathbf{N}^{T} \cdot \bar{\mathbf{t}} \, \mathrm{d}\partial\Omega = 0 \tag{4.87}$$

$$\mathbf{R}^{\hat{\phi}}(\mathbf{d}, \hat{\phi}, \delta\hat{\phi}) = \int_{\Omega} \nabla_{\mathbf{x}} \mathbf{N}^{\mathrm{T}} \cdot \mathbf{y} \, \mathrm{d}\Omega - \int_{\partial\Omega} \mathbf{N}^{\mathrm{T}} y \, \mathrm{d}\partial\Omega = 0 \tag{4.88}$$

For the application of Newton-type solution algorithms for the iterative solution of the boundary value problem, the linearization of the weak form is computed as follows:

$$\hat{L}[\mathbf{R}^{d}](\mathbf{d}, \delta\mathbf{d}, \Delta\mathbf{d}, \hat{\phi}, \Delta\hat{\phi}) = \mathbf{R}^{d}(\mathbf{d}, \delta\mathbf{d}, \hat{\phi}) + \Delta_{\mathbf{d}}\mathbf{R}^{d} \cdot \Delta\mathbf{d} + \Delta_{\hat{\phi}}\mathbf{R}^{d} \cdot \Delta\hat{\phi} \tag{4.89}$$

$$\hat{L}[\mathbf{R}^{\hat{\phi}}](\mathbf{d}, \hat{\phi}, \delta\hat{\phi}, \Delta\hat{\phi}) = \mathbf{R}^{\hat{\phi}}(\mathbf{d}, \hat{\phi}, \delta\hat{\phi}) + \Delta_{\mathbf{d}}\mathbf{R}^{\hat{\phi}} \cdot \Delta\mathbf{d} + \Delta_{\hat{\phi}}\mathbf{R}^{\hat{\phi}} \cdot \Delta\hat{\phi} \tag{4.90}$$

where $\Delta_{*}[\bullet]$ denotes the directional derivative operator with respect to the field $*$.

Computing the derivatives of the residuals, we reach the Jacobian expressions that are required to solve the global N-R scheme:

$$\mathbf{K^{dd}} = \frac{\partial \mathbf{R}^d}{\partial \mathbf{u}} = \int_\Omega \nabla_\mathbf{x} \mathbf{N^T} \cdot \mathbb{c} \cdot \nabla_\mathbf{x} \mathbf{N} \, \mathrm{d}\Omega + \int_\Omega \left[\nabla_\mathbf{x} \mathbf{N^T} \cdot \boldsymbol{\sigma} \cdot \nabla_\mathbf{x} \mathbf{N} \right] \cdot \mathbf{1} \, \mathrm{d}\Omega$$
(4.91)

$$\mathbf{K^{d\hat{\phi}}} = \frac{\partial \mathbf{R}^d}{\partial \phi} = \int_\Omega \nabla_\mathbf{x} \mathbf{N^T} \cdot \frac{\partial \boldsymbol{\sigma}}{\partial \phi} \cdot \mathbf{N^T} \, \mathrm{d}\Omega \tag{4.92}$$

$$\mathbf{K^{\hat{\phi} d}} = \frac{\partial \mathbf{R}^{\hat{\phi}}}{\partial \mathbf{u}} = \int_\Omega \mathbf{N} \cdot 2 \frac{\partial y}{\partial (\mathbf{FCF^T})} \cdot \nabla_\mathbf{x} \mathbf{N} \, \mathrm{d}\Omega \tag{4.93}$$

$$\mathbf{K^{\hat{\phi}\hat{\phi}}} = \frac{\partial \mathbf{R}^{\hat{\phi}}}{\partial \phi} = \int_\Omega \frac{\partial y}{\partial \phi} \mathbf{N^T} \cdot \mathbf{N} \, \mathrm{d}\Omega + \int_\Omega \nabla_\mathbf{x} \mathbf{N^T} \cdot \frac{\partial \mathbf{y}}{\partial \nabla_\mathbf{x} \phi} \cdot \nabla_\mathbf{x} \mathbf{N} \, \mathrm{d}\Omega \quad (4.94)$$

which leads to the following linearised system of equations that is solved by the global iterative N-R monolithic scheme

$$\begin{bmatrix} \mathbf{K^{dd}} & \mathbf{K^{d\hat{\phi}}} \\ \mathbf{K^{\hat{\phi} d}} & \mathbf{K^{\hat{\phi}\hat{\phi}}} \end{bmatrix} \begin{bmatrix} \Delta \mathbf{d} \\ \Delta \hat{\boldsymbol{\phi}} \end{bmatrix} = - \begin{bmatrix} \mathbf{R^d} \\ \mathbf{R}^{\hat{\phi}} \end{bmatrix} \tag{4.95}$$

FE formulation of the gradient-enhanced damage model EAS-based elements - `Q1Q1E24`

For its numerical implementation and in line with the previous investigations for Enhanced Assumed Strain (EAS) mixed FE formulations, we herewith recall a material formulation defined in the reference configuration of the body. This formulation has been exploited for its usage in the modelling for solid shells [146, 317, 309, 269, 318, 310, 319, 68, 35], as it is proven to block the appearance of shear locking in structures under bending configurations.

Recalling from Section 4.2.2, the Cauchy-Green right tensor is computed as follows:

$$\mathbf{C} = \mathbf{C}^u + \tilde{\mathbf{C}} = 2(\mathbf{E}^u + \tilde{\mathbf{E}}) + \mathbf{1} \tag{4.96}$$

The current definition of the enhancing part of the Green-Lagrange tensor relies on the formulation proposed by Andelfinger and Ramm [305] and Bischoff and Ramm [316], whose specific details are omitted for brevity reasons.

The enhanced strain field is defined at the element level via the matrix operator $\mathbf{M}(\boldsymbol{\xi})$

$$\tilde{\mathbf{E}} \approx \mathbf{M}(\boldsymbol{\xi}) \cdot \boldsymbol{\varsigma}, \ \ \delta\tilde{\mathbf{E}} \approx \mathbf{M}(\boldsymbol{\xi}) \cdot \delta\boldsymbol{\varsigma}, \ \ \Delta\tilde{\mathbf{E}} \approx \mathbf{M}(\boldsymbol{\xi}) \cdot \Delta\boldsymbol{\varsigma}. \tag{4.97}$$

where

$$\mathbf{M} = \frac{\det\mathbf{J_0}}{\det\mathbf{J_e}}\mathbf{T_0^{-T}} \cdot \mathbf{M_\xi} \tag{4.98}$$

where $\mathbf{T_0^{-T}}$ is the transpose of the inverse of a matrix that accounts for the terms of the Jacobian from the initial configuration $\mathbf{J_e}$ that reads:

$$\mathbf{T_0} = \begin{bmatrix} J_{0\,11}^2 & J_{0\,21}^2 & J_{0\,31}^2 & 2J_{0\,11}J_{0\,21} & 2J_{0\,21}J_{0\,31} & 2J_{0\,11}J_{0\,31} \\ J_{0\,12}^2 & J_{0\,22}^2 & J_{0\,32}^2 & 2J_{0\,12}J_{0\,22} & 2J_{0\,22}J_{0\,32} & 2J_{0\,12}J_{0\,32} \\ J_{0\,13}^2 & J_{0\,23}^2 & J_{0\,33}^2 & 2J_{0\,13}J_{0\,23} & 2J_{0\,23}J_{0\,33} & 2J_{0\,13}J_{0\,33} \\ J_{0\,11}J_{0\,12} & J_{0\,21}J_{0\,22} & J_{0\,31}J_{0\,32} & J_{0\,11}J_{0\,12}+J_{0\,21}J_{0\,12} & J_{0\,21}J_{0\,32}+J_{0\,31}J_{0\,22} & J_{0\,11}J_{0\,32}+J_{0\,31}J_{0\,12} \\ J_{0\,12}J_{0\,13} & J_{0\,22}J_{0\,23} & J_{0\,32}J_{0\,33} & J_{0\,12}J_{0\,23}+J_{0\,22}J_{0\,13} & J_{0\,22}J_{0\,33}+J_{0\,32}J_{0\,23} & J_{0\,12}J_{0\,33}+J_{0\,33}J_{0\,13} \\ J_{0\,11}J_{0\,13} & J_{0\,21}J_{0\,23} & J_{0\,31}J_{0\,33} & J_{0\,11}J_{0\,23}+J_{0\,21}J_{0\,13} & J_{0\,21}J_{0\,33}+J_{0\,31}J_{0\,23} & J_{0\,11}J_{0\,33}+J_{0\,31}J_{0\,13} \end{bmatrix} \tag{4.99}$$

Without any loss of generality, we recall the incompatible strain modes defined in [305] encompassing 24 incompatible modes leading to the following particular form of the matrix $\mathbf{M_\xi}$:

$$\mathbf{M_\xi} = \begin{bmatrix} \xi & 0 & 0 & 0 & 0 & 0 & 0 & 0 & 0 & 0 & 0 & 0 & 0 & 0 & 0 & \xi\eta & \xi\zeta & 0 & 0 & 0 & 0 & 0 & 0 & 0 \\ 0 & \eta & 0 & 0 & 0 & 0 & 0 & 0 & 0 & 0 & 0 & 0 & 0 & 0 & 0 & 0 & 0 & \xi\eta & \eta\zeta & 0 & 0 & 0 & 0 & 0 \\ 0 & 0 & \zeta & 0 & 0 & 0 & 0 & 0 & 0 & 0 & 0 & 0 & 0 & 0 & 0 & 0 & 0 & 0 & 0 & \xi\zeta & \eta\zeta & 0 & 0 & 0 \\ 0 & 0 & 0 & \xi & \eta & 0 & 0 & 0 & 0 & \xi\zeta & \eta\zeta & 0 & 0 & 0 & 0 & 0 & 0 & 0 & 0 & 0 & 0 & \xi\eta & 0 & 0 \\ 0 & 0 & 0 & 0 & 0 & 0 & \xi & \zeta & 0 & 0 & 0 & 0 & \xi\eta & \zeta\eta & 0 & 0 & 0 & 0 & 0 & 0 & 0 & 0 & 0 & \xi\zeta \\ 0 & 0 & 0 & 0 & 0 & \eta & \zeta & 0 & 0 & 0 & 0 & \xi\eta & \xi\zeta & 0 & 0 & 0 & 0 & 0 & 0 & 0 & 0 & 0 & \eta\zeta & 0 \end{bmatrix} \tag{4.100}$$

Therefore, the incompatible strains $\boldsymbol{\varsigma}$ are added into the FE implementation as an extra degree of freedom. The consistent linearization of this system is obtained through the Gateaux directional derivative concept, resulting in

$$\hat{L}[\mathbf{R^d}](\mathbf{d}, \delta\mathbf{d}, \Delta\mathbf{d}, \hat{\phi}, \Delta\hat{\phi}, \boldsymbol{\varsigma}, \Delta\boldsymbol{\varsigma}) = \mathbf{R^d}(\mathbf{d}, \delta\mathbf{d}, \hat{\phi}, \boldsymbol{\varsigma}) + \Delta_\mathbf{d}\mathbf{R^d} \cdot \Delta\mathbf{d}$$
$$+ \Delta_{\hat{\phi}}\mathbf{R^d} \cdot \Delta\hat{\phi} + \Delta_{\boldsymbol{\varsigma}}\mathbf{R^d} \cdot \Delta\boldsymbol{\varsigma} \tag{4.101}$$

$$\hat{L}[\mathbf{R^\varsigma}](\mathbf{d}, \Delta\mathbf{d}, \hat{\phi}, \Delta\hat{\phi}, \boldsymbol{\varsigma}, \delta\boldsymbol{\varsigma}, \Delta\boldsymbol{\varsigma}) = \mathbf{R^\varsigma}(\mathbf{d}, \hat{\phi}, \boldsymbol{\varsigma}, \delta\boldsymbol{\varsigma}) + \Delta_\mathbf{d}\mathbf{R^\varsigma} \cdot \Delta\mathbf{d}$$
$$+ \Delta_{\hat{\phi}}\mathbf{R^\varsigma} \cdot \Delta\hat{\phi} + \Delta_{\boldsymbol{\varsigma}}\mathbf{R^\varsigma} \cdot \Delta\boldsymbol{\varsigma} \tag{4.102}$$

137

$$\hat{L}[\mathbf{R}^{\hat{\phi}}](\mathbf{d}, \Delta\mathbf{d}, \hat{\phi}, \delta\hat{\phi}, \Delta\hat{\phi}, \varsigma, \Delta\varsigma) = \mathbf{R}^{\hat{\phi}}(\mathbf{d}, \hat{\phi}, \delta\hat{\phi}, \varsigma) + \Delta_{\mathbf{d}}\mathbf{R}^{\hat{\phi}} \cdot \Delta\mathbf{d}$$
$$+ \Delta_{\hat{\phi}}\mathbf{R}^{\hat{\phi}} \cdot \Delta\hat{\phi} + \Delta_{\varsigma}\mathbf{R}^{\hat{\phi}} \cdot \Delta\varsigma, \tag{4.103}$$

The linearised system of equations solved for the global N-R monolithic scheme reads

$$\begin{bmatrix} \mathbf{K^{dd}} & \mathbf{K^{d\hat{\phi}}} & \mathbf{K^{d\varsigma}} \\ \mathbf{K^{\hat{\phi}d}} & \mathbf{K^{\hat{\phi}\hat{\phi}}} & \mathbf{K^{\hat{\phi}\varsigma}} \\ \mathbf{K^{\varsigma d}} & \mathbf{K^{\varsigma\hat{\phi}}} & \mathbf{K^{\varsigma\varsigma}} \end{bmatrix} \begin{bmatrix} \Delta\mathbf{d} \\ \Delta\hat{\phi} \\ \Delta\varsigma \end{bmatrix} = - \begin{bmatrix} \mathbf{R}^d \\ \mathbf{R}^{\hat{\phi}} \\ \mathbf{R}^{\varsigma} \end{bmatrix} \tag{4.104}$$

where the term for the residual of the incompatible strains $\mathbf{R}^{\varsigma}$ is given by

$$\mathbf{R}^{\varsigma}(\mathbf{d}, \hat{\phi}, \varsigma, \delta\varsigma) = \int_{\Omega_0} \mathbf{M}^{\mathrm{T}} \cdot \mathbf{S} \, \mathrm{d}\Omega \tag{4.105}$$

and the tangent terms that form part of the Jacobian matrix read as

$$\mathbf{K^{\varsigma d}} = \int_{\Omega_0} \mathbf{M}^{\mathrm{T}} \cdot \mathbb{C} \cdot \nabla_{\mathbf{X}}\mathbf{N} \, \mathrm{d}\Omega \tag{4.106}$$

$$\mathbf{K^{\varsigma\hat{\phi}}} = \int_{\Omega_0} \mathbf{M}^{\mathrm{T}} \cdot \mathbb{C} \cdot \mathbf{N} \, \mathrm{d}\Omega \tag{4.107}$$

$$\mathbf{K^{\varsigma\varsigma}} = \int_{\Omega_0} \mathbf{M}^{\mathrm{T}} \cdot \mathbb{C} \cdot \mathbf{M} \, \mathrm{d}\Omega \tag{4.108}$$

where $\nabla_{\mathbf{X}}\mathbf{N}$ accounts for the nonlinear term that is added to the expression defined in Eq. (4.83), specific for material configuration schemes [134]. This is expressed for every node by:

$$\nabla_{\mathbf{X}}N_i = \begin{bmatrix} N_{i,x}F_{11} & N_{i,x}F_{21} & N_{i,x}F_{31} \\ N_{i,y}F_{12} & N_{i,y}F_{22} & N_{i,y}F_{32} \\ N_{i,z}F_{13} & N_{i,z}F_{23} & N_{i,z}F_{33} \\ N_{i,x}F_{12} + N_{i,y}F_{11} & N_{i,x}F_{22} + N_{i,y}F_{21} & N_{i,x}F_{32} + N_{i,y}F_{31} \\ N_{i,y}F_{13} + N_{i,z}F_{12} & N_{i,y}F_{23} + N_{i,z}F_{22} & N_{i,y}F_{33} + N_{i,z}F_{32} \\ N_{i,x}F_{13} + N_{i,z}F_{11} & N_{i,x}F_{23} + N_{i,z}F_{21} & N_{i,x}F_{33} + N_{i,z}F_{31} \end{bmatrix} \tag{4.109}$$

where $N_{i,j}$ is the derivative of the nodal shape function N_i with respect to the j-coordinate and F_{ij} accounts for the terms of the deformation gradient $\mathbf{F}$. This expression is also included in his respective terms for the

internal residuals and their associated Jacobians for the reference configuration.

Following the approach proposed by [309], since inter-element continuity is not required for the enhanced strains, they can be removed as a DOF through a standard static condensation process, thus reaching the system of equations proposed in Eq. (4.95), having the element stiffness contributions like

$$\tilde{\mathbf{K}}^{\mathbf{dd}} = \mathbf{K}^{\mathbf{dd}} - \mathbf{K}^{\mathbf{d\varsigma}} \cdot (\mathbf{K}^{\varsigma\varsigma})^{-1} \cdot \mathbf{K}^{\varsigma\mathbf{d}} \tag{4.110}$$

$$\tilde{\mathbf{K}}^{\mathbf{d}\hat{\phi}} = (\tilde{\mathbf{K}}^{\hat{\phi}\mathbf{d}})^{\mathsf{T}} = \mathbf{K}^{\mathbf{d}\hat{\phi}} - \mathbf{K}^{\mathbf{d\varsigma}} \cdot (\mathbf{K}^{\varsigma\varsigma})^{-1} \cdot \mathbf{K}^{\varsigma\hat{\phi}} \tag{4.111}$$

$$\tilde{\mathbf{K}}^{\hat{\phi}\hat{\phi}} = \mathbf{K}^{\hat{\phi}\hat{\phi}} - \mathbf{K}^{\hat{\phi}\varsigma} \cdot (\mathbf{K}^{\varsigma\varsigma})^{-1} \cdot \mathbf{K}^{\varsigma\hat{\phi}} \tag{4.112}$$

and the newly defined residuals as

$$\tilde{\mathbf{R}}^{\mathbf{d}} = \mathbf{R}^{\mathbf{d}} - \mathbf{K}^{\mathbf{d\varsigma}} \cdot (\mathbf{K}^{\varsigma\varsigma})^{-1} \cdot \mathbf{R}^{\varsigma} \tag{4.113}$$

$$\tilde{\mathbf{R}}^{\hat{\phi}} = \mathbf{R}^{\hat{\phi}} - \mathbf{K}^{\hat{\phi}\varsigma} \cdot (\mathbf{K}^{\varsigma\varsigma})^{-1} \cdot \mathbf{R}^{\hat{\phi}} \tag{4.114}$$

FE formulation of the gradient-enhanced damage model for spatial configuration employing a mixed FE formulation - `Q1Q1P0`

For the second novel approach that we have developed, the present formulation relies on the fundamental derivations by Simo et al. [129] and subsequently exploited by Miehe [299], whose effectiveness for modelling quasi-incompressible materials ($\nu \rightarrow 0.5$) has been profusely assessed in the last two decades. In this concern, we recall a particular model where the primary unknowns are: (i) the displacement field $\mathbf{u}$, (ii) the Lagrange multiplier for pressure $\tilde{p}$, and (iii) the independent kinematic variable $\tilde{J}$.

In line with the two previous approaches, we start by getting the residuals for these three primary unknowns by discretising from Eq. (4.48):

$$\mathbf{R^d}(\mathbf{d}, \delta\mathbf{d}, \hat{\phi}, \tilde{p}) = \int_{\Omega} \nabla_{\mathbf{x}}\mathbf{N}^{\mathrm{T}} \cdot (\boldsymbol{\sigma}_{\mathrm{iso}} + \boldsymbol{\sigma}_{\mathrm{vol}})\, \mathrm{d}\Omega$$
$$- \int_{\Omega} \mathbf{N}^{\mathrm{T}} \cdot \mathbf{f}^V\, \mathrm{d}\Omega - \int_{\partial\Omega} \mathbf{N}^{\mathrm{T}} \cdot \overline{\mathbf{t}}\, \mathrm{d}\partial\Omega = 0 \tag{4.115}$$

$$R^{\tilde{p}}(\mathbf{d}, \delta p, \tilde{J}) = \int_{\Omega} \frac{N^{\tilde{p}}(J(\mathbf{d}) - \tilde{J})}{J}\, \mathrm{d}\Omega = 0 \tag{4.116}$$

$$R^{\tilde{J}}(\tilde{p}, \tilde{J}, \delta\tilde{J}) = \int_{\Omega} \frac{N^{\tilde{J}}\left(\frac{\partial\Psi_{\mathrm{vol}}^{\mathrm{loc}}}{\partial\tilde{J}} - \tilde{p}\right)}{J}\, \mathrm{d}\Omega = 0 \tag{4.117}$$

The consistent linearization of this system is obtained through the Gateaux directional derivative concept, resulting in

$$\hat{L}[\mathbf{R}^d](\mathbf{d}, \delta\mathbf{d}, \Delta\mathbf{d}, \hat{\phi}, \Delta\hat{\phi}, \tilde{p}, \Delta\tilde{p}) = \mathbf{R}^d(\mathbf{d}, \delta\mathbf{d}, \hat{\phi}, \tilde{p}) + \Delta_{\mathbf{d}}\mathbf{R}^d \cdot \Delta\mathbf{d}$$
$$+ \Delta_{\hat{\phi}}\mathbf{R}^d \cdot \Delta\hat{\phi} + \Delta_{\tilde{p}}\mathbf{R}^d \cdot \Delta\tilde{p} \tag{4.118}$$

$$\hat{L}[R^{\tilde{p}}](\mathbf{d}, \Delta\mathbf{d}, \delta\tilde{p}, \tilde{J}, \Delta\tilde{J}) = R^{\tilde{p}}(\mathbf{d}, \delta p, \tilde{J}) + \Delta_{\mathbf{d}}R^{\tilde{p}} \cdot \Delta\mathbf{d}$$
$$+ \Delta_{\tilde{J}}R^{\tilde{p}} \cdot \Delta\tilde{J} \tag{4.119}$$

$$\hat{L}[R^{\tilde{J}}](\tilde{p}, \Delta\tilde{p}, \tilde{J}, \delta\tilde{J}, \Delta\tilde{J}) = R^{\tilde{J}}(\tilde{p}, \tilde{J}, \delta\tilde{J}) + \Delta_{\tilde{p}}R^{\tilde{J}} \cdot \Delta\tilde{p}$$
$$+ \Delta_{\tilde{J}}R^{\tilde{J}} \cdot \Delta\tilde{J} \tag{4.120}$$

$$\hat{L}[\mathbf{R}^{\hat{\phi}}](\mathbf{d}, \Delta\mathbf{d}, \hat{\phi}, \delta\hat{\phi}, \Delta\hat{\phi}) = \mathbf{R}^{\hat{\phi}}(\mathbf{d}, \hat{\phi}, \delta\hat{\phi}) + \Delta_{\mathbf{d}}\mathbf{R}^{\hat{\phi}} \cdot \Delta\mathbf{d}$$
$$+ \Delta_{\hat{\phi}}\mathbf{R}^{\hat{\phi}} \cdot \Delta\hat{\phi} \tag{4.121}$$

By deriving the residuals, we reach the expression for the Jacobian matrices:

$$\mathbf{K^{dd}} = \int_\Omega \nabla_\mathbf{x} \mathbf{N^T} \cdot \mathbb{c} \cdot \nabla_\mathbf{x} \mathbf{N} \, \mathrm{d}\Omega$$
$$+ \int_\Omega \left[\nabla_\mathbf{x} \mathbf{N^T} \cdot (\boldsymbol{\sigma}_\mathrm{iso} + \boldsymbol{\sigma}_\mathrm{vol}) \cdot \nabla_\mathbf{x} \mathbf{N} \right] \cdot \mathbf{1} \, \mathrm{d}\Omega \qquad (4.122)$$

$$\mathbf{K^{d\tilde{p}}} = (\mathbf{K^{\tilde{p}d}})^T = \int_\Omega (\nabla_\mathbf{x} \mathbf{N^T}) \cdot \mathbf{1} N^{\tilde{p}} \, \mathrm{d}\Omega \qquad (4.123)$$

$$K^{\tilde{p}\tilde{J}} = K^{\tilde{J}\tilde{p}} = -\int_\Omega \frac{N^{\tilde{p}} N^{\tilde{J}}}{J} \, \mathrm{d}\Omega \qquad (4.124)$$

$$K^{\tilde{J}\tilde{J}} = \int_\Omega \frac{N^{\tilde{J}} \frac{\partial^2 \Psi_\mathrm{vol}^\mathrm{loc}}{\partial \tilde{J}^2} N^{\tilde{J}}}{J} \, \mathrm{d}\Omega \qquad (4.125)$$

What is observed in this formulation is that in addition to the normal formulation, we have to introduce shape functions for the interpolations for the mixed variables related to the pressure $N^{\tilde{p}}$ and the dilatation $N^{\tilde{J}}$. However, since they do not have to satisfy the continuity between the elements, we can suppose that their values, $N^{\tilde{p}}$ and $N^{\tilde{J}}$, have a constant scalar value of 1.

As outlined above, this mixed finite element is herewith reformulated in order to accommodate gradient-enhanced damage models, taking Eq. (4.48) as the basis for its derivation. Therefore, we obtain that the baseline three-field mixed formulation is coupled with the non-local gradient-enhanced damage model, leading to a system of four residual equations.

$$\begin{bmatrix} \mathbf{K^{dd}} & \mathbf{K^{d\hat{\phi}}} & \mathbf{K^{d\tilde{p}}} & \mathbf{0} \\ \mathbf{K^{\hat{\phi}d}} & \mathbf{K^{\hat{\phi}\hat{\phi}}} & \mathbf{0} & \mathbf{0} \\ \mathbf{K^{\tilde{p}d}} & \mathbf{0} & 0 & K^{\tilde{p}\tilde{J}} \\ \mathbf{0} & \mathbf{0} & K^{\tilde{J}\tilde{p}} & K^{\tilde{J}\tilde{J}} \end{bmatrix} \begin{bmatrix} \Delta\mathbf{d} \\ \Delta\hat{\phi} \\ \Delta\tilde{p} \\ \Delta\tilde{J} \end{bmatrix} = - \begin{bmatrix} \mathbf{R^d} \\ \mathbf{R^{\hat{\phi}}} \\ R^{\tilde{p}} \\ R^{\tilde{J}} \end{bmatrix} \qquad (4.126)$$

As inter-element continuity is not required for both the pressure and the dilatation DOFs, they can be removed from the system of equations by employing a standard static condensation process, reaching the system proposed in Eq. (4.95), obtaining both the residual and stiffness contributions like

$$\tilde{\mathbf{R}}^{\mathbf{d}} = \mathbf{R}^{\mathbf{d}} + \overline{K}\mathbf{K}^{\mathbf{d}\tilde{p}}R^{\tilde{p}} - \mathbf{K}^{\mathbf{d}\tilde{p}}(K^{\tilde{p}\tilde{J}})^{-1}R^{\tilde{J}} \tag{4.127}$$

$$\tilde{\mathbf{K}}^{\mathbf{dd}} = \mathbf{K}^{\mathbf{dd}} + \overline{K}\mathbf{K}^{\mathbf{d}\tilde{p}} \cdot \mathbf{K}^{\tilde{p}\mathbf{d}} \tag{4.128}$$

where $\overline{K} = (K^{\tilde{p}\tilde{J}})^{-1}K^{\tilde{J}\tilde{J}}(K^{\tilde{J}\tilde{p}})^{-1}$.

4.4 Numerical examples

The forthcoming section is dedicated to the resolution of several numerical simulations involving compressible and incompressible hyperelastic materials in order to test the capabilities in damage modelling of the Q1Q1, Q1Q1E24 and Q1Q1P0 schemes.

The first of the experiments consists of a validation example employing a nearly-incompressible block under a compressive state, adopted from the work in Section 4.2 of Reese et al. [320]. Furthermore, this instance does not consider the gradient-enhanced CDM approach, and we aim to validate the mixed u-p-J formulation.

The next numerical experiment consists of a series of parametric studies carried out on a plate with a hole to study the influence of the regularisation properties of the model. We adopt the example in Section 5.2 of the work by Waffenschmidt et al. [111], replicating the dependence on the mechanical behavior for the compressible samples and analyzing the performance for nearly incompressible materials.

The last experiment aims to simulate a challenging example for a large deformation problem vulnerable to both shear and volumetric pathologies. For this, based on the proposed example in Section 4.1 in the work by Reese et al. [320], we propose a notched cylindrical shell subjected to an extreme bending load.

4.4.1 Benchmark example - Nearly incompressible block under compression

Taken from Reese et al. [320], it is modelled the quarter of a cubic brick (symmetry conditions are considered on the planes X and Y) with 1,000
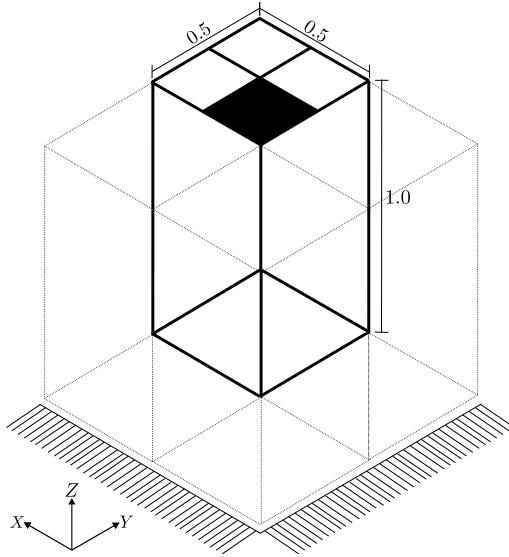
Figure 54: Scheme for the block under compressive load modelled. The area in bold corresponds with the region where the compressive u_z is applied on. The dimensions are given in mm. Dotted lines correspond to the regions generated by symmetry.

brick elements under a compressive status, i.e., a displacement of $u_z = -0.5$ mm is applied on the area in bold of Fig. 54, where it is observed the bottommost surface as fixed in the cubical structure. Mimicking the properties of the reference example, we consider a Shear Modulus $G = 80.194$ MPa and a Poisson ratio $\nu = 0.49999$, thus considering a nearly incompressible material. Since this model aims to analyze the potentiality of the three proposed approaches in modelling this highly deformed state, avoiding locking pathologies, no damage interaction is proposed within this example. This means that we model Q1, Q1E24 and Q1P0 FE formulations.

In order to quantify the differences in performance among the three proposed frameworks, it is plotted the deformed configuration (Fig. 55) and the reaction force-displacement curves (Fig. 56) for every algorithm. Emphasizing the main advantages and disadvantages of them, it is item-
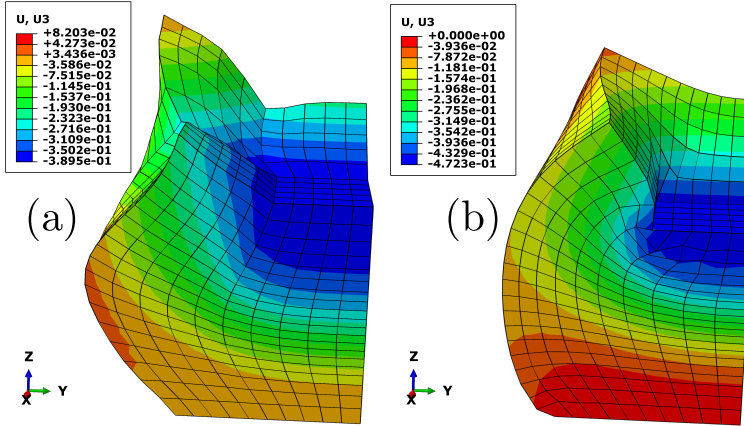
Figure 55: Isommetric view from the deformed of the benchmark problem run with (a) `Q1` and (b) `Q1P0` algorithms, respectively.

ized for every technique, in particular, the results obtained, also comparing with one sample run with ABAQUS C3D8H hybrid elements:

- **Q1 formulation**: It can be envisaged that the performance here is not satisfying overall. Starting from the left image in Fig. 55, it is observed a high deformation on the outer surfaces of the block due to the over-stiffening of the structure caused by the large deformation process. Confirming this aspect with the force-displacement curve in Fig. 56, it is deduced that the main reason for this behavior is the volumetric locking that exhibits the solid by employing this algorithm, whose force-displacement curve highly overestimates the mechanical answer of the material, compared with the result obtained for the ABAQUS hybrid element.

- **Q1E24 Formulation**: There were not found any results for this scheme due to convergence issues since the correction that the EAS method does on the global N-R scheme is considerably high in order to find an approximate solution for the software under incompressibility. To tackle this issue, it was tried to run the simulation
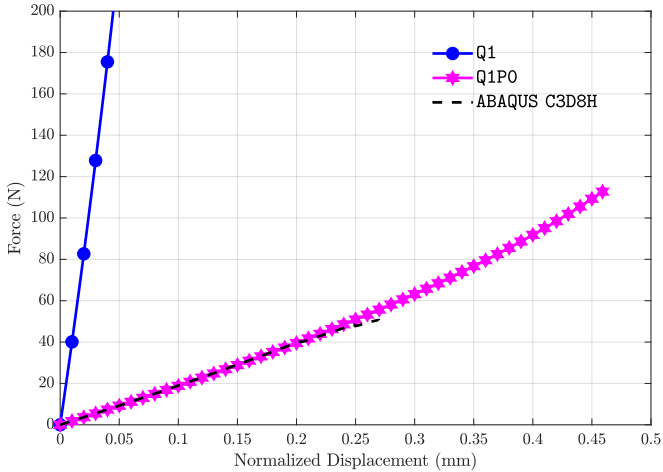
Figure 56: Reaction force-displacement curves for the benchmark problem run with `Q1` and `Q1P0` algorithms compared with `ABAQUS C3D8H` elements, respectively.

with different element sizes, but without any improvement in the convergence of the scheme, displaying the unsuitability of this formulation to model incompressible specimens.

- **Q1P0 Formulation**: Without any doubt, the mixed u-p-J FE formulation proves to comply as the most robust performance in order to avoid the volumetric locking pathology. Its deformed configuration (right image, Fig. 55) captures the performance of a material under a compressive load in the center of the upper surface. Furthermore, it shows a strong correlation in the mechanical behavior (see Fig. 56), yet considerably better performance in terms of convergence, with the hybrid two-field `ABAQUS` elements, as this latter shows, through mid-testing, premature failure (Fig. 57). These results exhibit that the mixed u-p-J formulation has a worth-mentioning potentiality in quantifying the response of the incompressible sample and, at the same time, avoiding locking patholo-

145
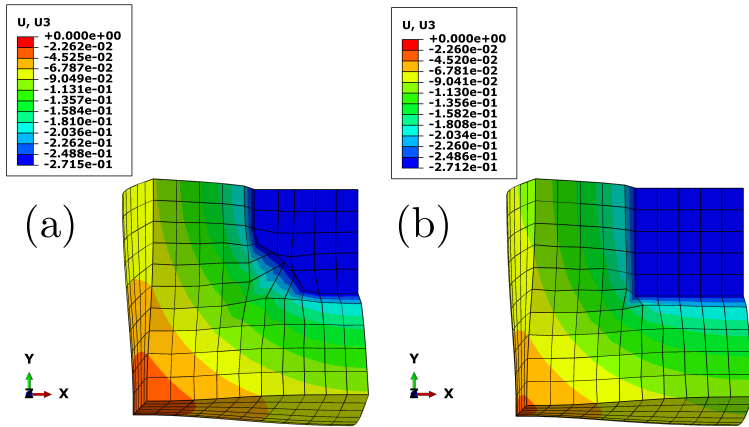
Figure 57: Top view from the deformed of the benchmark problem run with (a) `ABAQUS C3D8H` and (b) `Q1P0` algorithms, respectively. See in (a) the unphysical behavior in the `ABAQUS` element.

gies, unlike `Q1` discretization and the `ABAQUS C3D8H` element, thus providing its solid capability in modelling nearly incompressible hyperelastic materials under large deformation states.

4.4.2 Plate with a hole - compressible hyperelastic material

Test details

As for the second numerical example, the deformation of a plate with a hole under a traction load is considered. The geometry and boundary conditions for the full model are exhibited in Fig. 58. In line with the previous example, considering symmetry conditions on both X, Y, and Z planes, specifically, only one eighth part of the sample is modelled for the sake of reducing the computational cost. The bottommost surface is considered to be clamped, whereas the topmost one is subjected to a vertical displacement u_z up until the post-peak behavior of the sample. The material properties employed for this approach are plotted in Table
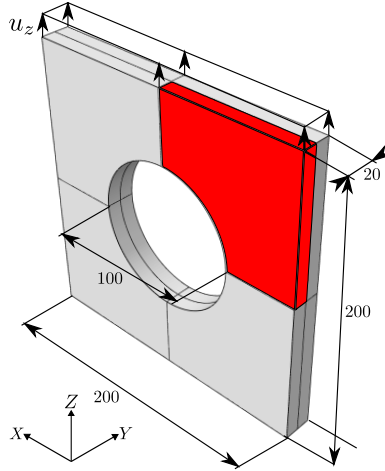
Figure 58: Geometry and BCs for the plate with a hole. The dimensions are in mm, and only an eighth of the sample is modelled, the region in red.

Table 23: Material properties employed for the plate with a hole.

G (MPa)	K (MPa)	β_d (MPa^{-1})	γ_d
176.2	734.2	1000	1

23 for a Poisson ratio of $\nu = 0.25$. Among the parameters for the non-local damage:

- The β_d parameter has been calibrated in order to ensure a solid convergence for the local N-R monolithic scheme.

- γ_d has the value of the unity to guarantee a non-local damage framework if $c_d > 0$.

These compressible specimens will be run with algorithms encompassing both Q1Q1 and Q1Q1E24 formulations, not considering Q1Q1P0 as they are not suitable to model problems with $\nu < 0.45$. The parameters related to the damage law i.e., both the damage threshold κ_d and the saturation η_d magnitudes along with the non-local regularisation parameter c_d will be modified throughout these series of tests where the

147

first aim will be the validation of the proposed CDM models with the constitutive behavior of the elements from ABAQUS, on one side, and the failure pattern, on the other. Once they are verified, a quick study to test the mesh objectivity is carried out. We study the mechanical performance of the sample with different discretizations. Subsequently, with the most suitable algorithm and in line with [111], we will run several numerical examples changing c_d in order to test the influence of this magnitude in the compressible specimens.

Quantitative and qualitative validation

First, in order to validate the CDM approaches, it is required to verify the mechanical performance of the proposed algorithms with the theoretical ABAQUS elements. To establish a quantitative standpoint with them, the damage parameters of both κ_d and η_d have to be adjusted properly. According to [111], higher values of η_d do accelerate the onset of the damage process, being deviated from the purely neo-Hookean response plotted by the ABAQUS elements at lower stages of the corresponding loading process. On the contrary, really small saturation parameters approximate the curve to the theory but do delay the damage onset considerably after the deformation range considered. In addition to this, by considering a damage threshold of $\kappa_d = 0$ MPa, i.e., the damage onset happens upon loading, not augmenting the stiffness of the mechanical curve. Thus, we have fixed a value of $\eta_d = 0.1$ MPa^{-1} and $\kappa_d = 0$ MPa for these validation tests with a discretization of 9,525 hexahedral elements and a regularisation parameter of $c_d = 1000$ MPa^{-1}mm^2. Having conducted all of them successfully, we display the reaction force-displacement curves for the samples with standard CDM (Q1Q1) and CDM + EAS (Q1Q1E24) formulations in comparison with the purely neo-Hookean response run with ABAQUS C3D8 elements and it is envisaged the same performance for each scheme, see Fig. 59. Both formulations display a solid equivalence with the ABAQUS elements' curve on the first stages of testing and, upon damage propagation, they both manage to capture the post-peak softening of the curve. Even though we get the same quantitative results, the most advantageous model for these configurations without shear

148
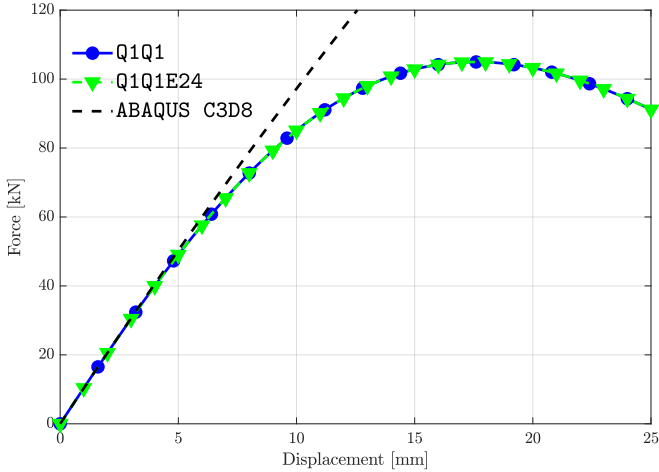
Figure 59: Reaction force-displacement curves for the compressible plate with a hole for the validation probes conducted with a standard CDM (`Q1Q1`) and CDM + EAS (`Q1Q1E24`), respectively, compared with `ABAQUS` `C3D8` elements. Employed non-local damage parameters encompass: $\eta_d = 0.1\,\text{MPa}^{-1}$, $\kappa_d = 0\,\text{MPa}$ and $c_d = 1000\,\text{MPa}^{-1}\text{mm}^2$.

locking is the `Q1Q1` formulation, as the CDM + EAS model (`Q1Q1E24`) considers incompatible strains, which add up computational cost to the problem.

Having tested the verification quantitatively with `ABAQUS` samples, for a qualitative address, we plot the evolution of crack propagation for three different displacements, see Figs. 60(a)-60(c). In order to get a clear damage pattern, we have calibrated the non-local damage parameters for a final failure around $u_z = 20$ mm, employing for this: $\eta_d = 1\,\text{MPa}^{-1}$, $\kappa_d = 1\,\text{MPa}$ and $c_d = 500\,\text{MPa}^{-1}\text{mm}^2$. Following an expected behavior, the first isocontour at Fig. 60(a) reveals its nucleation near the notched region (a stress concentrator) only to be continued by a mode I propagation, see Fig. 60(b). In the end, it is observed that upon reaching the end of the width of the plate, the crack grows in the direction of the height of the specimen, see Fig. 60(c). Therefore, with these micrographs
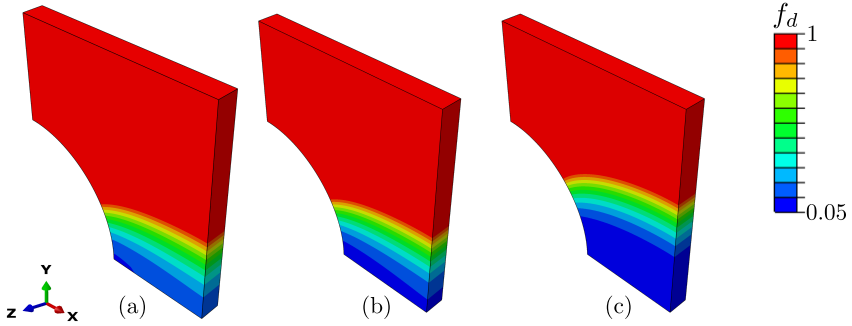
Figure 60: Isocontour plots for the damage function f_d of a plate with a hole plotting the crack pattern for several displacements: (a) $u_z = 7.32$ mm, (b) $u_z = 8.42$ mm and (c) $u_z = 19.10$ mm. Employed non-local damage parameters encompass: $\eta_d = 1$ MPa^{-1}, $\kappa_d = 1$ MPa and $c_d = 500$ MPa^{-1}mm^2

of a foreseeable failure pattern, we can also verify the proposed CDM approach qualitatively, obtaining similar results for Q1Q1 and Q1Q1E24 formulations. It is important to highlight that a tolerance in the function $f_d < 0.05$ has been established to avoid ill-conditioning in the equations; the reader is referred to [111] for further information on this aspect.

Mesh objectivity

Another required calibration for CDM approaches concerns the verification for mesh independence, as the condition for mesh-objectivity is associated with the damage evolution being independent of the discretisation for high enough regularisation parameters c_d. Therefore, we run a test for three different hexahedral meshes employing the non-local damage properties exhibited in Table 24: one coarse (810 elements), one medium-sized (9,595 elements) and one considerably refined (75,360 elements) mesh. The three simulations are compared by plotting the damage function isocontour f_d for a displacement of $u_z = 8$ mm in Fig. 61, and they turn out to be practically identical for both formulations Q1Q1 and Q1Q1E24, thus providing that the dissipation energy is independent of the size of the element.

Table 24: Non-local damage properties employed for the tests for verification of mesh objectivity.

c_d (MPa^{-1}mm^2)	κ_d (MPa)	η_d (MPa^{-1})
500	1	1
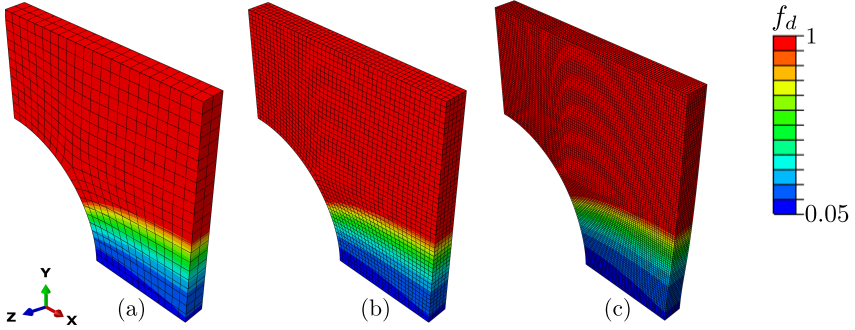
Figure 61: Isocontour plots for the damage function f_d comparing a (a) coarse, (b) medium-sized, and (c) fine discretisation of a plate with a hole with a fixed displacement of $u_z = 8$ mm. The obtained results are similar for Q1Q1 and Q1Q1E24 formulations.

Parametric study on the regularisation parameter c_d

Having proven that the results reasonably adjust to the theoretical non-linear elastic behavior and that the proposed frameworks are mesh-objective, with the medium-sized discretisation (9,525 hexahedral elements), we have carried out a parametric analysis by leaving the degree of regularisation parameter c_d as a free variable. As in [111], in order to quantify the dependence of the mechanical behavior to this parameter, a parametric analysis is made with a range of $c_d = \{10, 100, 500, 1000\}$ MPa^{-1}mm^2 for the three different proposed formulations with the mechanical properties in Table 23. The employed parameters for the degradation law are $\eta_d = 1$ MPa^{-1} and $\kappa_d = 1$ MPa.

Looking to prove the validity of both standard CDM and CDM + EAS approach to model this specimen, we exhibit the reaction-force displacement curves for values of $c_d = 1000$ MPa^{-1}mm^2, $c_d = 500$ MPa^{-1}mm^2
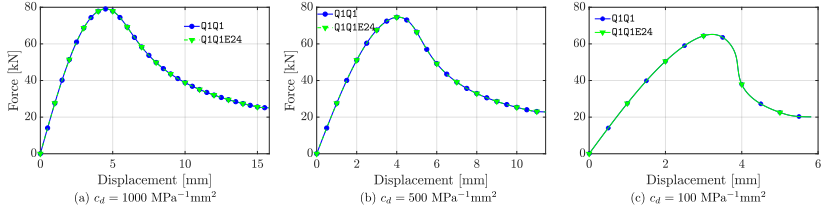
Figure 62: Reaction force-displacement curves for the compressible plate with a hole problem comparing standard CDM (`Q1Q1`) and CDM + EAS (`Q1Q1E24`) formulations varying c_d.
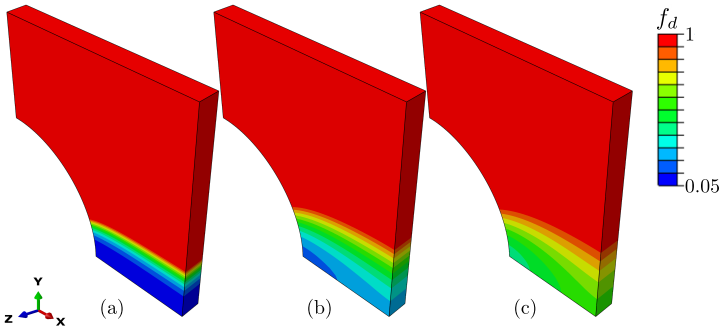
Figure 63: Isocontour plots for the damage function f_d for plates with a hole with different regularisation parameter c_d at $u_z = 6.5$ mm. In here: (a) $c_d = 100$ MPa^{-1}mm^2, (b) $c_d = 500$ MPa^{-1}mm^2 and (c) $c_d = 1000$ MPa^{-1}mm^2.

and $c_d = 100$ MPa^{-1}mm^2 plotted in Figs. 62(a)-62(c), respectively. In fact, we can establish that both the standard CDM approach referred to as the current configuration, and the combined CDM + EAS approach, referred to as the reference configuration, do manage to capture the full mechanical behavior of the specimen until the failure of the sample, even though this last one requires more computational cost due to the calculation of the incompatible strains.

Staying with the most computationally efficient formulation i.e., `Q1Q1`, we realize a further comparison for the results with different c_d in Figs. 63-64. For the first series of images (Fig. 63), we have plotted several contour plots of the damage function f_d for different c_d and, nucleating from
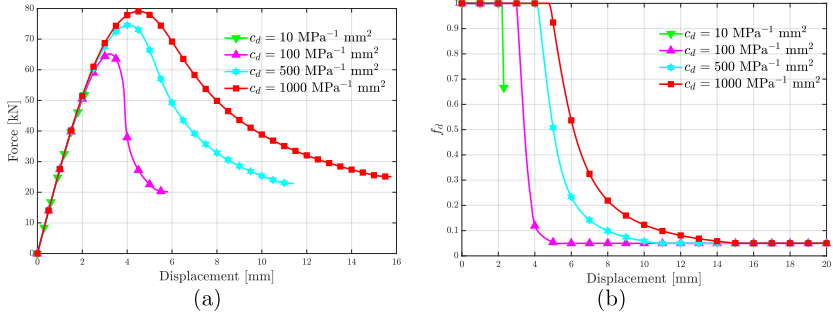
Figure 64: (a) Reaction force-displacement and (b) minimum value of f_d curves for the plate with a hole problem run with a standard spatial CDM approach for different cases of $c_d = \{10, 100, 500, 1000\}$ MPa^{-1}mm^2.

the notched region, the major difference is observed in the range of the affected region, being the gradient wider for lower values of c_d, and the minimum value of f_d, decreasing as the c_d parameter is augmented. Furthermore, by plotting the reaction force-displacement (Fig. 64(a)) and the minimum f_d value (Fig. 64(b)), we basically obtain that the failure of the specimen gets delayed by just increasing this regularisation parameter, increasing the maximum force and softening the collapse of the graph, being this result in line with what is exhibited in [111]. In addition to this, it is worth noting that the result for $c_d = 10$ MPa^{-1}mm^2 falls short of reaching the peak behavior of the curve as it displays convergence issues, being this due that the mesh is not discretised enough for this low value of c_d, meaning that for this mesh, the limit value of c_d for total convergence falls between this value and $c_d = 100$ MPa^{-1}mm^2.

4.4.3 Plate with a hole - quasi-incompressible hyperelastic material

Test details

The next numerical example that we have considered is an incompressible version of the previous example, i.e., we increase the value of the bulk modulus K up to a value $\sim 10^7$ MPa, associated with a Poisson ra-

tio of $\nu = 0.49999$. With only that subtle change, the same experiments that were carried out for the Section 4.4.3 are repeated, keeping the same geometry as Fig. 58 and the same material properties plotted in Table 23, except the aforementioned K.

For these series of tests, the schemes employed consist in both Q1Q1 and Q1Q1P0 formulations, as the EAS technique has been checked not to be appropriate to model nearly incompressible specimens (see Section 4.4.1). In line with the previous section for compressible samples (Section 4.4.2), we start with the verification of the CDM models by comparing them with the hybrid elements from ABAQUS. Upon verification, we repeat the parametric analysis of the previous sections where we study the dependence of c_d on the mechanical behavior of the now nearly incompressible specimens, where we end up elucidating which is the better formulation to conduct these numerical experiments.

Quantitative and qualitative validation

For the comparison between the standard (Q1Q1) and the three-field mixed CDM formulations (Q1Q1P0) with the referential two-field ABAQUS C3D8H element, required for computations with $\nu > 0.475$, we plot the force-displacement curves in Fig. 65 for the conducted experiments run with damage properties: $\eta_d = 0.5 \, \text{MPa}^{-1}$, $\kappa_d = 0 \, \text{MPa}$ and $c_d = 1000 \text{MPa}^{-1}\text{mm}^2$. It is observed that although the graphs manage to capture the post-peak behavior, it is the Q1Q1P0 formulation the better performer for this problem, as at the early stages of the curve, it solidly matches the ABAQUS referential graph, unlike the Q1Q1 which slightly overestimates the trajectory due to volumetric locking pathologies caused by $\nu \sim 0.5$. The failure pattern for both formulations resembles the one plotted in Fig. 60, which are not shown here for the sake of brevity but do provide the qualitative check for the testing of nearly incompressible specimens.

Parametric analysis on the regularisation parameter c_d

Considering the parameters for the degradation law to be $\eta_d = 1 \, \text{MPa}^{-1}$ and $\kappa_d = 1 \, \text{MPa}$, we perform the tests of extensive pulling for the nearly
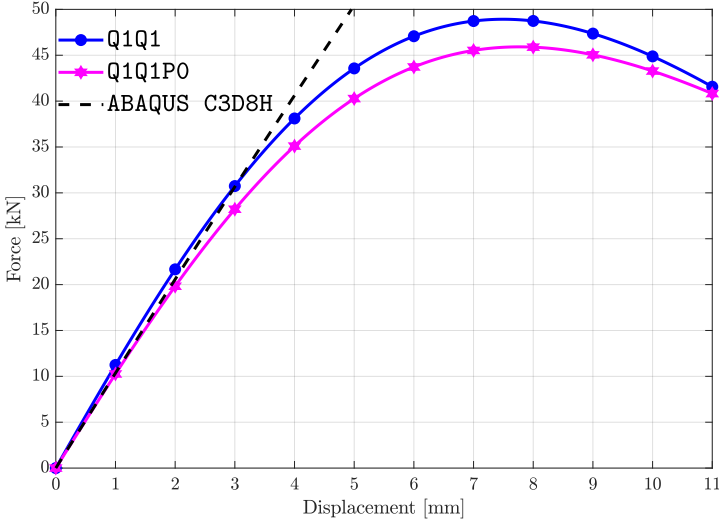
Figure 65: Reaction force-displacement curves for the nearly incompressible plate with a hole for the validation probes conducted with a standard (`Q1Q1`) and the mixed u-p-J CDM formulations (`Q1Q1P0`), respectively, compared with `ABAQUS C3D8H` elements. Employed non-local damage parameters encompass: $\eta_d = 0.5 \,\text{MPa}^{-1}$, $\kappa_d = 0\,\text{MPa}$ and $c_d = 1000\,\text{MPa}^{-1}\text{mm}^2$.

incompressible plates, conducting a parametric analysis in a range of $c_d = \{10, 100, 500, 1000\}\,\text{MPa}^{-1}\text{mm}^2$. The results for both `Q1Q1` and `Q1Q1P0` formulations at (a) $c_d = 1000\,\text{MPa}^{-1}\text{mm}^2$, (b) $c_d = 500\,\text{MPa}^{-1}\text{mm}^2$ and (c) $c_d = 100\,\text{MPa}^{-1}\text{mm}^2$ are represented in Fig. 66. According to what was aforementioned in the validation examples, standard CDM formulation provides an over-stiffened curve due to the incompressibility of the model that leads to the phenomenon of volumetric locking that does not address this scheme. For that reason, the most robust scheme to model this problem is deduced to be the Jacobian-pressure mixed framework. Even though that `Q1Q1` theory provides a more prolonged softening of the curve during crack propagation, it is deduced from these results that the `Q1Q1P0` element covers the volumetric locking pathology by considering both pressure and dilatation terms, see Eqs. (4.127)-

155
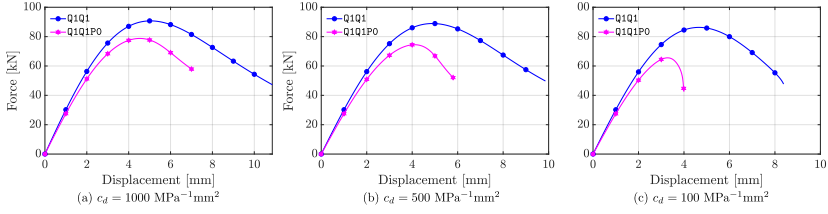
Figure 66: Reaction force-displacement curves for the compressible plate with a hole problem comparing standard CDM (Q1Q1) and mixed u-p-J + CDM (Q1Q1P0) formulations varying c_d.
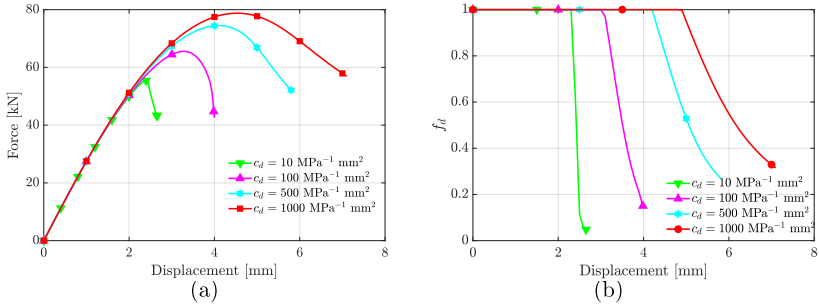
Figure 67: (a) Reaction force-displacement and (b) minimum value of f_d-displacement curves for the nearly incompressible plate with a hole problem run with a mixed u-p-J CDM (Q1Q1P0) approach for different cases of $c_d = \{10, 100, 500, 1000\}$ MPa^{-1}mm^2.

(4.128), and that is proven by the reduction in the stiffness of the constitutive response of the sample shown in all the examples in Fig. 66.

Subsequently, it is exhibited the (a) reaction force-displacement curves and (b) the evolution of the minimum value of the damage function f_d associated with every displacement in Fig. 67, where is envisaged an overall analogous pattern than the one plotted for the compressible cases conducted with the standard CDM formulation, see Fig. 64, i.e., both peak force and displacement are augmented monotonically with the increase of the regularisation parameter. In addition to this, the slope for the decrease of the minimum value of f_d for changing displacements is

also increased. Although not so robust on convergence as the `Q1Q1` formulation for compressible specimens, with the quantitative and qualitative results provided in this section, `Q1Q1P0` has provided to be a more solid formulation to model these incompressible experiments.

4.4.4 Cylindrical shell under a bending load - compressible materials

Test details

With the objective of addressing the further potential of the present frameworks (so far, the `Q1Q1` and the `Q1Q1E24` formulations have been proven to model large deformation problems for compressible specimens, while the `Q1Q1P0` scheme have performed very robustly with volumetric locking pathologies in an incompressible problem), we aim to model the challenging problem of a cylindrical shell under a bending load. For this, a notched cylindrical specimen with the geometry and BCs exhibited in Fig. 68 is analyzed under extreme bending conditions to capture the capabilities of both EAS and three-field mixed FE formulations in modelling this large deformation problem prone to show locking pathologies. In line with the previous example, we have modelled both series of compressible and nearly incompressible material specimens. The notch has been considered to induce the onset of damage happening in the center.

Starting with the former cases, we have carried out several experiments with the material and damage properties plotted at Table 25 for specimens with a discretisation of 12,328 hexahedral elements. In order to avoid boundary effects, for the extremities of the cylindrical shell (where the fixed and the displacement conditions are applied), the damage saturation parameter η_d has been increased, so the damage pattern is not affected by these phenomena. The final deformed configuration with the mesh for the bending experiments is displayed in Fig. 69, exhibiting the amount of deformation in the sample experiments.

In line with the plate tests, we have started this subsection by simulating this experiment to establish a comparison between the formulations suitable for compressible specimens modelling, i.e., `Q1Q1` and `Q1Q1E24`,
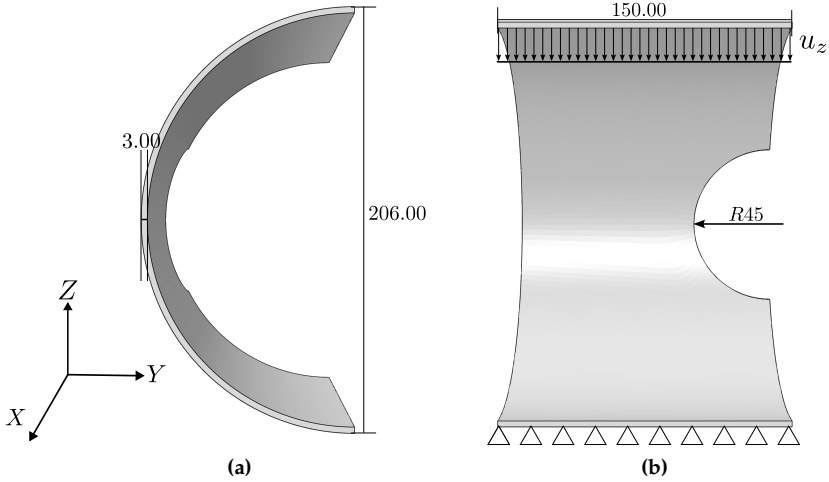
Figure 68: Geometry with boundary conditions and dimensions in mm with (a) profile and (b) frontal view.

Table 25: Material and fixed damage properties employed for the cylindrical shells.

G (MPa)	K (MPa)	β_d (MPa^{-1})	γ_d	κ_d (MPa)	c_d (MPa^{-1} mm^{-2})
40000	66667	1000	1	0	500

with the referential ABAQUS elements, additionally presenting the failure isocontour for this problem. Subsequently, a parametric analysis on addressing the damage saturation parameter η_d is carried out, where the main pursued aim is the comparison of both algorithms in displaying their potentiality to model this large deformation complex problem.

Quantitative and qualitative validation

To compare with a referential standpoint, we have conducted several tests with a damage saturation parameter $\eta_d = 0.1$ MPa^{-1} with Q1Q1 and Q1Q1E24 formulations, along with the theoretical ABAQUS elements
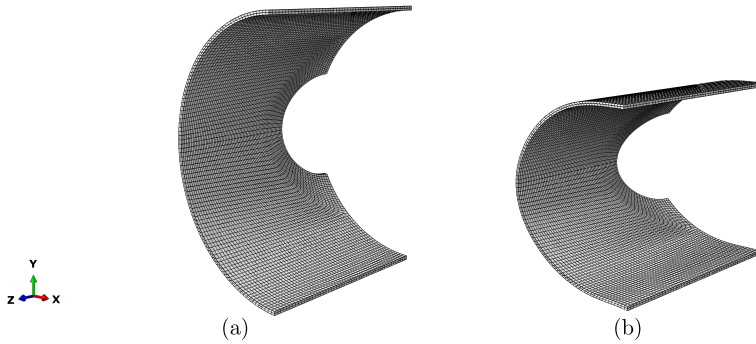
Figure 69: Cylindrical shell: undeformed and deformed configuration.

with (`C3D8I`) and without (`C3D8`) incompatible deformation modes.

The displayed force-displacement curves, exhibited in Fig. 70, do reveal that the standard CDM approach (`Q1Q1`) follows the trajectory described by the `ABAQUS C3D8` element in the early stages. However, both elements are affected by parasitic shear locking, showing an over-stiffening of the curve caused by this pathology. Concerning the CDM + EAS formulation (`Q1Q1E24`), it is observed a solid correlation between the mechanical performance of this element with the curve of the `ABAQUS C3D8I` element, which is the one required to model this kind of problems prone to locking, i.e., under bending loads. It is worth highlighting that the match of these two curves is not perfect due to the EAS contribution being regularised via f_d, affecting the terms in Eqs. (4.105)-(4.108), as these are multiplied by the function damage, meaning that the correction gets reduced as soon as the material gets damaged, being the EAS contribution eliminated upon total damage. This regularisation is done in order to avoid the convergence issues that arise by using this formulation, as the correction in the stiffness curve grows considerably throughout the experiment. However, this aspect does not undermine the potentiality of the CDM + EAS approach to model compressible materials under shear locking, as the correlation is very robust with the referential curve.

The damage evolution of the specimen during the test is displayed in Figs. 71(a)-71(c). The crack onset occurs in the center of the width of
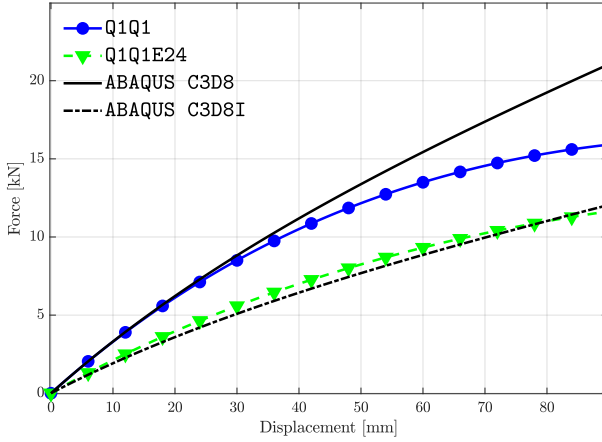
Figure 70: Load-displacement curves for the cylindrical shell test conducted for Q1Q1 and Q1Q1E24 formulations compared with the ABAQUS theoretical curves with (C3D8I) and without considering incompatible modes (C3D8). The employed saturation parameter has been $\eta_d = 0.1 \text{ MPa}^{-1}$.

the sample (Fig. 71(a)), being propagated afterwards in Mode I in the Z-direction, first to the extremities of the specimen (Fig. 71(b)) and then, in the direction towards the notch (Fig. 71(c)). These isocontours have been obtained from a test conducted by employing the for the Q1Q1E24 formulation with a damage saturation parameter of $\eta_d = 0.5 \text{ MPa}^{-1}$, demonstrating to be consistent with analysis until failure of a specimen under extreme bending conditions.

Parametric analysis on the saturation parameter η_d

This section is focused on analyzing the role of the saturation parameter in the mechanical performance of the specimen. Varying this η_d parameter in a range of $\eta_d = \{0.5, 1, 2\} \text{ MPa}^{-1}$ for both the Q1Q1 and the Q1Q1E24 formulations. The differences among them for $\eta_d = 0.5 \text{ MPa}^{-1}$ (Fig. 72(a)), $\eta_d = 1 \text{ MPa}^{-1}$ (Fig. 72(b)) and $\eta_d = 2 \text{ MPa}^{-1}$ (Fig. 72(c)) are exhibited by means of the force-displacement curves, where
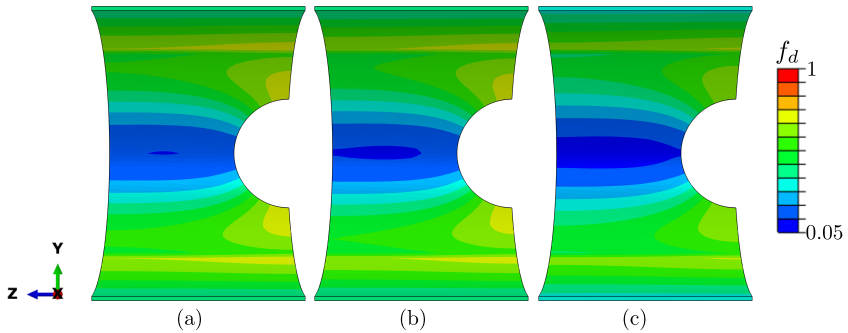
Figure 71: Isocontour plots for the evolution of the damage function f_d for a compressible cylindrical shell under bending load. It has been employed a saturation parameter for damage of $\eta_d = 0.5$ MPa^{-1} for the Q1Q1E24 formulation.
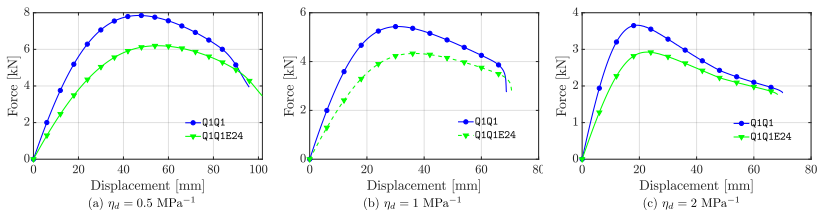
Figure 72: Load-displacement curves for compressible cylindrical shells under bending load conducted with formulations for standard CDM (Q1Q1) and the CDM + EAS (Q1Q1E24) approaches, respectively with different η_d.

it can be deduced that the CDM + EAS formulation (Q1Q1E24) is verified to be a very effective tool to conduct the problem of extreme bending for compressible notched cylindrical shells, as is the better performer to tackle the shear locking phenomenon that causes an over-stiffening in the curves.

Intending to plot the η_d dependence on one single image, we put together the reaction force-displacement curves for the Q1Q1E24 formulation, along with the evolution of the minimum value of f_d in Figs. 73(a) and 73(b). It is deduced that the role of this parameter is similar to the one of c_d, progressively delaying the failure of the sample along with
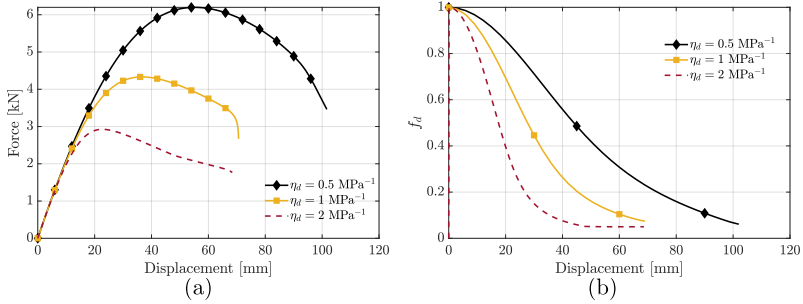
Figure 73: (a) Reaction force-displacement and (b) minimum value of f_d-displacement curves for compressible cylindrical shells under bending loads conducted with a CDM + EAS (`Q1Q1E24`) approach for different cases of $\eta_d = \{0.5, 1, 2\}$ MPa^{-1}.

augmenting the peak force when this saturation magnitude is increased.

4.4.5 Cylindrical shell under a bending load - incompressible materials

Test details

The last series of experiments consists of the modelling of the previous examples in Section 4.4.4, now for nearly incompressible specimens, carried out in order to test the validity of the mixed u-p-J CDM formulation (`Q1Q1P0`) to model this tricky problem. Employing the same configuration as in Figs. 68(a)-68(b) and the same properties as in Table 25, but this time, changing the bulk modulus K up to a value of $\sim 10^7$ MPa, associated with an established Poisson ratio of $\nu = 0.49999$ and in line with what has been realized in the previous sections, we start by comparing the results of `Q1Q1` and `Q1Q1P0` schemes with the same tests conducted with `ABAQUS` elements. Once this demonstration has been fulfilled, a last parametric analysis addressing the dependence on the saturation parameter η_d is conducted.
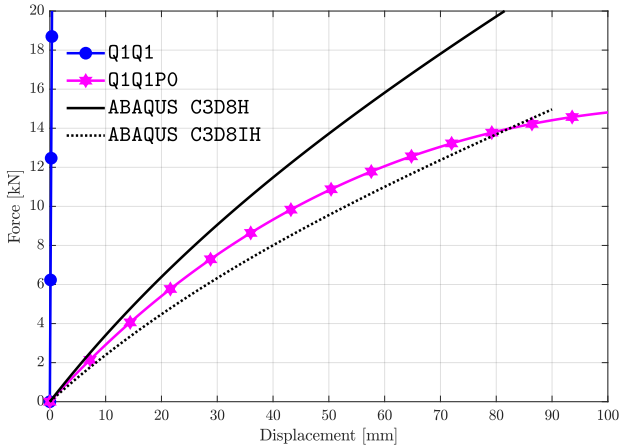
Figure 74: Load-displacement curves for the incompressible cylindrical shell test conducted for `Q1Q1` and `Q1Q1P0` formulations compared with the `ABAQUS` hybrid theoretical curves with (`C3D8IH`) and without considering incompatible modes (`C3D8H`). The employed saturation parameter has been $\eta_d = 0.1\,\mathrm{MPa}^{-1}$.

Quantitative and qualitative validation

Displaying the same failure pattern as the one exhibited for compressible specimens (see Fig. 70, which is not included here for the sake of brevity), we focus now on a quantitative viewpoint with the two proposed formulations along with the referential `ABAQUS` elements, see Fig. 74. First, we can definitely conclude that `Q1Q1` formulation is not suitable to model this problem as both the volumetric and shear locking cause a very abrupt rise of the load of the sample, justifying the invalidation of this formulation.

Concerning the mixed u-p-J CDM (`Q1Q1P0`) formulation, it can be observed that it covers the volumetric locking solidly, as the curve is below the one related to the behavior of the hybrid element `ABAQUS C3D8H`. However, it falls short of covering the shear locking, as this graph is considerably less compliant than the hybrid `ABAQUS` element that considers incompatible deformation modes (`C3D8IH`), i.e., the one required to run
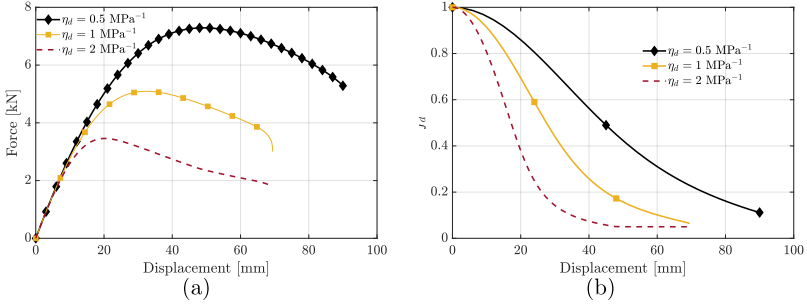
Figure 75: (a) Reaction force-displacement and (b) minimum value of f_d-displacement curves for incompressible cylindrical shells under bending loads conducted with a mixed u-p-J CDM (`Q1Q1P0`) approach for different cases of $\eta_d = \{0.5, 1, 2\}$MPa^{-1}.

this simulation. Observing how robustly did perform the `Q1Q1E24` formulation in the compressible cases analyzed in Section 4.4.4, the extension of the present formulation of `Q1Q1P0` to `Q1Q1P0E24` is proposed to model these specimens and will be addressed in future work.

Parametric analysis on the saturation parameter

Considering the same range for the damage saturation parameter $\eta_d = \{0.5, 1, 2\}$ MPa^{-1}, at last, we plot in a single curve all the load-displacement curves for different η_d conducted by `Q1Q1P0` (see Fig. 75(a)), along with the minimum value of the degradation law f_d for every displacement (see Fig. 75(b)). What is envisaged in this last representation is an analogy of what was exhibited before for the compressible specimens: with the reduction in η_d, the softening in the quantitative response associated with the mechanical performance is delayed. Therefore, even though there is no solid correlation with the theory, the `Q1Q1P0` formulation has proven to be the one among the three conducted schemes to proportionate conclusive results for the large deformation bending tests applied on cylindrical shells.

Chapter 5

Swelling on thermoresponsive hydrogels

The last coupled problem, encompassing the large deformation theory presented in Chapter 3 along the mixed element technology developed in Chapter 4, to be addressed within this thesis concerns the modelling of thermoresponsive hydrogels. As discussed in the introductory Chapter, these materials can be classified within two categories depending on their swelling behavior: some of them exhibit an upper critical swelling temperature (UCST), meaning that the extent of swelling is increased above this point; whereas there are others that display a lower critical swelling temperature (LCST), as the degree of swelling is augmented when they are cooled down that point.

Thermoresponsive hydrogels find their scope of application in biomedical uses, as their high water content and possible control over the swelling kinetics makes them very attractive. Several of them such as chitosan and cellulose-derivatives have shown their potential on the tissue engineering field as a role for cell carriers. Hydrogels based on poly(N-isopropylacrylamide) (pNiPAAm) can be useful for applications such as drug delivery systems, where the physiological temperature plays an

important role in stimulating and activating the liberation of the fluid content within the hydrogel onto the physiological environment. An extended literature review for the applications of the thermoresponsive hydrogels can be found in [176].

Within the field of Computational Mechanics, several proposed FEM simulations of the equilibrium swelling of gels have been developed so far. The variational formulation derived by Kang and Huang [321] and the pivotal works by Chester and Anand, first for isothermal problems [322], and, then for, thermoresponsive hydrogels [7] establish the landmark in considering the problem of hydrogel swelling as a coupled deformation-diffusion problem. This means that, for the numerical modeling of a thermo-responsive model, both the displacement, the chemical field and the temperature require separate approximation as the primary field driving forces of the chemo-thermomechanical problem [8, 323]. The short time behavior of hydrogels make them resemble a fully incompressible or quasi-compressible hyperelastic materials, as the diffusion of water occurs for a limited time. To tackle this, mixed methods are adopted to solve volumetric locking issues related to the incompressible limit, such as the F-bar method developed by [324] that is implemented in the referential work from Chester and Anand [7]. However, in addition to this, it is important to highlight that this independent discretization of primary fields carries the risk of the appearance of spurious oscillations in the solution of the chemical potential field, thus resulting in a violation of the Ladyzshenskaya-Babuška-Brezzi (LBB) conditions, also called the inf-sup condition [325, 326]. Therefore, in order to properly simulate hydrogel formulations with a fully coupled chemo-thermo-mechanical nature, the modelling of the continuous mass flow requires the usage of higher order interpolations to satisfy the balance of mass and, at the same time, fulfill the LBB conditions. Some examples of higher order stable mixed FE applied for hydrogels can be observed in the mixed element formulation based on the Enhanced Assumed Strain technique developed by Krischok and Linder [327] or in the multiple works carried out by Bouklas et al. [328, 329] where it is employed a Taylor-Hood element with quadratic displacement and a linear chemical

potential field.

Based on the previous arguments, a mixed displacement-pressure-temperature Finite Element to tackle such problem by employing a quadratic interpolation for the displacements and a linear interpolation for the pressure and the temperature is proposed. Such implementation is adopted in order to overcome volumetric locking issues, characteristic of the computational modelling for incompressible materials, while, at the same time, fulfilling LBB conditions in order to guarantee uniqueness of the solution for a saddle point problem. Throughout the content that encloses this Chapter, the proposed formulation will be validated by its capture of the LCST (also, extendable to UCST hydrogels) behavior that the thermoresponsive hydrogels display and subsequently, it will be used from a quantitative standpoint to address its robustness and accuracy in capturing experimental tests with different thermo-chemo-mechanical test conditions. The extension that this Chapter aims to represent within the Computational Mechanics field is to be the first inf-sup stable formulation for modelling of thermoresponsive hydrogels, while at the same time, proving its accuracy with the physics by resolving and capturing some representative experimental problems.

Chapter 5 is structured as follows. The basic concepts where we introduce the three-field problem and the local equations is included in Section 5.1. Section 5.2 displays the development of the balance of energy to shape the constitutive behavior and the material model and the derivation of the variational formulation to introduce the weak form of the problem. Further insight on the implementation is provided in Section 5.3, where the `Q2Q1Q1` element is presented to model the problem of thermoresponsive hydrogels. Within the range of covered examples, Section 5.4 is aimed to simulate simple numerical examples to verify the proposed numerical formulation and Section 5.5 compares the experimental results of free swelling for PNIPAAm hydrogels changing its crosslinking density with the numerical ones obtained out from the proposed variational formulation. At last, Section 5.6 provides the future implementation for fracture on these type of material among with its first preliminary results.

Nomenclature

$\mathbf{x}$	Arbitrary spatial point on the current configuration
$\boldsymbol{\varphi}$	Nonlinear deformation map
$\mathbf{X}$	Arbitrary spatial point on the initial configuration
t	Current time
Ω_0	Body domain in the initial configuration
$\mathbb{R}^n$	Collection of ordered lists of n real numbers
Ω	Body domain in the current configuration
$\partial\Omega_0$	Boundary of the solid in the initial configuration
$\partial\Omega$	Boundary of the solid in the current configuration
$\mathbf{u}$	Displacement field
$\mathbf{e}$	Unit vector field
$\mathbf{F}$	Deformation gradient
$\nabla_{\mathbf{X}}$	Gradient operator in the reference configuration
$\nabla_{\mathbf{x}}$	Gradient operator in the current configuration
$\mathbf{1}$	Second order identity tensor
$\mathbf{H}$	Material displacement gradient tensor
J	Jacobian, determinant of $\mathbf{F}$
det	Determinant operator
C	Concentration field
μ	Chemical potential
T	Temperature
$\mathbf{C}$	Right Cauchy-Green tensor
$\mathbf{b}$	Left Cauchy-Green tensor
$\partial\Omega_u$	Boundary region with a Dirichlet condition of prescribed displacements
$\partial\Omega_t$	Boundary region with a Neumann condition of prescribed tractions
$\mathbf{t}$	Cauchy traction vector
$\mathbf{n}$	Current normal outward vector
$\boldsymbol{\sigma}$	Cauchy's stress tensor
$\mathbf{P}$	First Piola-Kirchhoff stress tensor
$\mathbf{T}$	First Piola-Kirchhoff traction vector
$\mathbf{N}$	Initial normal outward vector
$\mathrm{d}A$	Differential of nominal area
$\mathrm{d}a$	Differential of engineering area
$\mathbf{S}$	Second Piola-Kirchhoff stress tensor
$\partial\Omega_p$	Boundary region with a Dirichlet condition of prescribed chemical potential
$\partial\Omega_j$	Boundary region with a Neumann condition of prescribed species flux
$\mathbf{j}$	Spatial species out-flux
j_n	Scalar mass flux
$\mathbf{j_R}$	Material species out-flux
$\mathbf{M}$	Mobility tensor
$\partial\Omega_T$	Boundary region with a Dirichlet condition of prescribed temperatures
$\partial\Omega_q$	Boundary region with a Neumann condition of prescribed heat flux
$\mathbf{q}$	Spatial heat flux
q_n	Scalar heat flux
$\mathbf{Q}$	Material heat flux
$\mathbf{K}$	Thermal conductivity tensor for the initial configuration
ρ_0	Density field in the reference configuration
ρ	Density field in the current configuration

Nomenclature

$\dot{[\bullet]}$	First time derivative operator
$\nabla \cdot [\bullet]$	Divergence operator
$\overline{\mathbf{F}}^V$	Prescribed body forces
η_R	Entropy
$\bar{p}$	Fluid pressure
ν	Number of solvent molecules per volume reference unit
e	Specific internal energy
R	External heat supply
$\mathcal{D}$	Dissipation energy
$\mathcal{D}_{loc}$	Dissipation due to local actions
$\mathcal{D}_{cond}$	Dissipation due to heat conduction
$\mathcal{D}_{diff}$	Dissipation due to mass diffusion
Ψ	Free energy density
$\partial_{[\bullet]}$	Partial derivative operator
c_p	Heat capacity
H	Latent heat
$\mathbf{Z}$	Second-order tensor associated with displacement-temperature coupling
Y	Scalar term associated with mass transport-temperature coupling
Π	Total potential of the system
Π_{int}	Internal potential of the system
Π_{ext}	External potential of the system
Δt	Time interval
t_{n+1}	Time in increment $n+1$. This subscript is used in other variables with the same meaning
t_n	Time in increment n. This subscript is used in other variables with the same meaning
ϕ	Convex dissipation potential
p	Interpolated fluid pressure
$\mathbb{p}$	Gradient of the fluid pressure in the current configuration
Ψ_{elas}	Free energy density term associated to elastic stretching
I_n	N-th invariant
N	Number of chains segments per unit reference volume
k_B	Boltzmann constant
Ψ_{mix}	Free energy density term associated to polymer mixing
χ	Interaction parameter
χ_L	Lower limit for the interaction parameter
χ_T	Upper limit for the interaction parameter
T_c	Critical temperature
Δ	Width of the transition in critical temperature in swelling behavior
Ψ_{temp}	Free energy density term associated to thermal contribution
T_0	Reference temperature
α	Coefficient for thermal expansion
κ	Bulk modulus
$\mathbb{C}$	Local tangent operator in the reference configuration
D	Diffusivity coefficient
$\mathbb{P}$	Nominal gradient of the fluid pressure
$\mathbf{k}$	Thermal conductivity tensor for the current configuration
$\mathbf{F_0}$	Deformation gradient associated with the pre-swelling state
$\mathbf{F}^*$	Deformation gradient associated with the deformation in the dry state
λ_0	Isotropic stretches

Nomenclature

$\mathrm{D}\,[\bullet]$	Gateaux derivative operator
$\mathbf{N_d}$	Shape functions for displacements
$\mathbf{d}$	Nodal displacements
$\mathbf{N_p}$	Shape functions for fluid pressure
$\hat{\mathbf{p}}$	Nodal fluid pressure
$\mathbf{N_T}$	Shape functions for temperature
$\hat{\mathbf{T}}$	Nodal temperature
$\boldsymbol{\xi}$	Parametric coordinate system
ξ, η, ζ	Parametric coordinates
$\mathbf{J_e}$	Material Jacobian matrix for the isoparametric transformation
$\mathbf{j_e}$	Spatial Jacobian matrix for the isoparametric transformation
$\mathbf{R^d}$	Residual force associated with the nodal displacements
$\mathbf{R}^{\hat{p}}$	Residual force associated with the nodal fluid pressure $\hat{p}$
$\mathbf{R}^{\hat{T}}$	Residual force associated with the nodal fluid pressure $\hat{T}$
$\hat{L}$	Operador for Lie derivative
$\mathbf{K^{dd}}$	Displacement-displacement Jacobian term for global N-R scheme
$\mathbf{K}^{\mathbf{d}\hat{p}}$	Displacement-pressure Jacobian term for global N-R scheme
$\mathbf{K}^{\mathbf{d}\hat{T}}$	Displacement-temperature Jacobian term for global N-R scheme
$\mathbf{K}^{\hat{p}\mathbf{d}}$	Pressure-displacement Jacobian term for global N-R scheme
$\mathbf{K}^{\hat{p}\hat{p}}$	Pressure-pressure Jacobian term for global N-R scheme
$\mathbf{K}^{\hat{p}\hat{T}}$	Pressure-temperature Jacobian term for global N-R scheme
$\mathbf{K}^{\hat{T}\mathbf{d}}$	Temperature-displacement Jacobian term for global N-R scheme
$\mathbf{K}^{\hat{T}\hat{p}}$	Temperature-pressure Jacobian term for global N-R scheme
$\mathbf{K}^{\hat{T}\hat{T}}$	Temperature-temperature Jacobian term for global N-R scheme
p_0	Initial fluid pressure
$\mathbf{\Delta d}$	Nodal displacement variation
$\mathbf{\Delta\hat{p}}$	Nodal fluid pressure variation
$\mathbf{\Delta\hat{T}}$	Nodal temperature variation
L	Square length
h_e	Element size
G	Shear modulus
$\mathcal{G}_C$	Critical energy release rate
$\mathfrak{d}$	Phase-field parameter
ℓ	Length scale parameter
γ_l	Crack surface density function
w	Geometric crack function
υ	Coefficient in geometric crack function
c_w	Scaling parameter in crack density functional
$g(\mathfrak{d})$	Degradation function
$\mathcal{K}$	Residual stiffness
$\mathcal{H}$	History field variable
$\mathbf{R}^{\hat{\mathfrak{d}}}$	Residual force associated with the nodal phase-field parameter $\hat{\mathfrak{d}}$
$\mathbf{N_{\mathfrak{d}}}$	Shape functions for phase-field parameter
$\hat{\mathfrak{d}}$	Nodal phase-field values
$\Delta\hat{\mathfrak{d}}$	Nodal phase-field variation
$\mathbf{K}^{\hat{\mathfrak{d}}\hat{\mathfrak{d}}}$	PF-PF Jacobian term for global N-R scheme

Nomenclature

u_y Vertical displacement

5.1 Theoretical formulation

This section outlines the fundamental concepts and definitions of the current numerical framework addressing the use of a mixed displacement-mass diffusion-temperature formulation for the large deformation analysis of diffusion in solids. The ultimate goal is to specialize this formulaton for the analysis of thermoresponsive hydrogels.

5.1.1 Basic definitions

Complying with standard nonlinear Continuum Mechanics, let an arbitrary spatial point defined in the current configuration be defined as $\mathbf{x} := \boldsymbol{\varphi}(\mathbf{X}, t)$, being $\boldsymbol{\varphi}(\mathbf{X}, t)$ the nonlinear deformation map which projects the material points $\mathbf{X}$ from the initial configuration $\Omega_0 \subset \mathbb{R}^n$ to the current one $\Omega \subset \mathbb{R}^n$. This transformation is plotted in Fig. 26. The transformation of the differential line elements throughout the deformation process is characterized by the deformation gradient $\mathbf{F}$ whose definition is introduced in Eq. (3.1).

The boundary-value problem for the modelling of this problem is treated as a coupled four-field problem, characterized by the displacement field $\mathbf{u}$, the concentration field C, the chemical potential μ and the temperature T. Adopting the approach of Miehe et al. at [330], the transition of the Cahn-Hilliard-type to standard Fickian-type is made for the degeneration of the definition of the chemical potential. As the chemical potential drives the flux $\dot{C}$ of the species, this transformation is made by optimizing the chemical potential with respect to the concentration, performing its local update at the integration points, defining a condensed incremental potential that only depends on the displacement field, the chemical potential and the temperature. The reader is referred to [330] for further information regarding this operation.

Following the scheme plotted in Fig. 76, we make a brief description
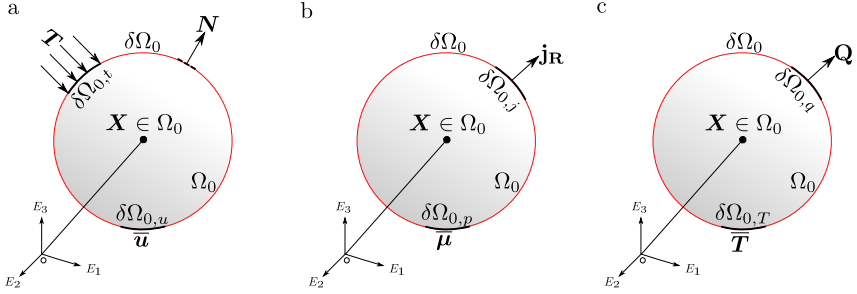
Figure 76: Schematic representation of the three-field boundary value problem: (a) displacement, (b) mass transport, and (c) temperature.

of the problem for both three fields. For the mechanical perspective, in order to track the motion of the body and the deformation of the non-linear problem, the reader is referred to Section 3.1.1 (Eqs. (3.1)-(3.6) and Fig. 26) for the sake of brevity.

Moving to the diffusion problem, again, this can be divided into two sub-domains: one where the chemical potential μ is prescribed through a Dirichlet BC, $\partial\Omega_{0,p}$; and $\partial\Omega_{0,j}$, where we perform an analogous operation to the nominal tractions theorem (Eq. (3.4) to obtain the referential species out-flux $\mathbf{j}_R$, that depends linearly on the outward normal $\mathbf{N}$

$$J_n = \mathbf{j}_R \cdot \mathbf{N} \tag{5.1}$$

where J_n denote the scalar mass flux. The spatial species flux $\mathbf{j}$ relies on a analogous relation to the Cauchy stress, therefore its definition yields as

$$\mathbf{j} = J^{-1}\mathbf{F} \cdot \mathbf{j_R} \tag{5.2}$$

Assuming that the fluid transport follows a Darcy-type relation, we can establish a relation to obtain the nominal fluid flux $\mathbf{j_R}$ from the product of the mobility tensor $\mathbf{M}$ with the variation of the chemical potential

$$\mathbf{j_R} = -\mathbf{M} \cdot \nabla_{\mathbf{X}}\mu \tag{5.3}$$

172

The remaining unknown in this three-field mixed-formulation problem is the thermal field and also can be traced into two sub-domains: the region $\partial\Omega_{0,T}$, where the temperature T is prescribed using a Dirichlet BC, and the region $\partial\Omega_{0,q}$, where the evolution of the heat flux $\mathbf{Q}$ follows the same structure as mass flux, considering the Stokes flux with the following definition.

$$Q_n = \mathbf{Q} \cdot \mathbf{N} \tag{5.4}$$

where Q_n denotes the scalar heat flux for the problem. Then, the spatial heat flux $\mathbf{q}$ can be obtained as

$$\mathbf{q} = J^{-1}\mathbf{F} \cdot \mathbf{Q} \tag{5.5}$$

And then, by establishing a Fourier-type relation, we trace the value of $\mathbf{Q}$ by the product of the thermal conductivity tensor $\mathbf{K}$ with the variation of the temperature

$$\mathbf{Q} = -\mathbf{K} \cdot \nabla_{\mathbf{X}}T \tag{5.6}$$

5.1.2 Local equations and balance of energy

The general equations that drive the coupled deformation-diffusion-temperature problem are presented in their local form for the reference configuration. Before the balance of total energy, we need to define some local balances for every field. The conservation of solid mass reads as:

$$\rho_0 = J\rho \tag{5.7}$$

where $\rho(\mathbf{x}, t)$ and $\rho_0(\mathbf{X})$ are the density fields in the current and reference configuration, respectively. From here, we can obtain the material version of the balance of linear momentum, which adopts the form of:

$$\rho_0\ddot{\boldsymbol{\varphi}} = \nabla_{\mathbf{X}} \cdot \mathbf{P} + \rho_0\overline{\mathbf{F}}^V = \mathbf{0} \tag{5.8}$$

where the operator $\nabla \cdot [\bullet]$ denotes the divergence operator; and $\overline{\mathbf{F}}^V$ identifies the prescribed body forces per unit of reference volume.

For the mass transport, we consider c as the concentration of fluid content inside the hydrogel, i.e. the number of moles of fluid molecules absorbed by the polymer network, reckoned per unit volume of the dry reference configuration. For this field, the balance species content equation takes the local form of

$$\dot{C} = -\nabla_{\mathbf{X}} \cdot \mathbf{j_R} \tag{5.9}$$

For the balance in the temperature, we refer to the entropy variable η_R by introducing the second law of thermodynamics as

$$\dot{\eta}_R \geq -\nabla_{\mathbf{X}} \cdot \left[\frac{\mathbf{Q}}{T} \right] + \frac{Q_n}{T} \tag{5.10}$$

All this information that we collect for the three-field formulation global balance is plotted in the box below as a summary in the reference configuration for this quasi-static problem

1. Balance of solid mass:	$\rho_0 = J\rho$	(5.11)
2. Balance of species content:	$\dot{C} = -\nabla_{\mathbf{X}} \cdot \mathbf{j_R}$	(5.12)
3. Balance of entropy:	$\dot{\eta}_R \geq -\nabla_{\mathbf{X}} \cdot \left[\dfrac{\mathbf{Q}}{T} \right] + \dfrac{R}{T}$	(5.13)
4. Balance of linear momentum:	$\rho_0 \ddot{\boldsymbol{\varphi}} = \nabla_{\mathbf{X}} \cdot \mathbf{P} + \rho_0 \overline{\mathbf{F}}^V = \mathbf{0}$	(5.14)
5. Constitutive stress:	$\mathbf{S} = 2\partial_{\mathbf{C}} \Psi(\mathbf{C}, C, \nabla_{\mathbf{X}} C, T)$	(5.15)
6. Chemical potential:	$\mu = \partial_C \Psi(\mathbf{C}, C, \nabla_{\mathbf{X}} C, T)$	(5.16)
7. Entropy:	$\eta_R = -\partial_T \Psi(\mathbf{C}, C, \nabla_{\mathbf{X}} C, T)$	(5.17)
8. Fourier's Law:	$\mathbf{Q} = -\mathbf{K} \cdot \nabla_{\mathbf{X}} T$	(5.18)
9. Darcy's Law:	$\mathbf{j_R} = -\mathbf{M} \cdot \nabla_{\mathbf{X}} \mu$	(5.19)

With these expressions at hand in the box, we can express the local form of the balance of the total energy like

$$\rho_0 \dot{e} = \mathbf{S} : \nabla_{\mathbf{X}} \mathbf{u} - \nabla_{\mathbf{X}} \cdot \mathbf{Q} + R + \mu \dot{C} - \mathbf{j_R} \cdot \nabla_{\mathbf{X}} \mu \tag{5.20}$$

where e is the specific internal energy, being given his temporal rate by the magnitude $\dot{e}$ and R the external heat supply per unit reference vol-

ume. The expression can be developed upon considering the second law of Thermodynamics, where the equation for the evolution of the entropy (Eq. (5.17)) can be extended as:

$$\nabla_{\mathbf{X}} \cdot \left[\frac{\mathbf{Q}}{T}\right] + \frac{R}{T} = \frac{1}{T}(R - \nabla_{\mathbf{X}} \cdot \mathbf{Q}) + \frac{1}{T^2}\mathbf{Q} \cdot \nabla_{\mathbf{X}}T \qquad (5.21)$$

Then, by considering Legendre transformation: $\Psi = e - T\eta_R$, and Eq. (5.20), we reach the expression for the Clausius-Duhem inequality that guarantees the local consistency of the equation, where the local dissipated global potential $\mathcal{D}$ is expressed as:

$$\mathcal{D} = \mathbf{S} : \nabla_{\mathbf{X}}\mathbf{u} + \mu\dot{C} - \mathbf{j_R} \cdot \nabla_{\mathbf{X}}\mu - \frac{1}{T}\mathbf{Q} \cdot \nabla_{\mathbf{X}}T - \rho_0(\dot{\Psi} + \dot{T}\eta_R) \geq 0 \quad (5.22)$$

Note that $\mathcal{D}$ can be split into three parts due to: (i) local actions $\mathcal{D}_{loc}$, (ii) heat conduction $\mathcal{D}_{cond}$ and (ii) mass diffusion $\mathcal{D}_{dif}$:

$$\mathcal{D}_{loc} = \mathbf{S} : \nabla_{\mathbf{X}}\mathbf{u} + \mu\dot{C} - \rho_0(\dot{\Psi} + \dot{T}\eta_R) \geq 0 \qquad (5.23)$$

$$\mathcal{D}_{cond} = -\frac{1}{T}\mathbf{Q} \cdot \nabla_{\mathbf{X}}T \geq 0 \qquad (5.24)$$

$$\mathcal{D}_{diff} = -\mathbf{j_R} \cdot \nabla_{\mathbf{X}}\mu \geq 0 \qquad (5.25)$$

where Eq. (5.23) is known as the Clausius-Planck inequality, Eq. (5.24) stands for the Fourier inequality and Eq. (5.25) is the Darcy inequality.

5.2 Constitutive formulation

5.2.1 Objective free energy function

The constitutive equations are constructed such that the dissipation condition recalled in Eq. (5.22) is a priori satisfied for all processes. The free energy is thought to depend on the primary variables and their gradients

$$\Psi = \tilde{\Psi}(\mathbf{C}, \nabla_{\mathbf{X}}\mathbf{C}, C, \nabla_{\mathbf{X}}C, T, \nabla_{\mathbf{X}}T) \qquad (5.26)$$

at $\mathbf{X} \in \Omega_0$. With a view towards determining the restrictions imposed by the local free energy imbalance (Eq. (5.22)), the temporal rate of Eq. (5.26) can be expressed as:

$$\dot{\Psi} = \frac{\partial \Psi}{\partial \mathbf{C}} : \dot{\mathbf{C}} + \frac{\partial \Psi}{\partial C} : \dot{C} + \frac{\partial \Psi}{\partial T} : \dot{T} \tag{5.27}$$

Substituting Eq. (5.27) into Eq. (5.22) and considering $\partial_{[\bullet]}$ as the partial derivative operator, we obtain

$$\mathcal{D} = \left[\frac{1}{2}\boldsymbol{S} - \partial_{\mathbf{C}}\Psi\right] : \dot{\mathbf{C}} + [\eta_R - \partial_T \Psi] : \dot{T} + [\mu - \partial_C \Psi] : \dot{C} - \mathbf{j_R} \cdot \nabla_{\mathbf{X}}\mu - \frac{1}{T}\mathbf{Q} \cdot \nabla_{\mathbf{X}}T \geq 0 \tag{5.28}$$

This inequality should hold for all values of $\mathbf{C}$, C, T, $\nabla_{\mathbf{X}}\mu$ and $\nabla_{\mathbf{X}}T$. Since there is a linear dependence on the temporal rates of deformation gradient, concentration and temperature, the terms between brackets must vanish, thus reaching the expressions for Eqs. (5.15)-(5.17). In addition to this, the expressions for the constraint on the fluid-flux inequality render

$$\mathbf{Q} \cdot \nabla_{\mathbf{X}}T < 0 \qquad \text{when} \quad \nabla_{\mathbf{X}}T \neq 0 \tag{5.29}$$

and the heat-flux inequality

$$\mathbf{j_R} \cdot \nabla_{\mathbf{X}}\mu < 0 \qquad \text{when} \quad \nabla_{\mathbf{X}}\mu \neq 0 \tag{5.30}$$

Further derivations can be done by considering the previous Legendre transformation carried out, where we reached the balance for the entropy

$$\rho_0 \dot{\eta}_R T = R - \nabla_{\mathbf{X}} \cdot \mathbf{Q} - \mathbf{j_R} \cdot \nabla_{\mathbf{X}}\mu \tag{5.31}$$

From the previous result, the rate of entropy yields

$$\rho_0 \dot{\eta}_R = \rho_0 [-\partial_{TT}^2 \Psi \dot{T} - \frac{1}{2}\partial_{T\mathbf{C}}^2 \Psi : \dot{\mathbf{C}} - \partial_{TC}^2 \Psi \dot{C}] \tag{5.32}$$

The left-hand side of Eq. (5.31) may be expressed as

$$\rho_0\dot{\eta}_R T = c_p \dot{T} - \rho_0 H \tag{5.33}$$

where the heat capacity c_p and the latent heat H are expressed as

$$c_p := -\rho_0 T \partial_{TT}^2 \Psi; \qquad H = \frac{1}{2}T\partial_{T\mathbf{C}}^2\Psi : \dot{\mathbf{C}} + T\partial_{TC}^2\Psi \dot{C} = \frac{1}{2}T\mathbf{Z} : \dot{\mathbf{C}} + TY\dot{C} \tag{5.34}$$

where $\mathbf{Z}$ and Y relate to the second-order tensor and the scalar term associated with the coupling of the motion and the mass transport in the Helmholtz free energy function, respectively. From here, the final expression for the transient heat equation reads

$$c_p\dot{T} := \rho_0 H + R - \nabla_{\mathbf{X}} \cdot \mathbf{Q} - \mathbf{j_R} \cdot \nabla_{\mathbf{X}}\mu \tag{5.35}$$

5.2.2 Material model

The total potential of the system can be divided into internal Π_{int} and external contributions Π_{ext}

$$\Pi(\mathbf{u}, C, \mu, T, t) = \Pi_{\text{int}}(\mathbf{u}, C, \mu, T, t) - \Pi_{\text{ext}}(\mathbf{u}, C, \mu, T, t) \tag{5.36}$$

Complying with the formulation proposed by Miehe and coauthors [330] for Cahn-Hilliard diffusion-type problems, the proposed potential in Eq. (5.36) can be adjusted for a displacement-potential-density-temperature problem or gradient type-dissipative solids at a time interval $\Delta t = t_{n+1} - t_n$.

$$\Pi(\mathbf{C}, \mu, \nabla_{\mathbf{X}}\mu, C, \nabla_{\mathbf{X}}C, T, \nabla_{\mathbf{X}}T) = \Psi(\mathbf{C}, T, \nabla_{\mathbf{X}}T) - \mu(C_{n+1} - C_n) \\ - \Delta t\, \phi(\nabla_{\mathbf{X}}\mu, \mathbf{F}_n, C_n) + \rho_0\dot{\eta}_R T \tag{5.37}$$

where ϕ is the convex dissipation potential. From here on, the subscript n refers to magnitudes of the previous increment.

Since the proposed framework is dedicated for hydrogels, the attention is driven to materials with a quasi-incompressible behavior. To account for this, they are considered to change their volume only due to

swelling when absorbing solvents, since both the cross-linked polymer network and the solvent molecules are incompressible [331, 7]. Thus, this constraint is introduced as follows:

$$J = 1 + \nu C \tag{5.38}$$

Considering the incremental character of the proposed model, this constraint is modified to:

$$J_{n+1} - J_n = \nu(C_{n+1} - C_n) \tag{5.39}$$

With the consideration of Eq. (5.39), the potential proposed in Eq. (5.37) can be postulated by reducing the set of arguments

$$\Pi(\mathbf{C}, p, T, \nabla_{\mathbf{X}} T) = \Psi(\mathbf{C}, T, \nabla_{\mathbf{X}} T) - p(J_{n+1} - J_n) - \Delta t\, \phi(\mathbb{p}, \mathbf{F}_n, T) + \rho_0 \dot{\eta}_R T \tag{5.40}$$

where p is the fluid pressure in the form of a scaled chemical potential. This magnitude and its gradient are introduced as follows:

$$p = \frac{\mu}{\nu}; \qquad \mathbb{p} = -\nabla_{\mathbf{x}} p \tag{5.41}$$

where ν is the number of solvent molecules per volume reference unit. Expressing the approach on the current configuration, based on the formulation proposed by Flory and Rehner [332], we postulate the existence of a local free energy function Ψ, which has three contributions, one associated to the stretching of the polymer Ψ_{elas}, which reads

$$\Psi_{\text{elas}}(\mathbf{C}) = \frac{1}{2} N k_B T (I_1 - 3 - 2 \log J) \tag{5.42}$$

and another one related to the mixing of the polymer and solvent molecules Ψ_{mix} [333, 334]

$$\Psi_{\text{mix}}(\mathbf{C}, T) = \frac{k_B T}{\nu} \left[(J - 1) \log\left(\frac{J - 1}{J}\right) + \frac{\chi(T)(J - 1)}{J} \right] \tag{5.43}$$

where I_1 is the first invariant of the left Cauchy-Green tensor that is defined as $I_1 := \text{tr}[\mathbf{C}]$, N is the number of chains segments per unit reference volume, k_B is the Boltzmann constant and $\chi(T)$ refers to a material-specific and temperature-dependent interaction parameter. $\chi(T)$ will follow the following expression proposed for LCST hydrogels in [7]:

$$\chi(T) = \frac{1}{2}(\chi_L + \chi_H) - \frac{1}{2}(\chi_L - \chi_H)\tanh\left(\frac{T - T_c}{\Delta}\right) \tag{5.44}$$

whereas, for UCST, the formula reads as

$$\chi(T) = \frac{1}{2}(\chi_L + \chi_H) + \frac{1}{2}(\chi_L - \chi_H)\tanh\left(\frac{T - T_c}{\Delta}\right) \tag{5.45}$$

where χ_L and χ_H are the lower and upper limits of the parameter; T_c, the LCST/UCST temperature and Δ is the width of temperature in the transition from both limits.

The final contribution of the energy is composed of the thermal contribution Ψ_{temp}, which follows a classical thermoelastic contribution

$$\Psi_{\text{temp}}(\mathbf{C}, T) = c_p\left[(T - T_0) - T\log\frac{T}{T_0}\right] - 3\kappa\alpha(T - T_0)\log J \tag{5.46}$$

where α stands for the coefficient for thermal expansion, κ is the bulk modulus of the gel and T_0 denotes the reference temperature.

The sum of these three contributions makes the expression for the local free energy function, for the term in Eq. (5.40)

$$\Psi = \Psi_{\text{elas}} + \Psi_{\text{mix}} + \Psi_{\text{temp}} \tag{5.47}$$

Then, from Eq. (5.47), the second Piola-Kirchhoff stress tensor $\mathbf{S}$ can be computed as follows

$$\mathbf{S} := 2\frac{\partial \Psi(\mathbf{C})}{\partial \mathbf{C}} - pJ\mathbf{C}^{-1}$$

$$= Nk_BT(\mathbf{1} - \mathbf{C}^{-1}) + \left[\frac{k_BT}{\nu}\left[\log\left(\frac{J-1}{J}\right) + \frac{1}{J} + \frac{\chi(T)}{J^2}\right]\right. \quad (5.48)$$

$$\left. - 3\kappa\alpha(T - T_0) - p\right]J\mathbf{C}^{-1}$$

In order to implement the present model into the general purpose FE software, ABAQUS via the UEL subroutine, the local tangent operator $\mathbb{C}$ is required to compute the Jacobians. $\mathbb{C}$ can be obtained directly from the derivation of Eq. (5.48) :

$$\mathbb{C} = 2\frac{\partial \mathbf{S}}{\partial \mathbf{C}} = 2J\left[Nk_BT - \frac{k_BT}{\nu}\left[\log\left(\frac{J-1}{J}\right) + \frac{1}{J} + \frac{\chi}{J^2}\right] + 3\kappa\alpha(T - T_0) + p\right]\mathbf{I}_{\mathbf{C}}^{\text{sym}}$$

$$- \left[\frac{k_BT}{\nu}\left[\frac{\chi}{J^2} - \log\left(\frac{J-1}{J}\right) - \frac{1}{J-1}\right] + 3\kappa\alpha(T - T_0) + p\right]J\mathbf{C}^{-1} \otimes \mathbf{C}^{-1}$$

$$(5.49)$$

where $\mathbf{I}_{\mathbf{C}}^{\text{sym}}$ is a fourth-order tensor that has the following expression: $\mathbf{I}_{\mathbf{C}}^{\text{sym}} := [\mathbf{C}^{-1}\overline{\otimes}\mathbf{C}^{-1} + \mathbf{C}^{-1}\underline{\otimes}\mathbf{C}^{-1}]/2 = [C_{ik}^{-1}C_{jl}^{-1} + C_{il}^{-1}C_{jk}^{-1}]/2$, which employs the non-standard dyadic products.

For the mass diffussion problem, a dissipation function ϕ is postulated

$$\phi(\mathbb{p}, T) = \frac{1}{2}(J_n - 1)\frac{D\nu}{k_BT}|\mathbb{p}|^2 \quad (5.50)$$

where D is the diffusivity coefficient. From this expression, one can derive it to obtain the true flux vector $\mathbf{j} = J_n^{-1}\frac{\partial \phi}{\partial \mathbb{p}}$, that reads as

$$\mathbf{j} = \frac{(J_n - 1)}{J_n}\frac{D\nu}{k_BT}\mathbb{p} \quad (5.51)$$

by doing the pull-back operation, we obtain the nominal mass flux $\mathbf{j_R}$

$$\mathbf{j_R} = \mathbf{F}_n^{-\mathsf{T}}(J_n - 1)\frac{D\nu}{k_BT}\mathbf{F}_n^{-\mathsf{T}} \cdot \mathbb{P} \quad (5.52)$$

where $\mathbb{P} = -\nabla_{\mathbf{X}} p$.

Finally, in order to account for the thermal problem, the entropy η_R is obtained from the derivation of the temperature on Eq. (5.46)

$$
\begin{aligned}
\eta_R = -\frac{\partial \Psi}{\partial T} &= 3\kappa\alpha \log J + c_p \log \frac{T}{T_0} - \frac{1}{2} N k_B (I_1 - 3 - 2\log J) \\
&- \frac{k_B}{\nu} \left[(J-1)\log\left(\frac{J-1}{J}\right) + \frac{\chi(T)(J-1)}{J} \right] - \frac{(J-1)k_B T}{J\nu} \frac{\partial \chi(T)}{\partial T}
\end{aligned}
\tag{5.53}
$$

Therefore, from this expression, the latent heat H reads

$$
H = \frac{1}{2} T \partial^2_{TC} \Psi : \dot{\mathbf{C}} + T \partial^2_{TC} \Psi : \dot{C} = \frac{1}{2} \mathbf{Z} : \dot{\mathbf{C}}
\tag{5.54}
$$

Obtained from Eq. (5.53), only the deformation problem contributes to the latent heat, therefore $Y = 0$ and $\mathbf{Z}$ (i.e., the structural heating for hydrogels) is easily obtained by deriving Eq. (5.48) with respect to the temperature. To conclude with the temperature part, we define the expression for the current heat flux which reads

$$
\mathbf{q} = -\mathbf{k} \cdot \nabla_{\mathbf{x}} T
\tag{5.55}
$$

and by performing the pullback operation we reach the nominal flux $\mathbf{Q}$

$$
\mathbf{Q} = -J\mathbf{F}^{-1} \cdot \mathbf{k} \cdot \mathbf{F}^{-\mathrm{T}} \cdot \nabla_{\mathbf{X}} T
\tag{5.56}
$$

where $\mathbf{k}$ is the thermal conductivity tensor for the current configuration. It is a common practice to not identify reference coordinates with a gel in the dry state, due to Ψ_{mix} being singular for $J = 1$ [335]. Therefore, there is a huge convenience in establishing a pre-swollen state in chemo-mechanical equilibrium as a referential state [336], which results in the decomposition for the deformation gradient as

$$
\mathbf{F}^* = \mathbf{F} \cdot \mathbf{F_0}
\tag{5.57}
$$

where $\mathbf{F_0} = \lambda_0 \mathbf{1}$ refers to the pre-swollen contribution dependent on the initial isotropic stretches λ_0 and $\mathbf{F}^*$ is the deformation gradient of the

total deformation referred to the dry state, establishing the superscript $[\bullet]^*$ to refer to all the magnitudes in this state. By defining this reference point, the expression for the potential is now expressed as

$$\Pi^*(\mathbf{C}^*, p, \mathbf{F_0}, \mathbf{F_n}, T, \Delta T) = \frac{1}{J_0}\Psi(\mathbf{C}^*, T, \Delta T) - p(J_{n+1} - J_n)$$
$$- \frac{1}{J_0}\Delta t \,\phi(\mathbf{F_0}, \mathbf{F_n}, T) + \rho_0 \dot{\eta}_R T \tag{5.58}$$

resulting this in an alternative representation for the stress, the mass flux and the displacement-temperature coupling tensor

$$\mathbf{S} := \frac{Nk_B T}{J_0}(J_0^{2/3}\mathbf{1} - \mathbf{C}^{-1})$$
$$+ \left[\frac{k_B T}{\nu}\left[\log\left(\frac{JJ_0 - 1}{JJ_0}\right) + \frac{1}{JJ_0} + \frac{\chi(T)}{J^2 J_0^2}\right] - \frac{3\kappa\alpha(T - T_0)}{J_0} - p\right]J\mathbf{C}^{-1} \tag{5.59}$$

$$\mathbf{j_R} = \frac{J_n}{J_0}\frac{(J_n J_0 - 1)}{J_n J_0}\frac{D\nu}{k_B T}\mathbf{F}_n^{-T}\cdot\mathbf{F}_n^{-T}\cdot\mathbb{P} = m\mathbf{F}_n^{-T}\cdot\mathbf{F}_n^{-T}\cdot\mathbb{P} \tag{5.60}$$

$$\mathbf{Z} = \frac{Nk_B}{J_0}(J_0^{2/3}\mathbf{1} - \mathbf{C}^{-1}) + \frac{k_B J}{\nu}\left[\log\left(\frac{J - 1}{J}\right) + \frac{1}{J} + \frac{\chi(T)}{J^2}\right]\mathbf{C}^{-1}$$
$$- \frac{k_B T J}{\nu J^2 J_0^2}\frac{\chi_L - \chi_H}{2\Delta\cosh^2\left(\frac{T - T_c}{\delta}\right)}\mathbf{C}^{-1} - 3\kappa\alpha\mathbf{1} \tag{5.61}$$

with $m = \frac{J_n}{J_0}\frac{(J_n J_0 - 1)}{J_n J_0}\frac{D\nu}{k_B T}$.

5.2.3 Variational formulation

In this subsection, the variational basis of the mixed coupled displacement-pressure-temperature problem is outlined. The total potential of the system can be expressed in the reference position of the arbitrary body under consideration as follows

$$\Pi(\mathbf{u}, p, T, t) = \int_{\Omega_0} \Pi_{\text{int}}(\mathbf{u}, p, T, t) \mathrm{d}V - \Pi_{\text{ext}}(\mathbf{u}, p, T, t) \tag{5.62}$$

Since the problem is governed by the principle of minimum potential energy, the expression for the equation concerning the mechanical problem in the material configuration is obtained as

$$
\boxed{
\begin{aligned}
&\text{Determine} \quad (\mathbf{u}, p, T) \quad \text{from} \\
&(\mathbf{u}^*, p^*, T^*) = \arg\left(\inf_{\Psi} \sup_{p} \inf_{T} \Pi(\mathbf{u}, p, T) \right),
\end{aligned}
}
\tag{5.63}
$$

The problem is ruled via the linear momentum equilibrium for the mechanical part, defined in Eq. (5.8); for the dissipation function for the mass transport, postulated in Eq. (5.50); and the energy balance in entropy form for the thermal part, defined in Eq. (5.35). By combining these three terms, we define the expression for total internal potential postulated in Eq. (5.37), and from here, we define the weak form of both equations, which stand for the most convenient setting to write the corresponding numerical approximation based on FEM based on the standard Galerkin procedure. We consider that for the thermal part there are no heat sources ($R = 0$).

$$\mathrm{D}\,\Pi(\delta\mathbf{u}) = \int_{\Omega_0} \left[\mathrm{D}\,\Psi(\delta\mathbf{u}) - p\mathrm{D}\,J[\delta\mathbf{u}] \right] \mathrm{d}V - \overline{\mathbf{F}}^V(\delta\mathbf{u}) = 0 \qquad \forall \delta\mathbf{u} \tag{5.64}$$

$$\mathrm{D}\,\Pi(\delta p) = \int_{\Omega_0} \left[-(J - J_n)\mathrm{D}\,p(\delta p) - \Delta t \mathrm{D}\,\phi(\delta p) \right] \mathrm{d}V - \mathrm{D}\,\Pi_{\text{ext}}(\delta p) = 0 \qquad \forall \delta p \tag{5.65}$$

$$
\begin{aligned}
\mathrm{D}\,\Pi(\delta T) = \int_{\Omega_0} \Big[& c_p \mathrm{D}\dot{T}(\delta T) + \mathrm{D}\,\nabla\cdot\mathbf{Q}(\delta T) - \mathrm{D}T(\delta T)\mathbf{Z} : \dot{\mathbf{C}} \\
& - \mathrm{D}m\nabla\mu(\delta T) \Big] \mathrm{d}V - \mathrm{D}\,\Pi_{\text{ext}}(\delta T) = 0 \qquad \forall \delta T
\end{aligned}
\tag{5.66}
$$

where the operator $\mathrm{D}\,\Pi(\delta\bullet)$ denotes the Gateaux derivative which reads as

$$\mathrm{D}\,\Pi(\delta\bullet) = \frac{\partial}{\partial \iota}\Pi(\bullet + \iota\partial\bullet)|_{\iota=0} \tag{5.67}$$

By introducing the second Piola-Kirchhoff stress $\mathbf{S}$, the nominal heat flux $\mathbf{Q}$ and the nominal mass flux $\mathbf{j_R}$, it is obtained the weak form of the coupled displacement-pressure-temperature problem for large deformation solids with diffusion problems:

$$\int_{\Omega_0} \mathbf{S} : \nabla_{\mathbf{X}}\mathbf{u}(\delta\mathbf{u})\,\mathrm{d}V - \overline{\mathbf{F}}^V(\delta\mathbf{u}) = 0 \qquad \forall \delta\mathbf{u} \tag{5.68}$$

$$\int_{\Omega_0} \Big[-(J - J_n)\delta p + \Delta t\,\mathbf{j_R} \cdot \nabla_{\mathbf{X}}p(\delta p) \Big]\mathrm{d}V - \mathrm{D}\,\Pi_{\text{ext}}(\delta p) = 0 \qquad \forall \delta p \tag{5.69}$$

$$\begin{aligned}
\int_{\Omega_0} \Big[c_p \dot{T}(\delta T) - \frac{1}{2}T\mathbf{Z} : \dot{\mathbf{C}}(\delta T) + J\nabla_{\mathbf{X}}T \cdot \mathbf{K} \cdot \nabla_{\mathbf{X}}T(\delta T) \\
- \mathbf{j_R}(\delta T) \cdot \nabla_{\mathbf{X}}p \Big]\mathrm{d}V - \mathrm{D}\,\Pi_{\text{ext}}(\delta T) = 0 \qquad \forall \delta T
\end{aligned} \tag{5.70}$$

5.3 Finite Element formulation and implementation details

5.3.1 Discretisation scheme

Being the domain discretized into finite elements, for which the displacement, fluid pressure and the temperature are approximated by Galerkin's method as it follows:

$$\mathbf{u} = \sum_{i=1}^{n} \mathbf{N_d} \cdot \mathbf{d}, \quad p = \sum_{i=1}^{m} \mathbf{N_p} \cdot \hat{\mathbf{p}}, \quad T = \sum_{i=1}^{m} \mathbf{N_T} \cdot \hat{\mathbf{T}} \tag{5.71}$$

where $\mathbf{d}$ represents the nodal displacement vector; $\hat{\mathbf{p}}$ is the nodal values of the pressure variable and $\hat{\mathbf{T}}$ stands for the nodal interpolation of the temperature. In order to satisfy the Babuska-Brezzi conditions [135]
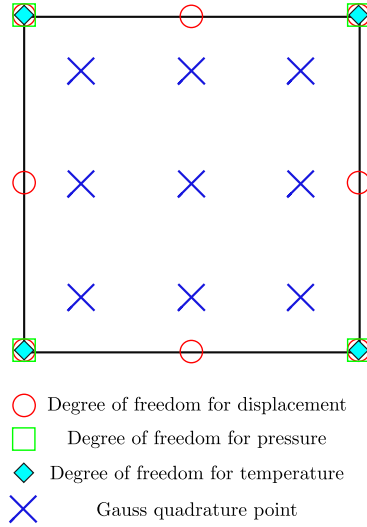
Figure 77: 2-D illustration of a **u**-p-T mixed finite element, displaying the degrees of freedom and the Gauss quadrature points. 8-node biquadratic element is used for the displacement while 4-node bilinear quadrilateral elements are utilized for pressure and temperature.

and avoid poor numerical performance, we employ a Taylor-Hood element discretization, where the displacement shape functions are taken to correspond to a biquadratic 8-node serendipity element (20-node in 3-D), while for temperature and fluid pressure we employ bilinear shape functions for a 4-node quadrilateral element (8-node in 3-D). A schematic illustration of the discretization for two dimensions is provided in Fig. 77.

The material and spatial gradients of the shape functions $\mathbf{N}$ can be read as

$$\nabla_{\mathbf{X}}\mathbf{N} = \mathbf{J_e}^{-T} \cdot \nabla_{\boldsymbol{\xi}}\mathbf{N}(\boldsymbol{\xi}), \qquad \nabla_{\mathbf{x}}\mathbf{N} = \mathbf{j_e}^{-T} \cdot \nabla_{\boldsymbol{\xi}}\mathbf{N}(\boldsymbol{\xi}) \qquad (5.72)$$

with $\boldsymbol{\xi}$ referring to the parametric coordinate system with coordinates

$\boldsymbol{\xi} = \{\xi, \eta, \zeta\}$; and $\mathbf{J_e}$ and $\mathbf{j_e}$ as the material and spatial Jacobians of the isoparametric transformation. With the previous definitions at hand, the corresponding material gradient quantities can be discretized as, for a material description,

$$\nabla_{\mathbf{X}}\delta\mathbf{u} \approx \delta\mathbf{d} \otimes \nabla_{\mathbf{X}}\mathbf{N_d}, \qquad \nabla_{\mathbf{X}}\delta p \approx \delta\overline{\boldsymbol{p}} \otimes \nabla_{\mathbf{X}}\mathbf{N_p}, \qquad \nabla_{\mathbf{X}}\delta T \approx \delta\overline{\boldsymbol{T}} \otimes \nabla_{\mathbf{X}}\mathbf{N_T} \tag{5.73}$$

where $\mathbf{N}_{[*]}$ denote the shape functions employed for the $[*]$ driving field variable.

5.3.2 Consistent linearization of the coupled displacement-pressure-temperature problem

Considering a finite time increment $\Delta t := t_{n+1} - t_n > 0$, where all the DOFs at t_n are assumed to be known. The target is to obtain the independent variables at the time t_{n+1}^k for the k-th iteration. To do so, we solve the coupled problem through the use of the incremental and iterative solvers. This requires the computation by the consistent lineralization of the previous residual equations in the sense of the Gateaux directional derivative. Within this frame, the temporal variation of the displacement, pressure and temperature reads

$$\dot{\mathbf{d}} = \frac{\mathbf{d}_{n+1} - \mathbf{d}_n}{\Delta t}; \qquad \dot{\hat{p}} = \frac{\hat{p}_{n+1} - \hat{p}_n}{\Delta t}; \qquad \dot{\hat{T}} = \frac{\hat{T}_{n+1} - \hat{T}_n}{\Delta t} \tag{5.74}$$

The point of departure for the finite element formulation of the displacement-pressure recalls the variational formalism defined in Eqs.(5.68)-(5.70), defining a coupled problem. The insertion of the interpolation scheme for $\mathbf{u}$, p and T leads to a discrete version of the residual forms denoted by $\mathbf{R^d}$, $\mathbf{R}^{\hat{p}}$ and $\mathbf{R}^{\hat{T}}$ that are defined as:

$$\mathbf{R^d}(\mathbf{d}, \delta\mathbf{d}, \hat{p}, \hat{T}, \Delta\hat{T}) = \int_{\Omega_0} \nabla_{\mathbf{X}} \mathbf{N_d^T} \cdot \mathbf{S} \, dV - \int_{\Omega_0} \mathbf{N_d^T} \cdot \overline{\mathbf{F}}^V \, dV - \int_{\partial\Omega_0} \mathbf{N_d^T} \cdot \overline{\mathbf{T}} \, d\partial V = 0$$

$$(5.75)$$

$$\mathbf{R}^{\hat{p}}(\mathbf{d}, \hat{p}, \delta p, \hat{T}) = \int_{\Omega_0} -\mathbf{N_p^T}(J - J_n) \, dV + \int_{\Omega_0} \frac{\Delta t}{J_0} \, \mathbf{F_n^{-T}} \cdot \nabla_{\mathbf{X}} \mathbf{N_p^T} \cdot \mathbf{j_R} \, dV = 0$$

$$(5.76)$$

$$\mathbf{R}^{\hat{T}}(\mathbf{d}, p, T, \delta T, \Delta\hat{T}) = \int_{\Omega_0} \mathbf{N_T^T} c_p \dot{T} \, dV + \int_{\Omega_0} \nabla_{\mathbf{X}} \mathbf{N_T^T} \cdot \mathbf{K} \cdot \nabla_{\mathbf{X}} T \, dV$$

$$- \int_{\Omega_0} \frac{\mathbf{N_T^T}}{2}(\mathbf{Z^T} : \dot{\mathbf{C}})T \, dV + \int_{\Omega_0} \mathbf{N_T^T} \cdot \mathbf{j_R} \cdot \nabla_{\mathbf{X}} p \, dV = 0$$

$$(5.77)$$

For the application of Newton-type solution algorithms for the iterative solution of the boundary value problem, the linearization of the weak form are computed as follows by the Lie's derivative operators:

$$\hat{L}[\mathbf{R}^d](\mathbf{d}, \delta\mathbf{d}, \Delta\mathbf{d}, \hat{p}, \Delta\hat{p}, \hat{T}, \Delta\hat{T}) = \mathbf{R}^d(\mathbf{d}, \delta\mathbf{d}, \hat{p}, \hat{T}, \Delta\hat{T}) + \Delta_{\mathbf{d}}\mathbf{R}^d \cdot \Delta\mathbf{d}$$
$$+ \Delta_{\hat{p}}\mathbf{R}^d \cdot \Delta\hat{p} + \Delta_{\hat{T}}\mathbf{R}^d \cdot \Delta\hat{T}$$

$$(5.78)$$

$$\hat{L}[\mathbf{R}^{\hat{p}}](\mathbf{d}, \Delta\mathbf{d}, \hat{p}, \delta p, \Delta p, \hat{T}, \Delta\hat{T}) = \mathbf{R}^{\hat{p}}(\mathbf{d}, \hat{p}, \delta\hat{p}, \hat{T}) + \Delta_{\mathbf{d}}\mathbf{R}^{\hat{p}} \cdot \Delta\mathbf{d}$$
$$+ \Delta_{\hat{p}}\mathbf{R}^{\hat{p}} \cdot \Delta\hat{p} + \Delta_{\hat{T}}\mathbf{R}^{\hat{p}} \cdot \Delta\hat{T}$$

$$(5.79)$$

$$\hat{L}[\mathbf{R}^{\hat{T}}](\mathbf{d}, \Delta\mathbf{d}, \hat{p}, \Delta\hat{p}, \hat{T}, \delta\hat{T}, \Delta\hat{T}) = \mathbf{R}^{\hat{T}}(\mathbf{d}, \delta\mathbf{d}, \hat{p}, \hat{T}, \delta\hat{T}, \Delta\hat{T}) + \Delta_{\mathbf{d}}\mathbf{R}^{\hat{T}} \cdot \Delta\mathbf{d}$$
$$+ \Delta_{\hat{p}}\mathbf{R}^{\hat{T}} \cdot \Delta\hat{p} + \Delta_{\hat{T}}\mathbf{R}^{\hat{T}} \cdot \Delta\hat{T}$$

$$(5.80)$$

where $\Delta_*[\bullet]$ denotes the directional derivative of the residual form $\bullet$ from the field $*$. This leads to the following linearised system of equations that is solved by the global N-R monolithic scheme

$$\begin{bmatrix} \mathbf{K^{dd}} & \mathbf{K^{d\hat{p}}} & \mathbf{K^{d\hat{T}}} \\ \mathbf{K^{pd}} & \mathbf{K^{\hat{p}\hat{p}}} & \mathbf{K^{\hat{p}\hat{T}}} \\ \mathbf{K^{\hat{T}d}} & \mathbf{K^{\hat{T}\hat{p}}} & \mathbf{K^{\hat{T}\hat{T}}} \end{bmatrix} \begin{bmatrix} \Delta\mathbf{d} \\ \Delta\hat{\mathbf{p}} \\ \Delta\hat{\mathbf{T}} \end{bmatrix} = - \begin{bmatrix} \mathbf{R^d} \\ \mathbf{R}^{\hat{p}} \\ \mathbf{R}^{\hat{T}} \end{bmatrix}$$

$$(5.81)$$

The linearized system of equations in matrix form is given by

$$\mathbf{K^{dd}} = \frac{\partial \mathbf{R}^d}{\partial \mathbf{u}} = \int_{\Omega_0} \nabla_{\mathbf{X}} \mathbf{N_d^T} \cdot \mathbb{C} \cdot \nabla_{\mathbf{X}} \mathbf{N_d} \, dV + \int_{\Omega_0} \left[\nabla_{\mathbf{X}} \mathbf{N_d^T} \cdot \mathbf{S} \cdot \nabla_{\mathbf{X}} \mathbf{N_d} \right] \cdot \mathbf{1} \, dV$$

(5.82)

$$\mathbf{K^{d\hat{p}}} = \frac{\partial \mathbf{R}^d}{\partial p} = \frac{\partial \mathbf{R}^{\hat{p}}}{\partial \mathbf{u}} = (\mathbf{K^{\hat{p}d}})^{\mathrm{T}} = - \int_{\Omega_0} J \, \nabla_{\mathbf{X}} \mathbf{N_d^T} \cdot \mathbf{C^{-1}} \cdot \mathbf{N_p^T} \, dV \quad (5.83)$$

$$\mathbf{K^{d\hat{T}}} = \frac{\partial \mathbf{R^d}}{\partial T} = \int_{\Omega_0} \nabla_{\mathbf{X}} \mathbf{N_d^T} \cdot \mathbf{Z} \cdot \mathbf{N_T^T} \, dV \tag{5.84}$$

$$\mathbf{K^{\hat{p}\hat{p}}} = \frac{\partial \mathbf{R}^{\hat{p}}}{\partial p} = - \int_{\Omega_0} \frac{\Delta t \, m \, J_n}{J_0} \mathbf{F_n^{-T}} \cdot \nabla_{\mathbf{X}} \mathbf{N_p^T} \cdot \mathbf{F_n^{-T}} \cdot \nabla_{\mathbf{X}} \mathbf{N_p} \, dV \tag{5.85}$$

$$\mathbf{K^{\hat{p}\hat{T}}} = \frac{\partial \mathbf{R}^{\hat{p}}}{\partial T} = - \int_{\Omega_0} \frac{\Delta t}{T J_0} \mathbf{F_n^{-T}} \cdot \nabla_{\mathbf{X}} \mathbf{N_p^T} \cdot \mathbf{j_R} \, dV \tag{5.86}$$

$$\mathbf{K^{\hat{T}d}} = \frac{\partial \mathbf{R}^{\hat{T}}}{\partial \mathbf{d}} = - \int_{\Omega_0} \frac{T}{\Delta t} \mathbf{N_T^T} \cdot \mathbf{Z^T} \cdot \nabla_{\mathbf{X}} \mathbf{N_d^T} \, dV \tag{5.87}$$

$$\mathbf{K^{\hat{T}\hat{p}}} = \frac{\partial \mathbf{R}^{\hat{T}}}{\partial \hat{p}} = \int_{\Omega_0} m \mathbf{N_T^T} \cdot \mathbf{j_R} \cdot \mathbf{F_n^{-T}} \cdot \nabla_{\mathbf{X}} \mathbf{N_p} \, dV \tag{5.88}$$

$$\mathbf{K^{\hat{T}\hat{T}}} = \frac{\partial \mathbf{R}^{\hat{T}}}{\partial T} = \int_{\Omega_0} \mathbf{N_T^T} \frac{c_p}{\Delta t} \cdot \mathbf{N_T} - \int_{\Omega_0} \mathbf{N_T^T} \frac{(\mathbf{Z^T} : \dot{\mathbf{C}})}{2} \cdot \mathbf{N_T} \, dV$$
$$+ \int_{\Omega_0} \nabla_{\mathbf{X}} \mathbf{N_T^T} \cdot \mathbf{K} \cdot \mathbf{F^{-T}} \cdot \nabla_{\mathbf{X}} \mathbf{N_T} \, dV - \int_{\Omega_0} \mathbf{N_T^T} \cdot \frac{\mathbf{j_R} \cdot \nabla_{\mathbf{X}} p}{T} \cdot \mathbf{N_T} \, dV$$

(5.89)

The `Q2Q1Q1` fully-coupled element that we are presenting in here is programmed via an `UEL` user element subroutine from the FE commercial package `ABAQUS`. The solution scheme employed for the aforementioned simulation is an incremental-iterative Newton-Raphson and the performance of the presented formulation will be put into test in the next two sections via the conduction of various numerical examples concerning several applications of thermoresponsive hydrogels.
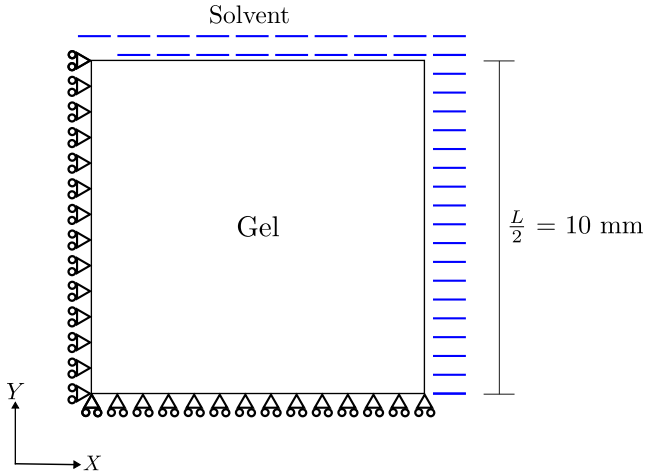
Figure 78: Configuration for the 2-D free swelling and thermal deswelling problem.

5.4 Verification examples

5.4.1 Verification: free swelling and thermal deswelling

The first of the experiments consists of a validation example employing the Q2Q1Q1 element under a free swelling state and subsequent deswelling caused by a temperature gradient, made in order to display the functionality of the proposed formulation. Adopted from the work in Section 10.4 of the work by Chester and Anand [7], it is modelled the quarter of a 2-D plane-strain square brick of $L = 20$ mm (symmetry conditions are considered on the planes X and Y), depicted in Fig. 78, with a discretization of 1,600 Q2Q1Q1 elements. The initial condition for the pressure with p_0 for the whole domain in a stress-free equilibrium state is $p_0 = -188.86$ MPa with the material properties employed in Table 26, characteristic of a Ni-PAAm gel. As a consequence of being a LCST hydrogel, Eq. (5.44) is employed for the interaction parameter. Regarding the chemical boundary conditions, the fixed edges are prescribed to a zero fluid flux, while the edges in contact with the solvent, the pressure is decreased via def-

Table 26: Material properties employed for a LCST hydrogel subject to isothermal square under free transient swelling and thermal-deswelling conditions.

$Nk_BT = G$ (MPa)	$N\nu$	T (K)	$\chi_L \approx \chi$	D (mm^2/s)	λ_0
0.4	0.01	298	0.1	5×10^{-3}	1.001

inition of a linear ramp in $t = 300$ s from p_0 to 0 MPa with a fixed time increment of $\Delta t = 3$ s, applied in this time lapse for numerical reasons, a phenomenon of interest that will be discussed in the following section. Subsequently, the solid is subject to free swelling for 24 h.

Concerning thermal BCs, the entire body is prescribed to a temperature of $T_0 = 298$ K under isothermal conditions (i.e., no external flux, $\mathbf{Z} = 0$), this means that the hydrogel is below the LCST temperature, therefore, according to Eq. 5.44, we can approximate $\chi_L \approx \chi$. Then, when the model has swollen for 24 h, simulating a heating of the solvent, the edges in contact with it are prescribed for a linear ramp in temperature from T_0 to 333 K in 1 h, thus meaning that the hydrogel will overpass the LCST, reducing its swelling rate considerably. This last temperature is held for 24 h to analyze properly how the hydrogel will react to this thermal ramp. Therefore, by adding up all, the test takes 49 hours to complete.

Figs. 79(a)-79(f) depict the contour of the hydrostatic pressure, p, plotted on the deformed solid after different times: (a) 0 s; (b) 300 s; (c) 12 h; (d) 24 h; (e) 25 h; (f) 49 h. In summary, the whole evolution of the square during the test can be observed. Fig. 79(a) shows the application of the initial p_0 conditions, while Fig. 79(b) exhibits the results of the decrease of the pressure in the edges in contact with the solvent. Figs. 79(c)-79(d) exhibit the swollen body at the middle and at the end of the swelling step; and we can relate that the sample loses its square shape due to the fluid flux that is coming from both edges in contact with the solvent to the center of the sample. We can see from Figs. 79(b)-79(c) that the specimen grows more than from Figs. 79(c)-79(d), due to the major difference in mass flux that is on the former state. Subsequently, the results
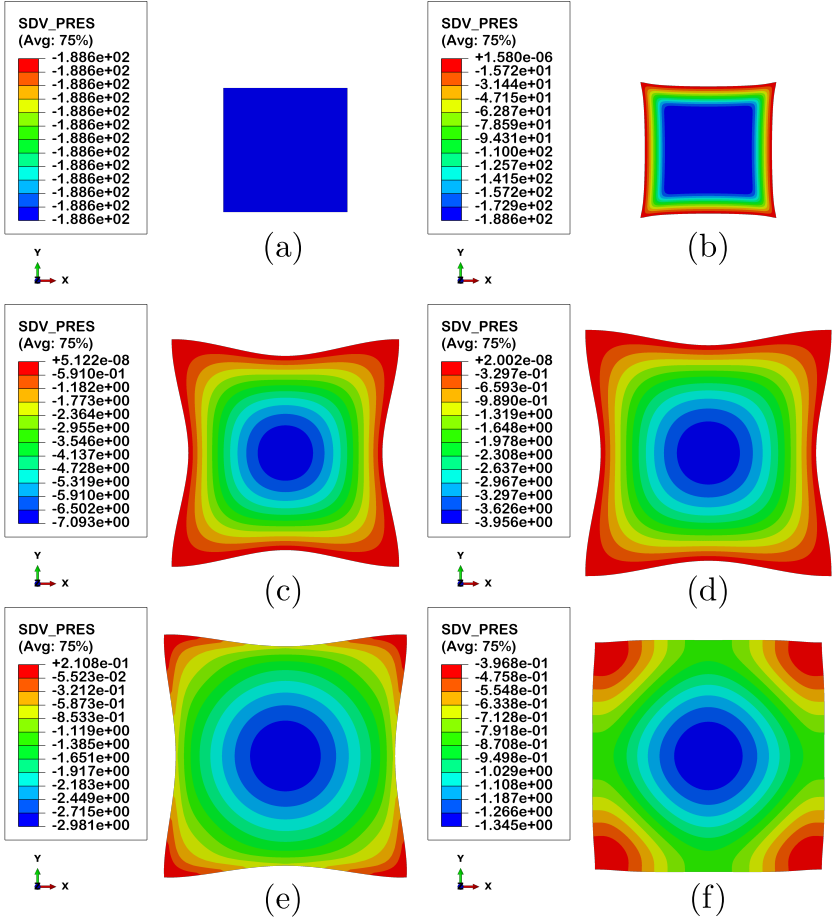
Figure 79: Steps of the swelling-deswelling process: states for (a) 0 s, (b) 300 s, (c) 12 h, (d) 24 h, (e) 25 h and (f) 49 h. Represented within this plots is the solvent pressure p.

from thermal deswelling are observed in the last pair of images, Figs. 79(e)-79(f). Both images exhibit that once the LCST of $T_c = 320$ K has been surpassed, there is a decrease of size in the swollen state, approaching again the initial square configuration of the body. The results that
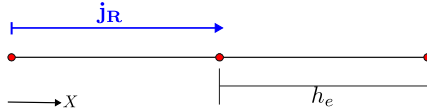
Figure 80: 1-D representation of the diffusion length problem.

we have displayed in this Section matches qualitatively with those presented in the aforementioned paper of Chester and Anand [7]. However, some remarks need to be addressed regarding the presented framework, being covered in the forthcoming subsections.

5.4.2 The diffusion length problem

The next particularity that we have to address for the presented chemothermomechanical mixed formulation has not been covered yet for diffusion problems in hydrogels: the diffusion length problem. Specifically, for smaller diffusivity coefficients D, as the diffusion length rate is decreasing, the mesh size is required to be finer in order to capture the transport problem.

Represented for a 1-D configuration in Fig. 80, we plot two elements with a size h_e which are experiencing mass diffusion under a referential flux $\mathbf{j_R}$. The problem states that in order to have a smooth transport problem, for an increment Δt, the flux should be fast enough to diffuse from at least one element of the mesh, meaning that the element size should be refined according to this. From here, a rule is obtained $h_e \leq \sqrt{D\Delta t}$ to establish the minimum discretization that is required to model this. The failure to meet this condition causes oscillations in the pressure field that leads to convergence issues for the loading step.

To test the mesh dependence, various discretizations of the 2-D square block disposed to free swelling are simulated, with the properties plotted in Table 26. The main target is to assess the pressure oscillations of the specimen in the step for the unloading pressure linear ramp in the edges of the hydrogel exposed to the solvent from p_0 to 0 MPa. Adopting a final time of $t_f = 50$ s with a fixed time increment of $\Delta t = 0.5$ s, we obtain from the condition that the maximum element size required to model the
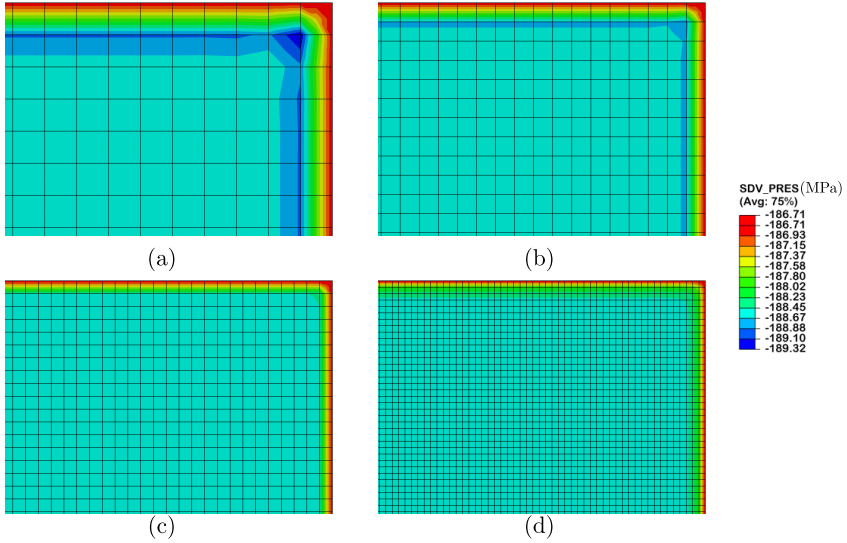
Figure 81: First increment of unloading pressure ramps conducted for discretizations with element sizes: (a) $h_e = 0.25$, (b) $h_e = 0.15$, (c) $h_e = 0.1$ and (d) $h_e = 0.05$ mm with a time step of $\Delta t = 0.5$ s. It is observed how by increasing discretization, the variation of the pressure becomes smooth.

hydrogel pre-swelling step is $h_e = 0.05$ mm. It is important to highlight that now we consider the full thermomechanical model, i.e., $\mathbf{Z} \neq 0$, this means that heat sources are considered. However, as no special thermal BCs are added, we do not address the thermal particularities, leaving that for the following Section.

Displaying the pressure isocontour for the first step of the unloading step in Fig. 81, it can be identified for the first maps that when the boundaries of the specimen are put in contact with the solvent, the pressure gradient in that area becomes irregular due to oscillations that are happening within this magnitude. These are due to the diffusion length problem that we are addressing in this section, since the aforementioned condition is not fulfilled. It is observed when the specimen is refined, this transition becomes less rough, leading to a total stable sample for Fig.81(d), when such criterion is met. A quantitative approach of this
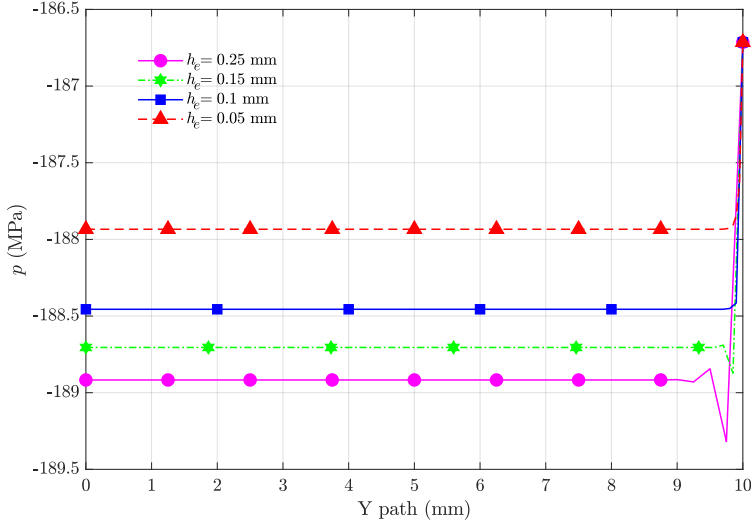
Figure 82: Evolution of the pressure for a vertical path in the sample at $x = L - h_e$ mm for different discretizations at the first increment of the pressure unloading step with a time step of $\Delta t = 0.5$ s. Oscillations in pressure are observed for coarser meshes near the top right corner.

phenomenon can be observed in Fig. 82, where we plot the evolution of the pressure from a vertical path in $x = L - h_e$ mm; it is observed how the oscillations in the top right corner are regularised when the sample is refined, in addition with a reduction in the minimum of the pressure reached in the bottommost edges of the specimen. Therefore, it is concluded that the only discretization that does not show any visible oscillations is the finest one, $h_e = 0.05$ mm, proving this that the condition of $h_e \leq \sqrt{D\Delta t}$ is required to ensure pressure stability of the sample.

Repeating the test, now for even a smaller time step: $\Delta t = 0.15$ s for a final unloading time of $t_f = 15$ s, we conduct again the tests for the different discretizations. According to the condition, the maximum element size to guarantee a stabilized simulation is $h_{\max} = 0.027$ mm. Therefore, none of the previous discretizations satisfy such constraint, so we will include in the simulations $h = 0.025$ mm. In line with the
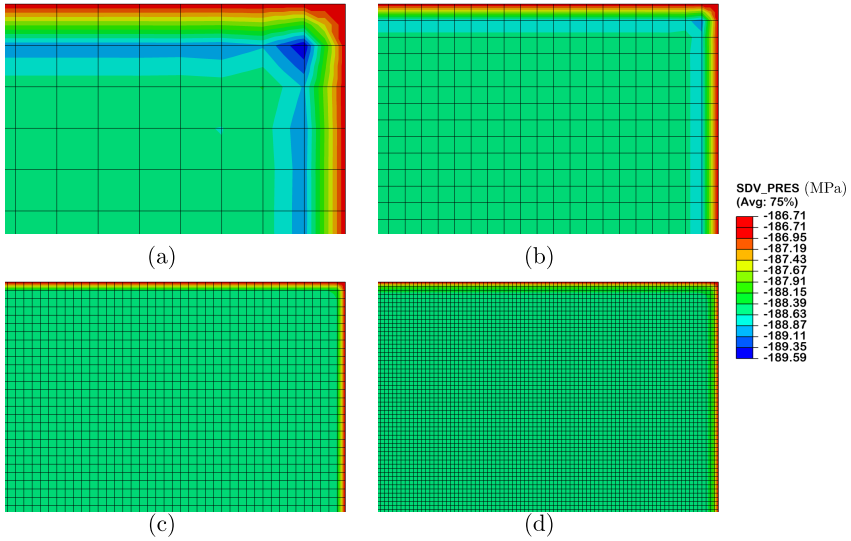
Figure 83: First increment of unloading pressure ramps conducted for discretizations with element sizes: (a) $h = 0.15$, (b) $h = 0.1$, (c) $h = 0.05$ and (d) $h = 0.025$ mm with a time step of $\Delta t = 0.15$ s. It is observed how by increasing discretization, the variation of the pressure becomes smooth.

previous test, we commence by plotting the isocontours for pressure near the top right corner in Fig. 83 and we observe that as we decrease the time steps, the oscillations are intensified for the coarser discretizations and further refinement is required to meet the conditions, leading it to a heavily refined model of 160,000 elements, that is characterized by a huge computational cost, meaning that reducing the time steps leads to an increase of this. The evolution of the pressure in the width of the thickness is quantified in Fig. 84 for a vertical path at the point $x = L - h_e$, confirming the discoveries of our finding and reinforcing the theory that such condition is required to meet the conditions for stability of the element.

It is worth highlighting another aspect that relies on the refinement of the mesh, but which is more visible during the swelling step: the appearance of swelling induced surface instabilities, a phenomenon due to
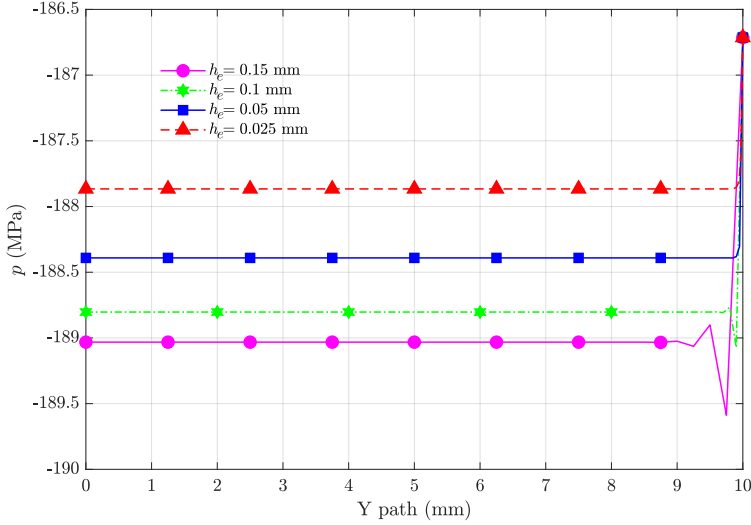
Figure 84: Evolution of the pressure for a vertical path in the sample at $x = L - h_e$ mm for different discretizations at the first increment of the pressure unloading step with a time step of $\Delta t = 0.15s$. Oscillations in pressure are observed for coarser meshes near the top right corner.

the induction of compressive in-plane stresses. These instabilities have been deeply studied in the bibliography and have appeared in the form of creasing [337, 338, 339, 340] and wrinkling [341, 342] in several experiments and numerical methods have addressed their appearance based on energy or equilibrium settings [343, 344, 345, 328, 346, 347, 348]. What is stated in the numerical approaches is that the appearance of these instabilities earlier during the swelling stage due to mesh refinement approaches the theoretical prediction of a instantaneous instability. Since unlike the diffusion length issue, this phenomenon has been deeply addressed in the theory, we just mention it here for the readers' consideration and do not address it further since we believe that the study of surface induced instabilities is out of the scope of the current investigation.
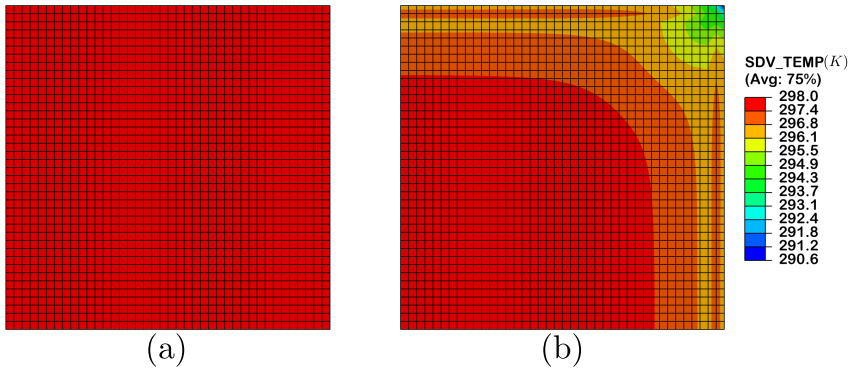
Figure 85: Isocontour displaying the temperature field (a) without and (b) with considering the fluid flow and elastic stretching influence on the temperature.

5.4.3 Influence in temperature terms of displacement and pressure field

The additional particularity to be addressed is the inclusion of the last two terms in Eq. (5.77), i.e. the temperature variation due to fluid flow and elastic stretching. The referential works of Chester and Anand [7] claims that both terms could be dismissed due to their relative minor influence on the hydrogel behavior compared to the other terms on the residual terms. This statement has been proven to be in line with other tests conducted for thermo-mechanical simulations of polymers such as [68, 36]. However, for hydrogels, our findings have revealed that both terms have a considerably major performance on the material behavior due to the properties of the hydrogel itself (lower shear modulus G). In order to address this claim, the comparison between the swelling-deswelling results of Section 5.4.1 is conducted with and without considering these coupling terms. The isocontours for the temperature field at the beginning of the swelling step may be observed in Fig. 85, where it is observed that by neglecting both terms, we have an isothermal case, whereas by considering both, we have a considerable temperature profile
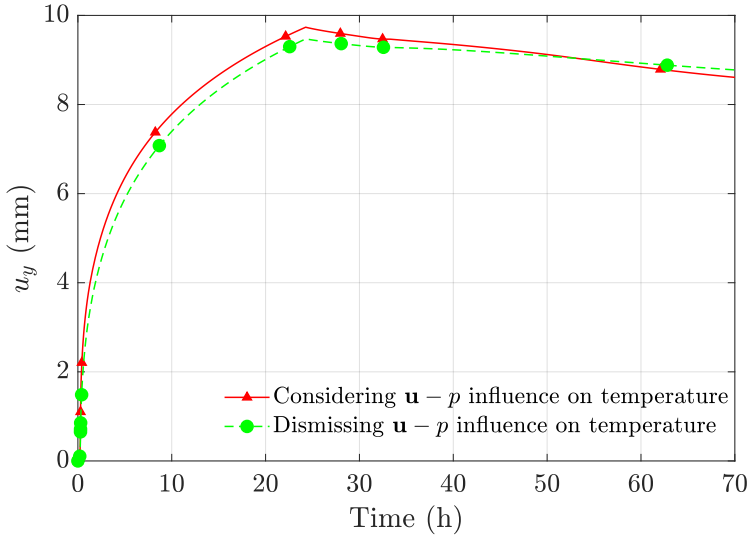
Figure 86: Time evolution of the vertical displacement in the top right node for the swelling-deswelling test with (red, continuous line) and without (green, dashed line) considering the fluid flow and elastic stretching influence on the temperature.

of around 8℃. If we were running this analysis near the critical temperature T_c, such gradient could cause the transition of the LCST which will lead to a dramatic change of the solvent capacity to make the hydrogel swell. Therefore, the consideration of these terms cause, by taking a look just on the temperature field itself, significant thermal changes that alter the swelling behavior, this is explained by the instantaneous change from a poor to good solvent and viceversa. Based on this argument the thermal fields should not be dismissed.

In addition to this, we pay attention on the time evolution of the displacement in the top right node during the full test on Fig. 86 and we observe that, now in the mechanical field, there are also quantitative modifications in the material behavior. It is envisaged how the trajectory for both tests is slightly different between both approaches, reaching a 5% difference on the peak of the specimen, and decaying quicker during

the deswelling stage for the full model. In addition to this, on numerical terms, it is important to highlight that the convergence of the approach considering both influences is more robust than the one dismissing both terms, which leads to more difficulties on conducting the test. We believe that with the distinct performances that we display here, we have presented solid arguments to encourage the usage of a full formulation considering all the involved terms. However, we expect to intensify the differences between both approaches when studying a problem with contact, where the thermal part is of a major importance than here; such task is currently being conducted for an experimental-numerical approach and will be presented in future works.

5.5 Experimental correlation: Free swelling of PNIPAAm hydrogels

After the validation of the functionality of the proposed framework and addressed its particularities, we will now focus to show the ability of our model to capture some experimental results, establishing a quantitative correlation with the experimental data reported by [349], where they study the effect of crosslinking density in the swelling behavior for PNIPAAm hydrogels for different temperatures.

It is well-known that the PNIPAAm/water system show the type of swelling for a LCST hydrogel. Therefore, for this system, Oh et al. [349] synthetized various *N*-isopropylacrylamide gel particles with various crosslinking concentrations and measured the free swelling behavior of these materials to predict the swelling equilibrium of the hydrogel/solvent system. The magnitude that they employ to measure the degree of swelling is the volume ratio of gel particles. Their study shows that, for temperatures below the LCST, hydrogels with less crosslinking density become considerably more swollen. However, when the temperature is increased above the LCST, the influence of the crosslinking density is almost negligible, as the volume that these systems grow is considerably minor compared to cooler temperatures.

Heading back to the current modelling framework, in order to cap-

Table 27: Material properties employed for the 3-D block under free transient swelling conditions associated to displacement-mass diffusion fields.

$Nk_BT = G$(MPa)	χ_L	χ_H	D (mm^2/s)	λ_0
0.4	0.05	0.85	5×10^{-2}	1.01

Table 28: Material properties employed for the 3-D block under free transient swelling conditions associated to thermal fields.

T_c (K)	Δ (K)	$c_p \left(\text{J}/(\text{mm}^3 \cdot \text{K})\right)$	α (K^{-1})	K $\left(\text{W}/(\text{mm·K})\right)$
305	5	5.02	73×10^{-6}	0.35×10^{-3}

ture this experimental behavior and correlate with the main findings of [349], we propose the following approach: as the experimental work gives not enough details regarding the geometry and dimensions of the sample, we assume that the authors mean that the swelling properties do not depend on these characteristics, but in the material itself. Therefore, we have modelled one-eighth of a 3-D square block swelling of 20x20x20 mm, imposing symmetry conditions on the X, Y and Z plane. The employed displacement-mass diffussion-related properties are plotted in Table 27, with the thermal ones being depicted in Table 28.

Imposed chemical BCs are quite similar with respect to those defined in Section 5.4.1, but now for 3-D: symmetry surfaces are imposed zero flux conditions, whereas in the surfaces in contact with the solvent, a pressure of $p = 0$ MPa is prescribed for an initial swelling ratio of $\lambda_0 = 1.01$, meaning that they are in equilibrium with the solvent. As the temperature has to remain constant for the whole analysis for proper correlation with the experiments, isothermal BCs are applied for the whole domain, meaning that $\mathbf{Z} = 0$. In accordance with the mesh sensitivity analysis carried out, a mesh of 8,000 20-node `Q2Q1Q1` elements is employed for the whole analysis. The sample is represented in Fig. 87 with both the un-swollen and swollen configuration.

The parameter of our model that is related to the crosslinking density of our model is $N\nu$; therefore, it is the one to be adjusted to capture the
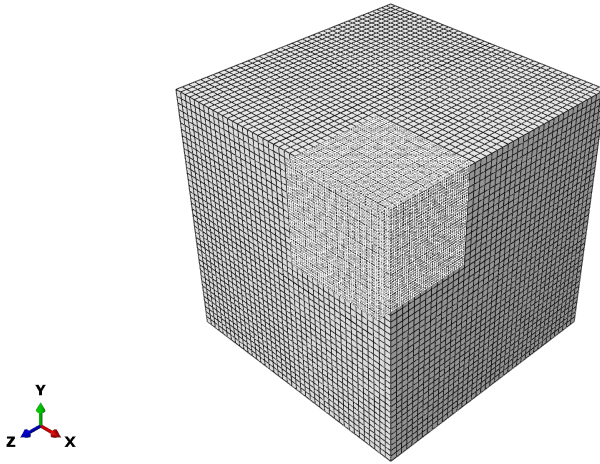
Figure 87: 3-D mesh for the block subject to free swelling: both un-swollen and swollen configurations are represented.

experimental results. To compare with the experimental results that refer to volume change, we have plotted in Fig. 88 the Jacobian J on the swollen state under equilibrium (remember that is the magnitude that maps the volume variation from the reference configuration to the current one like $\mathrm{d}v = J\mathrm{d}V$) in front of the imposed temperature on the hydrogel. Experimental results study a experimental crosslinking of 1.23%, 2.50% and 3.88% and we have calibrated such change. The results reveal that when reducing the $N\nu$ parameter, that is equivalent to reduce the crosslinking and then, the swelling ratio J of the hydrogel increases considerably when cooled below the LCST. In addition to this, above the LCST, it is observed how the results for the three analyzed samples do coincide, exhibiting the independence of this parameter when the hydrogel is heated above this temperature. Overall, it can be observed a strong correlation between the experiments and the numerical model, displaying the solidness that the proposed framework provides in capturing the behavior of thermosensitive hydrogels.
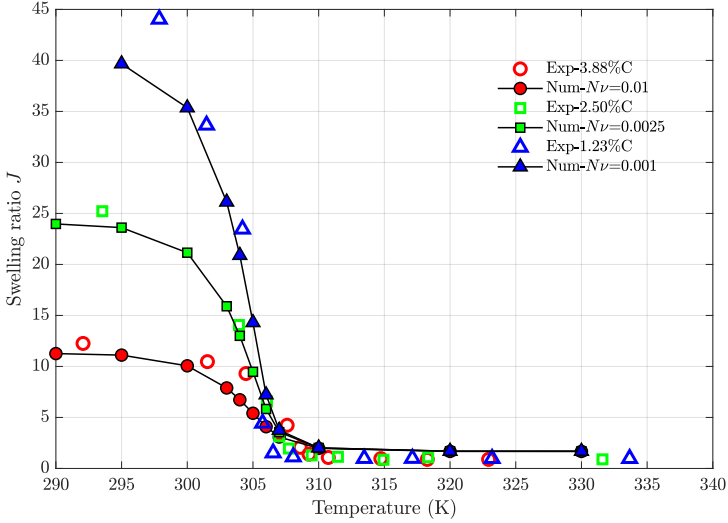
Figure 88: Volume of free-swelling hydrogel depending on temperature for different crosslinking densities. To adjust for the different experiments of [349], we have changed the parameter $N\nu$.

5.6 A preliminary formulation for fracture of thermoresponsive hydrogels

To close up this Chapter of the thesis, a preliminary theory for phase-field modelling of fracture of thermoresponsive hydrogels is presented. In order to avoid repetition, we refer the reader for the global potential postulated in Eqs. (1.1)-(1.8). As we are applying the AT-2 approach proposed by Bourdin et al. [46], the degradation function adopted is proposed in Eq. (1.9) and the crack density energy is included in Eq. (1.10). With these expressions at hand, we modify the hydrogel swelling formulation proposed in this Chapter to model fracture with a staggered scheme.

5.6.1 Inclusion of the phase-field technique in the variational formulation

With the addition of the phase-field parameter, the developed three-field formulation (see Fig. 76) is converted into a four-field element, whose DOFs are the displacement field $\mathbf{u}$, the fluid pressure p, the temperature T and the phase-field parameter $\mathfrak{d}$. Keeping the same material model as the one stated in Section 5.2.2, the variational basis of the mixed coupled displacement-pressure-temperature-phase field problem finds the total potential

$$
\begin{aligned}
\Pi(\mathbf{u}, p, \mathfrak{d}, T, t) &= \int_{\Omega_0} \Pi_{\text{int}}(\mathbf{u}, p, \mathfrak{d}, T, t) \mathrm{d}V - \Pi_{\text{ext}}(\mathbf{u}, p, \mathfrak{d}, T, t) \\
&= \int_{\Omega_0} g(\mathfrak{d}) \Psi(\mathbf{C}, T, \nabla T) \, \mathrm{d}V + \int_{\Omega_0} \mathcal{G}_C \gamma_l(\mathfrak{d}, \nabla_x \mathfrak{d}) \, \mathrm{d}V \\
&\quad - p(J - J_n) - \Delta t \, \mathfrak{d}(\mathbb{p}, \mathbf{F}_n, T) + \rho_0 \dot{\eta} T - \Pi^{\text{ext}}
\end{aligned} \tag{5.90}
$$

leading to an objective by the principle of minimum potential energy

$$
\boxed{
\begin{aligned}
&\text{Determine} \quad (\mathbf{u}, p, \mathfrak{d}, T) \quad \text{from} \\
&(\mathbf{u}^*, p^*, \mathfrak{d}^*, T^*) = \arg \left(\inf_{\Psi} \sup_{p} \inf_{\mathfrak{d}} \inf_{T} \Pi(\mathbf{u}, p, \mathfrak{d}, T) \right)
\end{aligned}
} \tag{5.91}
$$

The problem now is ruled via the linear momentum equilibrium proposed in Eq. (5.8); the dissipation function for mass transport, postulated in Eq. (5.50); the energy balance in entropy form for the thermal part, defined in Eq. (5.35); and the fracture energy density contribution, expressed in Eq. (1.12).

5.6.2 Consistent linearization of the coupled displacement-pressure-temperature-phase field problem

As mentioned before, the variational formulation encompasses four terms, this quadruplet set $(\mathbf{u}^*, p^*, \mathfrak{d}^*, T^*)$ is solved by taking a first derivative of

the total functional by assuming regularity of the involved fields. As the variable $\eth$ possesses the irreversibility property, for any admissible test function, we reach the following residuals for the multi-field problem:

$$\mathbf{R}^{\mathbf{d}}(\mathbf{d}, \delta\mathbf{d}, \hat{p}, \hat{\eth}, \hat{T}, \Delta\hat{T}) = \int_{\Omega_0} \nabla_{\mathbf{X}}\mathbf{N}_{\mathbf{d}}^{\mathsf{T}} \cdot g(\eth)\mathbf{S}\, \mathrm{d}V$$

$$- \int_{\Omega_0} \mathbf{N}_{\mathbf{d}}^{\mathsf{T}} \cdot \overline{\mathbf{F}}^{V}\, \mathrm{d}V - \int_{\partial\Omega_0} \mathbf{N}_{\mathbf{d}}^{\mathsf{T}} \cdot \overline{\mathbf{T}}\, \mathrm{d}\partial V = 0 \tag{5.92}$$

$$\mathbf{R}^{\hat{p}}(\mathbf{d}, \hat{p}, \delta p, \hat{T}) = \int_{\Omega_0} -\mathbf{N}_{\mathbf{p}}^{\mathsf{T}}(J - J_n)\, \mathrm{d}V + \int_{\Omega_0} \frac{\Delta t}{J_0} \mathbf{F}_{\mathbf{n}}^{-\mathsf{T}} \cdot \nabla_{\mathbf{X}}\mathbf{N}_{\mathbf{p}}^{\mathsf{T}} \cdot \mathbf{j}_{\mathbf{R}}\, \mathrm{d}V = 0 \tag{5.93}$$

$$\mathbf{R}^{\hat{\eth}}(\mathbf{d}, \hat{p}, \hat{\eth}, \delta\hat{\eth}, \hat{T}, \Delta\hat{T}) = \int_{\Omega_0} \mathcal{G}_C\left[\frac{1}{\ell}\mathbf{N}_{\eth}^{\mathsf{T}}\eth + \ell\nabla_{\mathbf{X}}\mathbf{N}_{\eth}^{\mathsf{T}} \cdot \nabla_{\mathbf{X}}\eth\right] \mathrm{d}V$$

$$- \int_{\Omega_0} 2(1 - \eth)\mathcal{H}\mathbf{N}_{\eth}^{\mathsf{T}}\eth\, \mathrm{d}V \tag{5.94}$$

$$\mathbf{R}^{\hat{T}}(\mathbf{d}, \hat{p}, \hat{\eth}, \hat{T}, \delta\hat{T}, \Delta\hat{T}) = \int_{\Omega_0} \mathbf{N}_{\mathbf{T}}^{\mathsf{T}}c_p\dot{T}\, \mathrm{d}V + \int_{\Omega_0} g(\eth)\nabla_{\mathbf{X}}\mathbf{N}_{\mathbf{T}}^{\mathsf{T}} \cdot \mathbf{K} \cdot \nabla_{\mathbf{X}}T\mathrm{d}V$$

$$- \int_{\Omega_0} g(\eth)\frac{\mathbf{N}_{\mathbf{T}}^{\mathsf{T}}}{2}(\mathbf{Z}^{\mathsf{T}} : \dot{\mathbf{C}})\, T\mathrm{d}V + \int_{\Omega_0} \mathbf{N}_{\mathbf{T}}^{\mathsf{T}} \cdot \mathbf{j}_{\mathbf{R}} \cdot \nabla_{\mathbf{X}}p\, \mathrm{d}V = 0 \tag{5.95}$$

where the history field variable $\mathcal{H}$ is found in the problem as

$$\mathcal{H} = \max_{t \in [0, t_f]} \Psi(\mathbf{C}, T, \Delta T, t). \tag{5.96}$$

where the expression for the local free energy function can be found in Eq. (5.47).

The element that we are presenting on this last Section of the chapter is Q1Q1Q1Q1, meaning that we employ the linear interpolation for the displacement, phase-field parameter, fluid pressure and temperature. It is based on the recently UHYPER/UMAT element subroutine presented by Zheng et al. [73, 74] along with the coupling of temperature presented in [69]. The main reason why we are presenting on this Chapter a formulation that clearly lacks the fulfillment of the LBB conditions is to establish a comparative standpoint with a future Q2Q2Q1Q1(quadratic in-

terpolation for phase-field) or `Q2Q1Q1Q1` (linear interpolation for phase-field) formulations that we will develop on a subsequent paper, highlighting the performance and stability of both schemes. However, at the time of presenting this thesis, we only have developed the scheme for a `Q1Q1Q1Q1` element, but we have discovered that the findings for fracture in our numerical examples do shed light on the problem of fracture in thermoresponsive hydrogels.

Within the FE framework, Eq. (5.71), now we include the expression to interpolate the phase-field parameter from the nodal results. Such variable is included in the residuals previously expressed within this Section:

$$\mathfrak{d} = \sum_{i=1}^{n} \mathbf{N}_{\mathfrak{d}} \cdot \hat{\mathfrak{d}} \tag{5.97}$$

along with its temporal variation

$$\dot{\hat{\mathfrak{d}}} = \frac{\hat{\mathfrak{d}}_{n+1} - \hat{\mathfrak{d}}_n}{t} \tag{5.98}$$

Now, for the application of Newton-type solution algorithms for the iterative solution of the boundary value problem, in order to linearize the weak form we have to consider also the phase-field parameter:

$$
\begin{aligned}
\hat{L}[\mathbf{R}^{\mathbf{d}}](\mathbf{d}, \delta\mathbf{d}, \Delta\mathbf{d}, \hat{p}, \Delta\hat{p}, \hat{\mathfrak{d}}, \Delta\hat{\mathfrak{d}}, \hat{T}, \Delta\hat{T}) &= \mathbf{R}^{\mathbf{d}}(\mathbf{d}, \delta\mathbf{d}, \hat{p}, \hat{\mathfrak{d}}, \hat{T}, \Delta\hat{T}) + \Delta_{\mathbf{d}}\mathbf{R}^{\mathbf{d}} \cdot \Delta\mathbf{d} \\
&\quad + \Delta_{\hat{p}}\mathbf{R}^{\mathbf{d}} \cdot \Delta\hat{p} + \Delta_{\hat{\mathfrak{d}}}\mathbf{R}^{\mathbf{d}} \cdot \Delta\hat{\mathfrak{d}} \\
&\quad + \Delta_{\hat{T}}\mathbf{R}^{\mathbf{d}} \cdot \Delta\hat{T}
\end{aligned} \tag{5.99}
$$

$$
\begin{aligned}
\hat{L}[\mathbf{R}^{\hat{p}}](\mathbf{d}, \Delta\mathbf{d}, \hat{p}, \delta p, \Delta p, \hat{T}, \Delta\hat{T}) &= \mathbf{R}^{\hat{p}}(\mathbf{d}, \hat{p}, \delta\hat{p}, \hat{T}) + \Delta_{\mathbf{d}}\mathbf{R}^{\hat{p}} \cdot \Delta\mathbf{d} \\
&\quad + \Delta_{\hat{p}}\mathbf{R}^{\hat{p}} \cdot \Delta\hat{p} + \Delta_{\hat{T}}\mathbf{R}^{\hat{p}} \cdot \Delta\hat{T}
\end{aligned} \tag{5.100}
$$

$$
\begin{aligned}
\hat{L}[\mathbf{R}^{\hat{\mathfrak{d}}}](\mathbf{d}, \Delta\mathbf{d}, \hat{p}, \Delta\hat{p}, \hat{\mathfrak{d}}, \delta\hat{\mathfrak{d}}, \Delta\hat{\mathfrak{d}}, \hat{T}, \Delta\hat{T}) &= \mathbf{R}^{\hat{\mathfrak{d}}}(\mathbf{d}, \hat{p}, \hat{\mathfrak{d}}, \delta\hat{\mathfrak{d}}, \hat{T}, \Delta\hat{T}) + \Delta_{\mathbf{d}}\mathbf{R}^{\hat{\mathfrak{d}}} \cdot \Delta\mathbf{d} \\
&\quad + \Delta_{\hat{p}}\mathbf{R}^{\hat{\mathfrak{d}}} \cdot \Delta\hat{p} + \Delta_{\hat{\mathfrak{d}}}\mathbf{R}^{\hat{\mathfrak{d}}} \cdot \Delta\hat{\mathfrak{d}} \\
&\quad + \Delta_{\hat{T}}\mathbf{R}^{\hat{\mathfrak{d}}} \cdot \Delta\hat{T}
\end{aligned} \tag{5.101}
$$

$$\hat{L}[\mathbf{R}^{\hat{T}}](\mathbf{d}, \Delta\mathbf{d}, \hat{p}, \Delta\hat{p}, \hat{\mathfrak{d}}, \Delta\hat{\mathfrak{d}}, \hat{T}, \delta\hat{T}, \Delta\hat{T}) = \mathbf{R}^{\hat{T}}(\mathbf{d}, \delta\mathbf{d}, \hat{p}, \hat{\mathfrak{d}}, \hat{T}, \delta\hat{T}, \Delta\hat{T}) + \Delta_{\mathbf{d}}\mathbf{R}^{\hat{T}} \cdot \Delta\mathbf{d}$$
$$+ \Delta_{\hat{p}}\mathbf{R}^{\hat{T}} \cdot \Delta\hat{p} + \Delta_{\hat{\mathfrak{d}}}\mathbf{R}^{\hat{T}} \cdot \Delta\hat{\mathfrak{d}}$$
$$+ \Delta_{\hat{T}}\mathbf{R}^{\hat{T}} \cdot \Delta\hat{T}$$

$$(5.102)$$

This leads to the following linearised system of equations represented by the global N-R monolithic scheme

$$
\begin{bmatrix}
\mathbf{K^{dd}} & \mathbf{K^{d\hat{p}}} & \mathbf{K^{d\hat{\mathfrak{d}}}} & \mathbf{K^{d\hat{T}}} \\
\mathbf{K^{\hat{p}d}} & \mathbf{K^{\hat{p}\hat{p}}} & \mathbf{K^{\hat{p}\hat{\mathfrak{d}}}} & \mathbf{K^{\hat{p}\hat{T}}} \\
\mathbf{K^{\hat{\mathfrak{d}}d}} & \mathbf{K^{\hat{\mathfrak{d}}\hat{p}}} & \mathbf{K^{\hat{\mathfrak{d}}\hat{\mathfrak{d}}}} & \mathbf{K^{\hat{p}\hat{T}}} \\
\mathbf{K^{\hat{T}d}} & \mathbf{K^{\hat{T}\hat{p}}} & \mathbf{K^{\hat{T}\hat{\mathfrak{d}}}} & \mathbf{K^{\hat{T}\hat{T}}}
\end{bmatrix}
\begin{bmatrix}
\Delta\mathbf{d} \\
\Delta\hat{\mathbf{p}} \\
\Delta\hat{\mathbf{\mathfrak{d}}} \\
\Delta\hat{\mathbf{T}}
\end{bmatrix}
= -
\begin{bmatrix}
\mathbf{R^d} \\
\mathbf{R^{\hat{p}}} \\
\mathbf{R^{\hat{\mathfrak{d}}}} \\
\mathbf{R^{\hat{T}}}
\end{bmatrix}
$$

$$(5.103)$$

which, in order to reduce the computational cost and the number of iterations required upon solving [49], we opt for a staggered scheme by employing only the terms in the diagonal. The system of equations now is expressed as:

$$
\begin{bmatrix}
\mathbf{K^{dd}} & \mathbf{0} & \mathbf{0} & \mathbf{0} \\
\mathbf{0} & \mathbf{K^{\hat{p}\hat{p}}} & \mathbf{0} & \mathbf{0} \\
\mathbf{0} & \mathbf{0} & \mathbf{K^{\hat{\mathfrak{d}}\hat{\mathfrak{d}}}} & \mathbf{0} \\
\mathbf{0} & \mathbf{0} & \mathbf{0} & \mathbf{K^{\hat{T}\hat{T}}}
\end{bmatrix}
\begin{bmatrix}
\Delta\mathbf{d} \\
\Delta\hat{\mathbf{p}} \\
\Delta\hat{\mathbf{\mathfrak{d}}} \\
\Delta\hat{\mathbf{T}}
\end{bmatrix}
= -
\begin{bmatrix}
\mathbf{R^d} \\
\mathbf{R^{\hat{p}}} \\
\mathbf{R^{\hat{\mathfrak{d}}}} \\
\mathbf{R^{\hat{T}}}
\end{bmatrix}
$$

$$(5.104)$$

where the Jacobian stiffness matrix have the following expression

$$\mathbf{K^{dd}} = \frac{\partial \mathbf{R}^d}{\partial \mathbf{u}} = g(\mathfrak{d}) \Big[\int_{\Omega_0} \nabla_{\mathbf{X}} \mathbf{N_d^T} \cdot \mathbb{C} \cdot \nabla_{\mathbf{X}} \mathbf{N_d} \, dV + \int_{\Omega_0} \big[\nabla_{\mathbf{X}} \mathbf{N_d^T} \cdot \mathbf{S} \cdot \nabla_{\mathbf{X}} \mathbf{N_d} \big] \cdot \mathbf{1} \, dV \Big]$$

$$(5.105)$$

$$\mathbf{K}^{\hat{p}\hat{p}} = \frac{\partial \mathbf{R}^{\hat{p}}}{\partial p} = -\int_{\Omega_0} \frac{\Delta t \, m \, J_n}{J_0} \, \mathbf{F_n^{-T}} \cdot \nabla_{\mathbf{X}} \mathbf{N_p^T} \cdot \mathbf{F_n^{-T}} \cdot \nabla_{\mathbf{X}} \mathbf{N_p} \, dV \quad (5.106)$$

$$\mathbf{K}^{\hat{\mathfrak{d}}\hat{\mathfrak{d}}} = \frac{\partial \mathbf{R}^{\hat{\mathfrak{d}}}}{\partial p} = \int_{\Omega_0} \Big[2\frac{\mathcal{G}_C}{\ell}\mathcal{H} \Big] \mathbf{N_{\mathfrak{d}}^T} \cdot \mathbf{N_{\mathfrak{d}}} \, dV + \int_{\Omega_0} 2\mathcal{G}_C \ell \, \nabla_{\mathbf{X}} \mathbf{N_{\mathfrak{d}}^T} \cdot \nabla_{\mathbf{X}} \mathbf{N_{\mathfrak{d}}} \, dV$$

$$(5.107)$$

$$\mathbf{K}^{\hat{T}\hat{T}} = \frac{\partial \mathbf{R}^{\hat{T}}}{\partial T} = \int_{\Omega_0} \mathbf{N_T^T} \cdot \frac{c_p}{\Delta t} \cdot \mathbf{N_T} \; - \int_{\Omega_0} g(\mathfrak{d})\mathbf{N_T^T} \cdot \frac{(\mathbf{Z^T} \cdot \dot{\mathbf{C}})}{2} \cdot \; \mathbf{N_T} \, dV$$

$$+ \int_{\Omega_0} g(\mathfrak{d})\nabla_{\mathbf{X}} \mathbf{N_T^T} \cdot \mathbf{K} \cdot \mathbf{F^{-T}} \cdot \nabla_{\mathbf{X}} \mathbf{N_T} \, dV - \int_{\Omega_0} \mathbf{N_T^T} \cdot \frac{\mathbf{j_R} \cdot \nabla_{\mathbf{X}} p}{T} \cdot \mathbf{N_T} \, dV$$

$$(5.108)$$

5.6.3 Numerical fracture of hydrogels: 2-D single edge notched gels

The effectiveness of the proposed Q1Q1Q1Q1 formulation to model fracture in hydrogels is put into test by performing an analysis into a single edge notched tension (SENT) sample, based on the example in Section 4.1 of the work by Zheng et al. [73]. The geometry the sample is plotted in Fig. 89(a) and is set up like this: with an initial crack length of 20 mm and by benefitting from symmetry conditions, we fix the bottommost side of the specimen, while we apply to the topmost edge a vertical displacement of $u_y = 20$ mm. The test is carried out on isothermal conditions, with a temperature of $T = 298$ K prescribed for the whole specimen. For this experiment, we employ a discretization of 8,540 first order quadrilateral elements, with a remeshing made in the area around the crack path of $h = 0.1$ mm; such mesh can be observed in Fig. 89(b). Concerning properties, the mechanical properties of the specimen are given in Table 29 and the thermal properties are the same as the ones displayed in Table 28.
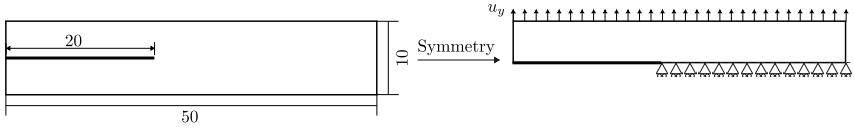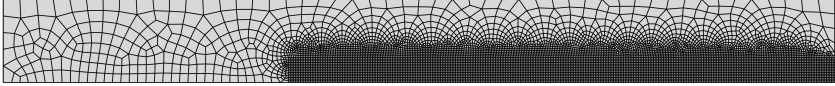
Figure 89: (a) Geometry of the SENT specimen with dimensions in mm; and (b) employed mesh. We depict the full probe and the conducted sample, with symmetry conditions applied.

Table 29: Material properties employed for the SENT specimen conducted to fracture associated to displacement-mass diffusion-phase-field fields.

$Nk_BT = G$(MPa)	$N\nu$	$\chi_L \approx \chi$	D (mm^2/s)	$\mathcal{G}_{\mathcal{C}}$(N/mm)	ℓ(mm)
0.4	0.01	0.1	5×10^{-2}	2.4	1

The experiment encompasses two steps, analog to the previous examples observed within this Chapter: the first one consists in the free swelling, absent from stresses and damage, where depending on the concentration of solvent present within the hydrogel, i.e. the parameter of λ_0, the specimen will get more or less swollen. Such step encompasses a total time of $t = 300$ s. Then, for a maximum time of 2 hours, in the second and final step, the specimen is pulled from the top upon total fracture of the hydrogel sample; for the tension step, aiming for the best convergence possible, we will employ a fixed time step of $\Delta t = 0.72$ s, resulting the experiment in a maximum of 10,000 steps. We will conduct four different tests varying the initial stretch parameter as
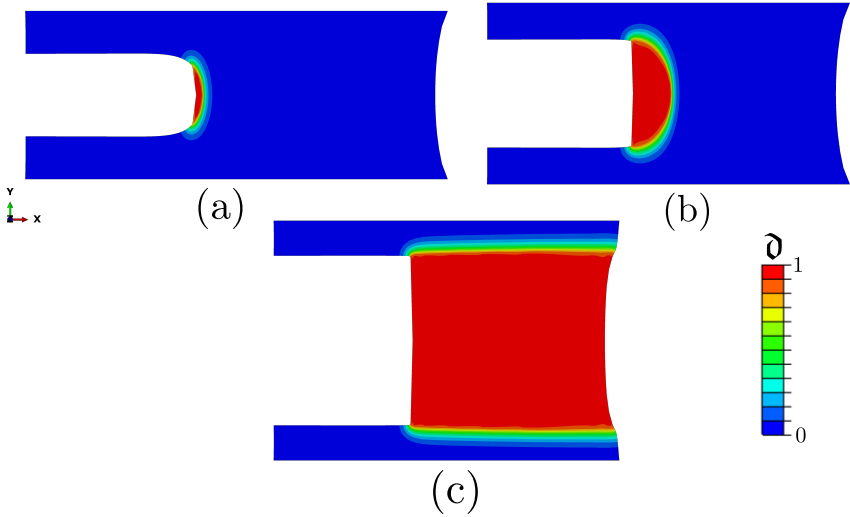
Figure 90: Phase-field isocontours depicting the (a) initiation, (b) propagation and (c) final states in crack propagation of the SENT hydrogel specimen with $\lambda_0 = 2.1544$.

$\lambda_0 = [2.1544, 1.7100, 1.4938, 1.3572]$.

From a qualitative standpoint, we have plotted the phase-field parameter at the deformed configuration of the hydrogel for the different cases changing λ_0. First, in the hydrogel with more solvent content, $\lambda_0 = 2.1544$, the pulling test runs smooth, with barely any complications in convergence until the end of test. In Fig. 90 is exhibited the crack evolution in the specimen; nucleating from the initial notch tip (Fig. 90(a)) and propagating in Mode I (Fig. 90(b)) until the solid is divided into two parts (Fig. 90(c)). Even though the `Q1Q1Q1Q1` formulation is known for not being LBB stable, it still manages to run this experiment without displaying any local instabilities.

As we reduce the content of water within the solvent, local instabilities start to show up during the crack fracture process, with elements in the crack notch tip becoming more distorted as the gradient of stresses increase. This is illustrated in Fig. 91, where, for $\lambda_0 = 1.3572$, we can observe the excessive distortion of such elements when the crack starts
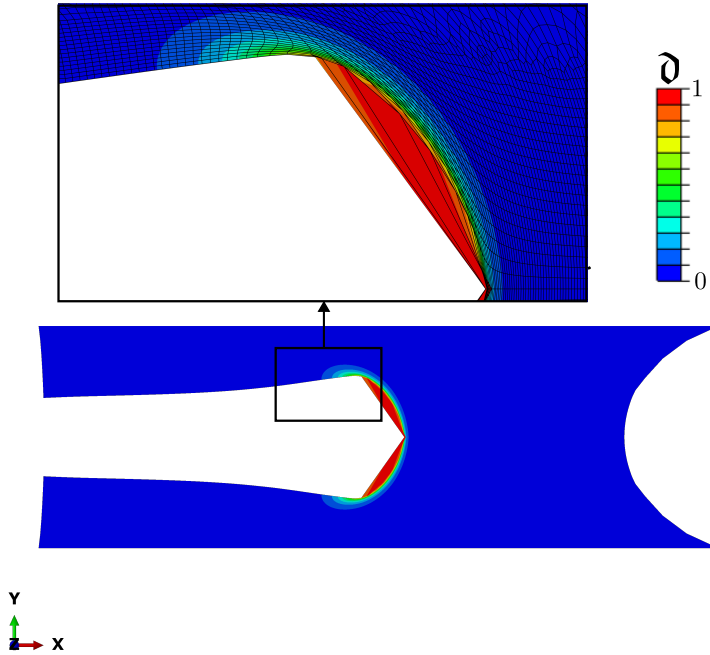
Figure 91: Illustration of the instability due to volumetric locking in the notch tip of the SENT hydrogel with initial stretch $\lambda_0 = 1.3572$.

to nucleate in the notch tip. The appearance of such instabilities is due to first order displacement interpolation schemes not fulfilling the LBB conditions in nearly incompressible materials for hydrogels modelling and, subsequently, leading to volumetric locking [327], that complicates convergence, causing the analysis to stop prematurely upon passing the maximum applied load on the model. Such imperfections also appear for the specimens with $\lambda_0 = 1.7100$ and $\lambda_0 = 1.4938$, but the analysis converges until the end, with a slight increase in the required number of iterations. We believe that by increasing the order of the displacement and the phase-field interpolation up to quadratic (Q2Q2Q1Q1 element) or even, just, the displacement (Q2Q1Q1Q1 element) could fix this problem. Therefore, this is proposed for the continuation of this project.

In order to compare quantitatively the performance of all the samples,
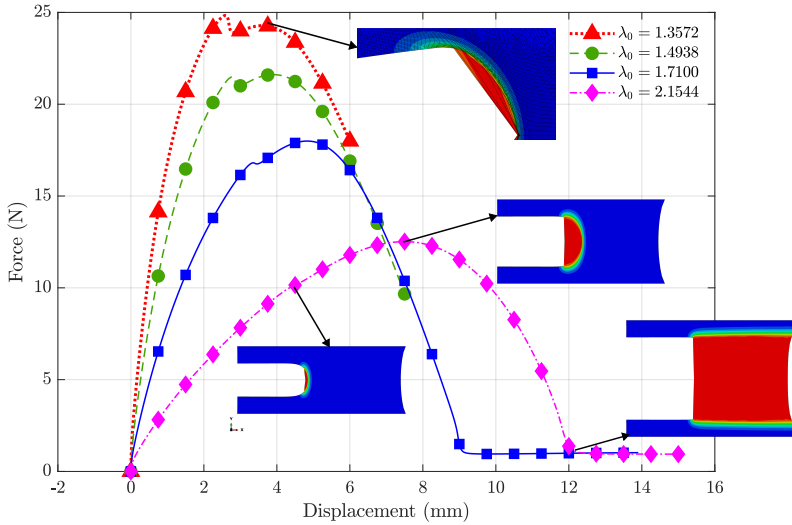
Figure 92: Reaction force-displacement curves for all the conducted SENT hydrogel tests for different initial stretch conditions λ_0. We have included also the micrographs for the evolution of crack fracture along with the instability.

we have plotted in Fig. 92 the force-displacement graphs for all the run SENT tests. In general, it is observed that as the water content is reduced, the stiffness of the curve increases considerably, leading to an augment in the maximum loading force and a slightly earlier failure. While the curve with $\lambda_0 = 2.1544$ does not show it, displaying a smooth crack propagation, all the other three graphs display an elbow in the middle of their trayectory, around the value for $u_y \approx 3$ mm, being this due to the appearance of the local instability caused by the volumetric locking of the specimen, an event that will be tackled in future approaches involving hydrogels modelling. It can be deducted that the combination of both quantitative and qualitative results for the SENT fracture modelling leaves the field open for a future implementation of a `Q2Q2Q1Q1/Q2Q1Q1Q1` element, being this covered series of experiments a suitable framework for comparison of the performance of both schemes.

211

Chapter 6

Conclusions and future developments (ENG) / Conclusiones y desarrollos futuros (ESP)

6.1   Conclusions and future developments (ENG)

The research work in this thesis has been dedicated to the application of diffuse damage models, specifically the phase-field and the continuum damage techniques, to diverse coupled problems in science and engineering. With the advent of multidisciplinary approaches in the industrial sector, there is a growing attention on the influence of chemical, electrical, biological fields, among others, in the structural integrity of the materials and a solid proof of that influence has been demonstrated by the performed computation of multi-physics failure by these continuum damage techniques.

The results for all the covered coupled approaches in this thesis are addressed in the forthcoming Sections, along with a brief discussion on likely future improvements.

6.1.1 Summary and final remarks for hydrogen-induced fracture in polycrystalline materials

Conclusions

We have presented in Chapter 2 a new microstructurally-sensitive deformation-diffusion-fracture formulation to predict hydrogen embrittlement in elastic-plastic solids. The modelling framework is able to explicitly resolve the microstructure and capture the transition from ductile transgranular fracture to hydrogen-assisted brittle intergranular cracking. This is achieved by combining a phase field description of transgranular cracks with a cohesive zone model that simulates decohesion at the grain boundary interfaces. The capabilities of the model in bringing new insight and understanding are demonstrated by addressing three representative boundary value problems.

First, the competition between transgranular and intergranular cracking is investigated with a single edge notched tension specimen that contains 10 and 50 grains. The expected qualitative trends are captured, with cracking mechanisms changing as a function of the environment. Second, recent slow strain rate test (SSRT) experiments on a Ni-Cu superalloy (Monel K-500) [218] are simulated to demonstrate the ability of the model to quantitatively predict failure times for different environments and material heats. The model is also used to discuss the suitability of SSRT experiments, showing that cracks nucleating along grain boundaries located near the surface can rapidly propagate inwards and significantly reduce the load carrying capacity. Finally, the paradigmatic experiments by Harris et al. [86] on polycristalline Ni samples at ambient and cryogenic temperatures are reproduced. The model is shown to predict both the qualitative cracking modes and the quantitative stress-strain responses for the four conditions (with and without hydrogen, at 77 K and 298 K). Furthermore, mechanistic insight into the embrittlement of polycrystalline Ni is gained, showing that grain boundary decohesion is a first order effect, and that the differences between the responses observed at ambient and cryogenic temperatures can be rationalised by the additional content of hydrogen accumulated in grain boundaries due to

diffusion. The numerical experiments conducted also showcase the computational robustness of the method, with significant cracking being predicted without convergence issues.

Further developments

Further insights will comprise deeper investigations concerning the interplay of the hydrogen diffusion with the microstructural phase. First, some preliminary studies have been carried out with the benchmark specimens concerning the trajectory of the crack during the transgranular fracture, see Figs. 12 and 16, where is observed that during its growth, while fracture follows a path within the grain, it goes along the direction of the grain boundaries. This is contrary to what is observed in seminal works such as the one by Harris et al. [86]. In their study, they observed that during ductile fracture, the nucleation and coalescence of the voids happening in the domain led to crack propagation splitting the grain into two different subdomains. Preliminary works represented in Fig. 93 for the 50-grain specimen conducted in Section 2.3.1 for a refined mesh of $h_e = 0.01$ mm exhibit a clear dependence of the crack trajectory in the length scale of the specimen. In fact, these micrographs reveal that the numerical example matches the experiment when $\ell = h_e$, see Fig. 93(c), as for these values, the crack propagates through the middle of the grains. This states that in order to obtain results closer to the experiments, the mesh refinement is a high priority when dealing with polycrystalline structures, as that is a condition to reduce ℓ in the analyzed specimen. Due to this numerical issue not being covered yet in the bibliography, we aim to address it in forthcoming journal publications concerning HE phenomena in polygrain specimens.

In parallel to this, some other phenomena favouring or hindering HE are to be addressed in further works employing this multiscale approach as a base. One of them is hydrogen trapping, that consists in the event where, upon diffusing through the lattice, hydrogen atoms may reside at either lattice sites or microstructural trapping sites such as dislocations, voids or grain boundaries. Whether HE is governed by each one of these methods is still a matter of debate [86, 206, 78], but the concentration of

(a) $\ell = 0.02$ mm   **(b) $\ell = 0.015$ mm**   **(c) $\ell = 0.01$ mm**
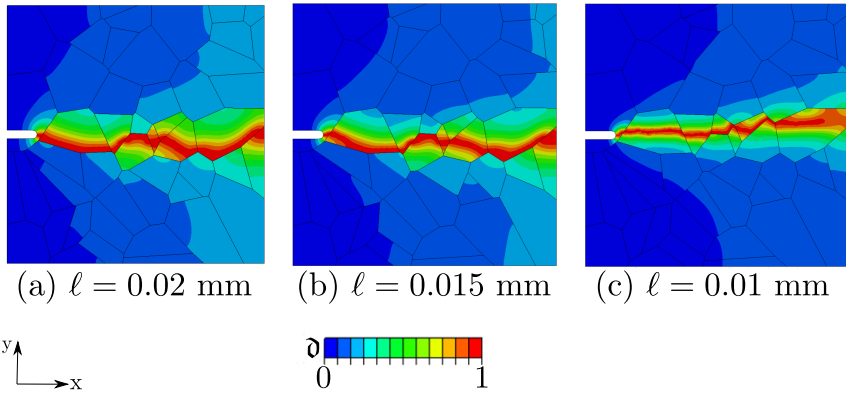
Figure 93: (ENG) Dependence of the crack propagation on the length scale ℓ: results for a mesh refinement of $h_e = 0.01$mm / (ESP) Dependencia en la propagación de grieta del parámetro *length scale* ℓ: resultados para una malla refinada de $h_e = 0.01$mm.

hydrogen in lattice sites is generally in equilibrium with the concentration in trapping sites [350]. As hydrogen trapping has been covered in the biliography concerning structural integrity issues [351, 352], the authors find that the developed deformation-diffusion-fracture framework combining the PF method for transgranular fracture and the CZM for intergranular fracture could be extended to model hydrogen trapping comprising the crystal plasticity (CP) formulation. This multi-scale process, consisting of a number of grains with random shapes and orientations with different mechanical properties assigned to each one of them, accounts for the role of dislocations at the atomic scale in controlling features of plastic deformation such as the glide planes, slip and twinning of dislocations, dislocation mobility, among other essential factors for crystallographic crack initiation and growth [353, 354]. The implementation of the CP approach into the framework of Chapter 2 along with the consideration of hydrogen trapping is currently under development.

6.1.2 Fracture in pre-stressed cylindrical bio-inspired elastomer-like materials: final remarks and future applications

Conclusions

Phase field methods for fracture simulation have evidenced several appealing aspects stemming from its inherent versatility to accommodate different mechanical behavior at the material point level. Exploiting a modular formalism, in Chapter 3, a novel coupled phase field approach has been developed to simulate fracture events for residually stressed hyperelastic (rate independent) and visco-hyperelastic (rate dependent) hollow cylinders. The current computational model relies on the already proposed visco-hyperelasticity theoretical formulation and it has been extended to consider residual stress fields in terms of an invariant-based formulation.

The proposed methodology was first validated against available experimental data featuring quasi-static fracture evolution. Subsequent parametric analysis examined the role of different mechanical aspects of the system in line with other works that use alternative phase field models for hyperelastic and visco-hyperelastic solids. Current simulations assessed the fracture of one-layered and two-layered cylindrical structures evaluating both viscous (τ and $\dot{u}$) and mechanical ($\mathcal{G}_C$ and μ mismatch) effects for several residual stress fields (which depend on the coordinates R and Z of the cylinder). Interestingly, the incorporation of residual stress fields in multi-layered cylindrical systems led to (a priori) unexpected results in terms of crack initiation and propagation mechanisms. This evidenced the need of the development of robust numerical frameworks that can take into consideration such effects.

Further developments

Therefore, growing from the last sentence of the previous Section, further extensions of this research would concern the application of this code to the analysis of bending and bulging instabilities in these kind of structures to simulate the fracture of arteries which suffer aneurysms. Based on the work carried out by Desena-Galarza et al. [296], the main goal
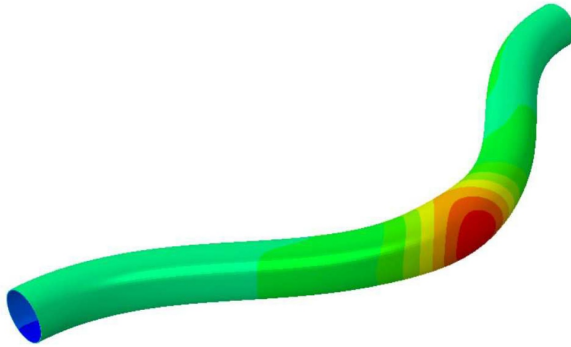
Figure 94: (ENG) Bulging instability ocurring at the middle of a cylinder. Image taken from a numerical analysis from Desena-Galarza et al. [296]. / (ESP) Inestabilidad de hinchazón sucediendo en el medio de un cilindro. Imagen tomada de un análisis numérico llevado a cabo por Desena-Galarza et al. [296].

of this analysis would be to establish a correlation of the structural integrity, computed by the PF method, with the initiation of arterial wall bifurcation in these cylindrical tubes, which is due to the onset of bulges like the one plotted in Fig. 94.

Another approach of interest that resembles a potential extension of the residual stress framework is the incorporation of anisotropic material laws in the layer-definition. In fact, the implementation of nonlinear anisotropic laws, such as the Gasser-Ogden-Holzapfel (GOH) [355], originally developed to model arterial tissue, holds significant importance within this formulation. This choice allows for a more precise representation of the complex and heterogeneous material behavior exhibited by the arterial wall. According to the GOH model, it separates the contributions of the extracellular matrix material and embedded collagen fibers, treating them as distinct components responsible for the material characteristics of the arteries [356]. The GOH model along with the study of bulding and bending instabilities is being currently implemented in the UMAT presented for Chapter 3.

6.1.3 Conclusions and future developments for gradient-enhanced damage models in compressible and nearly incompressible hyperelastic materials

Conclusions

Within Chapter 4, a duo of gradient-enhanced continuum damage formulations has been developed to model failure in compressible and incompressible isotropic hyperelastic specimens, with the main focus of addressing the volumetric and shear locking pathologies. Among these experiments, the samples have been tested to a wide range of different types of loading, including traction, compression, and bending, comparing the two novel schemes, `Q1Q1E24` and `Q1Q1P0`, with the `Q1Q1` referential CDM formulation.

Making a one-by-one analysis of the performance of the aforementioned schemes, first the spatial standard CDM framework (`Q1Q1`), based on the one proposed by [111], has been validated in this work to be a remarkable instrument in modelling damage in compressible structures subject to extensive pulling. However, it has exhibited both volumetric and shear locking in incompressible specimens under compression and bending status, respectively.

Therefore, in order to overcome these locking pathologies, the 24-incompatible modes EAS technique `Q1Q1E24` and the mixed displacement-Jacobian-pressure FE formulation `Q1Q1P0` have been proposed for their use. `Q1Q1E24` scheme is proven to solve the shear locking phenomenon in compressible samples, while the employment of `Q1Q1P0` formulation, by considering both the pressure and the dilatation as separate DOFs, has been demonstrated to be a more than a remarkable instrument in modelling complex incompressible cases, correcting the volumetric locking pathology.

Further developments

During our analysis, it has also been demonstrated that `Q1Q1E24` element performs poorly in predicting damage in incompressible materials, while `Q1Q1P0` overestimates the curve in structures subject to bending
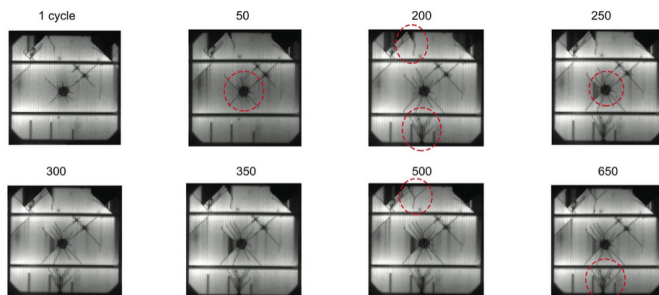
Figure 95: (ENG) Degradation of the electric response and increasing crack pattern at different bending cycles caused by fatigue. Taken from [358]. / (ESP) Degradación en la potencia eléctrica con el aumento de los ciclos de flexión a fatiga. Tomado de [358].

loads, i.e., displaying shear locking. Therefore, to tackle this, further approaches combining EAS with the mixed Jacobian-pressure formulations are to be proposed in the future. In addition to this, an extension to model anisotropic hyperelastic almost incompressible materials is proposed here for future work, being envisaged as a compelling but challenging extension of the proposed frameworks, considering the distortion that such kind of materials exhibit during pure pressure loading [357].

Aiming for more practical applications, the large deformation model for fracture along with the mixed formulations of displacement-pressure-Jacobian or the EAS interpolation is envisaged as a potential candidate to address the multi-scale and multi-physics problem for reliable fracture prediction and simulation of solar photovoltaic (PV) systems. PV structures generally operate in a multifield environment (including mechanical, thermal and electrical phenomena), subjected to different service conditions that can lead to degradation from different signatures where defects such as micro-cracks and delamination introduce significant power loss [358], see Fig. 95. As the solar pannels are comprised by a laminate disposal for silicon (Si) exhibited in Fig. 96, they are prone to display locking pathologies as their thickness is relatively small to the
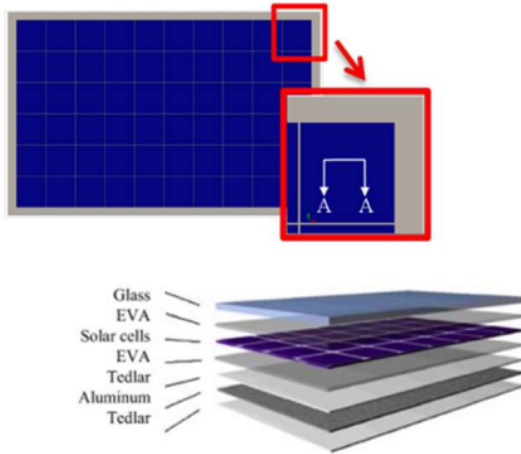
Figure 96: (ENG) Assembly of the laminate of a Si-based PV-module. / (ESP) Ensamblaje de un laminado de panel fotovoltaico de silicio.

other dimensions. This is where mixed interpolations, such as the EAS-ANS solid-shell elements [359], prove to be invaluable for modelling of laminates.

Considering these events, the next main goal of the CDM approach developed in Chapter 4 is to attain the simulation of such solar laminates by adapting it to solid shell formulation with either the CDM or the PF approach for analysis of the structural integrity of solar PV systems. The complex behavior of PV systems, with different scales of observations and multi-material arrangement, has motivated the use of numerical the application of homogenization-based multiscale and global-local methodologies for high-fidelity micromechanical analysis of silicon pannels. In the light of such approaches, currently, we are developing this multi-scale and multi-physics framework for solar pannels by considering the global-local approach implemented by Liu et al. for solid shells [360].

6.1.4 Swelling of thermoresponsive hydrogels: main results and future improvements

Conclusions

We have presented in Chapter 5 an inf-sup stable element for the modelling of thermoresponsive hydrogels in the form of a `UEL` subroutine. Specifically, we have adapted a mixed displacement-temperature-fluid pressure theory for its FE implementation in the analysis of transient free swelling in hydrogels. In order to achieve fulfillment of the LBB conditions and thus, gain inf-sup stability, we have adopted a quadratic interpolation for the displacement field and a linear interpolation for the temperature and the fluid pressure fields, thus employing a `Q2Q1Q1` formulation.

First, the functionality of the `Q2Q1Q1` element has been tested by analyzing a free swelling state followed by a subsequent deswelling caused by a temperature gradient, performing very solidly. Subsequently, the dependence of the diffusion length on the mesh, a topic that has hastily been covered, has been evaluated by checking the pressure variations in the specimen, proving the importance of picking an appropiate discretization to avoid any visible oscillations in the fluid pressure. To conclude the verification part, we have compared the importance in the free swelling behavior of the temperature variation due to fluid flow and elastic stretching, coupled terms that have been ignored in the referential works due to their minor influence; we have found that due to the low stiffness that hydrogels present, such terms should be considered for an appropiate swelling test, not only in terms of accuracy, but also in convergence. In addition to this, the model has achieved accuracy in capturing experimental results by correlating the effect of the cross-linking density on the swelling behavior for PNIPAAm hydrogels, varying temperature.

Simultaneously, the branch to model fracture of thermoresponsive hydrogels by employing the PF technique has been opened. In the light of this, we have developed a preliminary PF `Q1Q1Q1Q1` scheme to model them. Whereas the proposed displacement-phase field-temperature-fluid pressure scheme reaches conclusive results on the conduction of a SENT

specimen until fracture, important concerns regarding the inf-sup stability of the formulation are raised, which are reasoned in the forthcoming Section.

Further developments

Although the `Q1Q1Q1Q1` element manages to fully model fracture for the SENT specimens, it does not guarantee inf-sup stability. From here, we can extract that to fulfill this condition, the degree of interpolation will have to be increased, making the element `Q2Q1Q1Q1` or `Q2Q2Q1Q1` (the difference between both elements relies on the degree of interpolation for the PF DOFs). The choice of either discretization along with the realization of more representative examples is currently under development and will be presented in future journal articles.

Moving to more practical applications, an experiment that we are aiming to cover is the dependence on the temperature for the compression of agarose spheres, an UCST thermoresponsive hydrogel; currently under development in the lab, the main objective is to see how the decay in the swelling ratio by cooling down the specimen (see Fig. 8) affects the results of this mechanical test. In the context of fracture studies, another primary objective in applying the PF approach to model fracture of thermoresponsive hydrogels is to establish a correlation of the numerical results with experimental observations. To achieve this, we will employ the universal testing machine depicted in Fig. 97. Cleared to model fracture of hydrogels, these experiments will involve the use of a video extensometer and will encompass both tension and compression tests conducted until failure occurs. Furthermore, these tests will be carried out at various temperatures to establish a quantitative standpoint of the structural integrity with the swelling ratio.

6.1.5   To conclude

The efforts devoted in this thesis to implement the phase-field theory to model fracture in coupled problems are the pure reflection of the progress made in multidisciplinary processes, specifically in the concerns on the

Figure 97: (ENG) Instron 68SC-5 universal testing machine [361], which will be employed for hydrogel tensile and compressive experiments. / (ESP) Máquina de ensayos universal Instron 68SC-5 [361], que será utilizada para ensayos a tracción y compresión en hidrogeles.

structural integrity influenced by other fields. The conclusive results achieved in the branches of swelling of thermoresponsive hydrogels, fracture induced by hydrogen and failure of hyperelastic compressible and incompressible materials not only establish the phase-field technique as a versatile and accurate method to tackle this kind of problems, but also relatively straight forward to implement as the Euler-type equation can be modified to account for these outer variables. In summary, for the present, phase-field approach for fracture comprises a cutting edge application ideal for Computational Mechanics problems relying on multiphysical material laws. To make a prediction of where the future landscape for phase-field coupled approaches is leading to, besides the clas-

sical empirical material modeling step of conventional computing, it is worth stating that the data-driven methods, such as Deep Learning or Machine Learning, currently being exploited on another areas, will be of vital importance for the development of this research in the near future, with some preliminary works already being published [362, 363, 364, 365].

To close up this thesis, we start by referring the reader again to Fig. 1. Upon examining all the possible applications and at the same time, all the covered approaches from this work, one may extract that only the "top of the iceberg" has been addressed here, in this work. While that statement is true, it cannot be denied that the complexity that surrounds every coupled problem endows them with an importance that just the resolution for just one of them may constitute the central topic for a thesis by itself and given the wide range that this diagram presents, trying to cover the whole spectrum for coupled problems in Fracture Mechanics is a never ending task. Therefore, from this statement, we can extract that whilst multi-physics problems in Computational Fracture Mechanics still comprise a relevant subject in the literature, there will be always room for further research on this matter.

6.2 Conclusiones y desarrollos futuros (ESP)

El trabajo de investigación llevado a cabo en esta tesis se ha dedicado al estudio y a la aplicación de modelos de daño difuso: el método *phase-field*, principalmente, y la técnica de daño continuo; a diversos problemas acoplados en ciencia e ingeniería. Con el surgimiento de los enfoques multidisciplinares en el sector industrial, está habiendo un creciente interés en la influencia que campos químicos, eléctricos, biológicos, entre otros, pueden tener sobre la integridad estructural de los materiales. Una sólida prueba de ese impacto ha sido demostrado mediante el estudio a fractura en estos problemas de temática *multi-física* empleando estas técnicas de daño difuso.

Los resultados de todos los problemas acoplados cubiertos en esta tesis se abordarán en las siguientes secciones, junto con una breve dis-

cusión sobre posibles implementaciones futuras.

6.2.1 Resumen y observaciones finales sobre la fractura inducida por hidrógeno en materiales policristalinos.

Conclusiones

Hemos presentado en el Capítulo 2 una nueva formulación a microescala considerando deformación, difusión de hidrógeno y fractura para predecir la fragilización por hidrógeno en sólidos elasto-plásticos. Este marco es capaz de resolver explícitamente la microestructura y capturar la transición entre fractura dúctil transgranular a fractura frágil intergranular inducida por hidrógeno. Esto se logra mediante la combinación de una implementación de *phase-field* para modelar grietas transgranulares junto con un modelo de zona cohesiva (*cohesive zone model*) que simula la decohesión de los límites de granos. Las capacidades del modelo para ayudar a entender mejor el problema se han demostrado abordando tres problemas representativos.

En primer lugar, se investiga la competencia entre fractura transgranular e intergranular en una probeta a tracción que presenta una entalla en el borde. Se han evaluado dos tipos de estructura: una con 10 granos y otra con 50 granos. En estos casos, se han capturado las tendencias cualitativas esperadas, con los mecanismos de fractura cambiando en función de la concentración de hidrógeno en el entorno. A continuación, se han simulado los recientes experimentos a velocidad de deformación lenta (*slow strain rate test (SSRT)*) estudiados para una super-aleación de Ni-Cu (Monel K-500) [218] con el objetivo de evaluar la capacidad del modelo para predecir cuantitativamente los tiempos de fallo para diferentes entornos y materiales. El modelo también se ha utilizado para discutir la idoneidad de los experimentos de SSRT, demostrando que las grietas que se originan a lo largo de los límites de grano cercanos a la superficie pueden propagarse rápidamente hacia el interior y reducir significativamente la capacidad de carga. Finalmente, se han reproducido los experimentos paradigmáticos de Harris et al. [86] en muestras de Ni

policristalino a temperaturas ambiente y criogénicas. Se demuestra que el modelo predice tanto los mecanismos de fractura así como las curvas de tensión-deformación para las cuatro probetas analizadas (con y sin hidrógeno, a 77 K y 298 K). Además, se obtiene una mayor comprensión de la fragilización del Ni policristalino, mostrando que la decohesión en los límites de grano es un efecto de primer orden y que las diferencias entre las respuestas observadas a temperaturas ambiente y criogénicas pueden explicarse por la mayor cantiduad de hidrógeno acumulada en los límites de grano debido a la difusión. Los experimentos numéricos realizados también demuestran la robustez computacional del método, ya que predice una fractura significativa sin problemas de convergencia.

Desarrollos futuros

Se pretende llevar a cabo una investigación más profunda sobre la interacción entre la difusión de hidrógeno con la fase microestructural. En primer lugar, se han llevado a cabo algunos análisis preliminares en relación a la trayectoria de la grieta durante la fractura transgranular en los ejemplos de referencia representados en las Figs. 12 y 16. Aquí se observa que, durante su crecimiento, mientras la fractura sigue una trayectoria dentro del grano, esta va pegada y paralela a la dirección de los límites de grano. Esto difiere con lo que se observa en trabajos seminales como el de Harris et al. [86]. En su estudio, observaron que durante la fractura dúctil, la nucleación y coalescencia de las cavidades en el dominio es lo que lleva a la propagación de la grieta por el centro, dividiéndose el grano en dos subdominios diferentes. Las micrografías representadas en la Fig. 93 para la muestra de 50 granos estudiada en la Sección 2.3.1, ahora con una malla refinada de $h_e = 0.01$ mm, muestran una clara dependencia de la trayectoria de la grieta con el parámetro *length-scale*. De hecho, estos contornos revelan que el ejemplo numérico coincide con el experimento cuando $\ell = h_e$, véase la Fig. 93(c), ya que para estos valores, la grieta se propaga por el centro de los granos. Esto indica que, para obtener resultados más cercanos a los experimentos, el refinamiento de la malla debe ser tenido en cuenta al tratar con estructuras policristalinas, ya que esa es una condición necesaria para reducir

ℓ en la muestra analizada. Debido a que este problema numérico aún no se ha abordado en la bibliografía, tenemos como objetivo analizarlo para así poder incluir estos resultados en revistas científicas relacionadas con los fenómenos de fragilización por hidrógeno.

Paralelamente a esto, se abordarán en futuros trabajos algunos otros fenómenos que favorecen o dificultan la fragilización por hidrógeno utilizando un enfoque multiescala como base. Uno de ellos son las trampas de hidrógeno, que surgen de la competición que ocurre cuando los átomos de hidrógeno difunden a través de la red cristalina, ya que pueden residir o bien en sitios de la red o en trampas microestructurales como dislocaciones, cavidades o límites de grano. Si la fragilización de hidrógeno está gobernada principalmente por uno de estos mecanismos es todavía un motivo de debate [86, 206, 78], pero se puede establecer que la concentración de hidrógeno en los sitios de la red generalmente está en equilibrio con la concentración en los sitios donde está capturado [350]. Dado que las trampas de hidrógeno han sido estudiadas en la bibliografía en problemas de integridad estructural [351, 352], consideramos que el marco desarrollado de deformación-difusión-fractura, que combina el método *phase-field* para la fractura transgranular y el modelo de zona cohesiva para la fractura intergranular, podría extenderse para modelar las trampas de hidrógeno incorporando la formulación de plasticidad cristalina (*crystal plasticity*). Esta formulación a multiescala considera la estructura policristalina con formas y orientaciones aleatorias así como con diferentes propiedades mecánicas asignadas a cada grano. La plasticidad cristalina aplicada a fractura se centra en el papel que las dislocaciones tienen en el control de parámetros de la deformación plástica a escala atómica como: los planos de deslizamiento, el deslizamiento y unión de dislocaciones, la movilidad de las dislocaciones, entre otros factores esenciales, para la iniciación y propagación de grietas cristalográficas [353, 354]. La implementación de CP en el marco del Capítulo 2, junto con la consideración de las trampas de hidrógeno, se encuentra actualmente en desarrollo.

6.2.2 Fractura en tubos cilíndricos de elastómero con tensiones residuales: observaciones finales y aplicaciones futuras.

Conclusiones

Los métodos de *phase-field* para la simulación de fractura han demostrado varias ventajas derivadas de su inherente versatilidad para implementar diferentes comportamientos mecánicos. Por ello, en el Capítulo 3, se ha implementado un novedoso enfoque de la técnica de *phase-field* para simular fractura en cilindros huecos residualmente tensionados de material hiperelástico (independientes de la velocidad) y viscohiperelástico (dependientes de la velocidad). El modelo computacional parte de la formulación teórica ya propuesta de viscohiperelasticidad y se ha extendido para considerar campos de tensiones residuales, introducidos mediante una formulación basada en invariantes.

La metodología propuesta se ha validado primero con datos experimentales de probetas con una evolución de fractura bajo condiciones cuasiestáticas. A continuación, se han llevado a cabo varios análisis paramétricos para analizar la influencia que tienen diferentes propiedades mecánicas del sistema, estando esto en línea a lo que se hace con otros trabajos que utilizan la técnica de *phase-field* para materiales hiperelásticos y viscohiperelásticos. Las simulaciones llevadas a cabo han evaluado la fractura en estructuras cilíndricas con una y dos capas, evaluando tanto las magnitudes viscosas (τ y $\dot{u}$) así como las mecánicas ($\mathcal{G}_C$ y μ) y también para varios campos de tensiones residuales (que dependen de las coordenadas R y Z del cilindro). Curiosamente, llaman la atención los resultados (a priori) inesperados en cuanto a los mecanismos de iniciación y propagación de las grietas cuando se incorporan campos de tensiones residuales en estructuras cilíndricas multicapa. Esto pone de manifiesto la necesidad de desarrollar un marco numérico robusto que tenga en cuenta tales disposiciones.

Desarrollos futuros

Partiendo de la última oración de la sección anterior, esta .ínea de investigación se centrará en el futuro en la extensión de este código para el análisis de inestabilidades de flexión e hinchazón en este tipo de estructuras, con el fin de simular la fractura de arterias que sufren aneurismas. Basándonos en el trabajo realizado por Desena-Galarza et al. [296], el objetivo principal de este análisis sería establecer una correlación entre la integridad estructural, calculada mediante el método *phase-field*, y el inicio de la bifurcación de la pared arterial en estos tubos cilíndricos, que se debe al inicio de abultamientos como el que se muestra en la Fig. 94.

Otra aplicación de interés derivada de este marco de tensiones residuales es la consideración de leyes de material anisotrópico en la definición de capas. De hecho, la implementación de leyes anisotrópicas no lineales, como el material de Gasser-Ogden-Holzapfel (GOH) [355], concebido para modelar tejido arterial, tienen una importancia significativa. Esta aplicación logra una representación más fidedigna del heterogéneo comportamiento que presenta el material modelado como una pared arterial. Según el modelo GOH, se separan las contribuciones del material de la matriz extracelular y de las fibras de colágeno embebidas, contribuyendo de forma separada al comportamiento del tejido arterial [356]. El modelo GOH junto con las inestabilides de flexión y torsión está siendo implementando actualmente en la `UMAT` presentada en el Capítulo 3.

6.2.3 Conclusiones y futuros desarrollos para modelos de daño continuo de tipo gradiente aplicados a materiales hiperelásticos compresibles y cuasi incompresibles

Conclusiones

Dentro del Capítulo 4, se han desarrollado dos formulaciones de daño continuo de tipo gradiente para modelar la falla en materiales hiperelásticos compresibles y cuasi incompresibles, con un enfoque principal en abordar los problemas de *volumetric locking* y *shear locking* que presentan dichas probetas. En estas simulaciones, se ha testado con las muestras sometiéndolas

a varios tipos de cargas diferentes, incluyendo tracción, compresión y flexión, comparando estos dos elementos novedosos, `Q1Q1E24` y `Q1Q1P0`, con el de referencia, `Q1Q1`.

Se ha realizado un análisis pormenorizado del rendimiento de cada esquema propuesto. Primero, se ha validado el elemento de referencia de daño continuo (`Q1Q1`), basado en el propuesto por [111]. Se ha demostrado que es un instrumento más que notable para modelar el daño en estructuras compresibles sometidas a tracción. Sin embargo, ha mostrado *volumetric locking* y *shear locking* en muestras incompresibles bajo compresión y flexión, respectivamente.

Por lo tanto, para solucionar estas patologías de *locking*, se han propuesto la técnica de *enhanced assumed strain* empleando 24 modos incompatibles de deformación (`Q1Q1E24`) y la formulación de elementos finitos mixta que considera los campos de desplazamiento, presión y Jacobiano `Q1Q1P0`. El esquema `Q1Q1E24` se ha demostrado que resuelve el fenómeno de *shear locking* para materiales compresibles, mientras que con la formulación `Q1Q1P0`, al considerar tanto la presión como la dilatación como grados de libertad por separado, se ha demostrado que es un instrumento muy válido para modelar probetas incompresibles, corrigiendo la patología de *volumetric locking*.

Desarrollos futuros

Durante nuestro análisis, también se ha descubierto que el elemento `Q1Q1E24` no es adecuado para el modelado de daño continuo en materiales incompresibles, mientras que `Q1Q1P0` sobreestima la curva fuerza-desplazamiento en estructuras sometidas a cargas de flexión, es decir, muestra *shear locking*. Por lo tanto, para solucionar esto, se propone una formulación que combine tanto el EAS como las formulaciones mixtas de Jacobiano y presión. Además de esto, se propone aquí una extensión para modelar materiales hiperelásticos casi incompresibles anisotrópicos. Dicha extensión se muestra desafiante, debido a la distorsión que este tipo de materiales exhibe durante la carga de presión pura [357].

Con miras a aplicaciones más prácticas, este modelo de grandes deformaciones para fractura junto con la formulación mixta de desplazamiento-

presión-Jacobiano o la interpolación EAS se concibe como un candidato potencial para abordar el problema multi-escala y *multi-física* centrado en el modelado de fractura en paneles solares fotovoltaicos. Estas estructuras generalmente operan en un entorno multifísico (que incluye fenómenos mecánicos, térmicos y eléctricos, entre otros) y se encuentran sometidas a diferentes condiciones de servicio que pueden causar degradación en el servicio prestado, donde defectos como las microgrietas y la delaminación inducen una pérdida de potencia significativa [358], véase la Fig. 95. Dado que los paneles solares están compuestos por un laminado de silicio (Si) como se muestra en la Fig. 96, estos son propensos a mostrar problemas de *locking* ya que su espesor es relativamente pequeño en comparación con las otras dimensiones. Aquí es donde las interpolaciones mixtas, como los elementos tipo *EAS-ANS solid shells* [359], demuestran ser de mucha utilidad para su modelización.

Teniendo en cuenta lo expresado en este apartado, el próximo objetivo principal del marco de daño continuo desarrollado en el Capítulo 4 es lograr la simulación de paneles solares adoptándolo a una formulación de *solid shell* con cualquier técnica de daño difuso para evaluar la integridad estructural de dichos sistemas. El comportamiento complejo de las placas solares, con diferentes escalas y materiales en su composición, ha motivado la aplicación de metodologías numéricas *multi-level* y *global-local* basadas en homogeneización para conseguir un analisis micromecánico de alta fidelidad. A la luz de tales propuestas, se está desarrollando un marco multi-escala y *multi-física* para paneles solares considerando la formulación de *solid shells* implementada por Liu et al. empleando el enfoque *global-local* [360].

6.2.4 Hinchazón de hidrogeles termorresponsivos: principales resultados y mejoras futuras

Conclusiones

Se ha presentado en el Capítulo 5 un elemento estable *inf-sup* para el modelado de hidrogeles termorresponsivos empleando una subrutina `UEL`. Concretamente, se ha adaptado una interpolación mixta de desplaza-

miento, temperatura y presión de líquido para su implementación en elementos finitos con el objetivo de analizar el hinchazón en hidrogeles. Para cumplir con las condiciones LBB y, por lo tanto, obtener la estabilidad *inf-sup*, se ha utilizado una interpolación cuadrática para el campo de desplazamiento y una interpolación lineal para los campos de temperatura y presión de fluido, empleando así una formulación Q2Q1Q1.

En primer lugar, se ha estudiado la funcionalidad del elemento Q2Q1Q1 a través de la realización de un ensayo de hinchazón sin fuerzas externas aplicadas seguido de un desinflado causado por un gradiente de temperatura, obteniendo unos resultados sólidos. Posteriormente, se ha evaluado la dependencia de la discretización de la malla de elementos finitos en las oscilaciones en presión observadas en la muestra, demostrándose la importancia de seleccionar una malla apropiada para evitar cualquier oscilación que lleve a inestabilidades locales del hidrogel. Para finalizar con la verificación, se ha estudiado la importancia que los cambios de temperatura asociados a la difusión de líquido y al estiramiento elástico tienen en el comportamiento de inflado del gel. Este estudio se debe a que dichos gradientes fueron ignorados en los trabajos de referencia debido a su aparente influencia menor, afirmación que contrasta con lo demostrado aquí, ya que debido a la baja rigidez que presentan los hidrogeles, tales contribuciones deben considerarse no solo por términos de precisión, sino también por convergencia. Además de esto, el modelo ha demostrado precisión y robustez al replicar resultados experimentales correlacionando el efecto que tiene la densidad de entrecruzamiento en el comportamiento de inflado de hidrogeles de *PNIPAAm*, variando la temperatura.

Asimismo, también se ha estudiado la fractura de hidrogeles termorresponsivos empleando la técnica *phase-field*. A la luz de esto, se ha desarrollado un esquema preliminar Q1Q1Q1Q1 para modelar el análisis a falla de dichos materiales. Mientras que aplicando el marco propuesto a ensayos a tracción de una probeta de hidrogel con una entalla se obtienen resultados conclusivos, no se puede decir lo mismo de la estabilidad *inf-sup* de la formulación, lo cual se argumenta en la siguiente sección.

Desarrollos futuros

Aunque el elemento `Q1Q1Q1Q1` logra modelar completamente la fractura, no garantiza la estabilidad *inf-sup*. A partir de aquí, se puede deducir que para cumplir con dicha condición, el grado de interpolación deberá aumentarse, haciendo que el elemento sea `Q2Q1Q1Q1` o `Q2Q2Q1Q1` (la diferencia entre ambos elementos radica en el grado de interpolación para el *phase-field* nodal). La elección entre estas discretizaciones, junto con la realización de ejemplos más representativos, se encuentra actualmente en desarrollo y se presentará en futuros artículos.

Enfocando a aplicaciones más prácticas, un experimento que se está realizando consiste en la dependencia de la temperatura en la compresión de esferas de agarosa, un hidrogel termorresponsivo *UCST*; actualmente en desarrollo en el laboratorio. La meta principal consiste en observar como la disminución de la hinchazón al enfriar la muestra (ver Fig. 8) afecta a los resultados de esta prueba mecánica. En el contexto de estudios de fractura, otro objetivo principal del estudio de estos materiales es aplicar el enfoque con la técnica *phase-field* para modelar la falla de hidrogeles termorresponsivos y establecer una correlación de los resultados numéricos con experimentos. Para lograr esto, se utilizará la máquina de ensayos universal que se muestra en la Fig. 97. Diseñados para modelar la fractura de hidrogeles, estos experimentos involucrarán el uso de un videoextensómetro y comprenderán tanto pruebas de tensión como de compresión hasta fallo. Además, dichos tests se llevarán a cabo a diversas temperaturas para establecer un punto de vista cuantitativo en el que comparar la integridad estructural con el grado de hinchazón del hidrogel.

6.2.5 Para concluir

Los esfuerzos dedicados en esta tesis para implementar la técnica de *phase-field* para modelar fractura en problemas acoplados son el fiel reflejo del progreso realizado en procesos multidisciplinarios, específicamente en aquellos que conciernen a la integridad estructural. Los sólidos resultados alcanzados en los estudios de inflado de hidrogeles termorrespon-

sivos, fractura inducida por hidrógeno y falla de materiales hiperelásticos compresibles e incompresibles no solo dotan a la técnica de *phase-field* de una versatilidad sobresaliente para abordar estos problemas, sino también de una sencillez particular para implementar. En resumen, en la actualidad, las aplicaciones de *phase-field* a fractura están a la vanguardia para problemas de Mecánica Computacional que dependen de leyes multifísicas. Para hacer una predicción de hacia donde se dirigen los marcos basados en esta técnica, vale la pena resaltar los métodos basados en datos ya recogidos (*data-driven science*), como el *Deep Learning* o *Machine Learning*, que ya se están explotando en otras áreas. Se prevee que los métodos de aprendizaje avanzado serán de vital importancia para el desarrollo de esta investigación en el futuro inmediato, considerando que algunos trabajos preliminares ya se han publicado [362, 363, 364, 365].

Para concluir esta tesis, comenzamos refiriendo nuevamente al lector a la Fig. 1. Al examinar todas las posibles aplicaciones y, al mismo tiempo, todos las propuestas abordadas en este trabajo, se puede deducir que solo se ha cubierto la "punta del iceberg" en este trabajo. Si bien esa afirmación es cierta, no se puede negar que la complejidad que rodea cada problema acoplado les otorga una importancia tal que la resolución de solo uno de ellos podría constituir el tema central de una tesis en sí misma. Dado el amplio espectro que presenta este diagrama, intentar abarcar todo el espectro de problemas acoplados en Mecánica de Fractura es una tarea interminable. Por lo tanto, a partir de esta afirmación, podemos deducir que mientras que los problemas multifísicos en la Mecánica de Fractura Computacional sigan siendo un tema relevante en la literatura, siempre habrá espacio para investigaciones adicionales sobre este asunto.

Bibliography

[1] O. C. Zienkiewicz and A. H. C. Chan. "Coupled Problems and Their Numerical Solution". In: *Advances in Computational Nonlinear Mechanics*. Ed. by I. St. Doltsinis. Vienna: Springer Vienna, 1989, pp. 139–176. ISBN: 978-3-7091-2828-2. DOI: `https://doi.org/10.1007/978-3-7091-2828-2_4`.

[2] J.C. Simo and C. Miehe. "Associative coupled thermoplasticity at finite strains: Formulation, numerical analysis and implementation". In: *Computer Methods in Applied Mechanics and Engineering* 98.1 (1992), pp. 41–104. ISSN: 0045-7825. DOI: `https://doi.org/10.1016/0045-7825(92)90170-O`.

[3] Jifeng Li, Ignacio Romero, and Javier Segurado. "Development of a thermo-mechanically coupled crystal plasticity modeling framework: Application to polycrystalline homogenization". In: *International Journal of Plasticity* 119 (2019), pp. 313–330. ISSN: 0749-6419. DOI: `https://doi.org/10.1016/j.ijplas.2019.04.008`.

[4] M. Eftekhari and A. Fatemi. "Tensile, creep and fatigue behaviours of short fibre reinforced polymer composites at elevated temperatures: a literature survey". In: *Fatigue & Fracture of Engineering Materials & Structures* 38.12 (2015), pp. 1395–1418. DOI: `https://doi.org/10.1111/ffe.12363`.

[5] A. Dean et al. "A new invariant-based thermo-plastic model for finite deformation analysis of short fibre reinforced composites: Development and numerical aspects". In: *Composites Part B: Engineering* 125 (2017), pp. 241–258. ISSN: 1359-8368. DOI: `https://doi.org/10.1016/j.compositesb.2017.05.043`.

[6] Gerhard A. Holzapfel and Juan C. Simo. "A new viscoelastic constitutive model for continuous media at finite thermomechanical changes". In: *International Journal of Solids and Structures* 33.20 (1996), pp. 3019–3034. ISSN: 0020-7683. DOI: https://doi.org/10.1016/0020-7683(95)00263-4.

[7] Shawn A. Chester and Lallit Anand. "A thermo-mechanically coupled theory for fluid permeation in elastomeric materials: Application to thermally responsive gels". In: *Journal of the Mechanics and Physics of Solids* 59.10 (2011), pp. 1978–2006. ISSN: 0022-5096. DOI: https://doi.org/10.1016/j.jmps.2011.07.005.

[8] Zhiwei Ding et al. "A simplified coupled thermo-mechanical model for the transient analysis of temperature-sensitive hydrogels". In: *Mechanics of Materials* 97 (2016), pp. 212–227. ISSN: 0167-6636. DOI: https://doi.org/10.1016/j.mechmat.2016.02.018.

[9] M. Cerit, K. Genel, and S. Eksi. "Numerical investigation on stress concentration of corrosion pit". In: *Engineering Failure Analysis* 16.7 (2009), pp. 2467–2472. ISSN: 1350-6307. DOI: https://doi.org/10.1016/j.engfailanal.2009.04.004.

[10] Ravindra Duddu. "Numerical modeling of corrosion pit propagation using the combined extended finite element and level set method". In: *Computational Mechanics* 54.3 (Sept. 2014), pp. 613–627. ISSN: 1432-0924. DOI: https://doi.org/10.1007/s00466-014-1010-8.

[11] Dean Deng, Hidekazu Murakawa, and Wei Liang. "Numerical and experimental investigations on welding residual stress in multipass butt-welded austenitic stainless steel pipe". In: *Computational Materials Science* 42.2 (2008), pp. 234–244. ISSN: 0927-0256. DOI: https://doi.org/10.1016/j.commatsci.2007.07.009.

[12] Chuanjie Cui, Rujin Ma, and Emilio Martínez-Pañeda. "A phase field formulation for dissolution-driven stress corrosion cracking". In: *Journal of the Mechanics and Physics of Solids* 147 (2021), p. 104254. ISSN: 0022-5096. DOI: https://doi.org/10.1016/j.jmps.2020.104254.

[13] S. Serebrinsky, E.A. Carter, and M. Ortiz. "A quantum-mechanically informed continuum model of hydrogen embrittlement". In: *Journal of the Mechanics and Physics of Solids* 52.10 (2004), pp. 2403–2430. ISSN: 0022-5096. DOI: https://doi.org/10.1016/j.jmps.2004.02.010.

[14] Hamad ul Hassan, Kishan Govind, and Alexander Hartmaier. "Micromechanical modelling of coupled crystal plasticity and hydrogen diffusion". In: *Philosophical Magazine* 99.1 (2019), pp. 92–115. DOI: https://doi.org/10.1080/14786435.2018.1530466.

[15] C. Miehe et al. "A phase-field model for chemo-mechanical induced fracture in lithium-ion battery electrode particles". In: *International Journal for Numerical Methods in Engineering* 106.9 (2016), pp. 683–711. DOI: https://doi.org/10.1002/nme.5133.

[16] Ying Zhao et al. "A review on modeling of electro-chemo-mechanics in lithium-ion batteries". In: *Journal of Power Sources* 413 (2019), pp. 259–283. ISSN: 0378-7753. DOI: https://doi.org/10.1016/j.jpowsour.2018.12.011.

[17] Vikram S. Deshpande, Robert M. McMeeking, and Anthony G. Evans. "A bio-chemo-mechanical model for cell contractility". In: *Proceedings of the National Academy of Sciences* 103.38 (2006), pp. 14015–14020. DOI: https://doi.org/10.1073/pnas.0605837103.

[18] Stanislav Polzer et al. "A Numerical Implementation to Predict Residual Strains from the Homogeneous Stress Hypothesis with Application to Abdominal Aortic Aneurysms". In: *Annals of Biomedical Engineering* 41.7 (July 2013), pp. 1516–1527. ISSN: 1573-9686. DOI: https://doi.org/10.1007/s10439-013-0749-y.

[19] A.A. Alhayani, J. Rodríguez, and J. Merodio. "Competition between radial expansion and axial propagation in bulging of inflated cylinders with application to aneurysms propagation in arterial wall tissue". In: *International Journal of Engineering Science* 85 (2014), pp. 74–89. ISSN: 0020-7225. DOI: https://doi.org/10.1016/j.ijengsci.2014.08.008.

[20] Alejandro Font et al. "Modelling of residually stressed, extended and inflated cylinders with application to aneurysms". In: *Mechanics Research Communications* 111 (2021), p. 103643. ISSN: 0093-6413. DOI: https://doi.org/10.1016/j.mechrescom.2020.103643.

[21] James Lighthill. "Fundamentals concerning wave loading on offshore structures". In: *Journal of Fluid Mechanics* 173 (1986), pp. 667–681. DOI: https://doi.org/10.1017/S0022112086001313.

[22] M. Glück et al. "Computation of fluid–structure interaction on lightweight structures". In: *Journal of Wind Engineering and Industrial Aerodynamics* 89.14 (2001). Bluff Body Aerodynamics and Applications, pp. 1351–1368. ISSN: 0167-6105. DOI: https://doi.org/10.1016/S0167-6105(01)00150-7.

[23] Ming-Chen Hsu and Yuri Bazilevs. "Fluid–structure interaction modeling of wind turbines: simulating the full machine". In: *Computational Mechanics* 50.6 (Dec. 2012), pp. 821–833. ISSN: 1432-0924. DOI: https://doi.org/10.1007/s00466-012-0772-0.

[24] Federico Perini et al. "Piston geometry effects in a light-duty, swirl-supported diesel engine: Flow structure characterization". In: *International Journal of Engine Research* 19.10 (2018), pp. 1079–1098. DOI: https://doi.org/10.1177/1468087417742572.

[25] Alan Arnold Griffith and Geoffrey Ingram Taylor. "VI. The phenomena of rupture and flow in solids". In: *Philosophical Transactions of the Royal Society of London. Series A, Containing Papers of a Mathematical or Physical Character* 221.582-593 (1921), pp. 163–198. DOI: https://doi.org/10.1098/rsta.1921.0006.

[26] P. Novak et al. "A statistical, physical-based, micro-mechanical model of hydrogen-induced intergranular fracture in steel". In: *Journal of the Mechanics and Physics of Solids* 58.2 (2010), pp. 206–226. ISSN: 0022-5096. DOI: https://doi.org/10.1016/j.jmps.2009.10.005.

[27] Akihide Nagao et al. "Hydrogen-enhanced-plasticity mediated decohesion for hydrogen-induced intergranular and "quasi-cleavage" fracture of lath martensitic steels". In: *Journal of the Mechanics and Physics of Solids* 112 (2018), pp. 403–430. DOI: https://doi.org/10.1016/j.jmps.2017.12.016.

[28] Y.F. Gao and M. Zhou. "Coupled mechano-diffusional driving forces for fracture in electrode materials". In: *Journal of Power Sources* 230 (2013), pp. 176–193. ISSN: 0378-7753. DOI: https://doi.org/10.1016/j.jpowsour.2012.12.034.

[29] Mohammed A. Msekh et al. "Predictions of J integral and tensile strength of clay/epoxy nanocomposites material using phase field model". In: *Composites Part B: Engineering* 93 (2016), pp. 97–114. DOI: https://doi.org/10.1016/j.compositesb.2016.02.022.

[30]   Elisa A. Bergkamp et al. "A thermodynamically consistent J-integral formulation for fluid-driven fracture propagation in poroelastic continua". In: *Journal of the Mechanics and Physics of Solids* 170 (2023), p. 105082. ISSN: 0022-5096. DOI: https://doi.org/10.1016/j.jmps.2022.105082.

[31]   X.Y. Wu, K.T. Ramesh, and T.W. Wright. "The coupled effects of plastic strain gradient and thermal softening on the dynamic growth of voids". In: *International Journal of Solids and Structures* 40.24 (2003), pp. 6633–6651. DOI: https://doi.org/10.1016/S0020-7683(03)00439-6.

[32]   Emilio Martínez-Pañeda, Christian F. Niordson, and Richard P. Gangloff. "Strain gradient plasticity-based modeling of hydrogen environment assisted cracking". In: *Acta Materialia* 117 (2016), pp. 321–332. ISSN: 1359-6454. DOI: https://doi.org/10.1016/j.actamat.2016.07.022.

[33]   Benoit Carrier and Sylvie Granet. "Numerical modeling of hydraulic fracture problem in permeable medium using cohesive zone model". In: *Engineering Fracture Mechanics* 79 (2012), pp. 312–328. DOI: https://doi.org/10.1016/j.engfracmech.2011.11.012.

[34]   L. Wang et al. "Modeling of thermal properties and failure of thermal barrier coatings with the use of finite element methods: A review". In: *Journal of the European Ceramic Society* 36.6 (2016), pp. 1313–1331. DOI: https://doi.org/10.1016/j.jeurceramsoc.2015.12.038.

[35]   Pavan Kumar Asur Vijaya Kumar et al. "Non-linear thermoelastic analysis of thin-walled structures with cohesive-like interfaces relying on the solid shell concept". In: *Finite Elements in Analysis and Design* 202 (2022), p. 103696. ISSN: 0168-874X. DOI: https://doi.org/10.1016/j.finel.2021.103696.

[36]   Z. Liu, J. Reinoso, and M. Paggi. "A humidity dose-CZM formulation to simulate new end-of-life recycling methods for photovoltaic laminates". In: *Engineering Fracture Mechanics* 259 (2022), p. 108125. ISSN: 0013-7944. DOI: https://doi.org/10.1016/j.engfracmech.2021.108125.

[37]   Zhengyu Jenny Zhang, Glaucio H. Paulino, and Waldemar Celes. "Extrinsic cohesive modelling of dynamic fracture and microbranching instability in brittle materials". In: *International Journal for Numerical Methods in Engineering* 72.8 (2007), pp. 893–923. DOI: https://doi.org/10.1002/nme.2030.

[38]   ZdeneǨ P. Bazǎnt and Gilles Pijaudier-Cabot. "Nonlocal Continuum Damage, Localization Instability and Convergence". In: *Journal of Applied Mechanics* 55.2 (June 1988), pp. 287–293. ISSN: 0021-8936. DOI: https://doi.org/10.1115/1.3173674.

[39]   Milan Jirásek. "Nonlocal models for damage and fracture: Comparison of approaches". In: *International Journal of Solids and Structures* 35.31 (1998), pp. 4133–4145. ISSN: 0020-7683. DOI: https://doi.org/10.1016/S0020-7683(97)00306-5.

[40]   S.C. Yuan and J.P. Harrison. "A review of the state of the art in modelling progressive mechanical breakdown and associated fluid flow in intact heterogeneous rocks". In: *International Journal of Rock Mechanics and Mining Sciences* 43.7 (2006), pp. 1001–1022. DOI: https://doi.org/10.1016/j.ijrmms.2006.03.004.

[41]   V.H. Nguyen, B. Nedjar, and J.M. Torrenti. "Chemo-mechanical coupling behaviour of leached concrete. Part II: Modelling". In: *Nuclear Engineering and Design* 237.20-21 (2007), pp. 2090–2097. DOI: https://doi.org/10.1016/j.nucengdes.2007.02.012.

[42]   Yongxiang Wang and Haim Waisman. "From diffuse damage to sharp cohesive cracks: A coupled XFEM framework for failure analysis of quasi-brittle materials". In: *Computer Methods in Applied Mechanics and Engineering* 299 (2016), pp. 57–89. DOI: https://doi.org/10.1016/j.cma.2015.10.019.

[43]   Selda Oterkus, Erdogan Madenci, and Erkan Oterkus. "Fully coupled poroelastic peridynamic formulation for fluid-filled fractures". In: *Engineering Geology* 225 (2017), pp. 19–28. DOI: https://doi.org/10.1016/j.enggeo.2017.02.001.

[44]   Yan Gao and Selda Oterkus. "Fully coupled thermomechanical analysis of laminated composites by using ordinary state based peridynamic theory". In: *Composite Structures* 207 (2019), pp. 397–424. DOI: https://doi.org/10.1016/j.compstruct.2018.09.034.

[45] G.A. Francfort and J.-J. Marigo. "Revisiting brittle fracture as an energy minimization problem". In: *Journal of the Mechanics and Physics of Solids* 46.8 (1998), pp. 1319–1342. ISSN: 0022-5096. DOI: https://doi.org/10.1016/S0022-5096(98)00034-9.

[46] B. Bourdin, G.A. Francfort, and J-J. Marigo. "Numerical experiments in revisited brittle fracture". In: *Journal of the Mechanics and Physics of Solids* 48.4 (2000), pp. 797–826. ISSN: 0022-5096. DOI: https://doi.org/10.1016/S0022-5096(99)00028-9.

[47] C. Miehe, F. Welschinger, and M. Hofacker. "Thermodynamically consistent phase-field models of fracture: Variational principles and multi-field FE implementations". In: *International Journal for Numerical Methods in Engineering* 83.10 (2010), pp. 1273–1311. DOI: https://doi.org/10.1002/nme.2861.

[48] T. Gerasimov and L. De Lorenzis. "A line search assisted monolithic approach for phase-field computing of brittle fracture". In: *Computer Methods in Applied Mechanics and Engineering* 312 (2016). Phase Field Approaches to Fracture, pp. 276–303. ISSN: 0045-7825. DOI: https://doi.org/10.1016/j.cma.2015.12.017.

[49] Philip K. Kristensen and Emilio Martínez-Pañeda. "Phase field fracture modelling using quasi-Newton methods and a new adaptive step scheme". In: *Theoretical and Applied Fracture Mechanics* 107 (2020), p. 102446. ISSN: 0167-8442. DOI: https://doi.org/10.1016/j.tafmec.2019.102446.

[50] Michael J. Borden et al. "A higher-order phase-field model for brittle fracture: Formulation and analysis within the isogeometric analysis framework". In: *Computer Methods in Applied Mechanics and Engineering* 273 (2014), pp. 100–118. ISSN: 0045-7825. DOI: https://doi.org/10.1016/j.cma.2014.01.016.

[51] Bin Li et al. "Phase-field modeling and simulation of fracture in brittle materials with strongly anisotropic surface energy". In: *International Journal for Numerical Methods in Engineering* 102.3-4 (2015), pp. 711–727. DOI: https://doi.org/10.1002/nme.4726.

[52] Hanen Amor, Jean-Jacques Marigo, and Corrado Maurini. "Regularized formulation of the variational brittle fracture with unilateral contact: Numerical experiments". In: *Journal of the Mechanics and Physics of Solids* 57.8 (2009), pp. 1209–1229. ISSN: 0022-5096. DOI: https://doi.org/10.1016/j.jmps.2009.04.011.

241

[53]   Christian Miehe, Martina Hofacker, and Fabian Welschinger. "A phase field model for rate-independent crack propagation: Robust algorithmic implementation based on operator splits". In: *Computer Methods in Applied Mechanics and Engineering* 199 (2010), pp. 2765–2778. DOI: https://doi.org/10.1016/j.cma.2010.04.011.

[54]   M. Ambati, T. Gerasimov, and L. De Lorenzis. "Phase-field modeling of ductile fracture". In: *Computational Mechanics* 55.5 (May 2015), pp. 1017–1040. ISSN: 1432-0924. DOI: https://doi.org/10.1007/s00466-015-1151-4.

[55]   Michael J. Borden et al. "A phase-field formulation for fracture in ductile materials: Finite deformation balance law derivation, plastic degradation, and stress triaxiality effects". In: *Computer Methods in Applied Mechanics and Engineering* 312 (2016). Phase Field Approaches to Fracture, pp. 130–166. ISSN: 0045-7825. DOI: https://doi.org/10.1016/j.cma.2016.09.005.

[56]   Christian Miehe, Fadi Aldakheel, and Arun Raina. "Phase field modeling of ductile fracture at finite strains: A variational gradient-extended plasticity-damage theory". In: *International Journal of Plasticity* 84 (2016), pp. 1–32. ISSN: 0749-6419. DOI: https://doi.org/10.1016/j.ijplas.2016.04.011.

[57]   Michael J. Borden et al. "A phase-field description of dynamic brittle fracture". In: *Computer Methods in Applied Mechanics and Engineering* 217-220 (2012), pp. 77–95. ISSN: 0045-7825. DOI: https://doi.org/10.1016/j.cma.2012.01.008.

[58]   M. Hofacker and C. Miehe. "A phase field model of dynamic fracture: Robust field updates for the analysis of complex crack patterns". In: *International Journal for Numerical Methods in Engineering* 93.3 (2013), pp. 276–301. DOI: https://doi.org/10.1002/nme.4387.

[59]   Clemens V. Verhoosel and René de Borst. "A phase-field model for cohesive fracture". In: *International Journal for Numerical Methods in Engineering* 96.1 (2013), pp. 43–62. DOI: https://doi.org/10.1002/nme.4553.

[60]   V. Carollo, J. Reinoso, and M. Paggi. "A 3D finite strain model for intralayer and interlayer crack simulation coupling the phase field approach and cohesive zone model". In: *Composite Structures*

182 (2017), pp. 636–651. ISSN: 0263-8223. DOI: `https://doi.org/10.1016/j.compstruct.2017.08.095`.

[61] A. Quintanas-Corominas et al. "A phase field approach to simulate intralaminar and translaminar fracture in long fiber composite materials". In: *Composite Structures* 220 (2019), pp. 899–911. ISSN: 0263-8223. DOI: `https://doi.org/10.1016/j.compstruct.2019.02.007`.

[62] A. Dean et al. "A multi phase-field fracture model for long fiber reinforced composites based on the Puck theory of failure". In: *Composite Structures* 251 (2020), p. 112446. ISSN: 0263-8223. DOI: `https://doi.org/10.1016/j.compstruct.2020.112446`.

[63] Christian Miehe, Lisa-Marie Schänzel, and Heike Ulmer. "Phase field modeling of fracture in multi-physics problems. Part I. Balance of crack surface and failure criteria for brittle crack propagation in thermo-elastic solids". In: *Computer Methods in Applied Mechanics and Engineering* 294 (2015), pp. 449–485. ISSN: 0045-7825. DOI: `https://doi.org/10.1016/j.cma.2014.11.016`.

[64] C. Miehe et al. "Phase field modeling of fracture in multi-physics problems. Part II. Coupled brittle-to-ductile failure criteria and crack propagation in thermo-elastic–plastic solids". In: *Computer Methods in Applied Mechanics and Engineering* 294 (2015), pp. 486–522. ISSN: 0045-7825. DOI: `https://doi.org/10.1016/j.cma.2014.11.017`.

[65] SeonHong Na and WaiChing Sun. "Computational thermomechanics of crystalline rock, Part I: A combined multi-phase-field/crystal plasticity approach for single crystal simulations". In: *Computer Methods in Applied Mechanics and Engineering* 338 (2018), pp. 657–691. DOI: `https://doi.org/10.1016/j.cma.2017.12.022`.

[66] Thanh-Tung Nguyen, Danièle Waldmann, and Tinh Quoc Bui. "Computational chemo-thermo-mechanical coupling phase-field model for complex fracture induced by early-age shrinkage and hydration heat in cement-based materials". In: *Computer Methods in Applied Mechanics and Engineering* 348 (2019), pp. 1–28. ISSN: 0045-7825. DOI: `https://doi.org/10.1016/j.cma.2019.01.012`.

[67] Lampros Svolos, Curt A. Bronkhorst, and Haim Waisman. "Thermal-conductivity degradation across cracks in coupled thermo-mechanical systems modeled by the phase-field fracture method". In: *Journal of the Mechanics and Physics of Solids* 137 (2020). DOI: `https://doi.org/10.1016/j.jmps.2019.103861`.

[68] Pavan Kumar Asur Vijaya Kumar et al. "Nonlinear thermo-elastic phase-field fracture of thin-walled structures relying on solid shell concepts". In: *Computer Methods in Applied Mechanics and Engineering* 396 (2022), p. 115096. ISSN: 0045-7825. DOI: `https://doi.org/10.1016/j.cma.2022.115096`.

[69] Pavan Kumar Asur Vijaya Kumar et al. "Thermo-elastic solid shell formulation with phase field fracture for thin-walled FGMs". In: *Thin-Walled Structures* 179 (2022), p. 109535. ISSN: 0263-8231. DOI: `https://doi.org/10.1016/j.tws.2022.109535`.

[70] Christian Miehe, Steffen Mauthe, and Stephan Teichtmeister. "Minimization principles for the coupled problem of Darcy-Biot-type fluid transport in porous media linked to phase field modeling of fracture". In: *Journal of the Mechanics and Physics of Solids* 82 (2015), pp. 186–217. DOI: `https://doi.org/10.1016/j.jmps.2015.04.006`.

[71] Christian Miehe and Steffen Mauthe. "Phase field modeling of fracture in multi-physics problems. Part III. Crack driving forces in hydro-poro-elasticity and hydraulic fracturing of fluid-saturated porous media". In: *Computer Methods in Applied Mechanics and Engineering* 304 (2016), pp. 619–655. DOI: `https://doi.org/10.1016/j.cma.2015.09.021`.

[72] Lukas Böger, Marc-André Keip, and Christian Miehe. "Minimization and saddle-point principles for the phase-field modeling of fracture in hydrogels". In: *Computational Materials Science* 138 (2017), pp. 474–485. ISSN: 0927-0256. DOI: `https://doi.org/10.1016/j.commatsci.2017.06.010`.

[73] Shoujing Zheng et al. "A phase field solution for modelling hyperelastic material and hydrogel fracture in ABAQUS". In: *Engineering Fracture Mechanics* 276 (2022). DOI: `https://doi.org/10.1016/j.engfracmech.2022.108894`.

[74] Shoujing Zheng et al. "A model for fracture of temperature-sensitive hydrogel with diffusion and large deformation". In: *Engineering Fracture Mechanics* 281 (2023), p. 109138. ISSN: 0013-7944. DOI: `https://doi.org/10.1016/j.engfracmech.2023.109138`.

[75] Emilio Martínez-Pañeda, Alireza Golahmar, and Christian F. Niordson. "A phase field formulation for hydrogen assisted cracking". In: *Computer Methods in Applied Mechanics and Engineering* 342 (2018), pp. 742–761. ISSN: 0045-7825. DOI: `https://doi.org/10.1016/j.cma.2018.07.021`.

[76] Philip K. Kristensen, Christian F. Niordson, and Emilio Martínez-Pañeda. "A phase field model for elastic-gradient-plastic solids undergoing hydrogen embrittlement". In: *Journal of the Mechanics and Physics of Solids* 143 (2020), p. 104093. ISSN: 0022-5096. DOI: `https://doi.org/10.1016/j.jmps.2020.104093`.

[77] Jian-Ying Wu, Tushar Kanti Mandal, and Vinh Phu Nguyen. "A phase-field regularized cohesive zone model for hydrogen assisted cracking". In: *Computer Methods in Applied Mechanics and Engineering* 358 (2020). DOI: `https://doi.org/10.1016/j.cma.2019.112614`.

[78] Mehrdad Isfandbod and Emilio Martínez-Pañeda. "A mechanism-based multi-trap phase field model for hydrogen assisted fracture". In: *International Journal of Plasticity* 144 (2021), p. 103044. ISSN: 0749-6419. DOI: `https://doi.org/10.1016/j.ijplas.2021.103044`.

[79] M. Paggi and J. Reinoso. "Revisiting the problem of a crack impinging on an interface:A modeling framework for the interaction between the phase field approach for brittle fracture and the interface cohesive zone model". In: *Computer Methods in Applied Mechanics and Engineering* 321 (2017), pp. 145–172. ISSN: 0045-7825. DOI: `https://doi.org/10.1016/j.cma.2017.04.004`.

[80] M. Paggi, M. Corrado, and J. Reinoso. "Fracture of solar-grade anisotropic polycrystalline Silicon: A combined phase field–cohesive zone model approach". In: *Computer Methods in Applied Mechanics and Engineering* 330 (2018), pp. 123–148. ISSN: 0045-7825. DOI: `https://doi.org/10.1016/j.cma.2017.10.021`.

[81] A. Quintanas-Corominas et al. "A phase field approach enhanced with a cohesive zone model for modeling delamination induced by matrix cracking". In: *Computer Methods in Applied Mechanics and Engineering* 358 (2020), p. 112618. ISSN: 0045-7825. DOI: https://doi.org/10.1016/j.cma.2019.112618.

[82] M.R. Marulli et al. "A combined phase-field and cohesive zone model approach for crack propagation in layered structures made of nonlinear rubber-like materials". In: *Computer Methods in Applied Mechanics and Engineering* 395 (2022), p. 115007. ISSN: 0045-7825. DOI: https://doi.org/10.1016/j.cma.2022.115007.

[83] R. P. Gangloff. "Hydrogen-assisted Cracking". In: *Comprehensive Structural Integrity Vol. 6*. Ed. by I. Milne, R.O. Ritchie, and B. Karihaloo. New York, NY: Elsevier Science, 2003, pp. 31–101. DOI: https://doi.org/10.1016/B0-08-043749-4/06134-6.

[84] R. P. Gangloff and B. P. Somerday. *Gaseous Hydrogen Embrittlement of Materials in Energy Technologies*. Cambridge: Woodhead Publishing Limited, 2012, p. 520. ISBN: 9781845696733. DOI: https://doi.org/10.1016/B978-1-84569-677-1.50024-7.

[85] Milos B. Djukic et al. "The synergistic action and interplay of hydrogen embrittlement mechanisms in steels and iron: Localized plasticity and decohesion". In: *Engineering Fracture Mechanics* 216 (2019), p. 106528. ISSN: 00137944. DOI: https://doi.org/10.1016/j.engfracmech.2019.106528.

[86] Z. D. Harris et al. "Elucidating the contribution of mobile hydrogen-deformation interactions to hydrogen-induced intergranular cracking in polycrystalline nickel". In: *Acta Materialia* 158 (2018), pp. 180–192. ISSN: 13596454. DOI: https://doi.org/10.1016/j.actamat.2018.07.043.

[87] Julia Kollewe. *Cheesegrater tower loses third bolt in three months*. 2015. URL: https://www.theguardian.com/business/2015/jan/14/cheesegrater-leadenhall-building-bolt-city-london.

[88] Thomas Langill. *Lessons Learned from the Bay Bridge Bolt Failure*. 2017. URL: https://www.structuremag.org/?p=11041.

[89] © User:Colin / Wikimedia Commons / CC BY-SA 4.0. *File:Cheesegrater and Gherkin.jpg*. URL: https://commons.wikimedia.org/w/index.php?curid=33297697.

[90] © User:Carolyn / Wikimedia Commons / CC BY-SA 2.0. *File:San Francisco Oakland Bay Bridge-2.jpg*. URL: `https://commons.wik imedia.org/wiki/File:San_Francisco_Oakland_Bay_ Bridge-2.jpg`.

[91] Y. Abou Msallem et al. "Material characterization and residual stresses simulation during the manufacturing process of epoxy matrix composites". In: *Composites Part A: Applied Science and Manufacturing* 41.1 (2010). Special Issue: Flow Processes in Composite Materials, pp. 108–115. ISSN: 1359-835X. DOI: `https://doi. org/10.1016/j.compositesa.2009.09.025`.

[92] Gerhard A. Holzapfel and Ray W. Ogden. "Modelling the layer-specific three-dimensional residual stresses in arteries, with an application to the human aorta". In: *Journal of The Royal Society Interface* 7.46 (2010), pp. 787–799. DOI: `https://doi.org/10. 1098/rsif.2009.0357`.

[93] N.-K. Jha et al. "A computational model for fiber-reinforced composites: hyperelastic constitutive formulation including residual stresses and damage". In: *Computational Mechanics* 63.5 (May 2019), pp. 931–948. ISSN: 1432-0924. DOI: `https://doi.org/10. 1007/s00466-018-1630-5`.

[94] J. D. Humphrey. "Vascular Adaptation and Mechanical Homeostasis at Tissue, Cellular, and Sub-cellular Levels". In: *Cell Biochemistry and Biophysics* 50.2 (Feb. 2008), pp. 53–78. ISSN: 1559-0283. DOI: `https://doi.org/10.1007/s12013-007-9002- 3`.

[95] J. Merodio and D.M. Haughton. "Bifurcation of thick-walled cylindrical shells and the mechanical response of arterial tissue affected by Marfan's syndrome". In: *Mechanics Research Communications* 37.1 (2010), pp. 1–6. ISSN: 0093-6413. DOI: `https://doi. org/10.1016/j.mechrescom.2009.10.006`.

[96] A.A. Alhayani et al. "Computational modelling of bulging of inflated cylindrical shells applicable to aneurysm formation and propagation in arterial wall tissue". In: *Finite Elements in Analysis and Design* 73 (2013), pp. 20–29. ISSN: 0168-874X. DOI: `https: //doi.org/10.1016/j.finel.2013.05.001`.

[97] Hasan Demirkoparan and Jose Merodio. "Bulging bifurcation of inflated circular cylinders of doubly fiber-reinforced hyperelastic material under axial loading and swelling". In: *Mathematics and Mechanics of Solids* 22.4 (2017), pp. 666–682. DOI: `https://doi.org/10.1177/1081286515600045`.

[98] The Marfan Foundation. *Familial Thoracic Aortic Aneurysm and Dissection*. URL: `https://marfan.org/conditions/familial-aortic-aneurysm/`.

[99] David Lasry and Ted Belytschko. "Localization limiters in transient problems". In: *International Journal of Solids and Structures* 24.6 (1988), pp. 581–597. ISSN: 0020-7683. DOI: `https://doi.org/10.1016/0020-7683(88)90059-5`.

[100] C. Polizzotto, G. Borino, and P. Fuschi. "A thermodynamically consistent formulation of nonlocal and gradient plasticity". In: *Mechanics Research Communications* 25.1 (1998), pp. 75–82. ISSN: 0093-6413. DOI: `https://doi.org/10.1016/S0093-6413(98)00009-3`.

[101] J.H.P. de Vree, W.A.M. Brekelmans, and M.A.J. van Gils. "Comparison of nonlocal approaches in continuum damage mechanics". In: *Computers & Structures* 55.4 (1995), pp. 581–588. ISSN: 0045-7949. DOI: `https://doi.org/10.1016/0045-7949(94)00501-S`.

[102] R. DE BORST and J. PAMIN. "SOME NOVEL DEVELOPMENTS IN FINITE ELEMENT PROCEDURES FOR GRADIENT-DEPENDENT PLASTICITY". In: *International Journal for Numerical Methods in Engineering* 39.14 (1996), pp. 2477–2505. DOI: `https://doi.org/10.1002/(SICI)1097-0207(19960730)39:14<2477::AID-NME962>3.0.CO;2-E`.

[103] Jerzy Pamin. "Gradient plasticity and damage models: a short comparison". In: *Computational Materials Science* 32.3 (2005). IWCMM, pp. 472–479. ISSN: 0927-0256. DOI: `https://doi.org/10.1016/j.commatsci.2004.09.018`.

[104] R. H. J. PEERLINGS et al. "GRADIENT ENHANCED DAMAGE FOR QUASI-BRITTLE MATERIALS". In: *International Journal for Numerical Methods in Engineering* 39.19 (1996), pp. 3391–3403. DOI: `https://doi.org/10.1002/(SICI)1097-0207(19961015)39:19<3391::AID-NME7>3.0.CO;2-D`.

[105] Ellen Kuhl and Ekkehard Ramm. "Simulation of strain localization with gradient enhanced damage models". In: *Computational Materials Science* 16.1 (1999), pp. 176–185. ISSN: 0927-0256. DOI: https://doi.org/10.1016/S0927-0256(99)00060-9.

[106] Ellen Kuhl, Ekkehard Ramm, and René Borst. "An anisotropic gradient damage model for quasi-brittle materials". In: *Computer Methods in Applied Mechanics and Engineering* 183 (Mar. 2000), pp. 87–103. DOI: https://doi.org/10.1016/S0045-7825(99)00213-3.

[107] Paul Steinmann. "Formulation and computation of geometrically non-linear gradient damage". In: *International Journal for Numerical Methods in Engineering* 46.5 (1999), pp. 757–779. DOI: https://doi.org/10.1002/(SICI)1097-0207(19991020)46:5<757::AID-NME731>3.0.CO;2-N.

[108] Tina Liebe, Andreas Menzel, and Paul Steinmann. "Theory and numerics of geometrically non-linear gradient plasticity". In: *International Journal of Engineering Science* 41.13 (2003). Damage and failure analysis of materials, pp. 1603–1629. ISSN: 0020-7225. DOI: https://doi.org/10.1016/S0020-7225(03)00030-2.

[109] B Dimitrijevic and Klaus Hackl. "A method for gradient enhancement of continuum damage models". In: *Technische Mechanik* 1 (Sept. 2008), pp. 43–52.

[110] Balbina Wcisło, Jerzy Pamin, and Katarzyna Kowalczyk-Gajewska. "Gradient-enhanced damage model for large deformations of elastic-plastic materials". In: *Archives of Mechanics* 65 (Jan. 2013).

[111] Tobias Waffenschmidt et al. "A gradient-enhanced large-deformation continuum damage model for fibre-reinforced materials". In: *Computer Methods in Applied Mechanics and Engineering* 268 (2014), pp. 801–842. ISSN: 0045-7825. DOI: https://doi.org/10.1016/j.cma.2013.10.013.

[112] Rashid K. Abu Al-Rub and George Z. Voyiadjis. "A Finite Strain Plastic-damage Model for High Velocity Impact using Combined Viscosity and Gradient Localization Limiters: Part I - Theoretical Formulation". In: *International Journal of Damage Mechanics* 15.4 (2006), pp. 293–334. DOI: https://doi.org/10.1177/1056789506058046.

[113] Tim Brepols, Stephan Wulfinghoff, and Stefanie Reese. "Gradient-extended two-surface damage-plasticity: Micromorphic formulation and numerical aspects". In: *International Journal of Plasticity* 97 (2017), pp. 64–106. ISSN: 0749-6419. DOI: https://doi.org/10.1016/j.ijplas.2017.05.010.

[114] Atefeh Alipour, Stefanie Reese, and Stephan Wulfinghoff. "A grain boundary model for gradient-extended geometrically nonlinear crystal plasticity: Theory and numerics". In: *International Journal of Plasticity* 118 (2019), pp. 17–35. ISSN: 0749-6419. DOI: https://doi.org/10.1016/j.ijplas.2019.01.009.

[115] Tim Brepols, Stephan Wulfinghoff, and Stefanie Reese. "A gradient-extended two-surface damage-plasticity model for large deformations". In: *International Journal of Plasticity* 129 (2020), p. 102635. ISSN: 0749-6419. DOI: https://doi.org/10.1016/j.ijplas.2019.11.014.

[116] Thomas Hughes. *The Finite Element Method: Linear Static and Dynamic Finite Element Analysis*. Vol. 78. Jan. 2000.

[117] T. Belytschko, Y. Y. Lu, and L. Gu. "Element-free Galerkin methods". In: *International Journal for Numerical Methods in Engineering* 37.2 (1994), pp. 229–256. DOI: https://doi.org/10.1002/nme.1620370205.

[118] S. N. Atluri and T.-L. Zhu. "The meshless local Petrov-Galerkin (MLPG) approach for solving problems in elasto-statics". In: *Computational Mechanics* 25.2 (Mar. 2000), pp. 169–179. ISSN: 1432-0924. DOI: https://doi.org/10.1007/s004660050467.

[119] A. Ortiz, M.A. Puso, and N. Sukumar. "Maximum-entropy meshfree method for compressible and near-incompressible elasticity". In: *Computer Methods in Applied Mechanics and Engineering* 199.25 (2010), pp. 1859–1871. ISSN: 0045-7825. DOI: https://doi.org/10.1016/j.cma.2010.02.013.

[120] G.Y. Zhang et al. "A three-dimensional nonlinear meshfree algorithm for simulating mechanical responses of soft tissue". In: *Engineering Analysis with Boundary Elements* 42 (2014). Advances on Meshfree and other Mesh reduction methods, pp. 60–66. ISSN: 0955-7997. DOI: https://doi.org/10.1016/j.enganabound.2013.08.014.

[121] K.Y. Dai, G.R. Liu, and T.T. Nguyen. "An n-sided polygonal smoothed finite element method (nSFEM) for solid mechanics". In: *Finite Elements in Analysis and Design* 43.11 (2007), pp. 847–860. ISSN: 0168-874X. DOI: https://doi.org/10.1016/j.finel.2007.05.009.

[122] G.R. Liu, T. Nguyen-Thoi, and K.Y. Lam. "An edge-based smoothed finite element method (ES-FEM) for static, free and forced vibration analyses of solids". In: *Journal of Sound and Vibration* 320.4 (2009), pp. 1100–1130. ISSN: 0022-460X. DOI: https://doi.org/10.1016/j.jsv.2008.08.027.

[123] T. Nguyen-Thoi et al. "A face-based smoothed finite element method (FS-FEM) for 3D linear and geometrically non-linear solid mechanics problems using 4-node tetrahedral elements". In: *International Journal for Numerical Methods in Engineering* 78.3 (2009), pp. 324–353. DOI: https://doi.org/10.1002/nme.2491.

[124] Peter Hansbo and Mats G. Larson. "Discontinuous Galerkin methods for incompressible and nearly incompressible elasticity by Nitsche's method". In: *Computer Methods in Applied Mechanics and Engineering* 191.17 (2002), pp. 1895–1908. ISSN: 0045-7825. DOI: https://doi.org/10.1016/S0045-7825(01)00358-9.

[125] Peter Kaufmann et al. "Flexible simulation of deformable models using discontinuous Galerkin FEM". In: *Graphical Models* 71.4 (2009). Special Issue of ACM SIGGRAPH / Eurographics Symposium on Computer Animation 2008, pp. 153–167. ISSN: 1524-0703. DOI: https://doi.org/10.1016/j.gmod.2009.02.002.

[126] N.C. Nguyen and J. Peraire. "Hybridizable discontinuous Galerkin methods for partial differential equations in continuum mechanics". In: *Journal of Computational Physics* 231.18 (2012), pp. 5955–5988. ISSN: 0021-9991. DOI: https://doi.org/10.1016/j.jcp.2012.02.033.

[127] Stephan Wulfinghoff et al. "A low-order locking-free hybrid discontinuous Galerkin element formulation for large deformations". In: *Computer Methods in Applied Mechanics and Engineering* 323 (2017), pp. 353–372. ISSN: 0045-7825. DOI: https://doi.org/10.1016/j.cma.2017.05.018.

[128] David S. Malkus and Thomas J.R. Hughes. "Mixed finite element methods — Reduced and selective integration techniques: A unification of concepts". In: *Computer Methods in Applied Mechanics and Engineering* 15.1 (1978), pp. 63–81. ISSN: 0045-7825. DOI: https://doi.org/10.1016/0045-7825(78)90005-1.

[129] J.C. Simo, R.L. Taylor, and K.S. Pister. "Variational and projection methods for the volume constraint in finite deformation elastoplasticity". In: *Computer Methods in Applied Mechanics and Engineering* 51.1 (1985), pp. 177–208. ISSN: 0045-7825. DOI: https://doi.org/10.1016/0045-7825(85)90033-7.

[130] M. Pastor, M. Quecedo, and O.C. Zienkiewicz. "A mixed displacement-pressure formulation for numerical analysis of plastic failure". In: *Computers & Structures* 62.1 (1997), pp. 13–23. ISSN: 0045-7949. DOI: https://doi.org/10.1016/S0045-7949(96)00208-8.

[131] K.P. Li and S. Cescotto. "An 8-node brick element with mixed formulation for large deformation analyses". In: *Computer Methods in Applied Mechanics and Engineering* 141.1 (1997), pp. 157–204. ISSN: 0045-7825. DOI: https://doi.org/10.1016/S0045-7825(96)01071-7.

[132] J. Bonet and A. J. Burton. "A simple average nodal pressure tetrahedral element for incompressible and nearly incompressible dynamic explicit applications". In: *Communications in Numerical Methods in Engineering* 14.5 (1998), pp. 437–449. DOI: https://doi.org/10.1002/(SICI)1099-0887(199805)14:5<437::AID-CNM162>3.0.CO;2-W.

[133] M. Chiumenti, M. Cervera, and R. Codina. "A mixed three-field FE formulation for stress accurate analysis including the incompressible limit". In: *Computer Methods in Applied Mechanics and Engineering* 283 (2015), pp. 1095–1116. ISSN: 0045-7825. DOI: https://doi.org/10.1016/j.cma.2014.08.004.

[134] Peter Wriggers. "Nonlinear Finite Element Methods". In: vol. 4. Jan. 2008. DOI: https://doi.org/10.1007/978-3-642-56865-7.

[135] I. Babuska, B. A. Szabo, and I. N. Katz. "The p-Version of the Finite Element Method". In: *SIAM Journal on Numerical Analysis* 18.3 (1981), pp. 515–545. DOI: https://doi.org/10.1137/0718033.

[136] A. Düster et al. "A Numerical Investigation of High-Order Finite Elements for Problems of Elastoplasticity". In: *Journal of Scientific Computing* 17.1 (Dec. 2002), pp. 397–404. ISSN: 1573-7691. DOI: https://doi.org/10.1023/A:1015189706770.

[137] Alexander Düster, Stefan Hartmann, and Ernst Rank. "p-FEM applied to finite isotropic hyperelastic bodies". In: *Computer Methods in Applied Mechanics and Engineering* 192.47 (2003), pp. 5147–5166. ISSN: 0045-7825. DOI: https://doi.org/10.1016/j.cma.2003.07.003.

[138] T.J.R. Hughes, J.A. Cottrell, and Y. Bazilevs. "Isogeometric analysis: CAD, finite elements, NURBS, exact geometry and mesh refinement". In: *Computer Methods in Applied Mechanics and Engineering* 194.39 (2005), pp. 4135–4195. ISSN: 0045-7825. DOI: https://doi.org/10.1016/j.cma.2004.10.008.

[139] L. Beirão da Veiga, C. Lovadina, and A. Reali. "Avoiding shear locking for the Timoshenko beam problem via isogeometric collocation methods". In: *Computer Methods in Applied Mechanics and Engineering* 241-244 (2012), pp. 38–51. ISSN: 0045-7825. DOI: https://doi.org/10.1016/j.cma.2012.05.020.

[140] Chien H. Thai et al. "Generalized shear deformation theory for functionally graded isotropic and sandwich plates based on isogeometric approach". In: *Computers & Structures* 141 (2014), pp. 94–112. ISSN: 0045-7949. DOI: https://doi.org/10.1016/j.compstruc.2014.04.003.

[141] Shuohui Yin et al. "Isogeometric locking-free plate element: A simple first order shear deformation theory for functionally graded plates". In: *Composite Structures* 118 (2014), pp. 121–138. ISSN: 0263-8223. DOI: https://doi.org/10.1016/j.compstruct.2014.07.028.

[142] Ted Belytschko, Wing Kam Liu, and Brian Moran. *Nonlinear Finite Elements for Continua and Structures*. English. John Wiley & Sons, Ltd, 2000. DOI: https://doi.org/10.1055/s-2006-943830.

[143] Hamid Reza Bayat et al. "On the use of reduced integration in combination with discontinuous Galerkin discretization: application to volumetric and shear locking problems". In: *Advanced Modeling and Simulation in Engineering Sciences* 5.1 (May 2018),

p. 10. ISSN: 2213-7467. DOI: https://doi.org/10.1186/s40323-018-0103-x.

[144]   E.L. Wilson et al. "Incompatible Displacement Models". In: *Numerical and Computer Methods in Structural Mechanics*. Ed. by STEVEN J. FENVES et al. Academic Press, 1973, pp. 43–57. ISBN: 978-0-12-253250-4. DOI: https://doi.org/10.1016/B978-0-12-253250-4.50008-7.

[145]   J. C. Simo and M. S. Rifai. "A class of mixed assumed strain methods and the method of incompatible modes". In: *International Journal for Numerical Methods in Engineering* 29.8 (1990), pp. 1595–1638. DOI: https://doi.org/10.1002/nme.1620290802.

[146]   J. C. Simo and F. Armero. "Geometrically non-linear enhanced strain mixed methods and the method of incompatible modes". In: *International Journal for Numerical Methods in Engineering* 33.7 (1992), pp. 1413–1449. DOI: https://doi.org/10.1002/nme.1620330705.

[147]   D. S. Mueller-Hoeppe, S. Loehnert, and P. Wriggers. "A finite deformation brick element with inhomogeneous mode enhancement". In: *International Journal for Numerical Methods in Engineering* 78.10 (2009), pp. 1164–1187. DOI: https://doi.org/10.1002/nme.2523.

[148]   D J Beebe et al. "Functional hydrogel structures for autonomous flow control inside microfluidic channels". en. In: *Nature* 404.6778 (Apr. 2000), pp. 588–590. DOI: https://doi.org/10.1038/35007047.

[149]   Jing Wang et al. "Self-Actuated, Thermo-Responsive Hydrogel Valves for Lab on a Chip". In: *Biomedical Microdevices* 7.4 (Dec. 2005), pp. 313–322. ISSN: 1572-8781. DOI: https://doi.org/10.1007/s10544-005-6073-z.

[150]   Shannon E. Bakarich et al. "4D Printing with Mechanically Robust, Thermally Actuating Hydrogels". In: *Macromolecular Rapid Communications* 36.12 (2015), pp. 1211–1217. DOI: https://doi.org/10.1002/marc.201500079.

[151]   Daniel Buenger, Fuat Topuz, and Juergen Groll. "Hydrogels in sensing applications". In: *Progress in Polymer Science* 37.12 (2012), pp. 1678–1719. ISSN: 0079-6700. DOI: https://doi.org/10.1016/j.progpolymsci.2012.09.001.

[152] Ying Guan and Yongjun Zhang. "Boronic acid-containing hydrogels: synthesis and their applications". In: *Chem. Soc. Rev.* 42 (20 2013), pp. 8106–8121. DOI: `http://dx.doi.org/10.1039/C3CS60152H`.

[153] Guofa Cai et al. "Extremely Stretchable Strain Sensors Based on Conductive Self-Healing Dynamic Cross-Links Hydrogels for Human-Motion Detection". In: *Advanced Science* 4.2 (2017), p. 1600190. DOI: `https://doi.org/10.1002/advs.201600190`.

[154] Yan-Jun Liu et al. "Ultrasensitive Wearable Soft Strain Sensors of Conductive, Self-healing, and Elastic Hydrogels with Synergistic "Soft and Hard" Hybrid Networks". In: *ACS Applied Materials & Interfaces* 9.30 (2017), pp. 25559–25570. DOI: `https://doi.org/10.1021/acsami.7b07639`.

[155] Jeanie L. Drury and David J. Mooney. "Hydrogels for tissue engineering: scaffold design variables and applications". In: *Biomaterials* 24.24 (2003). Synthesis of Biomimetic Polymers, pp. 4337–4351. ISSN: 0142-9612. DOI: `https://doi.org/10.1016/S0142-9612(03)00340-5`.

[156] Gail Chan and David J Mooney. "New materials for tissue engineering: towards greater control over the biological response". en. In: *Trends Biotechnol* 26.7 (May 2008), pp. 382–392. DOI: `https://doi.org/10.1016/j.tibtech.2008.03.011`.

[157] Mustapha Jamal et al. "Bio-Origami Hydrogel Scaffolds Composed of Photocrosslinked PEG Bilayers". In: *Advanced Healthcare Materials* 2.8 (2013), pp. 1142–1150. DOI: `https://doi.org/10.1002/adhm.201200458`.

[158] Nasim Annabi et al. "25th anniversary article: Rational design and applications of hydrogels in regenerative medicine". en. In: *Adv Mater* 26.1 (Jan. 2014), pp. 85–123. DOI: `https://doi.org/10.1002/adma.201303233`.

[159] R. Dinarvand and A. D'Emanuele. "The use of thermoresponsive hydrogels for on-off release of molecules". In: *Journal of Controlled Release* 36.3 (1995), pp. 221–227. ISSN: 0168-3659. DOI: `https://doi.org/10.1016/0168-3659(95)00035-7`.

[160] Yong Qiu and Kinam Park. "Environment-sensitive hydrogels for drug delivery". In: *Advanced Drug Delivery Reviews* 53.3 (2001). Triggering in Drug Delivery Systems, pp. 321–339. ISSN: 0169-409X. DOI: https://doi.org/10.1016/S0169-409X(01)00203-4.

[161] N. A. Peppas et al. "Hydrogels in Biology and Medicine: From Molecular Principles to Bionanotechnology". In: *Advanced Materials* 18.11 (2006), pp. 1345–1360. DOI: https://doi.org/10.1002/adma.200501612.

[162] Jianyu Li and David J. Mooney. "Designing hydrogels for controlled drug delivery". In: *Nature Reviews Materials* 1.12 (Oct. 2016), p. 16071. ISSN: 2058-8437. DOI: https://doi.org/10.1038/natrevmats.2016.71.

[163] Heidi R. Culver, John R. Clegg, and Nicholas A. Peppas. "Analyte-Responsive Hydrogels: Intelligent Materials for Biosensing and Drug Delivery". In: *Accounts of Chemical Research* 50.2 (2017), pp. 170–178. DOI: https://doi.org/10.1021/acs.accounts.6b00533.

[164] Dirk Schmaljohann. "Thermo- and pH-responsive polymers in drug delivery". In: *Advanced Drug Delivery Reviews* 58.15 (2006). 2006 Supplementary Non-Thematic Collection, pp. 1655–1670. ISSN: 0169-409X. DOI: https://doi.org/10.1016/j.addr.2006.09.020.

[165] Andreas Richter et al. "Review on Hydrogel-based pH Sensors and Microsensors". In: *Sensors* 8.1 (2008), pp. 561–581. ISSN: 1424-8220. DOI: https://doi.org/10.3390/s8010561.

[166] Toyoichi Tanaka et al. "Phase Transitions in Ionic Gels". In: *Phys. Rev. Lett.* 45 (20 Nov. 1980), pp. 1636–1639. DOI: https://doi.org/10.1103/PhysRevLett.45.1636.

[167] Toyoichi Tanaka et al. "Collapse of Gels in an Electric Field". In: *Science* 218.4571 (1982), pp. 467–469. DOI: https://doi.org/10.1126/science.218.4571.467.

[168] Atsushi Suzuki and Toyoichi Tanaka. "Phase transition in polymer gels induced by visible light". In: *Nature* 346.6282 (July 1990), pp. 345–347. ISSN: 1476-4687. DOI: https://doi.org/10.1038/346345a0.

[169]   Roberto Brighenti and Mattia Pancrazio Cosma. "Mechanics of multi-stimuli temperature-responsive hydrogels". In: *Journal of the Mechanics and Physics of Solids* 169 (2022), p. 105045. ISSN: 0022-5096. DOI: https://doi.org/10.1016/j.jmps.2022.105045.

[170]   Robert A. Barry and Pierre Wiltzius. "Humidity-Sensing Inverse Opal Hydrogels". In: *Langmuir* 22.3 (2006), pp. 1369–1374. URL: https://doi.org/10.1021/la0519094.

[171]   Yang Liu et al. "Long-Period Grating Relative Humidity Sensor With Hydrogel Coating". In: *IEEE Photonics Technology Letters* 19.12 (2007), pp. 880–882. DOI: https://doi.org/10.1109/LPT.2007.897551.

[172]   Lev E Bromberg and Eyal S Ron. "Temperature-responsive gels and thermogelling polymer matrices for protein and peptide delivery". In: *Advanced Drug Delivery Reviews* 31.3 (1998). Peptide Release from Polymer Matrices, pp. 197–221. ISSN: 0169-409X. DOI: https://doi.org/10.1016/S0169-409X(97)00121-X.

[173]   S. R. Sershen et al. "Temperature-sensitive polymer–nanoshell composites for photothermally modulated drug delivery". In: *Journal of Biomedical Materials Research* 51.3 (2000), pp. 293–298. DOI: https://doi.org/10.1002/1097-4636(20000905)51:3<293::AID-JBM1>3.0.CO;2-T.

[174]   Marianne E Harmon, Mary Tang, and Curtis W Frank. "A microfluidic actuator based on thermoresponsive hydrogels". In: *Polymer* 44.16 (2003), pp. 4547–4556. ISSN: 0032-3861. DOI: https://doi.org/10.1016/S0032-3861(03)00463-4.

[175]   Byeongmoon Jeong, Sung Wan Kim, and You Han Bae. "Thermosensitive sol–gel reversible hydrogels". In: *Advanced Drug Delivery Reviews* 64 (2012). MOST CITED PAPERS IN THE HISTORY OF ADVANCED DRUG DELIVERY REVIEWS: A TRIBUTE TO THE 25TH ANNIVERSARY OF THE JOURNAL, pp. 154–162. ISSN: 0169-409X. DOI: https://doi.org/10.1016/j.addr.2012.09.012.

[176]   Leda Klouda. "Thermoresponsive hydrogels in biomedical applications: A seven-year update". In: *European Journal of Pharmaceutics and Biopharmaceutics* 97 (2015). Polymers for Drug Delivery Systems, pp. 338–349. ISSN: 0939-6411. DOI: https://doi.org/10.1016/j.ejpb.2015.05.017.

[177] Lina Altomare et al. "Biopolymer-based strategies in the design of smart medical devices and artificial organs". en. In: *Int J Artif Organs* 41.6 (Apr. 2018), pp. 337–359. DOI: https://doi.org/10.1177/0391398818765323.

[178] Takehiko Gotoh, Yuko Nakatani, and Shuji Sakohara. "Novel synthesis of thermosensitive porous hydrogels". In: *Journal of Applied Polymer Science* 69.5 (1998), pp. 895–906. DOI: https://doi.org/10.1002/(SICI)1097-4628(19980801)69:5<895::AID-APP8>3.0.CO;2-H.

[179] Jie Zhang et al. "Dual thermo- and pH-sensitive poly(N-isopropylacrylamide-co-acrylic acid) hydrogels with rapid response behaviors". In: *Polymer* 48.6 (2007), pp. 1718–1728. ISSN: 0032-3861. DOI: https://doi.org/10.1016/j.polymer.2007.01.055.

[180] Shengqiang Cai and Zhigang Suo. "Mechanics and chemical thermodynamics of phase transition in temperature-sensitive hydrogels". In: *Journal of the Mechanics and Physics of Solids* 59.11 (2011), pp. 2259–2278. ISSN: 0022-5096. DOI: https://doi.org/10.1016/j.jmps.2011.08.008.

[181] Sajjad Ashraf et al. "Snapshot of phase transition in thermoresponsive hydrogel PNIPAM: Role in drug delivery and tissue engineering". In: *Macromolecular Research* 24.4 (Apr. 2016), pp. 297–304. ISSN: 2092-7673. DOI: 10.1007/s13233-016-4052-2. URL: https://doi.org/10.1007/s13233-016-4052-2.

[182] Narayan Bhattarai et al. "PEG-grafted chitosan as an injectable thermosensitive hydrogel for sustained protein release". In: *Journal of Controlled Release* 103.3 (2005), pp. 609–624. ISSN: 0168-3659. DOI: https://doi.org/10.1016/j.jconrel.2004.12.019.

[183] Weitai Wu et al. "Core–shell hybrid nanogels for integration of optical temperature-sensing, targeted tumor cell imaging, and combined chemo-photothermal treatment". In: *Biomaterials* 31.29 (2010), pp. 7555–7566. ISSN: 0142-9612. DOI: https://doi.org/10.1016/j.biomaterials.2010.06.030.

[184] Gertjan Vancoillie, Daniel Frank, and Richard Hoogenboom. "Thermoresponsive poly(oligo ethylene glycol acrylates)". In: *Progress in Polymer Science* 39.6 (2014), pp. 1074–1095. DOI: https://doi.org/10.1016/j.progpolymsci.2014.02.005.

[185] Daniele Boffi, Franco Brezzi, and Michel Fortin. *Mixed Finite Element Methods and Applications*. Vol. 44. Springer Berlin, Heidelberg, Jan. 2013. ISBN: 978-3-642-36518-8. DOI: `https://doi.org/10.1007/978-3-642-36519-5`.

[186] Ted Belytschko, Wing Liu, and Brian Moran. "Nonlinear Finite Elements For Continua and Structures". In: 2 (Jan. 2013).

[187] A. Valverde-González et al. "Computational modelling of hydrogen assisted fracture in polycrystalline materials". In: *International Journal of Hydrogen Energy* 47.75 (2022), pp. 32235–32251. ISSN: 0360-3199. DOI: `https://doi.org/10.1016/j.ijhydene.2022.07.117`.

[188] W. H. Johnson. "On Some Remarkable Changes Produced in Iron and Steel by the Action of Hydrogen and Acids". In: *Proceedings of the Royal Society of London* 23 (1875), pp. 168–179. DOI: `https://doi.org/10.1098/rspl.1874.0024`.

[189] Andrej Atrens et al. "Influence of Hydrogen on Steel Components for Clean Energy". In: *Corrosion and Materials Degradation* 1 (June 2018), p. 2. DOI: `https://doi.org/10.3390/cmd1010002`.

[190] I. M. Robertson et al. "Hydrogen Embrittlement Understood". In: *Metallurgical and Materials Transactions B* 46.3 (2015), pp. 1085–1103. ISSN: 10735623. DOI: `https://doi.org/10.1007/s11663-015-0325-y`.

[191] R. P. Gangloff. "Probabilistic fracture mechanics simulation of stress corrosion cracking using accelerated laboratory testing and multiscale modeling". In: *Corrosion* 72.7 (2016), pp. 862–880. ISSN: 00109312. DOI: `https://doi.org/10.5006/1920`.

[192] S. Lynch. "Discussion of some recent literature on hydrogen-embrittlement mechanisms: Addressing common misunderstandings". In: *Corrosion Reviews* 37.5 (2019), pp. 377–395. ISSN: 03346005. DOI: `https://doi.org/10.1515/corrrev-2019-0017`.

[193] Laura Vergani et al. "Hydrogen Effect on Fatigue Behavior of a Quenched&tempered Steel". In: *Procedia Engineering* 74 (2014). XVII International Colloquium on Mechanical Fatigue of Metals (ICMFM17), pp. 468–471. ISSN: 1877-7058. DOI: `https://doi.org/10.1016/j.proeng.2014.06.299`.

[194] M. Dadfarnia et al. "Recent advances in the study of structural materials compatibility with hydrogen". In: *Advanced Materials* 22.10 (2010), pp. 1128–1135. ISSN: 09359648. DOI: https://doi.org/10.1002/adma.200904354.

[195] Ivaylo H. Katzarov and A. T. Paxton. "Hydrogen embrittlement II. Analysis of hydrogen-enhanced decohesion across (111) planes in α -Fe". In: *Physical Review Materials* 1.3 (2017), pp. 1–10. DOI: https://doi.org/10.1103/PhysRevMaterials.1.033603.

[196] H. Yu, A. C. F. Cocks, and E. Tarleton. "Simulating hydrogen in fcc materials with discrete dislocation plasticity". In: *International Journal of Hydrogen Energy* 45.28 (2020), pp. 14565–14577. ISSN: 03603199. DOI: https://doi.org/10.1016/j.ijhydene.2020.01.118.

[197] S. S. Shishvan, Gábor Csányi, and V. S. Deshpande. "Hydrogen induced fast-fracture". In: *Journal of the Mechanics and Physics of Solids* 134 (2020), p. 103740. ISSN: 00280836. DOI: https://doi.org/10.1016/j.jmps.2019.103740.

[198] V. Olden, A. Alvaro, and O. M. Akselsen. "Hydrogen diffusion and hydrogen influenced critical stress intensity in an API X70 pipeline steel welded joint-Experiments and FE simulations". In: *International Journal of Hydrogen Energy* 37.15 (2012), pp. 11474–11486. ISSN: 03603199. DOI: https://doi.org/10.1016/j.ijhydene.2012.05.005.

[199] T. Matsumoto et al. "Threshold stress intensity factor for hydrogen-assisted cracking of CR-MO steel used as stationary storage buffer of a hydrogen refueling station". In: *International Journal of Hydrogen Energy* 42.11 (2017), pp. 7422–7428. ISSN: 03603199. DOI: https://doi.org/10.1016/j.ijhydene.2016.05.124.

[200] A. Díaz, J. M. Alegre, and I. I. Cuesta. "Numerical simulation of hydrogen embrittlement and local triaxiality effects in notched specimens". In: *Theoretical and Applied Fracture Mechanics* 90 (2017), pp. 294–302. ISSN: 01678442. DOI: https://doi.org/10.1016/j.tafmec.2017.06.017.

[201] P. K. Kristensen, C. F. Niordson, and E. Martínez-Pañeda. "Applications of phase field fracture in modelling hydrogen assisted failures". In: *Theoretical and Applied Fracture Mechanics* 110 (2020), p. 102837. DOI: https://doi.org/10.1016/j.tafmec.2020.102837.

[202] C. Moriconi, G. Hénaff, and D. Halm. "Cohesive zone modeling of fatigue crack propagation assisted by gaseous hydrogen in metals". In: *International Journal of Fatigue* 68 (2014), pp. 56–66. ISSN: 01421123. DOI: https://doi.org/10.1016/j.ijfatigue.2014.06.007.

[203] H. Yu et al. "A uniform hydrogen degradation law for high strength steels". In: *Engineering Fracture Mechanics* 157 (2016), pp. 56–71. ISSN: 00137944. DOI: https://doi.org/10.1016/j.engfracmech.2016.02.001.

[204] S. del Busto, C. Betegón, and E. Martínez-Pañeda. "A cohesive zone framework for environmentally assisted fatigue". In: *Engineering Fracture Mechanics* 185 (2017), pp. 210–226. ISSN: 00137944. DOI: https://doi.org/10.1016/j.engfracmech.2017.05.021.

[205] F. P. Duda et al. "A phase-field model for solute-assisted brittle fracture in elastic-plastic solids". In: *International Journal of Plasticity* 102 (2018), pp. 16–40. ISSN: 07496419. DOI: https://doi.org/10.1016/j.ijplas.2017.11.004.

[206] L. Anand, Y. Mao, and B. Talamini. "On modeling fracture of ferritic steels due to hydrogen embrittlement". In: *Journal of the Mechanics and Physics of Solids* 122 (2019), pp. 280–314. ISSN: 00225096. DOI: https://doi.org/10.1016/j.jmps.2018.09.012.

[207] C. Huang and X. Gao. "Phase field modeling of hydrogen embrittlement". In: *International Journal of Hydrogen Energy* 45.38 (2020), pp. 20053–20068. ISSN: 03603199. DOI: https://doi.org/10.1016/j.ijhydene.2020.05.015.

[208] Gustavo M. Castelluccio, Clint B. Geller, and David L. McDowell. "A rationale for modeling hydrogen effects on plastic deformation across scales in FCC metals". In: *International Journal of Plasticity* 111 (2018), pp. 72–84. ISSN: 07496419. DOI: https://doi.org/10.1016/j.ijplas.2018.07.009.

[209] Rakesh Kumar and Dhiraj K. Mahajan. "Hydrogen distribution in metallic polycrystals with deformation". In: *Journal of the Mechanics and Physics of Solids* 135 (2020), p. 103776. ISSN: 00225096. DOI: https://doi.org/10.1016/j.jmps.2019.103776.

[210] Eugene Ogosi et al. "Crystal plasticity based study to understand the interaction of hydrogen, defects and loading in austenitic stainless-steel single crystals". In: *International Journal of Hydrogen Energy* 45.56 (2020), pp. 32632–32647. ISSN: 03603199. DOI: https://doi.org/10.1016/j.ijhydene.2020.08.181.

[211] Abdelrahman Hussein et al. "The effect of hydrogen content and yield strength on the distribution of hydrogen in steel: a diffusion coupled micromechanical FEM study". In: *Acta Materialia* 209 (2021), p. 116799. ISSN: 13596454. DOI: https://doi.org/10.1016/j.actamat.2021.116799.

[212] Alireza Tondro and Hamidreza Abdolvand. "On the effects of texture and microstructure on hydrogen transport towards notch tips: A CPFE study". In: *International Journal of Plasticity* 152.January (2022), p. 103234. ISSN: 07496419. DOI: https://doi.org/10.1016/j.ijplas.2022.103234.

[213] Tuhin Das et al. "Understanding microstructural influences on hydrogen diffusion characteristics in martensitic steels using finite element analysis (FEA)". In: *International Journal of Hydrogen Energy* 47.2 (2022), pp. 1343–1357. ISSN: 03603199. DOI: https://doi.org/10.1016/j.ijhydene.2021.10.048.

[214] J. J. Rimoli and M. Ortiz. "A three-dimensional multiscale model of intergranular hydrogen-assisted cracking". In: *Philosophical Magazine* 90.21 (2010), pp. 2939–2963. ISSN: 14786435. DOI: https://doi.org/10.1080/14786431003752134.

[215] Ivano Benedetti, Vincenzo Gulizzi, and Alberto Milazzo. "Grain-boundary modelling of hydrogen assisted intergranular stress corrosion cracking". In: *Mechanics of Materials* 117.November 2017 (2018), pp. 137–151. ISSN: 01676636. DOI: https://doi.org/10.1016/j.mechmat.2017.11.001.

[216] Unai De Francisco, N. O. Larrosa, and Matthew J. Peel. "Development of a microstructural cohesive zone model for intergranular hydrogen environmentally assisted cracking". In: *Engineering Fracture Mechanics* 260 (2022), p. 108167. ISSN: 00137944. DOI: https://doi.org/10.1016/j.engfracmech.2021.108167.

[217]   A. Tehranchi and W. A. Curtin. "The role of atomistic simulations in probing hydrogen effects on plasticity and embrittlement in metals". In: *Engineering Fracture Mechanics* 216 (2019), p. 106502. ISSN: 00137944. DOI: https://doi.org/10.1016/j.engfracmech.2019.106502.

[218]   E. Martínez-Pañeda et al. "On the suitability of slow strain rate tensile testing for assessing hydrogen embrittlement susceptibility". In: *Corrosion Science* 163 (2020), p. 108291. ISSN: 0010-938X. DOI: https://doi.org/10.1016/j.corsci.2019.108291.

[219]   Antonio Alvaro, V. Olden, and Odd Magne Akselsen. "3D cohesive modelling of hydrogen embrittlement in the heat affected zone of an X70 pipeline steel - Part II". In: *International Journal of Hydrogen Energy* 39.7 (2014), pp. 3528–3541. ISSN: 03603199. DOI: https://doi.org/10.1016/j.ijhydene.2013.12.097.

[220]   Rebeca Fernández-Sousa, Covadonga Betegón, and Emilio Martínez-Pañeda. "Analysis of the influence of microstructural traps on hydrogen assisted fatigue". In: *Acta Materialia* 199 (2020), pp. 253–263. ISSN: 13596454. DOI: https://doi.org/10.1016/j.actamat.2020.08.030.

[221]   E. Martínez-Pañeda et al. "Strain gradient plasticity modeling of hydrogen diffusion to the crack tip". In: *International Journal of Hydrogen Energy* 41.24 (2016), pp. 10265–10274. ISSN: 03603199. DOI: https://doi.org/10.1016/j.ijhydene.2016.05.014.

[222]   Emilio Martínez-Pañeda, Susana del Busto, and C. Betegón. "Nonlocal plasticity effects on notch fracture mechanics". In: *Theoretical and Applied Fracture Mechanics* 92 (2017), pp. 276–287. ISSN: 01678442. DOI: https://doi.org/10.1016/j.tafmec.2017.09.007.

[223]   E. Orowan. "Fracture and Strength of Solids". In: *Reports on Progress in Physics* XII (1948), p. 185. DOI: https://doi.org/10.1088/0034-4885/12/1/309.

[224]   F. P. Duda et al. "A phase-field/gradient damage model for brittle fracture in elastic-plastic solids". In: *International Journal of Plasticity* 65 (2015), pp. 269–296. ISSN: 07496419. DOI: https://doi.org/10.1016/j.ijplas.2014.09.005.

[225] P. K. Kristensen, C. F. Niordson, and E. Martínez-Pañeda. "An assessment of phase field fracture: crack initiation and growth". In: *Philosophical Transactions of the Royal Society A: Mathematical, Physical and Engineering Sciences* 379 (2021), p. 20210021. DOI: `https://doi.org/10.1098/rsta.2021.0021`.

[226] D. E. Jiang and E. A. Carter. In: *Acta Materialia* 52.16 (2004), pp. 4801–4807. ISSN: 13596454. DOI: `https://doi.org/10.1016/j.actamat.2004.06.037`.

[227] A. Alvaro et al. "Hydrogen embrittlement in nickel, visited by first principles modeling, cohesive zone simulation and nanomechanical testing". In: *International Journal of Hydrogen Energy* 40.47 (2015), pp. 16892–16900. ISSN: 03603199. DOI: `https://doi.org/10.1016/j.ijhydene.2015.06.069`.

[228] G. Papazafeiropoulos, M. Muñiz-Calvente, and E. Martínez-Pañeda. "Abaqus2Matlab: A suitable tool for finite element post-processing". In: *Advances in Engineering Software* 105 (2017), pp. 9–16. ISSN: 18735339. DOI: `https://doi.org/10.1016/j.advengsoft.2017.01.006`.

[229] Jia He Ai et al. "Hydrogen diffusion and trapping in a precipitation-hardened nickel-copper-aluminum alloy Monel K-500 (UNS N05500)". In: *Acta Materialia* 61.9 (2013), pp. 3186–3199. ISSN: 13596454. DOI: `https://doi.org/10.1016/j.actamat.2013.02.007`.

[230] W. Y. Choo and J. Y. Lee. "Thermal Analysis of Trapped Hydrogen in Pure Iron". In: *Metallurgical Transactions A* 13 (1982), pp. 423–427. DOI: `https://doi.org/10.1007/BF02642424`.

[231] A. Valverde-González et al. "A phase field approach to fracture for hyperelastic and visco-hyperelastic materials applied to pre-stressed cylindrical structures". In: *Mechanics of Advanced Materials and Structures* 0.0 (2022), pp. 1–20. DOI: `https://doi.org/10.1080/15376494.2022.2121452`.

[232] N.K. Jha, J. Merodio, and J. Reinoso. "A general non-local constitutive relation for residually stressed solids". In: *Mechanics Research Communications* 101 (2019), p. 103421. ISSN: 0093-6413. DOI: `https://doi.org/10.1016/j.mechrescom.2019.103421`.

[233] Christian Linder, Mykola Tkachuk, and Christian Miehe. "A micromechanically motivated diffusion-based transient network model and its incorporation into finite rubber viscoelasticity". In: *Journal of the Mechanics and Physics of Solids* 59.10 (2011), pp. 2134–2156. ISSN: 0022-5096. DOI: `https://doi.org/10.1016/j.jmps.2011.05.005`.

[234] Christian Miehe and Joachim Keck. "Superimposed finite elastic–viscoelastic–plastoelastic stress response with damage in filled rubbery polymers. Experiments, modelling and algorithmic implementation". In: *Journal of the Mechanics and Physics of Solids* 48.2 (2000), pp. 323–365. ISSN: 0022-5096. DOI: `https://doi.org/10.1016/S0022-5096(99)00017-4`.

[235] J.C. Simo. "On a fully three-dimensional finite-strain viscoelastic damage model: Formulation and computational aspects". In: *Computer Methods in Applied Mechanics and Engineering* 60.2 (1987), pp. 153–173. ISSN: 0045-7825. DOI: `https://doi.org/10.1016/0045-7825(87)90107-1`.

[236] Sanjay Govindjee and Juan C. Simo. "Mullins' effect and the strain amplitude dependence of the storage modulus". In: *International Journal of Solids and Structures* 29.14 (1992), pp. 1737–1751. ISSN: 0020-7683. DOI: `https://doi.org/10.1016/0020-7683(92)90167-R`.

[237] G. A. HOLZAPFEL. "ON LARGE STRAIN VISCOELASTICITY: CONTINUUM FORMULATION AND FINITE ELEMENT APPLICATIONS TO ELASTOMERIC STRUCTURES". In: *International Journal for Numerical Methods in Engineering* 39.22 (1996), pp. 3903–3926. DOI: `https://doi.org/10.1002/(SICI)1097-0207(19961130)39:22<3903::AID-NME34>3.0.CO;2-C`.

[238] M. Kaliske and H. Rothert. "Formulation and implementation of three-dimensional viscoelasticity at small and finite strains". In: *Computational Mechanics* 19.3 (1997), pp. 228–239. ISSN: 1432-0924. DOI: `https://doi.org/10.1007/s004660050171`.

[239] N.K. Jha et al. "Constitutive modeling framework for residually stressed viscoelastic solids at finite strains". In: *Mechanics Research Communications* 95 (2019), pp. 79–84. ISSN: 0093-6413. DOI: `https://doi.org/10.1016/j.mechrescom.2019.01.003`.

[240] J.S. Bergström and M.C. Boyce. "Constitutive modeling of the large strain time-dependent behavior of elastomers". In: *Journal of the Mechanics and Physics of Solids* 46.5 (1998), pp. 931–954. ISSN: 0022-5096. DOI: https://doi.org/10.1016/S0022-5096(97)00075-6.

[241] Stefanie Reese and Sanjay Govindjee. "A theory of finite viscoelasticity and numerical aspects". In: *International Journal of Solids and Structures* 35.26 (1998), pp. 3455–3482. ISSN: 0020-7683. DOI: https://doi.org/10.1016/S0020-7683(97)00217-5.

[242] J. Merodio and K. R. Rajagopal. "On Constitutive Equations For Anisotropic Nonlinearly Viscoelastic Solids". In: *Mathematics and Mechanics of Solids* 12.2 (2007), pp. 131–147. DOI: https://doi.org/10.1177/1081286505055472.

[243] Oscar Lopez-Pamies, Martín I. Idiart, and Toshio Nakamura. "Cavitation in elastomeric solids: I—A defect-growth theory". In: *Journal of the Mechanics and Physics of Solids* 59.8 (2011), pp. 1464–1487. ISSN: 0022-5096. DOI: https://doi.org/10.1016/j.jmps.2011.04.015.

[244] Wolfgang G. Knauss. "A review of fracture in viscoelastic materials". In: *International Journal of Fracture* 196.1 (2015), pp. 99–146. ISSN: 1573-2673. DOI: https://doi.org/10.1007/s10704-015-0058-6.

[245] Michele L. Cooke and David D. Pollard. "Fracture propagation paths under mixed mode loading within rectangular blocks of polymethyl methacrylate". In: *Journal of Geophysical Research: Solid Earth* 101.B2 (1996), pp. 3387–3400. DOI: https://doi.org/10.1029/95JB02507.

[246] Antonio J Pons and Alain Karma. "Helical crack-front instability in mixed-mode fracture". In: *Nature* 464.7285 (2010), pp. 85–89. ISSN: 00280836. DOI: https://doi.org/10.1038/nature08862.

[247] R. A. Schapery. "Correspondence principles and a generalizedJ integral for large deformation and fracture analysis of viscoelastic media". In: *International Journal of Fracture* 25.3 (July 1984), pp. 195–223. ISSN: 1573-2673. DOI: https://doi.org/10.1007/BF01140837.

[248] N. Aït Hocine, M. Naït Abdelaziz, and A. Imad. "Fracture problems of rubbers: J-integral estimation based upon η factors and an investigation on the strain energy density distribution as a local criterion". In: *International Journal of Fracture* 117.1 (Sept. 2002), pp. 1–23. ISSN: 1573-2673. DOI: https://doi.org/10.1023/A:1020967429222.

[249] Martin Kroon. "Steady-state crack growth in rubber-like solids". In: *International Journal of Fracture* 169.1 (May 2011), pp. 49–60. ISSN: 1573-2673. DOI: https://doi.org/10.1007/s10704-010-9583-5.

[250] Gordon Geißler et al. "Peel process simulation of sealed polymeric film computational modelling of experimental results". In: *Engineering Computations* 24.6 (Jan. 2007), pp. 586–607. ISSN: 0264-4401. DOI: https://doi.org/10.1108/02644400710774798.

[251] Imadeddin Zreid, Robert Fleischhauer, and Michael Kaliske. "A thermomechanically coupled viscoelastic cohesive zone model at large deformation". In: *International Journal of Solids and Structures* 50.25 (2013), pp. 4279–4291. ISSN: 0020-7683. DOI: https://doi.org/10.1016/j.ijsolstr.2013.08.031.

[252] Thomas L. Warren et al. "A non-ordinary state-based peridynamic method to model solid material deformation and fracture". In: *International Journal of Solids and Structures* 46.5 (2009), pp. 1186–1195. ISSN: 0020-7683. DOI: https://doi.org/10.1016/j.ijsolstr.2008.10.029.

[253] Yunke Huang et al. "Peridynamic model for visco-hyperelastic material deformation in different strain rates". In: *Continuum Mechanics and Thermodynamics* (Nov. 2019). ISSN: 1432-0959. DOI: https://doi.org/10.1007/s00161-019-00849-0.

[254] Charlotte Kuhn and Ralf Müller. "A continuum phase field model for fracture". In: *Engineering Fracture Mechanics* 77.18 (2010), pp. 3625–3634. ISSN: 00137944. DOI: https://doi.org/10.1016/j.engfracmech.2010.08.009.

[255] J.-Y. Wu. "A unified phase-field theory for the mechanics of damage and quasi-brittle failure". In: *Journal of the Mechanics and Physics of Solids* 103 (2017), pp. 72–99. ISSN: 00225096. DOI: https://10.1016/j.jmps.2017.03.015.

[256] J.-Y. Wu and V. P. Nguyen. "A length scale insensitive phase-field damage model for brittle fracture". In: *Journal of the Mechanics and Physics of Solids* 119 (2018), pp. 20–42. ISSN: 00225096. DOI: `https://10.1016/j.jmps.2018.06.006`.

[257] Charlotte Kuhn, Timo Noll, and Ralf Müller. "On phase field modeling of ductile fracture". In: *GAMM Mitteilungen* 39.1 (2016), pp. 35–54. ISSN: 09367195. DOI: `https://doi.org/10.1002/gamm.201610003`.

[258] R. Alessi et al. "Comparison of Phase-Field Models of Fracture Coupled with Plasticity". In: *Advances in Computational Plasticity*. Cham: Springer International Publishing, 2018, pp. 1–21. ISBN: 978-3-319-60884-6. DOI: `https://doi.org/10.1007/978-3-319-60885-3\_1`.

[259] A. Dean et al. "A phase field approach for ductile fracture of short fibre reinforced composites". In: *Theoretical and Applied Fracture Mechanics* 106 (2020), p. 102495. ISSN: 0167-8442. DOI: `https://doi.org/10.1016/j.tafmec.2020.102495`.

[260] Bo Yin and Michael Kaliske. "A ductile phase-field model based on degrading the fracture toughness: Theory and implementation at small strain". In: *Computer Methods in Applied Mechanics and Engineering* 366 (2020), p. 113068. ISSN: 0045-7825. DOI: `https://doi.org/10.1016/j.cma.2020.113068`.

[261] Siamak S. Shishvan, Saeid Assadpour-asl, and Emilio Martínez-Pañeda. "A mechanism-based gradient damage model for metallic fracture". In: *Engineering Fracture Mechanics* 255 (2021), p. 107927. ISSN: 0013-7944. DOI: `https://doi.org/10.1016/j.engfracmech.2021.107927`.

[262] Bin Li et al. "Phase-field modeling and simulation of fracture in brittle materials with strongly anisotropic surface energy". In: *International Journal for Numerical Methods in Engineering* 102.3-4 (2015), pp. 711–727. DOI: `https://doi.org/10.1002/nme.4726`.

[263] Arun Raina and Christian Miehe. "A phase-field model for fracture in biological tissues". In: *Biomechanics and Modeling in Mechanobiology* 15.3 (June 2016), pp. 479–496. ISSN: 1617-7940. DOI: `https://doi.org/10.1007/s10237-015-0702-0`.

[264] Osman Gültekin, Hüsnü Dal, and Gerhard A. Holzapfel. "Numerical aspects of anisotropic failure in soft biological tissues favor energy-based criteria: A rate-dependent anisotropic crack phase-field model". In: *Computer Methods in Applied Mechanics and Engineering* 331 (2018), pp. 23–52. ISSN: 0045-7825. DOI: https://doi.org/10.1016/j.cma.2017.11.008.

[265] J. Storm, D. Supriatna, and M. Kaliske. "The concept of representative crack elements for phase-field fracture: Anisotropic elasticity and thermo-elasticity". In: *International Journal for Numerical Methods in Engineering* 121.5 (2020), pp. 779–805. DOI: https://doi.org/10.1002/nme.6244.

[266] Bo Yin and Michael Kaliske. "An anisotropic phase-field model based on the equivalent crack surface energy density at finite strain". In: *Computer Methods in Applied Mechanics and Engineering* 369 (2020), p. 113202. ISSN: 0045-7825. DOI: https://doi.org/10.1016/j.cma.2020.113202.

[267] Christian Steinke et al. "A comparative study of the r-adaptive material force approach and the phase-field method in dynamic fracture". In: *International Journal of Fracture* 201.1 (Sept. 2016), pp. 97–118. ISSN: 1573-2673. DOI: https://doi.org/10.1007/s10704-016-0125-7.

[268] H.L. Ren et al. "An explicit phase field method for brittle dynamic fracture". In: *Computers & Structures* 217 (2019), pp. 45–56. ISSN: 0045-7949. DOI: https://doi.org/10.1016/j.compstruc.2019.03.005.

[269] J. Reinoso, M. Paggi, and C. Linder. "Phase field modeling of brittle fracture for enhanced assumed strain shells at large deformations: formulation and finite element implementation". In: *Computational Mechanics* 59.6 (2017), pp. 981–1001. ISSN: 01787675. DOI: https://doi.org/10.1007/s00466-017-1386-3.

[270] V. Carollo et al. "Recent advancements on the phase field approach to brittle fracture for heterogeneous materials and structures". In: *Advanced Modeling and Simulation in Engineering Sciences* 5.1 (May 2018), p. 8. ISSN: 2213-7467. DOI: https://doi.org/10.1186/s40323-018-0102-y.

[271] T. Guillén-Hernández et al. "A micromechanical analysis of inter-fiber failure in long reinforced composites based on the phase field approach of fracture combined with the cohesive zone model". In: *International Journal of Fracture* 220.2 (Dec. 2019), pp. 181–203. ISSN: 1573-2673. DOI: https://doi.org/10.1007/s10704-019-00384-8.

[272] A. Quintanas-Corominas et al. "A phase field approach to simulate intralaminar and translaminar fracture in long fiber composite materials". In: *Composite Structures* 220 (2019), pp. 899–911. ISSN: 02638223. DOI: https://doi.org/10.1016/j.compstruct.2019.02.007.

[273] Rilin Shen, Haim Waisman, and Licheng Guo. "Fracture of viscoelastic solids modeled with a modified phase field method". In: *Computer Methods in Applied Mechanics and Engineering* 346 (2019), pp. 862–890. ISSN: 0045-7825. DOI: https://doi.org/10.1016/j.cma.2018.09.018.

[274] Pascal J. Loew, Bernhard Peters, and Lars A.A. Beex. "Rate-dependent phase-field damage modeling of rubber and its experimental parameter identification". In: *Journal of the Mechanics and Physics of Solids* 127 (2019), pp. 266–294. ISSN: 0022-5096. DOI: https://doi.org/10.1016/j.jmps.2019.03.022.

[275] Bo Yin and Michael Kaliske. "Fracture simulation of viscoelastic polymers by the phase-field method". In: *Computational Mechanics* 65 (2020), p. 293309. ISSN: 1432-0924. DOI: https://doi.org/10.1007/s00466-019-01769-1.

[276] J. Song et al. "Coupling of phase field and viscoplasticity for modelling cyclic softening and crack growth under fatigue". In: *European Journal of Mechanics - A/Solids* 92 (Nov. 2021), p. 104472. DOI: https://doi.org/10.1016/j.euromechsol.2021.104472.

[277] Franz Dammaß, Marreddy Ambati, and Markus Kästner. "A unified phase-field model of fracture in viscoelastic materials". In: *Continuum Mechanics and Thermodynamics* 33.4 (July 2021), pp. 1907–1929. ISSN: 1432-0959. DOI: https://doi.org/10.1007/s00161-021-01013-3.

[278] P. Thamburaja et al. "Fracture of viscoelastic materials: FEM implementation of a non-local & rate form-based finite-deformation constitutive theory". In: *Computer Methods in Applied Mechanics and Engineering* 354 (2019), pp. 871–903. ISSN: 0045-7825. DOI: h ttps://doi.org/10.1016/j.cma.2019.05.032.

[279] K. Sarah et al. "Numerical simulations of damage and fracture in viscoelastic solids using a nonlocal fracture criterion". In: *Mechanics of Advanced Materials and Structures* 27.13 (2020), pp. 1085–1097. DOI: https://doi.org/10.1080/15376494.2020.1716414.

[280] Osman Gültekin, Hüsnü Dal, and Gerhard A. Holzapfel. "A phase-field approach to model fracture of arterial walls: Theory and finite element analysis". In: *Computer Methods in Applied Mechanics and Engineering* 312 (2016). Phase Field Approaches to Fracture, pp. 542–566. ISSN: 0045-7825. DOI: https://doi.org/10.1016/j.cma.2016.04.007.

[281] J. Rodríguez and J. Merodio. "Helical buckling and postbuckling of pre-stressed cylindrical tubes under finite torsion". In: *Finite Elements in Analysis and Design* 112 (2016), pp. 1–10. ISSN: 0168-874X. DOI: https://doi.org/10.1016/j.finel.2015.12.003.

[282] Jose Merodio and Ray W. Ogden. "Extension, inflation and torsion of a residually-stressed circular cylindrical tube". In: *Continuum Mechanics and Thermodynamics* 28.1 (Mar. 2016), pp. 157–174. DOI: https://doi.org/10.1007/s00161-015-0411-z.

[283] N.T. Nam et al. "The effect of initial stress on the propagation of surface waves in a layered half-space". In: *International Journal of Solids and Structures* 88-89 (2016), pp. 88–100. ISSN: 0020-7683. DOI: https://doi.org/10.1016/j.ijsolstr.2016.03.019.

[284] Jose Merodio and Raymond Ogden. *Constitutive Modelling of Solid Continua*. Vol. 262. Solid Mechanics and its Applications. Berlin: Springer, Nov. 2020. ISBN: 978-3-030-31546-7. DOI: https://doi.org/10.1007/978-3-030-31547-4.

[285] H. Dehghani et al. "Bifurcation and post-bifurcation of an inflated and extended residually-stressed circular cylindrical tube with application to aneurysms initiation and propagation in arterial wall tissue". In: *Finite Elements in Analysis and Design* 161 (2019),

pp. 51–60. ISSN: 0168-874X. DOI: https://doi.org/10.1016/j.finel.2019.04.004.

[286]   Teng Li et al. "Stretchability of thin metal films on elastomer substrates". In: *Applied Physics Letters* 85.16 (2004), pp. 3435–3437. DOI: https://doi.org/10.1063/1.1806275.

[287]   Teng Li, Zhao Zhang, and Benoit Michaux. "Competing failure mechanisms of thin metal films on polymer substrates under tension". In: *Theoretical and Applied Mechanics Letters* 1.4 (2011), p. 041002. ISSN: 2095-0349. DOI: https://doi.org/10.1063/2.1104102.

[288]   Jose Merodio, Ray W. Ogden, and Javier Rodrguez. "The influence of residual stress on finite deformation elastic response". In: *International Journal of Non-Linear Mechanics* 56 (Nov. 2013), pp. 43–49. DOI: https://doi.org/10.1016/j.ijnonlinmec.2013.02.010.

[289]   D. Balzani, J. Schröder, and D. Gross. "Numerical simulation of residual stresses in arterial walls". In: *Computational Materials Science* 39.1 (2007). Proceedings of the 15th International Workshop on Computational Mechanics of Materials, pp. 117–123. ISSN: 0927-0256. DOI: https://doi.org/10.1016/j.commatsci.2005.11.014.

[290]   Richard Ostwald, Ellen Kuhl, and Andreas Menzel. "On the implementation of finite deformation gradient-enhanced damage models". In: *Computational Mechanics* 64.3 (Sept. 2019), pp. 847–877. ISSN: 1432-0924. DOI: https://doi.org/10.1007/s00466-019-01684-5.

[291]   Yousef Navidtehrani, Covadonga Betegón, and Emilio Martínez-Pañeda. "A Unified Abaqus Implementation of the Phase Field Fracture Method Using Only a User Material Subroutine". In: *Materials* 14.8 (2021). ISSN: 1996-1944. DOI: https://doi.org/10.3390/ma14081913.

[292]   Yousef Navidtehrani, Covadonga Betegón, and Emilio Martínez-Pañeda. "A simple and robust Abaqus implementation of the phase field fracture method". In: *Applications in Engineering Science* 6 (2021), p. 100050. ISSN: 2666-4968. DOI: https://doi.org/10.1016/j.apples.2021.100050.

[293] Christian Hortig. "Local and non-local thermomechanical modeling and finite-element simulation of high-speed cutting". PhD thesis. Jan. 2010. DOI: https://doi.org/10.17877/DE290R-15992.

[294] Christian Miehe and Lisa-Marie Schänzel. "Phase field modeling of fracture in rubbery polymers. Part I: Finite elasticity coupled with brittle failure". In: *Journal of the Mechanics and Physics of Solids* 65 (2014), pp. 93–113. ISSN: 0022-5096. DOI: https://doi.org/10.1016/j.jmps.2013.06.007.

[295] Arne Hansen-Dörr. "Phase Field Modelling and Simulation of Interface Failure". PhD thesis. July 2017. DOI: https://doi.org/10.13140/RG.2.2.33904.35847.

[296] D. Desena-Galarza et al. "Computational bifurcation analysis for hyperelastic residually stressed tubes under combined inflation and extension and aneurysms in arterial tissue". In: *Finite Elements in Analysis and Design* 197 (2021), p. 103636. ISSN: 0168-874X. DOI: https://doi.org/10.1016/j.finel.2021.103636.

[297] A. Valverde-González et al. "Locking treatment of penalty-based gradient-enhanced damage formulation for failure of compressible and nearly incompressible hyperelastic materials". In: *Computational Mechanics* 72.4 (Oct. 2023), pp. 635–662. ISSN: 1432-0924. DOI: https://doi.org/10.1007/s00466-023-02314-x.

[298] Juan C. Simo and Robert L. Taylor. "Quasi-incompressible finite elasticity in principal stretches. continuum basis and numerical algorithms". In: *Computer Methods in Applied Mechanics and Engineering* 85.3 (1991), pp. 273–310. ISSN: 0045-7825. DOI: https://doi.org/10.1016/0045-7825(91)90100-K.

[299] C. Miehe. "Aspects of the formulation and finite element implementation of large strain isotropic elasticity". In: *International Journal for Numerical Methods in Engineering* 37.12 (1994), pp. 1981–2004. DOI: https://doi.org/10.1002/nme.1620371202.

[300] Stefan Loehnert and Lukas Munk. "A mixed extended finite element for the simulation of cracks and heterogeneities in nearly incompressible materials and metal plasticity". In: *Engineering Fracture Mechanics* 237 (2020), p. 107217. ISSN: 0013-7944. DOI: https://doi.org/10.1016/j.engfracmech.2020.107217.

[301] R. Bargellini et al. "A non-local finite element based on volumetric strain gradient: Application to ductile fracture". In: *Computational Materials Science* 45.3 (2009). Proceedings of the 17th International Workshop on Computational Mechanics of Materials, pp. 762–767. ISSN: 0927-0256. DOI: https://doi.org/10.1016/j.commatsci.2008.09.020.

[302] R. Alessi, F. Freddi, and L. Mingazzi. "Phase-field numerical strategies for deviatoric driven fractures". In: *Computer Methods in Applied Mechanics and Engineering* 359 (2020), p. 112651. ISSN: 0045-7825. DOI: https://doi.org/10.1016/j.cma.2019.112651.

[303] Katrin Mang, Thomas Wick, and Winnifried Wollner. "A phase-field model for fractures in nearly incompressible solids". In: *Computational Mechanics* 65.1 (Jan. 2020), pp. 61–78. ISSN: 1432-0924. DOI: https://doi.org/10.1007/s00466-019-01752-w.

[304] Fucheng Tian et al. "Mixed displacement–pressure-phase field framework for finite strain fracture of nearly incompressible hyperelastic materials". In: *Computer Methods in Applied Mechanics and Engineering* 394 (2022), p. 114933. ISSN: 0045-7825. DOI: https://doi.org/10.1016/j.cma.2022.114933.

[305] U. Andelfinger and E. Ramm. "EAS-elements for two-dimensional, three-dimensional, plate and shell structures and their equivalence to HR-elements". In: *International Journal for Numerical Methods in Engineering* 36.8 (1993), pp. 1311–1337. DOI: https://doi.org/10.1002/nme.1620360805.

[306] P. Betsch and E. Stein. "An assumed strain approach avoiding artificial thickness straining for a non-linear 4-node shell element". In: *Communications in Numerical Methods in Engineering* 11.11 (1995), pp. 899–909. DOI: https://doi.org/10.1002/cnm.1640111104.

[307] S. Klinkel, F. Gruttmann, and W. Wagner. "A continuum based three-dimensional shell element for laminated structures". In: *Computers & Structures* 71.1 (1999), pp. 43–62. ISSN: 0045-7949. DOI: https://doi.org/10.1016/S0045-7949(98)00222-3.

[308] R. Eberlein and P. Wriggers. "Finite element concepts for finite elastoplastic strains and isotropic stress response in shells: theoretical and computational analysis". In: *Computer Methods in Applied Mechanics and Engineering* 171.3 (1999), pp. 243–279. ISSN:

0045-7825. DOI: https://doi.org/10.1016/S0045-7825(98)00212-6.

[309] J. Reinoso and A. Blázquez. "Application and finite element implementation of 7-parameter shell element for geometrically nonlinear analysis of layered CFRP composites". In: *Composite Structures* 139 (2016), pp. 263–276. ISSN: 0263-8223. DOI: https://doi.org/10.1016/j.compstruct.2015.12.009.

[310] J. Reinoso et al. "Surface-based and solid shell formulations of the 7-parameter shell model for layered CFRP and functionally graded power-based composite structures". In: *Mechanics of Advanced Materials and Structures* 26.15 (2019), pp. 1271–1289. DOI: https://doi.org/10.1080/15376494.2018.1432802.

[311] P. Wriggers and S. Reese. "A note on enhanced strain methods for large deformations". In: *Computer Methods in Applied Mechanics and Engineering* 135.3 (1996), pp. 201–209. ISSN: 0045-7825. DOI: https://doi.org/10.1016/0045-7825(96)01037-7.

[312] Oliver Barfusz et al. "Gradient-extended damage analysis with reduced integration-based solid-shells at large deformations". In: *Computer Methods in Applied Mechanics and Engineering* 389 (2022), p. 114317. ISSN: 0045-7825. DOI: https://doi.org/10.1016/j.cma.2021.114317.

[313] T. Liebe, P. Steinmann, and A. Benallal. "Theoretical and computational aspects of a thermodynamically consistent framework for geometrically linear gradient damage". In: *Computer Methods in Applied Mechanics and Engineering* 190.49 (2001), pp. 6555–6576. ISSN: 0045-7825. DOI: https://doi.org/10.1016/S0045-7825(01)00250-X.

[314] Samuel Forest. "Micromorphic Approach for Gradient Elasticity, Viscoplasticity, and Damage". In: *Journal of Engineering Mechanics* 135.3 (2009), pp. 117–131. DOI: https://doi.org/10.1061/(ASCE)0733-9399(2009)135:3(117).

[315] J.C. Simo and T.J.R. Hughes. *Computational Inelasticity*. Interdisciplinary Applied Mathematics. Springer New York, 2000. ISBN: 9780387975207. DOI: https://doi.org/10.1007/b98904.

[316] M. Bischoff and E. Ramm. "Shear deformable shell elements for large strains and rotations". In: *International Journal for Numerical Methods in Engineering* 40.23 (1997), pp. 4427–4449. DOI: `https://doi.org/10.1002/(SICI)1097-0207(19971215)40:23<4427::AID-NME268>3.0.CO;2-9`.

[317] Christian Miehe. "A theoretical and computational model for isotropic elastoplastic stress analysis in shells at large strains". In: *Computer Methods in Applied Mechanics and Engineering* 155.3 (1998), pp. 193–233. ISSN: 0045-7825. DOI: `https://doi.org/10.1016/S0045-7825(97)00149-7`.

[318] P.R. Budarapu, J. Reinoso, and M. Paggi. "Concurrently coupled solid shell-based adaptive multiscale method for fracture". In: *Computer Methods in Applied Mechanics and Engineering* 319 (2017), pp. 338–365. ISSN: 0045-7825. DOI: `https://doi.org/10.1016/j.cma.2017.02.023`.

[319] T. Guillén-Hernández, J. Reinoso, and M. Paggi. "Phase field model for fracture analysis of functionally graded power-based shell structures". In: *Mechanics of Advanced Materials and Structures* 29.1 (2022), pp. 78–88. DOI: `https://doi.org/10.1080/15376494.2020.1751354`.

[320] S. Reese, P. Wriggers, and B.D. Reddy. "A new locking-free brick element technique for large deformation problems in elasticity". In: *Computers & Structures* 75.3 (2000), pp. 291–304. ISSN: 0045-7949. DOI: `https://doi.org/10.1016/S0045-7949(99)00137-6`.

[321] Min Kyoo Kang and Rui Huang. "A Variational Approach and Finite Element Implementation for Swelling of Polymeric Hydrogels Under Geometric Constraints". In: *Journal of Applied Mechanics* 77.6 (Aug. 2010). ISSN: 0021-8936. DOI: `https://doi.org/10.1115/1.4001715`.

[322] Shawn A. Chester and Lallit Anand. "A coupled theory of fluid permeation and large deformations for elastomeric materials". In: *Journal of the Mechanics and Physics of Solids* 58.11 (2010), pp. 1879–1906. ISSN: 0022-5096. DOI: `https://doi.org/10.1016/j.jmps.2010.07.020`.

[323] Jianying Hu, Nan Jiang, and Jianke Du. "Thermally controlled large deformation in temperature-sensitive hydrogels bilayers". In: *International Journal of Smart and Nano Materials* 12.4 (2021), pp. 450–471. DOI: `https://doi.org/10.1080/19475411.2021.1958091`.

[324] E.A. de Souza Neto et al. "Design of simple low order finite elements for large strain analysis of nearly incompressible solids". In: *International Journal of Solids and Structures* 33.20 (1996), pp. 3277–3296. ISSN: 0020-7683. DOI: `https://doi.org/10.1016/0020-7683(95)00259-6`.

[325] Ivo Babuška. "The finite element method with Lagrangian multipliers". In: *Numerische Mathematik* 20.3 (June 1973), pp. 179–192. ISSN: 0945-3245. DOI: `https://doi.org/10.1007/BF01436561`.

[326] F. Brezzi. "On the existence, uniqueness and approximation of saddle-point problems arising from lagrangian multipliers". en. In: *Revue française d'automatique, informatique, recherche opérationnelle. Analyse numérique* 8.R2 (1974), pp. 129–151. DOI: `https://doi.org/10.1051/m2an/197408R201291`.

[327] Andreas Krischok and Christian Linder. "On the enhancement of low-order mixed finite element methods for the large deformation analysis of diffusion in solids". In: *International Journal for Numerical Methods in Engineering* 106.4 (2016), pp. 278–297. DOI: `https://doi.org/10.1002/nme.5120`.

[328] Nikolaos Bouklas, Chad M. Landis, and Rui Huang. "A nonlinear, transient finite element method for coupled solvent diffusion and large deformation of hydrogels". In: *Journal of the Mechanics and Physics of Solids* 79 (2015), pp. 21–43. ISSN: 0022-5096. DOI: `https://doi.org/10.1016/j.jmps.2015.03.004`.

[329] Nikolaos Bouklas, Chad M. Landis, and Rui Huang. "Effect of Solvent Diffusion on Crack-Tip Fields and Driving Force for Fracture of Hydrogels". In: *Journal of Applied Mechanics* 82.8 (Aug. 2015). ISSN: 0021-8936. DOI: `https://doi.org/10.1115/1.4030587`.

[330] C. Miehe, S. Mauthe, and H. Ulmer. "Formulation and numerical exploitation of mixed variational principles for coupled problems of Cahn–Hilliard-type and standard diffusion in elastic solids". In: *International Journal for Numerical Methods in Engineering* 99.10 (2014), pp. 737–762. DOI: `https://doi.org/10.1002/nme.4700`.

[331]   Wei Hong et al. "A theory of coupled diffusion and large deformation in polymeric gels". In: *Journal of the Mechanics and Physics of Solids* 56.5 (2008), pp. 1779–1793. ISSN: 0022-5096. DOI: https://doi.org/10.1016/j.jmps.2007.11.010.

[332]   Paul J. Flory and John Rehner. "Statistical Mechanics of Cross-Linked Polymer Networks II. Swelling". In: *The Journal of Chemical Physics* 11.11 (1943), pp. 521–526. DOI: https://doi.org/10.1063/1.1723792.

[333]   Maurice L. Huggins. "Solutions of Long Chain Compounds". In: *The Journal of Chemical Physics* 9.5 (1941), pp. 440–440. DOI: https://doi.org/10.1063/1.1750930.

[334]   Paul J. Flory. "Thermodynamics of High Polymer Solutions". In: *The Journal of Chemical Physics* 10.1 (1942), pp. 51–61. DOI: https://doi.org/10.1063/1.1723621.

[335]   Wei Hong, Zishun Liu, and Zhigang Suo. "Inhomogeneous swelling of a gel in equilibrium with a solvent and mechanical load". In: *International Journal of Solids and Structures* 46.17 (2009), pp. 3282–3289. ISSN: 0020-7683. DOI: https://doi.org/10.1016/j.ijsolstr.2009.04.022.

[336]   Qing-Sheng Yang, Lian-Hua Ma, and Jun-Jun Shang. "The chemo-mechanical coupling behavior of hydrogels incorporating entanglements of polymer chains". In: *International Journal of Solids and Structures* 50.14 (2013), pp. 2437–2448. ISSN: 0020-7683. DOI: https://doi.org/10.1016/j.ijsolstr.2013.03.039.

[337]   E. Southern and A. G. Thomas. "Effect of constraints on the equilibrium swelling of rubber vulcanizates". In: *Journal of Polymer Science Part A: General Papers* 3.2 (1965), pp. 641–646. DOI: https://doi.org/10.1002/pol.1965.100030220.

[338]   Toyoichi Tanaka. "Kinetics of phase transition in polymer gels". In: *Physica A: Statistical Mechanics and its Applications* 140.1 (1986), pp. 261–268. ISSN: 0378-4371. DOI: https://doi.org/10.1016/0378-4371(86)90230-X.

[339]   Verónica Trujillo, Jungwook Kim, and Ryan C. Hayward. "Creasing instability of surface-attached hydrogels". In: *Soft Matter* 4 (3 2008), pp. 564–569. DOI: http://dx.doi.org/10.1039/B713263H.

[340] Jinhwan Yoon, Jungwook Kim, and Ryan C. Hayward. "Nucleation, growth, and hysteresis of surface creases on swelled polymer gels". In: *Soft Matter* 6 (22 2010), pp. 5807–5816. DOI: http://dx.doi.org/10.1039/C0SM00372G.

[341] Toyoichi Tanaka et al. "Mechanical instability of gels at the phase transition". In: *Nature* 325.6107 (Feb. 1987), pp. 796–798. ISSN: 1476-4687. DOI: https://doi.org/10.1038/325796a0.

[342] Murat Guvendiren, Jason A. Burdick, and Shu Yang. "Solvent induced transition from wrinkles to creases in thin film gels with depth-wise crosslinking gradients". In: *Soft Matter* 6 (22 2010), pp. 5795–5801. DOI: http://dx.doi.org/10.1039/C0SM00317D.

[343] Min Kyoo Kang and Rui Huang. "Swell-induced surface instability of confined hydrogel layers on substrates". In: *Journal of the Mechanics and Physics of Solids* 58.10 (2010), pp. 1582–1598. ISSN: 0022-5096. DOI: https://doi.org/10.1016/j.jmps.2010.07.008.

[344] Zhigen Wu, Nikolaos Bouklas, and Rui Huang. "Swell-induced surface instability of hydrogel layers with material properties varying in thickness direction". In: *International Journal of Solids and Structures* 50.3 (2013), pp. 578–587. ISSN: 0020-7683. DOI: https://doi.org/10.1016/j.ijsolstr.2012.10.022.

[345] William Toh et al. "Wrinkling of a Polymeric Gel During Transient Swelling". In: *Journal of Applied Mechanics* 82.6 (June 2015). ISSN: 0021-8936. DOI: https://doi.org/10.1115/1.4030327.

[346] Fan Xu and Michel Potier-Ferry. "A multi-scale modeling framework for instabilities of film/substrate systems". In: *Journal of the Mechanics and Physics of Solids* 86 (2016), pp. 150–172. ISSN: 0022-5096. DOI: https://doi.org/10.1016/j.jmps.2015.10.003.

[347] Berkin Dortdivanlioglu and Christian Linder. "Diffusion-driven swelling-induced instabilities of hydrogels". In: *Journal of the Mechanics and Physics of Solids* 125 (2019), pp. 38–52. ISSN: 0022-5096. DOI: https://doi.org/10.1016/j.jmps.2018.12.010.

[348] Arne Ilseng et al. "Buckling initiation in layered hydrogels during transient swelling". In: *Journal of the Mechanics and Physics of Solids* 128 (2019), pp. 219–238. ISSN: 0022-5096. DOI: https://doi.org/10.1016/j.jmps.2019.04.008.

[349]   Kwang Suk Oh et al. "Effect of Cross-Linking Density on Swelling Behavior of NIPA Gel Particles". In: *Macromolecules* 31.21 (1998), pp. 7328–7335. DOI: https://doi.org/10.1021/ma971554y.

[350]   R.A. Oriani and P.H. Josephic. "Equilibrium aspects of hydrogen-induced cracking of steels". In: *Acta Metallurgica* 22.9 (1974), pp. 1065–1074. ISSN: 0001-6160. DOI: https://doi.org/10.1016/0001-6160(74)90061-3.

[351]   A. Díaz et al. "Simulation of hydrogen permeation through pure iron for trapping and surface phenomena characterisation". In: *Theoretical and Applied Fracture Mechanics* 110 (2020), p. 102818. ISSN: 0167-8442. DOI: https://doi.org/10.1016/j.tafmec.2020.102818.

[352]   Rebeca Fernández-Sousa, Covadonga Betegón, and Emilio Martínez-Pañeda. "Cohesive zone modelling of hydrogen assisted fatigue crack growth: The role of trapping". In: *International Journal of Fatigue* 162 (2022), p. 106935. ISSN: 0142-1123. DOI: https://doi.org/10.1016/j.ijfatigue.2022.106935.

[353]   Javier Segurado, Ricardo A. Lebensohn, and Javier LLorca. "Chapter One - Computational Homogenization of Polycrystals". In: *Advances in Crystals and Elastic Metamaterials, Part 1*. Ed. by Mahmoud I. Hussein. Vol. 51. Advances in Applied Mechanics. Elsevier, 2018, pp. 1–114. DOI: https://doi.org/10.1016/bs.aams.2018.07.001.

[354]   Weiling Wang and Wei Wen. "Modeling in Crystal Plasticity: From Theory to Application". In: *Encyclopedia of Materials: Metals and Alloys*. Ed. by Francisca G. Caballero. Oxford: Elsevier, 2022, pp. 552–560. ISBN: 978-0-12-819733-2. DOI: https://doi.org/10.1016/B978-0-12-819726-4.00058-2.

[355]   Thomas Gasser, Ray Ogden, and Gerhard Holzapfel. "Hyperelastic modeling of arterial layers with distributed collagen fibre orientations". In: *Journal of the Royal Society, Interface / the Royal Society* 3 (Sept. 2005), pp. 15–35. DOI: https://doi.org/10.1098/rsif.2005.0073.

[356]   Heleen Fehervary et al. "How to implement user-defined fiber-reinforced hyperelastic materials in finite element software". In: *Journal of the Mechanical Behavior of Biomedical Materials* 110 (2020),

p. 103737. ISSN: 1751-6161. DOI: https://doi.org/10.1016/j.jmbbm.2020.103737.

[357] Thomas J. Pence. "Distortion of Anisotropic Hyperelastic Solids Under Pure Pressure Loading: Compressibility, Incompressibility and Near-Incompressibility". In: *Journal of Elasticity* 114.2 (Feb. 2014), pp. 251–273. ISSN: 1573-2681. DOI: https://doi.org/10.1007/s10659-013-9438-1.

[358] Marco Paggi et al. "Fatigue degradation and electric recovery in Silicon solar cells embedded in photovoltaic modules". In: *Scientific Reports* 4.1 (Mar. 2014), p. 4506. ISSN: 2045-2322. DOI: https://doi.org/10.1038/srep04506.

[359] Rui P. R. Cardoso et al. "Enhanced assumed strain (EAS) and assumed natural strain (ANS) methods for one-point quadrature solid-shell elements". In: *International Journal for Numerical Methods in Engineering* 75.2 (2008), pp. 156–187. DOI: https://doi.org/10.1002/nme.2250.

[360] Z. Liu, J. Reinoso, and M. Paggi. "Phase field modeling of brittle fracture in large-deformation solid shells with the efficient quasi-Newton solution and global–local approach". In: *Computer Methods in Applied Mechanics and Engineering* 399 (2022), p. 115410. ISSN: 0045-7825. DOI: https://doi.org/10.1016/j.cma.2022.115410.

[361] Instron. *Model 68SC-5 Single Column Table Model Preinstallation Manual*. English. Instron. 2020. 68 pp.

[362] Somdatta Goswami et al. "Transfer learning enhanced physics informed neural network for phase-field modeling of fracture". In: *Theoretical and Applied Fracture Mechanics* 106 (2020), p. 102447. ISSN: 0167-8442. DOI: https://doi.org/10.1016/j.tafmec.2019.102447.

[363] S.Z. Feng et al. "A phase field and deep-learning based approach for accurate prediction of structural residual useful life". In: *Computer Methods in Applied Mechanics and Engineering* 383 (2021), p. 113885. ISSN: 0045-7825. DOI: https://doi.org/10.1016/j.cma.2021.113885.

[364] Yuan Feng et al. "Machine learning aided phase field method for fracture mechanics". In: *International Journal of Engineering Science* 169 (2021), p. 103587. ISSN: 0020-7225. DOI: https://doi.org/10.1016/j.ijengsci.2021.103587.

[365]   Xue-Ling Luo et al. "Data-driven enhanced phase field models for highly accurate prediction of Mode I and Mode II fracture". In: *Computer Methods in Applied Mechanics and Engineering* 400 (2022), p. 115535. ISSN: 0045-7825. DOI: https://doi.org/10.1016/j.cma.2022.115535.